Dissertation

submitted to the

Combined Faculties for the Natural Sciences and for
Mathematics

of the

Ruperto-Carola University of Heidelberg, Germany

for the degree of

Doctor of Natural Sciences

Put forward by

Dipl.-Phys.: Ryan Carlos Gonçalves Chaves

born in: Springfield, Massachusetts, USA

Oral examination: 4 February 2011

The extended H.E.S.S. Galactic Plane survey: Discovering and identifying new sources of VHE γ-rays

The extended H.E.S.S. Galactic Plane Survey: Discovering and identifying new sources of VHE γ-rays

Contents

Abstract

H.E.S.S. is an array of four imaging atmospheric-Cherenkov telescopes located in Namibia and designed to detect γ-rays in the very-high-energy (VHE; $0.1 \lesssim E \lesssim 100\,\text{TeV}$) domain. The full array has been in operation and observing the Galaxy since late 2003. The H.E.S.S. array's large field-of-view, high sensitivity, and location in the southern hemisphere have made it well-suited for both systematic surveying and for deeply observing specific sources of interest. The efforts of the H.E.S.S. Galactic Plane Survey (GPS), the first comprehensive survey of the inner Galaxy (current $\ell \approx 280°$ to $\ell \approx 60°$, $b \lesssim 4°$) at TeV energies, have contributed to the discovery of an unexpectedly large and diverse population of over 60 sources of VHE γ-rays. In this thesis, the latest dataset of the H.E.S.S. GPS is presented in detail, providing the most complete view of the Galaxy in the VHE γ-ray regime to date. The resulting discoveries of four previously unknown VHE γ-ray sources — HESS J1708−443, HESS J1503−582, HESS J1832−084, and HESS J1848−018 — are reported in particular, and their associations with astrophysical phenomena seen at lower energies are investigated with the aid of both dedicated and archival multi-wavelength data, in an attempt to reveal their physical nature. In addition, deep observations of the youngest Galactic supernova remnant (SNR) G 1.9+0.3 are used to probe its VHE γ-ray emission in light of theoretical predictions. Finally, the first study to correlate bright MeV–GeV γ-ray sources with VHE γ-ray sources is presented. Although the current population of VHE γ-ray emitters is found to be dominated by pulsar wind nebulae (PWNe) and SNRs, nearly a third still remain unidentified or confused, illustrating both the challenges and scientific potential that pervade Galactic TeV astronomy.

Preface

Our Galaxy, the Milky Way, is brimming with electromagnetic radiation, from low-energy radio waves to infrared radiation, through the visible light to which human eyes are sensitive, all the way across the spectrum to X-rays and the highest-energy gamma-ray photons (γ-rays). The Milky Way has been explored extensively at most energies, with the observations of hundreds of telescope both on the ground and in space, but until recently virtually nothing was known about the Galaxy at the highest energies, the domain now known as very-high-energy (VHE) γ-ray astronomy.

Just six years ago, only a handful of objects in the Galaxy were known to emit VHE γ-rays[1] (also called TeV γ-rays), compared to, for example, the billions of stars known to emit visible light (with energies ~ 1 eV). It was not clear which — or how many — objects could actually emit VHE γ-ray photons, which are so energetic that only extreme astrophysical processes could be responsible. In 2004, the H.E.S.S. telescope array (see Chapter 1 for a brief summary of its most important properties) in Namibia became fully operational and began to investigate this VHE side of the Milky Way by systematically observing and mapping our disc-shaped Galaxy.

H.E.S.S. is no ordinary telescope; it is actually an array of four so-called imaging atmospheric Cherenkov telescopes (IACTs) which work in concert and employ very fast electronics, uniquely-designed cameras, and specialized detection techniques which have been under development for decades. It is able to indirectly detect VHE γ-rays, which are themselves unable to reach the telescopes because they inevitably collide with air molecules in the upper atmosphere, by imaging the complex cascade of particle decays and interactions resulting from the initial collision. From its preferred vantage point in the southern hemisphere, H.E.S.S. is well posed to search the inner Galaxy — not visible to IACTs in the northern hemisphere — for evidence of new VHE γ-ray emitting objects and to piece together our first complete picture of the Galaxy. Not only will this answer the basic question of "What does our Galaxy look like in VHE γ-rays?", but it may also shed light on a similar

---

[1]A VHE γ-ray is a photon with energy E in the range $100\,\mathrm{GeV} \lesssim E \lesssim 100\,\mathrm{TeV}$, where $1\,\mathrm{GeV} = 10^9$ electron volts (eV) and $1\,\mathrm{TeV} = 10^{12}$ eV.

question, that of the mystery surrounding cosmic rays, highly energetic particles whose arrival at the Earth can be detected but whose origin remains unclear after more than a century of research.

The H.E.S.S. Galactic Plane Survey (GPS) has indeed provided our first panoramic VHE view of the inner Galaxy. Extensive maps of the Galaxy are shown in Chapter 2 and Appendix A, revealing the Galaxy in unprecedented detail. Six years after H.E.S.S. first began scanning the Galaxy, the unparalleled dataset consists of over 2 300 hours of observations. The survey has led to numerous discoveries by uncovering an unexpectedly large population of VHE γ-ray sources (Fig. 1), currently ~60 in number (of nearly 80 known Galactic sources in total). and still growing as surveying efforts continue. This has, for the first time in history, opened up the VHE γ-ray sky to astronomers eagerly waiting to study the inner Galaxy at these extreme energies. Four of the more recently discovered H.E.S.S. sources are presented in detail in Chapters 3–6.

Thanks to H.E.S.S., we now know that Galactic sources of VHE γ-rays belong to a number of diverse astronomical sources classes, but that the vast majority are related to the late
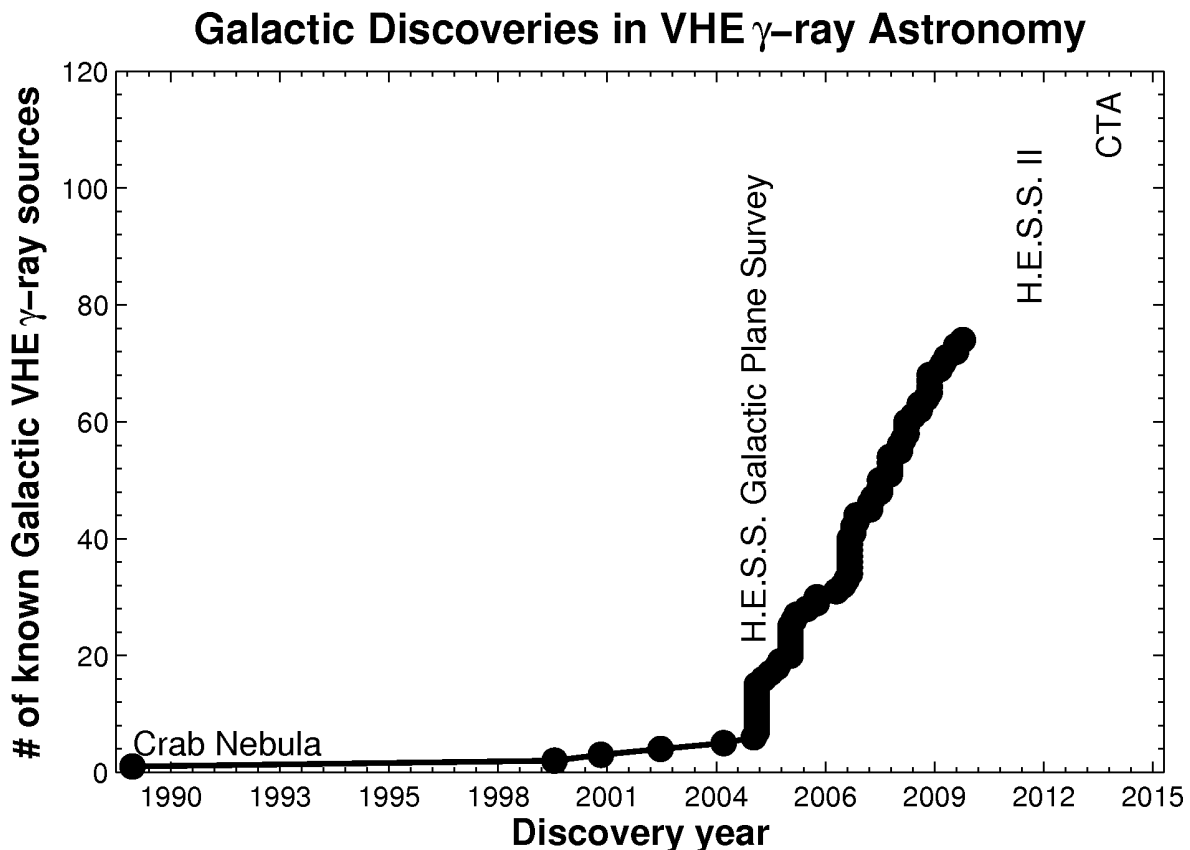

Figure 1: Illustrating the recent and rapid progress in the emerging field of Galactic VHE γ-ray astronomy. The starting date of the H.E.S.S. GPS is labelled, as are the projected starting dates of H.E.S.S.-II and the next-generation Cherenkov Telescope Array (CTA).

stages of stellar evolution, in particular the violent aftermath that follows a massive stars' su-pernova explosion. Supernova remnants (SNRs) and pulsar wind nebulae (PWNe), objects well-studied at other energies (e.g. in the X-ray or radio domains), represent the largest frac-tion of currently known VHE γ-ray sources. Chapter 7 deals with the potential VHE γ-ray emission from a very unique shell-type SNR, G 1.9+0.3. This SNR was recently revealed to be the youngest in the Galaxy, which provides a unique opportunity to probe the VHE γ-rays thought to be emitted even during the early stages of an SNR's evolution.

As many as one third of VHE γ-ray sources remain unidentified, and some even appear to be dark when observed with other telescopes at lower energies (i.e. at longer wavelengths). Motivated by the relatively large number of well-established TeV PWNe which have been discovered by H.E.S.S., many of these unidentified TeV sources have been tentatively classi-fied as PWNe candidates. The presence of a nearby pulsar observed at radio wavelengths is often used as preliminary evidence. The pulsar must also be energetic enough to power the observed γ-ray luminosity which originates in the pulsar's nebula, comprised of a wind of relativistic particles accelerated by the pulsar. Two recently discovered VHE γ-ray sources, HESS J1708−443 (Chapter 3) and HESS J1832−084 (Chapter 5), have been identified as such PWN candidates. However, like many others in this class, their identification is compli-cated by certain characteristics that do not agree with theoretical expectations or with those of other confirmed TeV PWNe. These sources await follow-up multi-wavelength (MWL) observations with H.E.S.S. and/or other telescopes to confirm their true natures, while theo-retical models are being explored to explain their unusual properties.

For all of the Galactic sources discovered by H.E.S.S., supplementary MWL observa-tions have become crucial for determining their identities and the underlying mechanisms (e.g. leptonic or hadronic particle acceleration processes) responsible for the emission of such energetic photons. This approach aims to give us additional morphological and spectral evidence in complementary energy regimes which can be used to help establish a confident identification of the TeV source. Unfortunately, many TeV sources cannot be firmly associ-ated with known astrophysical objects due to a lack of sufficient MWL data. Observations with space-based X-ray telescopes are often proposed and used together with archival ob-servations from radio, infrared, or high-energy (HE; $0.1 \lesssim E \lesssim 100\,\mathrm{GeV}$) γ-ray telescopes to address this shortcoming. The VHE γ-ray sources HESS J1503−582 (Chapter 4) and HESS J1848−018 (Chapter 6) are two enigmatic sources recently discovered by H.E.S.S. whose analyses employ significant MWL data in an attempt to determine their identity.

This thesis focuses primarily on H.E.S.S., its extended survey of the Galaxy, and in-depth reports of a few selected sources of VHE γ-rays discovered in the Galaxy. It also contains the first study (Chapter 8) aiming to correlate the Galactic population of known TeV sources with the brightest HE GeV γ-ray sources discovered by the recently launched *Fermi Gamma-ray Observatory*. A seemingly off-topic appendix (Appendix B) is included to demonstrate how certain problems, namely the proper fitting of power laws and their interpretation, similarly

challenge research fields as different as ecology and astrophysics. Finally, a brief outlook on the future of VHE γ-ray astronomy is given in Chapter 9, in the context of the upgraded H.E.S.S.-II array and the next-generation Cherenkov Telescope Array (CTA).

Chapter 1

Observing VHE γ-rays with the H.E.S.S. telescope array

The atmosphere is opaque to γ-rays, suggesting that a space- or balloon-based telescope would be necessary in order to rise above the atmosphere and detect them. The incoming fluxes from γ-ray sources are also very low in general, requiring the telescope to have a large photon collecting area in order to detect a sufficient number of γ-rays. This is practical for high-energy (HE) γ-rays and satellites like the *Fermi Gamma-ray Observatory*, which uses a detector with a surface area of order $1\,\mathrm{m}^2$ to detect photons up to energies of $\sim 100\,\mathrm{GeV}$. However, the spectra of most astrophyiscal sources follow a power law at high energies, so their fluxes quickly diminish with increasing energy. In the VHE/TeV energy regime, a satellite- or balloon-borne telescope would not be practical due to the financial and logistical constraints of launching such a massive instrument. Blackett (1948) postulated that γ-rays could in fact be detected from the ground indirectly via their atmospheric Cherenkov radiation (Fig. 1.1). The subsequent development of the so-called imaging atmopsheric Cherenkov telescope (IACT), which essentially uses the atmosphere itself as part of the detection system, took place over the next forty years. The development of this technique culminated with the first discovery of an astrophysical source of VHE γ-rays, the Crab Nebula, by Weekes et al. (1989) using the Whipple telescope in Arizona.

1.1 Extensive air showers and Cherenkov radiation

The atmospheric Cherenkov radiation detected by an IACT is observed as a very-short (on the order of $10^{-9}\,\mathrm{s}$) flash of faint, visible blue light. When a VHE γ-ray enters the upper atmosphere at an altidude of $\sim 25\,\mathrm{km}$, it collides with the nucleus of an air molecule and indirectly produces this light. The initial collision produces a cascade composed of thousands of secondary particle interactions and decays known collectively as an extensive air shower (EAS; Fig. 1.2). The number of particles in an EAS reaches a maximum at an altitude of
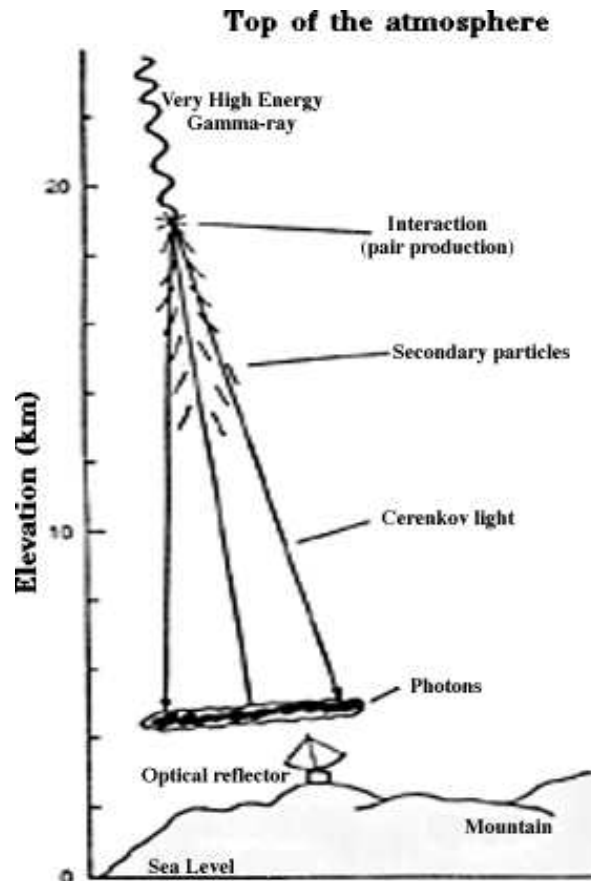
Figure 1.1: Plot illustrating how atmospheric Cherenkov radiation can be used to indirectly detect VHE γ-rays with telescopes like H.E.S.S.. *Credit*: NASA.

~10 km and then diminishes as the EAS progresses deeper into the atmopshere, dissipating the energy provided by the original γ-ray.

The secondary charged particles (e.g. electrons) which are produced are extremely energetic and initially travel at speeds greater than the speed of light of the medium (here, air, a dielectric insulator). As they pass through the local electromagnetic fields of the air molecules, they polarize the atoms which make up the molecules. The atoms quickly return to their ground states, jointly emitting Cherenkov radiation, which can be observed by an IACT on the ground. This process is analagous to the sonic boom emitted when an object travels faster than the speed of sound in a medium.

Gamma-rays constitute only a small fraction ($< 1\%$) of the total number of photons and particles impinging on the Earth's atmosphere. The majority (~87%) are in fact cosmic-ray protons, which, when entering the atmosphere, also collide with molecules in the air and produce EASs. However, EASs initiated by protons develop differently than those initiated by γ-rays(see Fig. 1.2 for a comparison). Gamma-rays produce purely electromagnetic EASs dominated by $e^{\pm}$ (electron/positron) pair production and subsequent bremsstrahlung

Development of gamma—ray air showers

Primary particle
(gamma ray)

first interaction
with nucleus in air
(pair production)

bremsstrahlung
on nucleus in air

pair production

bremsstrahlung

(C) 1999 K. Bernlöhr

Development of cosmic—ray air showers

Primary particle
(e.g. iron nucleus)

first interaction

pion decays

pion—nucleus
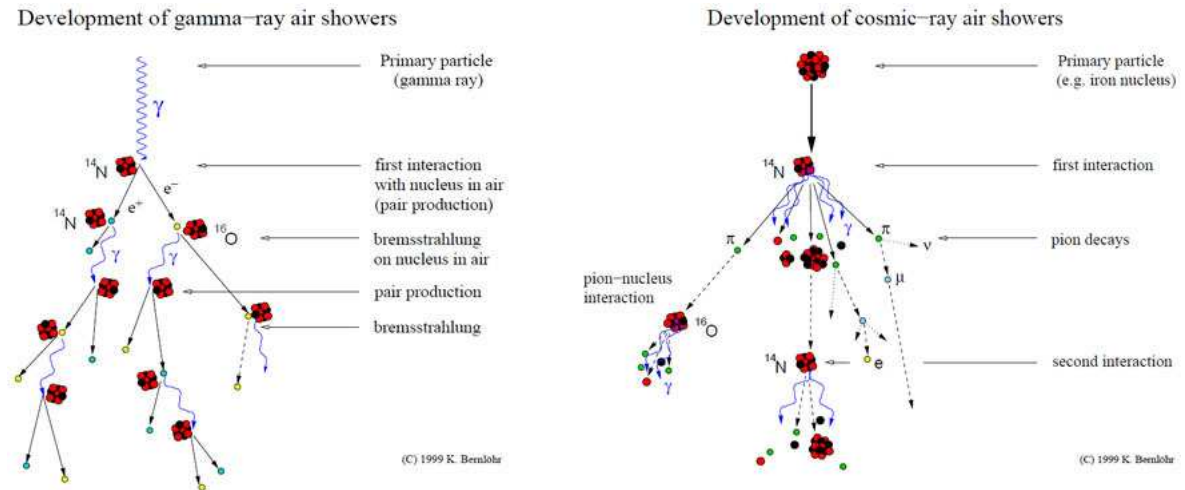interaction

second interaction

(C) 1999 K. Bernlöhr

Figure 1.2: Diagram illustrating the development of γ-ray-induced and cosmic-ray-induced extensive air showers (EASs). *Credit*: K. Bernlöhr.

radiation. In contrast, hadronic EAS are characterized by pion (π) production, π-nucleus interactions, and π decays. These differences lead to notable differences in the geometry of the EASs, which can be used to differentiate EASs created by VHE γ-rays (signal) or by cosmic-rays (background) when their Cherenkov radiation is imaged by an IACT. The *Hillas method* (Hillas 1985) exploits the geometrical differences between these EAS images to remove more than 99.9% of the hadronic background, a step sometimes referred to as γ-*hadron separation*.

1.2   H.E.S.S.

H.E.S.S. (High Energy Stereoscopic System) is a ground-based array of four IACTs (Fig. 1.3) which work together as a system to observe astrophysical VHE γ-rays. As explained above, IACTs are able to detect individual γ-rays by imaging the Cherenkov light emitted by the EASs they produce. The original direction of the incident γ-ray can be reconstructed using the shape of the Cherenkov light image recorded by the IACTs' cameras. The γ-ray's energy can also be determined since it correlates with the intensity of that image. The "stereoscopic" approach employed by H.E.S.S. relies on simultaneously imaging each EAS with multiple telescopes arranged in an array (Fig. 1.4). This improves the ability of the array to discriminate between γ-rays (signal) and cosmic rays (background) and also results in an improved angular resolution, energy resolution, and sensitivity compared to a single telescope.

H.E.S.S. was operated as a two-telescope array during its commissioning phase from February to December 2003. In the seven years since then, however, the full four-telescope array has been in operation, although occassionally data is taken with only two- or three-

Figure 1.3: One of the four H.E.S.S. imaging atmospheric Cherenkov telescopes (IACTs) used to detect VHE γ-rays.

telescopes due to temporary technical problems or maintenance, such as the recent and on-going refurbishment of the telescope mirrors in 2010–2011.

The H.E.S.S. array is located at an altitude of 1 800 m above sea level in the Khomas Highlands of Namibia (23°16′17″ S 16°29′58″ E). Its location in the southern hemisphere facilitates observations of the inner Galaxy, in contrast to the two other current-generation IACT arrays, MAGIC and VERITAS, which are located in the northern hemisphere and, as a result, cannot observe the majority of the inner Galaxy, where the bulk of the known Galactic VHE γ-ray emitters reside.

The four telescopes are identical, and each is equipped with a tessellated, spherical, 12-m-diameter mirror providing a total photon collecting area of 107 m^2 (Bernlöhr et al. 2003). The Davies-Cotton optical design permits a comparatively large field-of-view (FoV) 5° in diameter, the largest of the current generation of IACTs. The mirrors focus the Cherenkov light onto a unique camera comprised of 960 pixels, each a photomultiplier tube capable of detecting the faint and very brief flashes.

The telescopes are arranged on a square with sides of 120 m length and operated in *stereo trigger mode* (Funk et al. 2004). This trigger is implemented at the hardware level and requires that at least two telescopes observe a γ-ray event in order to trigger (confirm) the
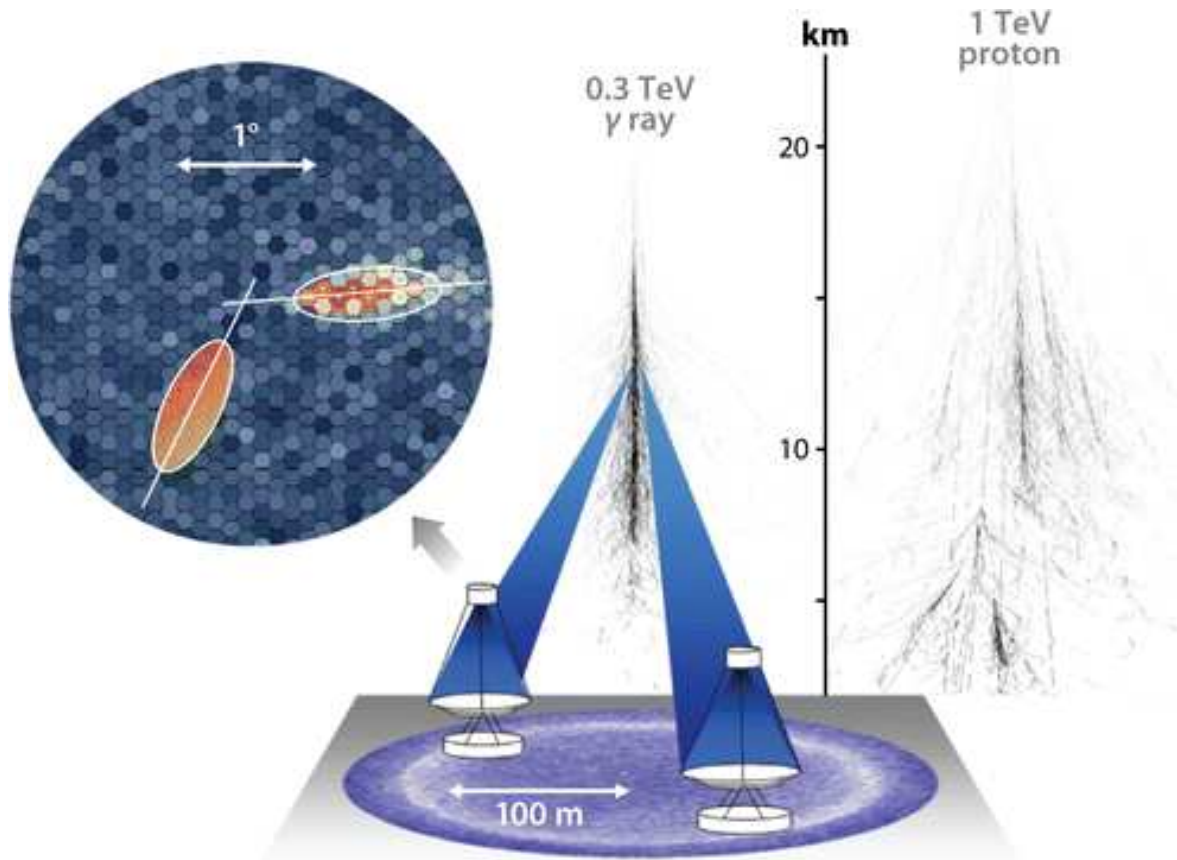
Figure 1.4: Multiple IACTs can be used to simultaneously image a γ-ray-induced EAS and determine the incoming direction of the γ-ray.

detection of an EAS. During its commissioning phase, H.E.S.S. used a less-efficient offline triggering mode, since the central hardware trigger had not yet been installed. In this *software stereo mode*, each recorded EAS receives a time stamp via a GPS (Global Positioning System) clock. The time stamps are then used in the offline data analysis to identify EASs which were observed in coincidence by two (or more) telescopes. This stereoscopic approach results in an angular resolution $\lesssim 0.1°$ (or $\sim 5'$) per event and a significantly improved background rejection (Aharonian et al. 2006a) compared to single-telescope arrays.

The H.E.S.S. telescopes are sensitive to γ-rays above ~ 0.1 TeV, up to ~ 100 TeV (provided the source being observed is both bright and has a sufficiently hard spectrum), and an energy resolution of $\sim 15\%$ (on average). H.E.S.S. can detect point sources near zenith at levels of $\sim 1\%$ of the Crab Nebula flux with a statistical significance of $5\,\sigma$ in 25 h of observations, or less if advanced techniques are used for EAS image analysis (e.g. de Naurois & Rolland 2009; Ohm et al. 2009; Naumann-Godó et al. 2009; Fiasson et al. 2010). Its large FoV and off-axis sensitivity not only make it ideally suited for surveying the Galactic Plane (Chapter 2), but also for studying sources like HESS J1708−443, HESS J1503−582,

HESS J1832−084, and HESS J1848−018, since the background can be estimated from regions within each FoV as opposed to using dedicated OFF observations which double the total exposure needed (Berge et al. 2007).

Further details concerning H.E.S.S. and the imaging atmospheric Cherenkov technique can be found, for example, in Hinton (2004) and references therein.

Chapter 2

The extended H.E.S.S. Galactic Plane Survey

This chapter presents an overview of the H.E.S.S. Galactic Plane Survey (GPS), which was extended after the success of the original survey in 2004–2005 and which is still ongoing at present. The results presented here expand upon what has been published in three conference proceedings:

Chaves, R.C.G. (H.E.S.S. Collaboration)
Proc. of the 25th Texas Symposium on Relativistic Astrophysics, 2010, in preparation

Chaves, R.C.G. (H.E.S.S. Collaboration)
Proc. of the 31st Intl. Cosmic-ray Conference, 2009, arXiv:0907.0768

Chaves, R.C.G., de Oña Wilhelmi, E. & Hoppe, S. (H.E.S.S. Collaboration)
AIP Conf. Series (Proc. of the 4th Intl. Mtg. on High Energy Gamma-ray Astronomy), 2008, 1085, 219

2.1 Motivation

The current generation of IACTs has opened a new astronomical window onto the Universe, allowing us to observe objects which emit VHE γ-ray photons. Over 100 VHE γ-ray sources have now been detected[1], and over two-thirds of these sources are located in our Galaxy, most of which were discovered by the IACT array H.E.S.S. during its Galactic Plane Survey (GPS), which began in 2004 and continues through the present.

VHE γ-rays carry valuable information about the most extreme environments in the local Universe. Although nearly a third of the Galactic sources do not appear to have obvious counterparts at other wavelengths (e.g. Aharonian et al. 2008a), the majority of them are in fact associated with the violent, late phases of massive stars' evolution, in particular the

---

[1]See TeVCat, an online TeV γ-ray catalog, at `http://tevcat.uchicago.edu`.

environments that result when such short-lived stars collapse in a supernova (SN) explosion. These objects, namely the remnants of SNe (SNRs; Green 2009) and the nebulae created by the winds of energetic pulsars (pulsar wind nebulae or PWNe; Gaensler & Slane 2006), have distributions similar to those of their pregenitor Population I stars and therefore also follow other markers for Galactic structure, such as molecular matter (e.g. ^{12}CO clouds, Dame et al. 2001).

Since SNRs, pulsars, massive stars, and molecular clouds — as well as X-ray binaries and star-forming regions — are all known to densely cluster along the Galactic plane, a comprehensive and systematic survey of this region is an obvious and (in retrospect) effective approach for discovering new sources of VHE γ-rays. Further motivation comes from the population of high-energy (HE) GeV γ-ray sources, emitting in a lower but complementary energy range, which was revealed along the Galactic plane first by *COS B* (Swanenburg et al. 1981), then by *Compton*/EGRET (Thompson et al. 1996), and presently by *AGILE* (Pittori et al. 2009) and *Fermi*/LAT (Abdo et al. 2010). In 2004, it was not anticipated that so many sources of VHE γ-rays would be present in the Galaxy. However, the strongest source then known (the Crab Nebula), and other early detections, such as the SNRs Cas A (Aharonian et al. 2001) and RX J1713.7−3946 (Muraishi et al. 2000), do belong to the SNR or PWNe source classes which were already then being considered as prime candidates for VHE γ-ray emission and which are now well-established source classes in the VHE γ-ray domain, seven years later.

2.2 Previous surveys at TeV energies

H.E.S.S. was not the first to systematically survey the Galaxy in search of discrete sources of VHE γ-rays. The four-telescope stereoscopic HEGRA (High Energy Gamma Ray Astronomy) IACT array, the predecessor of H.E.S.S., had a reasonably large ~4° FoV and in 1997–1998 surveyed a large part of the plane in the Galactic longitude range $\ell = -2°$ to 85° (Aharonian et al. 2002), i.e. from the Galactic center (GC) to the Cygnus region, and latitudes $b \pm \sim 1.7°$. The region of the plane observable was restricted due to HEGRA's location in the northern hemisphere (Canary Islands, Spain). This location severely limits the visibility of the inner Galaxy, such that the first Galactic quadrant ($0° < \ell < 90°$) is only observable at large zenith angles, and to the point where the fourth quadrant $\ell < 0°$ ($\ell < 360°$) cannot be observed at all.

No new sources of VHE γ-rays were discovered during the 115-h survey, although upper limits to the VHE γ-ray flux were derived for the first time (Aharonian et al. 2002) for over 150 SNRs, pulsars, and GeV γ-ray sources. Among the sources probed were two that have been revisited in detail with H.E.S.S.: SNR G 1.9+0.3, discussed in Chapter 7, and PSR J1832−0827, discussed in Chapter 5. The flux upper limits ranged from ~7% Crab to 18 Crab units, depending strongly on both the observation time (exposure) and the zenith

angles covered during the observation; for example, a typical, large zenith angle of 45° would lead to a correspondingly high energy threshold of ~1.8 TeV (HEGRA Collaboration et al. 1999). While no new sources were discovered, the HEGRA survey did serve to validate the general scheme for surveying the Galactic plane with IACT arrays, a scheme that was largely adopted for subsequent surveys with H.E.S.S..

The water-Cherenkov Milagro Gamma-ray Observatory also surveyed the northern sky in 2000–2003, searching for point-like (here, point-like refers to a bin size of 2.1° × 2.1°) sources of TeV γ-rays (Atkins et al. 2004). Detectors based on the water-Cherenkov principle, like Milagro, have the ability to observe nearly the entire visible sky (~2π steradians) at once but require long integration times. After three years of observations, the Crab Nebula was detected, but no other Galactic sources were revealed. Flux upper limits (95% confidence level) were reported for the rest of the sky, ranging from ~28% to ~60% Crab above a threshold of 1 TeV.

2.3   The original H.E.S.S. survey

H.E.S.S., in 2004, was the first to survey the Galaxy from the southern hemisphere, thereby gaining access to the central region of the Galaxy which is so densely populated with potential VHE γ-ray sources (Aharonian et al. 2005f). The inner Galaxy was observed from Galactic longitudes $\ell = -30°$ (330°) to 30° and latitudes $-3°$ to 3°, from May to September 2004, yielding a total of ~230 h of quality-selected data with a mean zenith angle (ZA) of 26°. The survey consisted of *scanning* observations, follow-up *wobble* observations of promising source candidates, and deep observations of both the GC and RX J1713.7−3946. Eight new sources of VHE γ-rays were discovered by (Aharonian et al. 2005f), bringing the total number[2]. of known Galactic sources to 13. Most of the sources were tentatively associated with SNRs, PWNe, and/or GeV γ-ray sources, although two were unidentified, leading to the first speculation of a class of "dark" cosmic particle accelerators. This first H.E.S.S. Galactic Plane Survey (GPS) more than doubled the number of VHE γ-ray sources known in the Galaxy, confirmed that they did indeed cluster along the plane as suspected ($b = -0.25°$ ± 0.25°), and clearly motivated further surveying with H.E.S.S..

The work on this first H.E.S.S. GPS dataset continued, and, in 2006, an updated and more comprehensive analysis was published (Aharonian et al. 2006d). The survey was in general sensitive to sources (with a presumed spectral photon index $\Gamma = 2.5$) with fluxes ~2–3% Crab above 200 GeV and located within 1.5° of the Galactic plane. Apart from the eight sources previously reported, six additional sources were reported[3], each with a post-trial significance

---

[2]The five Galactic VHE γ-ray sources discovered before the H.E.S.S. GPS was first published (Aharonian et al. 2005f) were the Crab Nebula, TeV J2023+4130, Cas A, GC, and RX J1713.7−3946.

[3]These have been subsequently confirmed with post-trial signnificances greater than 5 σ, the standard criteria for establishing a suggestive excess of γ-rays, or *hotspot*, as a confidently detected source.

greater than 4σ (Aharonian et al. 2006d). Furthermore, in the preceding year, data from the GC as well as non-survey Galactic observations had revealed still four more sources, bringing the grand total to 23 sources of VHE γ-rays. What was two years earlier an astronomy based on only a few sources was now quickly becoming a field which could claim a veritable population of Galactic VHE γ-ray sources distributed among emerging but discernable source classes. Furthermore, a sizable fraction of the sources had enigmatic origins, with unclear associations at lower energies, which motivated further studies and multi-wavelength observation campaigns to obtain more comprehensive data at lower energies.

2.4   Observational strategy of the extended survey

In the four years since the first GPS dataset was published, a significant fraction of H.E.S.S. observations (roughly 25%) have been devoted to the continuation of the successful GPS, although the strategies employed have evolved over the years. In general, however, the observations have been motivated by the basic goals of extending the survey in both Galactic longitude (and to a lesser extent, latitude) to the limits of the H.E.S.S. visibility, to increase the depth of the H.E.S.S. exposure, especially in regions dense with VHE γ-ray source candidates, and, more recently, to increase the uniformity of the sensitivity across the survey region. Since Aharonian et al. (2006d), incremental updates on the status of the H.E.S.S. GPS have been published by Hoppe (2008); Chaves et al. (2008a); Hoppe (2008); Chaves & for the H.E.S.S. Collaboration (2009).

2.4.1   Systematic scans

The H.E.S.S. telescopes have very large FoVs, with diameters of $5°$, the largest of all IACTs currently in operation. A single H.E.S.S. observation (or *pointing*) therefore covers an impressive $20\,deg^2$ of the sky (or $\sim7\,deg^2$ at FWHM[4]), highlighting H.E.S.S.'s unique capability to quickly survey extremely large regions such as the Galactic plane (e.g. $\sim580\,deg^2$ have been surveyed to date by H.E.S.S.). Nonetheless, a great quantity of individual 28-min observations are necessary to fully survey the Galactic plane (Fig. 2.1). Initially, these pointings were arranged systematically on a regular grid representing the plane.

When the inner Galaxxy ($\ell \pm 60°$) was first scanned in this manner in 2004, the pointings were distributed in three rows (or strips) of Galactic latitude $b = -1, 0,$ and $0°$, with a $0.7°$ spacing in longitude betweem pointings. This procedure was similar to the strategy used by HEGRA, which only had one strip along $b = 0°$ and a $1°$-spacing in longitude. The relatively short spacing between pointings allows the FoV of adjacent observations to overlap significantly. This overlap facilitates a smoother distribution of exposure, leveraging the

---

[4]FWHM is defined here as the full-width (diameter) of the FoV where the γ-ray acceptance efficiency is half the maximum value (at the center of the camera).
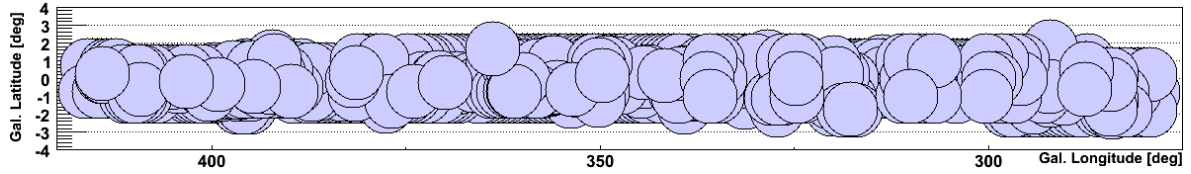
Figure 2.1: Plot illustrating the distribution of individiual observation positions (*pointings*) in the H.E.S.S. GPS, from March 2004 through June 2010. Each pointing is represented by a circle of diameter 3°, equal to the approximate FWHM of the H.E.S.S. FoV (which extends out to a 5° diameter). All two-, three-, and four-telescope observations quality-selected using the *all-weather* criteria are shown. Longitudinal strips of *scan*-mode observations from 2004–2006 are visible, with more recent observations of individual sources overlaid. Pointings near the borders of the surveyed region have been ommitted for clarity. N.B. Longitude $400° = 40°$.

good off-axis performance (FWHM ~3°), or *acceptance*, of the H.E.S.S. telescopes (see e.g. Fig. 1 in Aharonian et al. 2006d).

Motivated by the results of the first scan, where the detected sources were all found very near the plane ($b = -0.25° \pm 0.25°$, Aharonian et al. 2006d), future scans from 2005 onward typically used only two strips along $b \pm 0.7°$ instead of the three strips previously used. This revised strategy accumulated more exposure close to the plane where the majority of VHE γ-ray sources appeared to cluster. The distribution of matter in the Galaxy, seen via the proxy ^{12}CO in radio observations (Fig. 2.2), was also used as a guide to latitudinally shift these strips as necessary in certain regions of the Galaxy in order to better follow the matter distribution. The 2.6-mm carbon monoxide emisison line is a good indictator of regions of enhanced star formation, and the molecular cloud survey by Dame et al. (2001) has excellent coverage of Galactic plane in both the first and fourth quadrants. Star-forming regions are related to the molecular cloud complexes from which they are formed and typically harbor young, massive stars as well as the supernova remnents and pulsars resulting from the death of those stars.
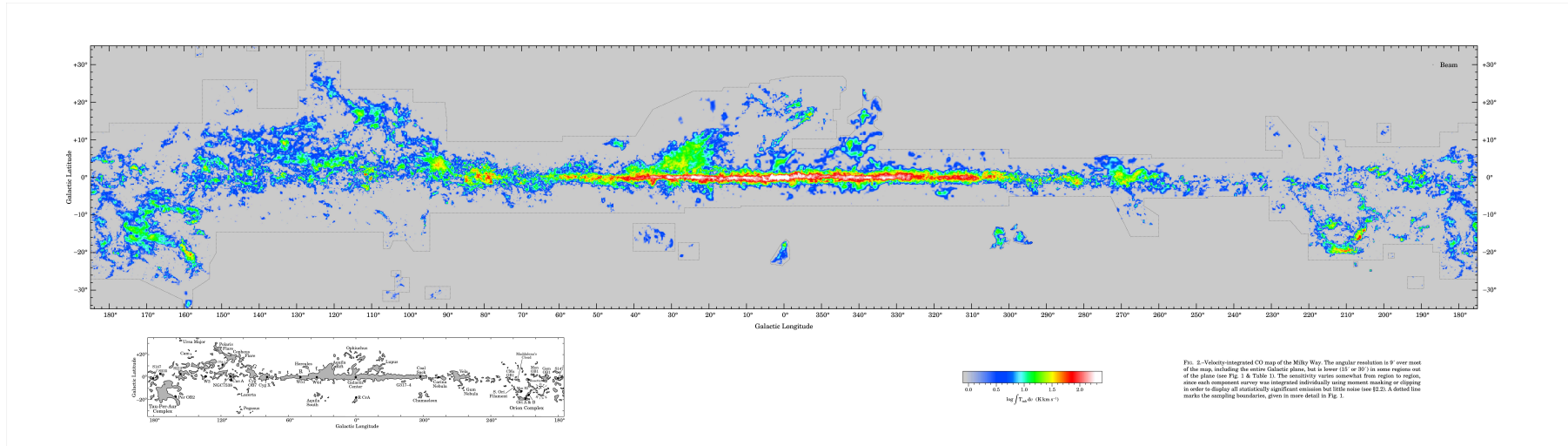
Figure 2.2: Velocity-integrated ^{12}CO map of the Galaxy from Dame et al. (2001). The distribution of molecular matter in the Galaxy is used to guide the placement of pointings in the H.E.S.S. Galactic Plane Survey.

2.4.2 Miniscans

As the VHE γ-ray exposure across the Galactic plane increased, new sources continued to be discovered. By 2007, the Galactic was densely populated with VHE γ-ray sources, many of which were extended well-beyond the H.E.S.S. PSF, and a blind systematic scan was no longer the most efficient strategy, for two primary reasons. First, many of the sources were already being re-observed in *wobble*-mode in the context of dedicated observation programs, and systematically scanning over these already high-exposure sources would not add significant value to the survey dataset. Second, it would have by chance resulted in many pointings within sources themselves, i.e. observations which cannot be used for spectral analyses with the *reflected background method* (Berge et al. 2007). As a result, survey-related observations from 2008 onward began focusing on scanning smaller regions-of-interest (ROIs) in so-called *miniscans*. The goal of the miniscans in was to scan relatively small ROIs ($\sim 10 \deg^2$) which contained multiple source candidates, so that single observations could potentially benefit more than one source. Seven (published) sources were discovered largely due to the 2008–2009 miniscans, namely SNR G 292.2−0.5 / PSR J1119−6127[5], HESS J1457−593[6], HESS J1503−582 (Chapter 4), HESS J1832−084 (Chapter 5), HESS J1848−018 (Chapter 6), HESS J1849−000 (Terrier et al. 2008), and HESS J1852−000[6].

2.4.3 Uniform sensitivity

By 2008, the numerous campaigns to follow-up and deeply observe individual H.E.S.S. sources had resulted in a very inhomogeneous exposure across the Galactic plane, differing by over an order of magnitude, e.g. from over 150 h at the GC to less than 10 h in some regions (c.f. Sect. 2.6.2). Due to the deep exposures which already exist in some regions, the H.E.S.S. GPS will never achieve a perfectly uniform coverage over the full extent of the survey. It would take thousands of hours of observations (i.e. decades) to cover the Galactic plane with the level of exposure accumulated on the GC region. These deep exposure are very important, allowing us to detect faint sources and to study bright sources in unprecendented detail. However, it is nonetheless desirable to greatly reduce the exposure (or sensitivity) contrast in the GPS and to achieve a more uniform minimum detectable flux.

The fifth IACT (CT5) is expected to begin operations in early to mid-2012, forming H.E.S.S.-II. Scientific priorities are likely to change, especially with regards to surveying, since CT5 has a smaller FoV and lower energy threshold. As a result, there is interest in

---

[5]This source, which does not yet have an official H.E.S.S. identifier, was announced in an oral presentation by Djannati-Ataï et al. (H.E.S.S. Collaboration) at the Workshop "Supernova Remnants and Pulsar Wind Nebulae in the *Chandra* Era" in 2009. The proposed SNR and pulsar counterparts are given here. See `http://cxc.harvard.edu/cdo/snr09/pres/DjannatiAtai\_Arache\_v2.pdf`.

[6]This source was very recently announced at the 25th Texas Symposium on Relativistic Astrophysics in December 2010. A respective proceeding is in preparation.

moving toward the limited release of a H.E.S.S.-I Legacy Survey (HLS) dataset. By achieving a more uniform and complete coverage of the Galactic plane, we hope to add value to this dataset, for example, by facilitating population studies as well as studies of the global distribution of sources in the Galaxy.

In 2009, ~13 h of obserations were taken in order to fill in the largest gaps in effective exposure across the core GPS region. In 2010, a more comprehensive approach was adopted, aiming to achieve a more uniform sensitivity in this large region, and ~85 h of observations was performed. Sensitivity is a more appropriate metric for evaluating the coverage of the H.E.S.S. GPS since it is depends not only of effective exposure but also takes into account, for example, the varying zenith angle of observations across the plane. Regions were prioritized also according to their overlap with spiral arm tangents (Vallée 2008), where the amount of molecular matter and number of VHE γ-ray source candidates is greater along the line-of-sight. This approach is being continued into the 2011 observation season and will not only add value to the GPS/HLS datasets but also likely reveal new sources of VHE γ-rays in these previously neglected regions. Images showing the current sensitivity in the GPS are presented in Sect. 2.6.4.

2.5   The H.E.S.S. GPS dataset

2.5.1   Observation properties

The H.E.S.S. GPS dataset presented here comprises a total of 5 113 observations from 21 March 2004 through 20 June 2010[7]. Each observation lasts aproximately 28 min (Fig. 2.3), with a mean deadtime-corrected livetime of 27 ± 3 min, giving a total livetime of 2 331 h — *the largest dataset ever accumulated in the VHE γ-ray domain and a factor of ~10 larger than the first published H.E.S.S. GPS dataset* (Aharonian et al. 2005f). Approximately 5% of the observations have livetimes less than 20 min; truncated observations can be due to an interruption from a triggered target-of-opportunity (ToO) observation or to avoid contaminating light from the rising moon or sun. The vast majority (83%) of the observations used the full four-telescope array. The remaining 17% represent observations with only two or three telescopes, when other telescopes were not being used, e.g. due to technical problems or mirror refurbishment. Although the observation schedule was optimized (when possible) such that observations occurred near the target's culmination, the zenith angle (ZA; 90° − altitude) of the observations varies considerably (Fig. 2.4), with a mean of 32° ± 13°. The ZA depends primarily on the declination of the target observation position and thus also varies as a function of Galactic longitude. This in turn results in a varying minimum energy threshold as a function of longitude.

---

[7]For comparison, the results in Hoppe (2008) included data until 12 October 2007 and the results in Chaves & for the H.E.S.S. Collaboration (2009) included data until 22 October 2008.
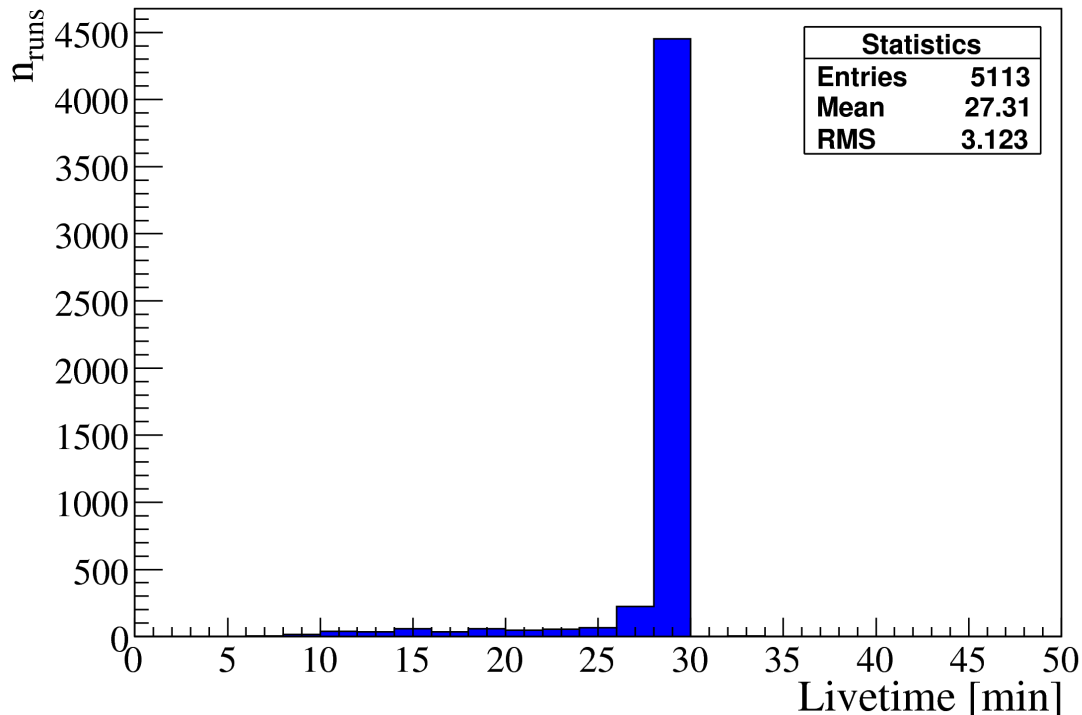
Figure 2.3: Histogram of individual observation livetimes (deadtime-corrected exposure) in the H.E.S.S. GPS. 95% of the observations have livetimes greater than 20 min.

The large H.E.S.S. GPS dataset was selected using the *all-weather* quality criteria[8], which relaxes cuts on weather-related parameters in order to maximize the amount of data usable for source discovery (via, for example, significance maps). A stricter *spectral* quality criteria is used to select observations suitable for performing reliable spectral analyses, which include the calculation of sensitivity or integral flux. These also typically omit two-telescope observations, to ensure the highest quality possible. The spectral-quality dataset used in this thesis comprises 4 261 observations and has a livetime of 1 973 h.

2.6 VHE γ-ray images of the Galaxy

2.6.1 Significance

Figures 2.5 and 2.6 present maps of the Galaxy which show the statistical significance of the VHE γ-ray emission across the plane, using the latest full H.E.S.S. GPS dataset. Gamma-ray/hadron separation is performed individually for each observation according to Hillas

---

[8]Throughout this thesis, the "Heidelberg" quality selection was used, as defined on 11 November 2010. There exist multiple quality selection criteria within H.E.S.S. for the purpose of cross-checking primary results.
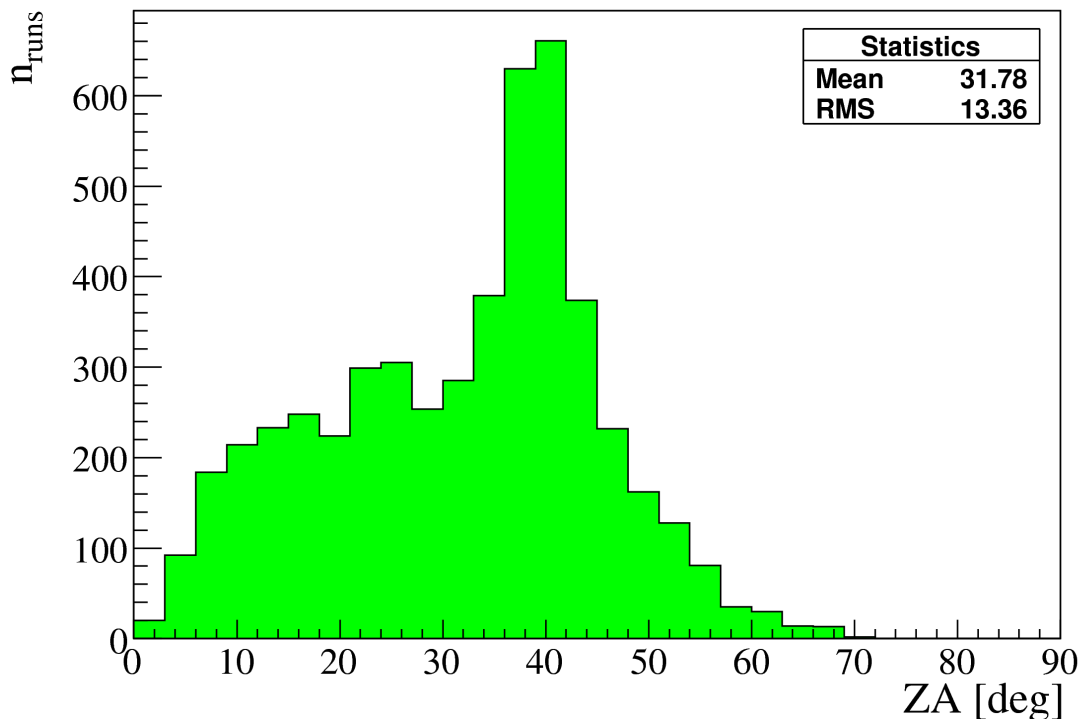
Figure 2.4: Histogram of individual observation zenith angles (ZAs) in the H.E.S.S. GPS.

(1985) and using *hard cuts*, which require each image of the EAS to have a minimum charge of 200 p.e in order to be selected. This relatively strict cut improves rejection of the hadron-induced background at the expense of a slightly higher energy threshold. Large maps are then created by aligning and superimposing individual maps of γ-ray events from each observation.

The γ-ray acceptance of each observation is estimated from a database of extragalactic observations which do not contain any known γ-ray sources in the FoV. This database of so-called OFF observations is used to create an acceptance *template* as a function of the ZA of the observation. The individual acceptance maps are scaled to account for: 1) the livetime of the respective observation; and 2) the varying event rates (e.g. due to different weather conditions), by normalizing to the number of events in each FoV which do not fall within an *exclusion region*. *Exclusion regions* are areas of the Galactic plane which contain significant signal from known VHE γ-ray sources and source candidates. Corresponding large maps of the γ-ray acceptance are also created.

At each test position (grid point, or pixel), the number of γ-ray events N_{ON} (signal) is integrated over the so-called ON-source circular region (radius $\theta = 0.22°$ in Fig. 2.5 and $\theta = 0.10°$ in Fig. 2.6). The background (OFF-source) is estimated using the *ring background method* (Berge et al. 2007). The number of events N_{OFF} is calculated within a ring-shaped

Figure 2.5: Image showing the pre-trials statistical significance in the H.E.S.S. GPS region, divided into four panels. The significance is correlated over a circular region of radius $\theta = 0.22°$, the standard size used to search for extended VHE γ-ray sources. The significance is truncated in the image above $15\,\sigma$ to increase visibility, and the color transition (from blue to red) is set at $7.4\,\sigma$ pre-trials significance, which (conservatively) corresponds to $\sim 5\,\sigma$ post-trials significance. Maps such as this are used to search for evidence of new VHE γ-ray sources. N.B. Some very recently detected sources are not yet labeled. For an unlabeled version of this plot, see Fig.A.1.

region defined by a mean radius $r_{mean} = 0.9°$ and an area $\gtrsim 7$ times the ON-source region ($\alpha \lesssim 1/7(0.14)$). To avoid contamination of the background with real signal, events from any overlapping *exclusion regions* are not included in the background determination. The significance at each position is then calculated according to Li & Ma (1983) to create the maps shown.

The irregular borders of the significance maps were not always evident in previously-published maps, due to two reasons: 1) previous maps were typically truncated at lower Galactic latitudes (e.g. at $b = -2.8°$ and $+1.8°$ in Chaves et al. (2008a) and Hoppe (2008) and at $b \pm 3.0°$ in Chaves & for the H.E.S.S. Collaboration (2009)) and 2) for the first time, additional cuts on the minimum number of events required is implemented. For each test
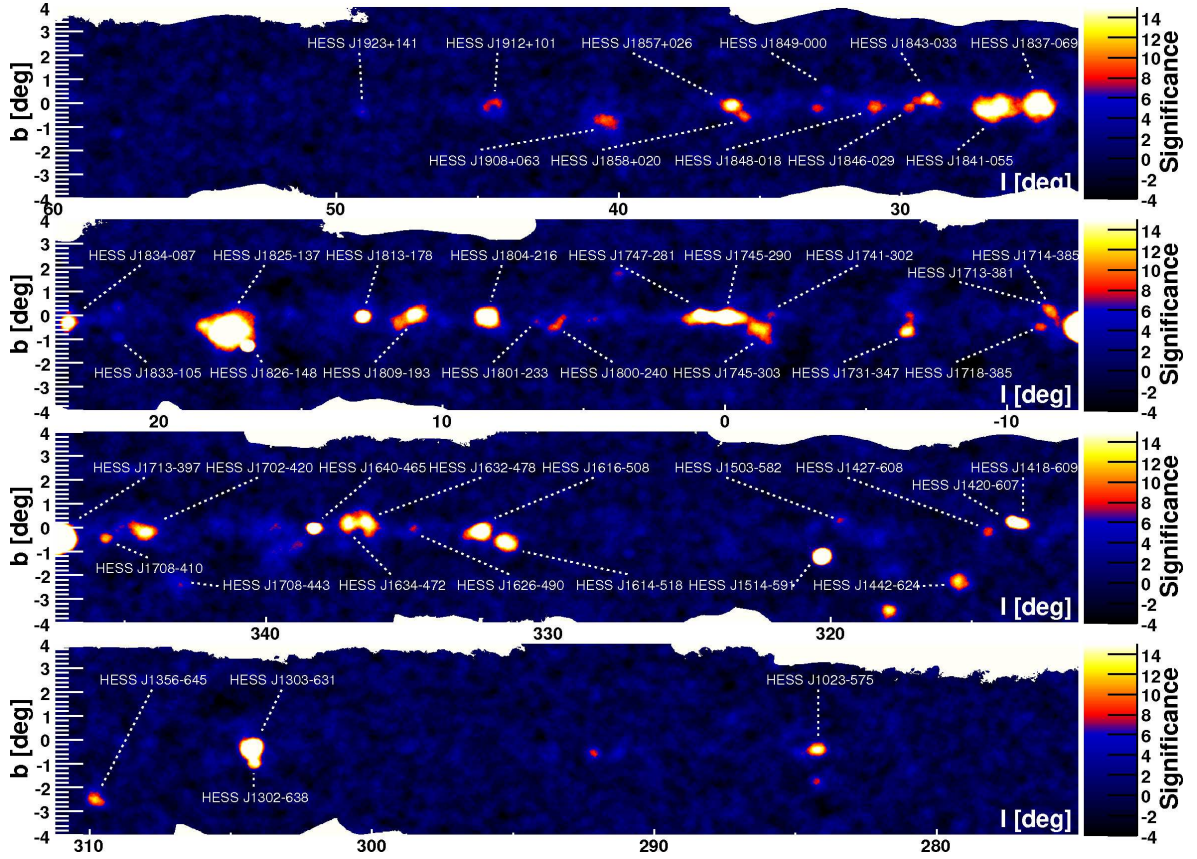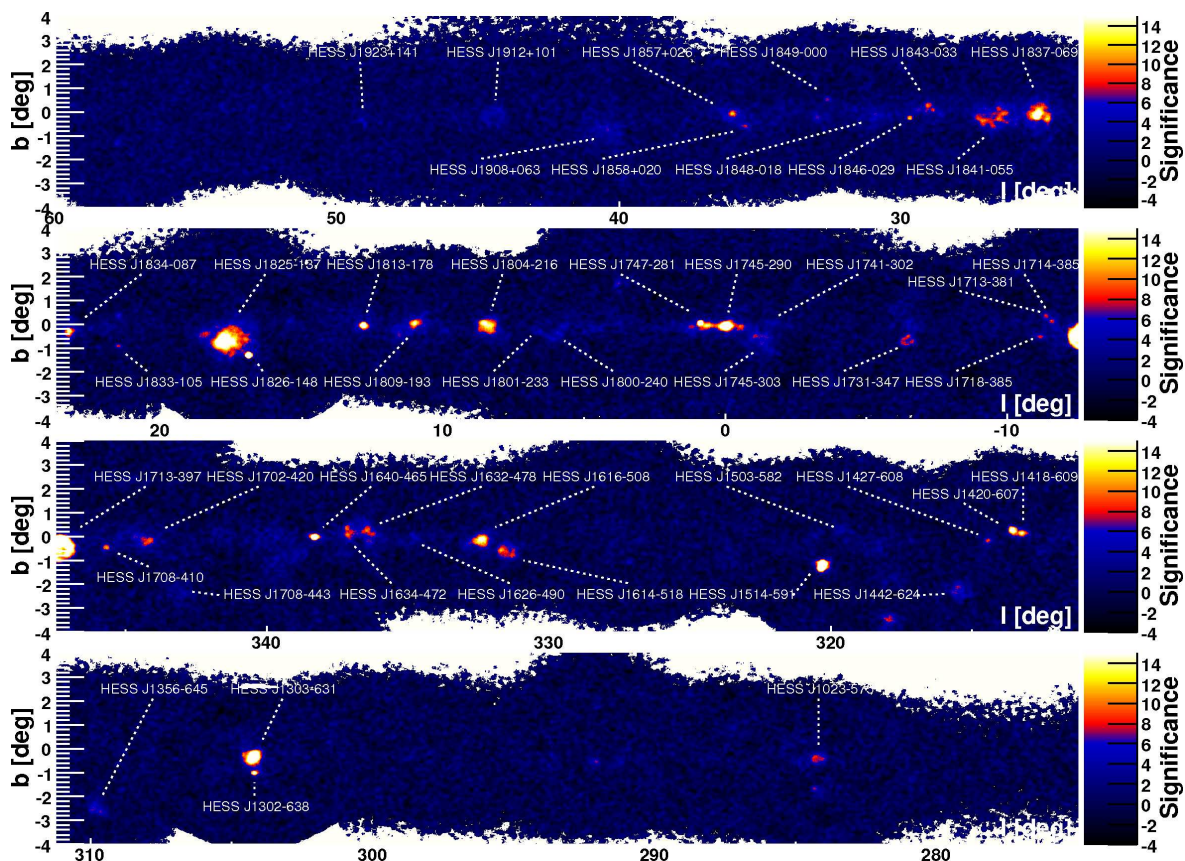
Figure 2.6: Image showing the pre-trials statistical significance in the H.E.S.S. GPS region, divided into four panels. The significance is correlated over a point-like circular region of radius $\theta = 0.10°$, and is truncated in the image above $15\,\sigma$ to increase visibility. The color transition (from blue to red) is set at $7.4\,\sigma$ pre-trials significance, which (conservatively) corresponds to $\sim5\,\sigma$ post-trials significance. Maps such as this are used to search for evidence of new VHE γ-ray sources. Known VHE γ-ray sources are labeled with their H.E.S.S. identifiers. N.B. Some very recently detected sources are not yet labeled. For an unlabeled version of this plot, see Fig.A.2.

position on the map, N_{ON} and N_{OFF} must both be greater than or equal to ten in order for the significance to be calculated (and displayed). This cut is required to ensure that the equation used to calculate the significance of the γ-ray excess (Eq. 17 in Li & Ma 1983) is valid. The implementation of this cut, together with the gradual increase of off-plane exposure in recent years, allows us to confidently reveal a much larger region of the Galaxy plane ($\sim20\%$ more) by excluding regions with a very low number of events (a result of a corresponding very low exposure), at the minor expense of having ragged borders in the significance maps shown in Figs. **??**.

Significance maps such as those shown in Figs. 2.5 and 2.6 are used to search for new sources of VHE γ-rays. A thorough inspection of these maps is regularly performed, and

follow-up H.E.S.S. observations of the most promising source candidates, or *hotspots*, are scheduled for the following year. In this manner, sources like HESS J1848−018, HESS J1832−084, HESS J1503−582, and numerous others have been discovered. The threshold for claiming a statistically-significance source detection is set at a conservative 5σ (post-trials). The maps, however, show the pre-trial significance. The number of trials is dominated by the number of positions in the surveyed region which were searched for significant emission. As a general rule, a 7σ pre-trial significance correponds to a 5σ post-trials, after accounting for the large number of trials, $O(10^6)$, employed in the H.E.S.S. GPS. However, the exact number of trials is calculated on a source-by-source basis. For example, some sources are initially found after a blind search of the the survey dataset, but subsequent follow-up observations are performed at an *a priori* determined location; the second part of the dataset therefore has greatly reduced trial factors, usually $O(10^1)$ or less.

Significance maps are also very useful for visualizing the current distribution of known sources in the Galaxy. However, since the observation ZA and effective exposure vary significantly across the surveyed region, the minimum energy threshold and sensitivity also vary. Significance maps do not correct for these differences and are thus not suitable for more advanced analyses. For example, two sources or regions in a significance map cannot be directly compared to one another, and suggestive structures which may be visible do not necessarily correlate with real morphological features. A 2D map of the significance cannot be used to infer any characteristics of a VHE γ-ray source other than the statistical significance of its detection (the ability to discriminate its signal from the background). Furthermore, areas of low significance (dark blue and black regions in the figures) cannot be interpreted as a lack of γ-ray emission from that area — in many cases, it is simply due to a relatively lower exposure. Therefore, the next sections present additional maps which show the effective exposure, integral flux, and sensitivity across the H.E.S.S. GPS, in order to provide a more comprehensive and physically-meaningful view of the Galaxy.

2.6.2   Effective exposure

Effective exposure is defined here as the offset-corrected livetime. First, the total exposure of each observation is deadtime-corrected, giving the livetime of the observation. A 2D map of the livetime is then generated and weighted by the telescope acceptance to γ-rays, which drops off a function of distance from the camera center and is also ZA dependent. Finally, a large map of the effective exposure across the H.E.S.S. GPS region (Fig. 2.7) is produced by aligning and superimposing all of the observations in the full dataset. The effective exposure at a given pixel in the map then represents the contributions from all (offset) observations whose FoVs fall within 3.0° of that pixel.

The effective exposure of the H.E.S.S. GPS has steadily increased from 2004 to 2010, illustrated in Fig. 2.8. The first released dataset (Aharonian et al. 2006d) only covered the
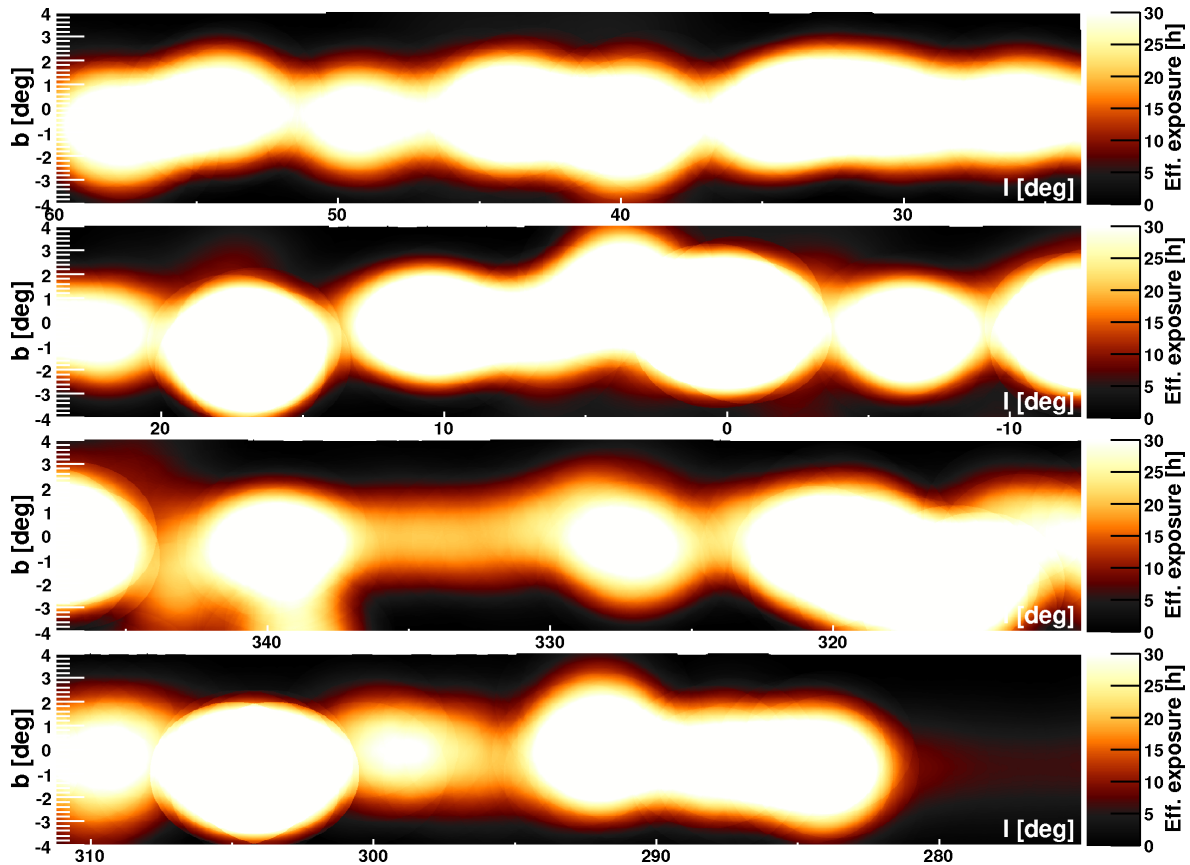
Figure 2.7: Image showing the current effective exposure in the H.E.S.S. GPS region, divided into four panels. The exposure is truncated above 30 h to increase visibility, and the color transition (from black to red) is set at 7.5 h.

innermost section of the Galaxy ($l \pm 30°$ with respect to the GC) with a relatively shallow exposure, having a mean of 8 h ± 11 h along the Galactic plane. The large standard deviation was due to early, deep exposures of the GC and RX J1713.7−3946. A subsequent dataset (Hoppe 2008) showed a significant improvement, more than tripling the average exposure to 29 h ± 28 h along the plane. The current dataset continues this trend, raising the average exposure to 43 h ± 26 h — a more than five-fold increase since the original survey. The high standard deviations persist and are essentially unavoidable. H.E.S.S. is not solely a surveying instrument; dedicated campaigns are regularly initiated to observe specific sources of interest with *wobble*-mode observations (these result in the peaks seen in projections of the exposure). Nonetheless, it should be noted that the standard deviation is now much lower with respect to the mean, largely due to the success of the 2009–2010 observational strategy to fill in gaps in exposure and increase the uniformity of the sensitivity along the Galactic plane (see also Sect. 2.4.3).
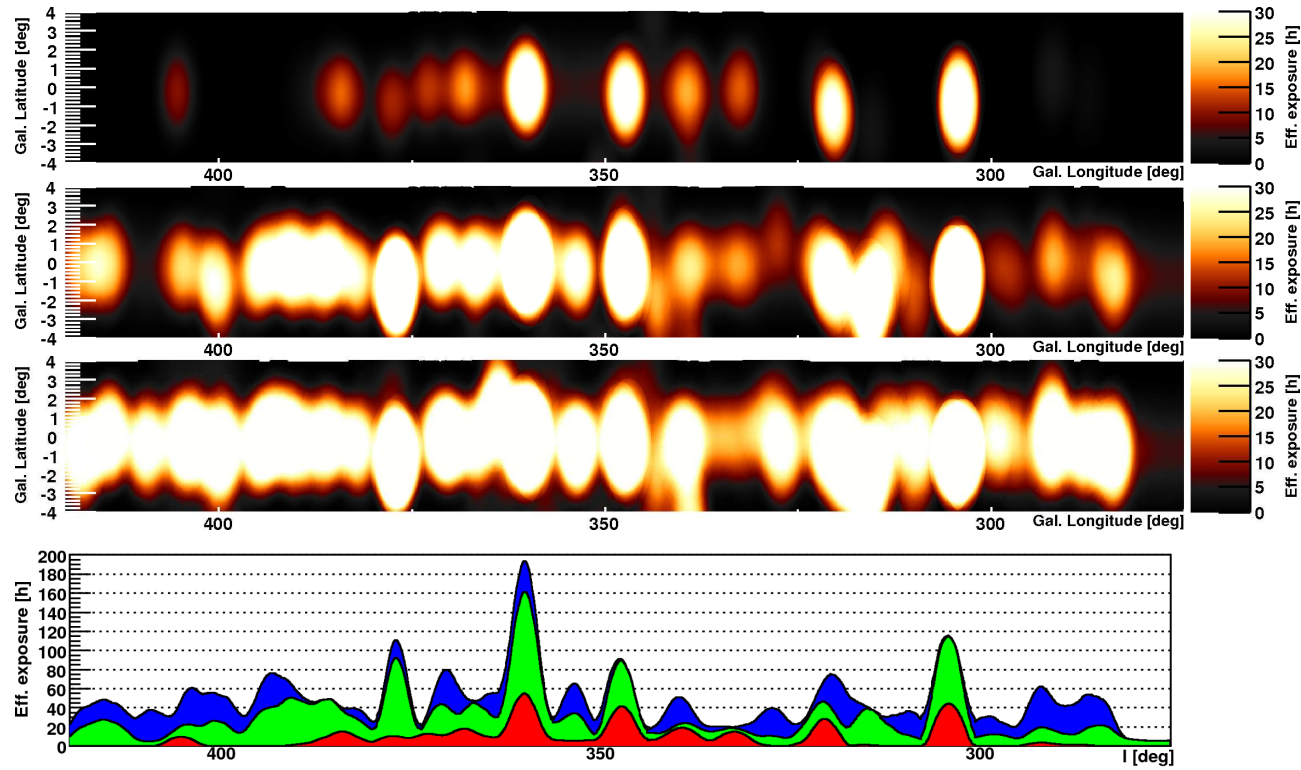
Figure 2.8: Effective exposure and its evolution during the H.E.S.S. GPS. The top three panels show images of the cumulative exposure in the H.E.S.S. GPS region at the end of three different epochs, while the bottom panel shows projections of these three maps along the Galactic plane ($b = 0°$). *Panel 1*: Exposure of the dataset presented in Aharonian et al. (2006d), including data until 21 March 2004. *Panel 2*: Exposure of the dataset presented in Hoppe (2008), including data until 12 October 2007. *Panel 3*: Exposure of the dataset presented in this thesis, including data until 20 June 2010. *Panel 4*: Exposure projections along the plane (Panel 1 in red, Panel 2 in green, Panel 3 in blue). The exposure is truncated above 30 h to increase visibility, and the color transition (from black to red) is set at 7.5 h. The aspect ratio of the top three panels has been stretched vertically for better visibility.
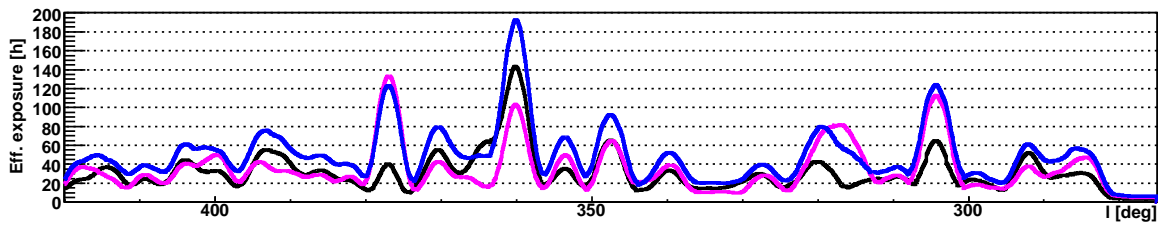
Figure 2.9: Comparison of effective exposure on the Galactic plane and ±1.5° off-plane. The plane is defined here as $b = -0.3°$, the mean Galactic latitude of the sources in the H.E.S.S. GPS. Shown are projections of effective exposure along the Galactic plane ($b = -0.3°$, blue), above the plane ($b = +1.2°$, black), and below the plane ($b = -1.8°$, magenta).

The effective exposure is noticeably lower and increasingly uneven off-plane, i.e. at relatively high Galactic latitudes (see e.g. 2.9). This is a result of the systematic scans focusing on very low Galactic latitudes, where the majority of H.E.S.S. sources have been discovered and where the majority of Galactic VHE γ-ray source candidates are located. However, some Galactic H.E.S.S. sources are found off the Galactic plane. Dedicated observations of these sources have contributed to increased off-plane exposure in certain regions (Fig. 2.9) thanks to H.E.S.S.'s large FoV and have sometimes resulted in serendepitous discoveries of off-plane sources, e.g. HESS J1507−622.

2.6.3   Flux

Due to the inherent limitations of significance maps, it is natural to want an image of the Galaxy which corrects for effects such as varying exposure and which has real, physical units so that it can be used to infer actual source properties. The obvious choice is that of flux, which has units of photons detected per unit area per unit time (typically $cm^{-2}\,s^{-1}$), integrated over an appropriate energy range (integral flux).

The procedure used to produce large flux maps is similar to that used to produce the significance maps previously shown, with the main difference being that the expected γ-ray flux from each location in the map must be calculated. This takes takes into account the observation livetime (as a function of ZA) and the respective effective area. The latter depends on the observation ZA, muon correction factor, selected energy range, distance from the camera center, and the integration region being considered. It is thus also necessary to assume the spectral shape of the expected VHE γ-ray flux. In this case, source spectra are assumed to follow a power-law with a slope $\Gamma = 2.5$, similar to that of the Crab Nebula, to which flux is often normalized. As noted earlier, a reduced dataset is used for the purpose of generating flux maps; in this case, the spectral-quality H.E.S.S. GPS dataset is used.

Regarding the selection of energy range, no cuts are imposed on the γ-ray events from

each observation which are included in the final flux map. This has the benefit incorporating the maximum amount of statistics available, similar to the significance maps. Further details have already been presented elsewhere (Hoppe 2008); most importantly, tests using the Crab Nebula demonstrate that the integral flux is consistent with that found from a dedicated spectral analysis to within an uncertainty of 5%. This result holds also if a cut is applied to the energy range to restrict the γ-ray events to those above the so-called safe energy threshold, as is done in dedicated spectral analyses (Hoppe 2008).

Regarding the choice of effective area, the effective area to detect a point source is used to produce flux maps with a point-like correlation region (circle with radius $\theta = 0.10°$). The flux is thus corrected for leakage of the signal outside of the correlation radius, and the flux at each position in the map should be interpreted as the flux measured from a putative point source centered at that position. However, since most VHE γ-ray sources are not point-like, flux maps are also created with a larger correlation region (circle with radius $\theta = 0.22°$) . These maps are produced using the effective area to detect a source of exactly that size, with no correction for leakage outside of that region. The flux at each position in these maps should thus be interpreted as the flux from a region of the sky equal in size to the correlation region.

Figure 2.10 shows such an image of the integral flux across the H.E.S.S. GPS region, where the flux at a given pixel represents the integral flux of a point-like source ($\theta = 0.10°$) centered at that position. The calculation of the integral flux is integrated in energy from 1 TeV to infinity. Since the minimum energy threshold varies considerably with Galactic longitude (due to varying ZAs), ranging from roughly 0.6 TeV to 1.5 TeV, this avoids large extrapolations to lower energies. However, it also renders sources with steeper (soft) spectra less visible on the maps shown. Since most VHE γ-ray sources are extended, many of them do not appear bright on this map since they lack sufficient statistics (excess γ-ray events) to be detected over a point-like integration region which is small compared to their actual size. Those that do appear are either actual point sources (e.g., the γ-ray binary HESS J1826−148 at $(\ell, b) \approx (16.9°, -1.4°)$) or very bright, high-statistics sources (e.g., HESS J1303−631 at $(\ell, b) \approx (304.2°, -0.4°)$). Additionally, sources with spectral slopes which differ significantly from the assumed $\Gamma = 2.5$ may not be visible. In contrast to significance maps, real morphological features are revealed in flux maps, an obvious example being the clear shell-type morphology seen from HESS J1713−397 (RX J1713.7−3946) at $(\ell, b) \approx (347.3°, -0.5°)$). Figure 2.11 shows a similar map, but for extended sources ($\theta = 0.22°$), where the majority of VHE γ-ray sources are clearly visible.

2.6.4 Sensitivity

Images of H.E.S.S. sensitivity across the H.E.S.S. GPS region are produced in the same way as for the integral flux. The sensitivity above an energy E is defined as the integral flux above

Figure 2.10: Image showing the integral flux ($E > 1\,\text{TeV}$) in the H.E.S.S. GPS region, divided into four panels. The flux is integrated over a point-like circular region of radius $\theta = 0.10°$, and is truncated in the image above $1.1\times10^{-12}\,\text{cm}^{-2}\,\text{s}^{-1}$, equivalent to 5% Crab above 1 TeV, to increase visibility. The color transition (from blue to red) is set at $5.7\times10^{-13}\,\text{cm}^{-2}\,\text{s}^{-1}$, equivalent to 2.5% Crab. Fluxes are only calculated for regions of the plane where the point-source sensitivity is better than 3% Crab.

E which is currently detectable by H.E.S.S. at significance of $5\,\sigma$. It depends primarily on the effective exposure and ZA of the observations at a given position on the plane. Like the calculation of flux, it assumes a Crab-like power-law index of $\Gamma = 2.5$. The point source sensitivity and the extended source sensitivity are shown in Figs. 2.12 and 2.13, respectively.

The best sensitivity is reached at the GC, which has an extremely deep exposure of ~190 h and is typically observed at low zenith angles, resulting in a point-source sensitivity at the mCrab level, 0.6% Crab (again, for $E > 1\,\text{TeV}$ and assuming $\Gamma = 2.5$). In general, the sensitivity is better than 6% Crab over the majority of the surveyed region, and typically ~2% Crab or better along the Galactic plane itself. Efforts to make the sensitivity more uniform along the plane will continue in 2011.
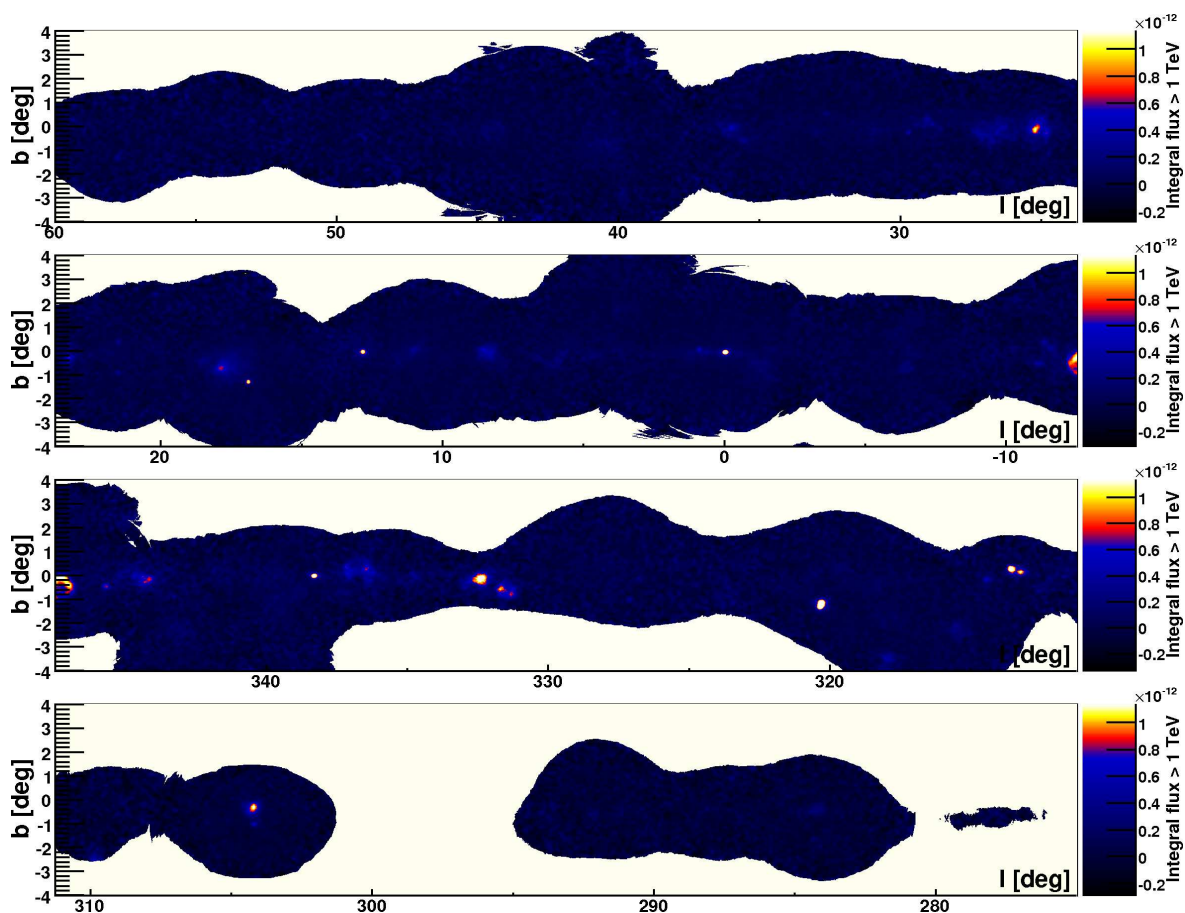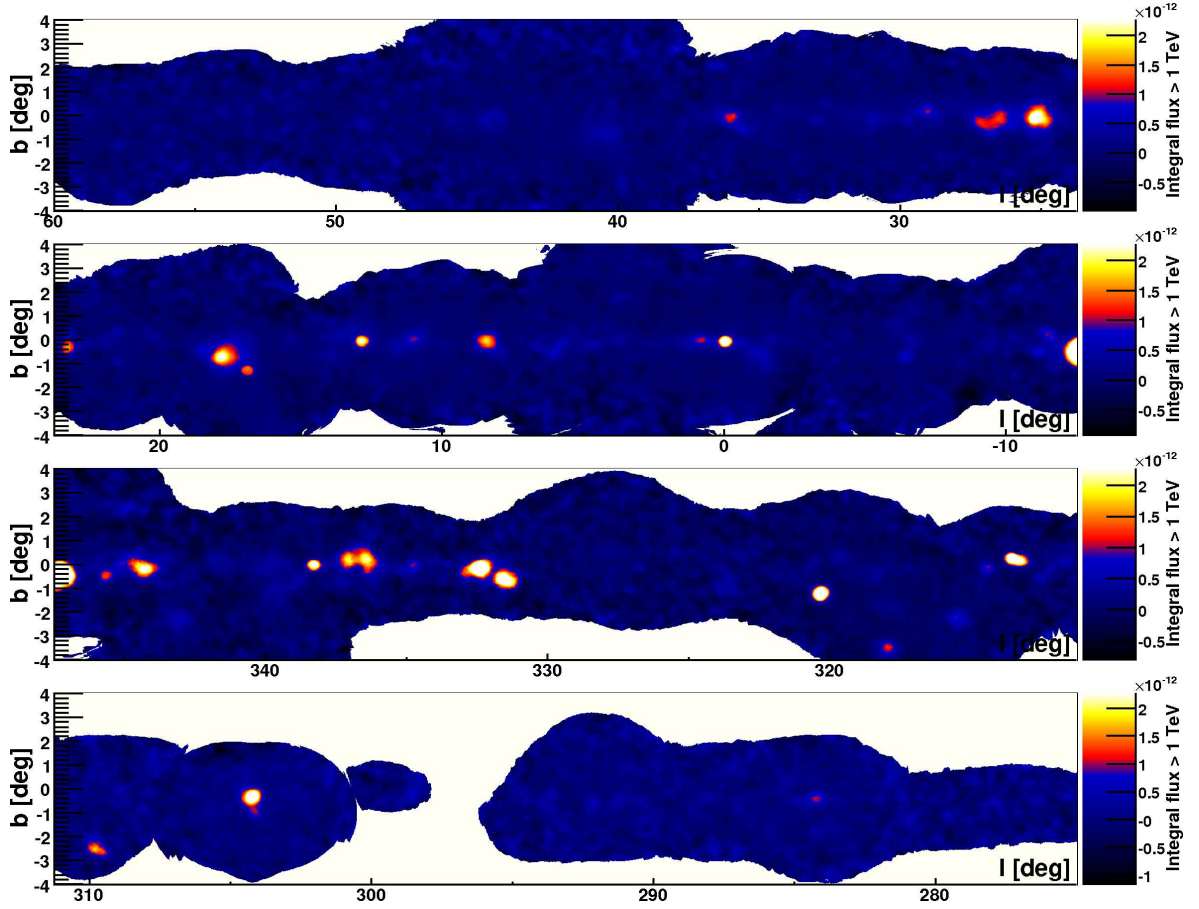
Figure 2.11: Image showing the integral flux ($E > 1\,\text{TeV}$) in the H.E.S.S. GPS region, divided into four panels. The flux is integrated over an extended circular region of radius $\theta = 0.22°$, and is truncated in the image above $2.3 \times 10^{-12}\,\text{cm}^{-2}\,\text{s}^{-1}$, equivalent to 10% Crab above 1 TeV, to increase visibility. The color transition (from blue to red) is set at $1.1 \times 10^{-12}\,\text{cm}^{-2}\,\text{s}^{-1}$, equivalent to 5% Crab. Fluxes are only calculated for regions of the plane where the extended-source sensitivity is better than 8% Crab.

2.7 Spatial distribution of Galactic H.E.S.S. sources

A total of 66 VHE γ-ray sources have now been detected by H.E.S.S. in the Galaxy, summarized in Table 2.1 which lists the H.E.S.S. identifier, best-fit position in Galactic coordinates, and the respective reference. Sixty of the sources fall within the region observed by the H.E.S.S. Galactic Plane Survey. The remaining six sources are either high-latitude sources (HESS J0534+220 / Crab Nebula, HESS J0632+057 / Monoceros, HESS J1502−421 / SN 1006 SW, and HESS J1504−418 / SN 1006 NE) or are in the outer Galaxy (HESS J0852−463 / Vela Jr and HESS J0835−455 / Vela X). Three H.E.S.S. sources do not yet have official H.E.S.S. identifiers and are instead listed by their potential counterparts (PSR J1119−6127, IGR J18490−0000, and W49B). A subtotal of 15 sources have been recently discovered in

Figure 2.12: Image showing the point-source sensitivity ($E > 1\,\mathrm{TeV}$) in the H.E.S.S. GPS region, divided into four panels. The VHE γ-ray spectrum of the putative emission is assumed to follow a power law with a Crab Nebula-like index $\Gamma = 2.5$. The sensitivity is given in units of the percentage of the Crab Nebula flux which is detectable by H.E.S.S. at a level of $5\,\sigma$ (pre-trial) significance. The sensitivity in the image is truncated above 12% Crab for visibility, and regions which have a higher (worse) sensitivity are not shown. The color transition (from color to grayscale) is set at 6% Crab.

the last two years alone, since the last major update on the H.E.S.S. GPS by Hoppe (2008), demonstrating the continued success of the H.E.S.S. survey at revealing new sources of VHE γ-rays.

The spatial distribution of the H.E.S.S. sources is illustrated in Figs. 2.14 and 2.15, which show their latitudinal and longitudinal distribution, respectively. The VHE γ-ray sources indeed cluster closely (rms 0.8°) to the Galactic plane (Fig. 2.14), with a mean latitude $b = -0.5°$. The rms implies that the Galactic plane as seen in VHE γ-rays has a thickness $O(100\,\mathrm{pc})$ in the inner Galaxy, compatible with the distribution of a presumed parent population comprised mostly of SNRs and pulsars. Although the main peak in the latitudinal distribution is somewhat offset toward negative latitudes, the mean is particularly skewed due to a handful of sources around $b \approx -3°$.
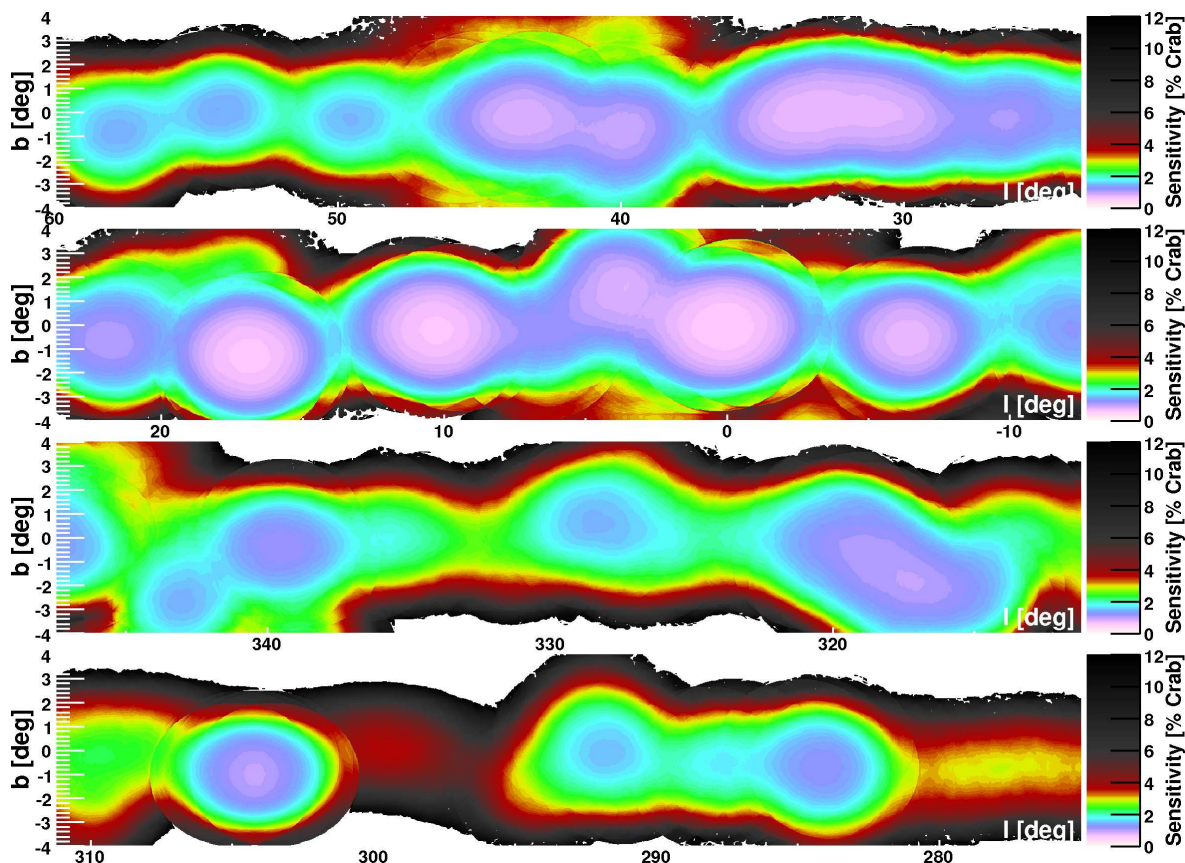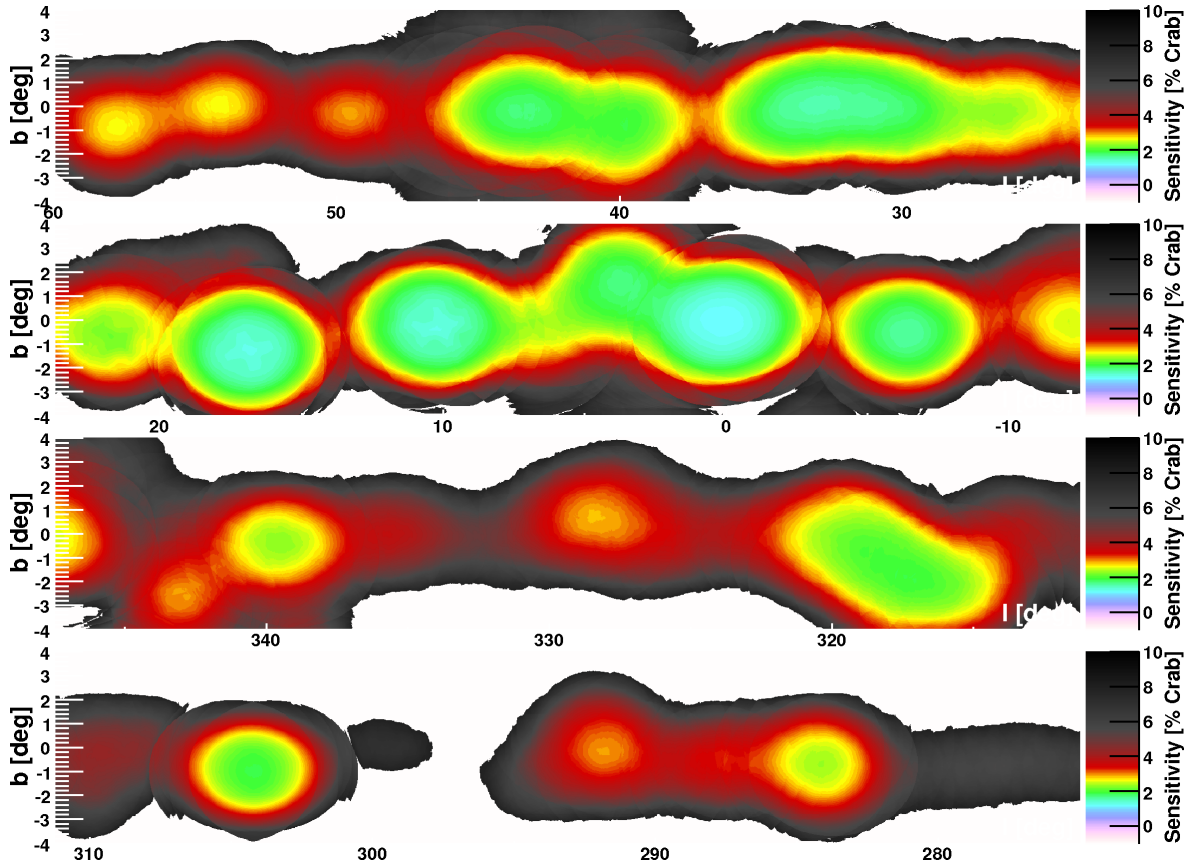
Figure 2.13: Image showing the extended-source sensitivity ($E > 1\,\mathrm{TeV}$) in the H.E.S.S. GPS region, divided into four panels. The VHE γ-ray spectrum of the putative emission is assumed to follow a power law with a Crab Nebula-like index $\Gamma = 2.5$. The sensitivity is given in units of the percentage of the Crab Nebula flux which is detectable by H.E.S.S. at a level of $5\,\sigma$ (pre-trial) significance. The sensitivity in the image is truncated above 10% Crab for visibility, and regions which have a higher (worse) sensitivity are not shown. The color transition (from color to grayscale) is set at 6% Crab.

The longitudinal distribution (Fig. 2.15) shows a fairly even distribution of sources across the inner Galaxy, peaking toward the center of the Galaxy. Interestingly, most of the peaks in the distribution appear to roughly coincide with the Galactic spiral arm structures traced at other wavelengths (Vallée 2008), notably the Scutum-Crux tangent at $\ell = 31° \pm 3°$, the start of the Perseus arm at $\ell = 339°(-21°) \pm 2°$, the Crux-Scutum tangent at $\ell = 310°(-50°) \pm 3°$, and the Carina-Sagittarius tangent at $\ell = 284°(-76°) \pm 2°$. The lack of sources above longitudes $\ell \approx 60°$ is due to H.E.S.S.'s location in the southern hemisphere, which prevents it from observing regions farther north. It is not possible at this time to draw any firm conclusions based on these distributions since the sensitivity of the H.E.S.S. GPS is considerably non-uniform across the survey region. For example, it is not clear if the distribution of VHE γ-ray sources toward negative latitudes is real or a result of the surveying strategy employed.

Figure 2.14: Histogram of the latitudinal distribution of Galactic H.E.S.S. sources. Outliers beyond $b \pm 4°$ have been omitted.
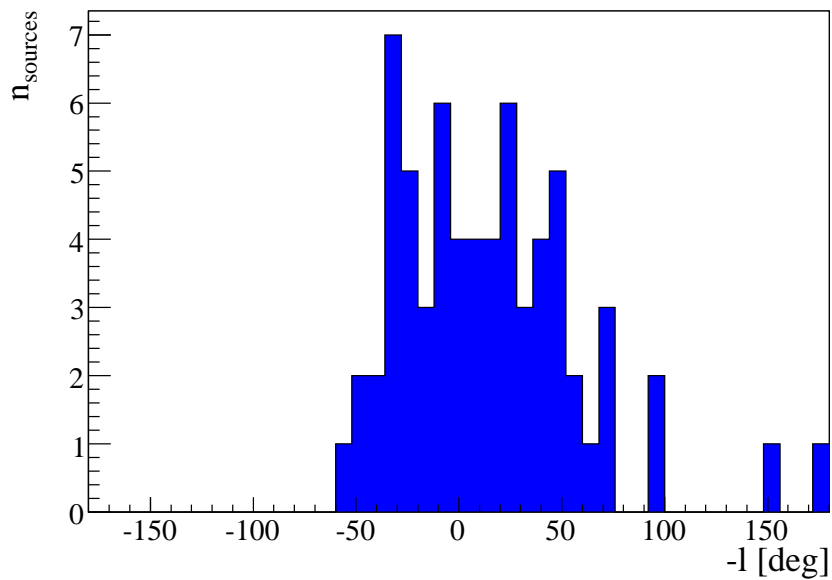
Figure 2.15: Histogram of the longitudinal distribution of Galactic H.E.S.S. sources. *N.B.* The horizontal axis shows negative longitudes.

Table 2.1: Names and positions of the 66 Galactic VHE γ-ray sources detected by H.E.S.S. to date, sorted by increasing right ascension. 60 of these are located within the region surveyed by H.E.S.S.. The positions were determined by fitting the uncorrelated γ-ray excesses with 2D symmetr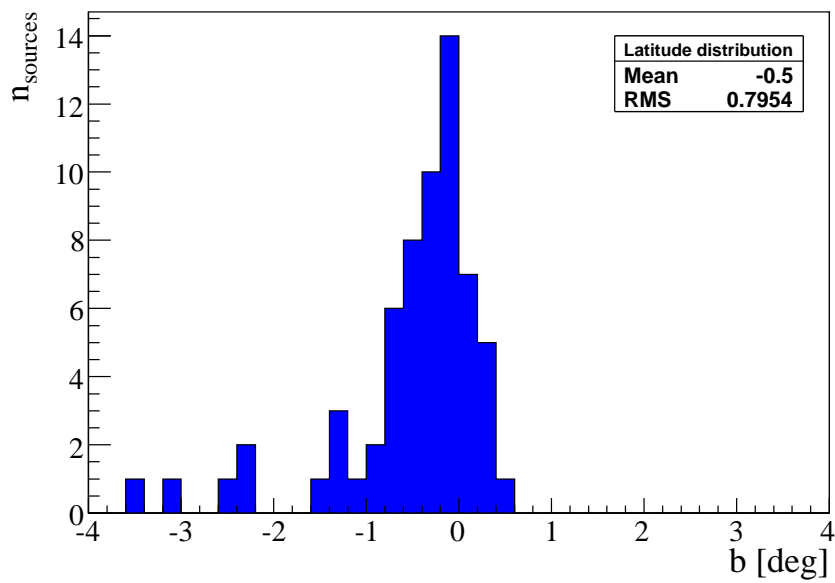ic Gaussian profiles convolved with the H.E.S.S. PSF; they are given in Galactic coordinates. The references for the most recent H.E.S.S. publication with positional data are given in the last column. New sources detected since Hoppe (2008) are denoted by a superscript dagger. References to H.E.S.S. Source of the Month (SOM) articles can be found at `http://www.mpi-hd.mpg.de/hfm/HESS/pages/home/som`; respective journal publications are in preparation. References to TEXAS2010 refer to proceedings of the 25th Texas Symposium on Relativistic Astrophysics which are in preparation. Uncertainties in position are as low as $10''$ in the case of the GC (HESS J1745$-$290) but more typically between $0.01°$ and $0.05°$ (see respective references for details).

Identifier	ℓ	b	Reference
HESS J0534+220	184.56°	−5.78°	Aharonian et al. (2006a)
HESS J0632+057	205.66°	−1.44°	Aharonian et al. (2007e)
HESS J0835−455	263.86°	−3.09°	Aharonian et al. (2006b)
HESS J0852−463	266.29°	−1.24°	Aharonian et al. (2007d)
HESS J1018−589†	284.80°	−0.52°	SOM 2010-08
HESS J1023−575	284.22°	−0.40°	Abramowski et al. (2011)
HESS J1026−582†	284.80°	−0.52°	Abramowski et al. (2011)
PSR J1119−6127†	292.14°	−0.60°	SOM 2009-11
HESS J1302−638	304.19°	−0.99°	Aharonian et al. (2005c)
HESS J1303−631	304.24°	−0.36°	Aharonian et al. (2005d)
HESS J1356−645	309.81°	−2.49°	Renaud et al. (2008b)
HESS J1418−609	313.25°	0.15°	Aharonian et al. (2006e)
HESS J1420−607	313.56°	0.27°	Aharonian et al. (2006e)
HESS J1427−608	314.41°	−0.14°	Aharonian et al. (2008a)
HESS J1442−624	315.41°	−2.30°	Aharonian et al. (2009c)
HESS J1457−593†	318.3°	−0.3°	Hofverberg et al. (TEXAS2010)
HESS J1502−421†	327.35°	14.48°	Acero et al. (2010a)
HESS J1503−582†	319.60°	0.30°	Chapter 4

Table 2.1: Names and positions of the 66 Galactic VHE γ-ray sources detected by H.E.S.S. to date, sorted by increasing right ascension. 60 of these are located within the region surveyed by H.E.S.S.. The positions were determined by fitting the uncorrelated γ-ray excesses with 2D symmetric Gaussian profiles convolved with the H.E.S.S. PSF; they are given in Galactic coordinates. The references for the most recent H.E.S.S. publication with positional data are given in the last column. New sources detected since Hoppe (2008) are denoted by a superscript dagger. References to H.E.S.S. Source of the Month (SOM) articles can be found at `http://www.mpi-hd.mpg.de/hfm/HESS/pages/home/som`; respective journal publications are in preparation. References to TEXAS2010 refer to proceedings of the 25th Texas Symposium on Relativistic Astrophysics which are in preparation. Uncertainties in position are as low as $10''$ in the case of the GC (HESS J1745−290) but more typically between $0.01°$ and $0.05°$ (see respective references for details).

Identifier	ℓ	b	Reference
HESS J1504−418[†]	327.84°	14.57°	Acero et al. (2010a)
HESS J1507−622	317.95°	−3.49°	Acero et al. (2011)
HESS J1514−591	320.33°	−1.19°	Aharonian et al. (2005g)
HESS J1614−518	331.52°	−0.58°	Aharonian et al. (2006d)
HESS J1616−508	332.39°	−0.14°	Aharonian et al. (2006d)
HESS J1626−490	334.77°	0.05°	Aharonian et al. (2008a)
HESS J1632−478	336.38°	0.19°	Aharonian et al. (2006d)
HESS J1634−472	337.11°	0.22°	Aharonian et al. (2006d)
HESS J1640−465	338.32°	−0.02°	Aharonian et al. (2006d)
HESS J1648−458[†]	339.55°	−0.35°	Ohm et al. (TEXAS2010)
HESS J1702−420	344.30°	−0.18°	Aharonian et al. (2008a)
HESS J1708−410	345.66°	−0.44°	Aharonian et al. (2008a)
HESS J1708−443	343.06°	−2.38°	Chapter 3
HESS J1713−381	348.65°	0.38°	Aharonian et al. (2008d)
HESS J1713−397	347.33°	−0.47°	Aharonian et al. (2007c)
HESS J1714−385	348.39°	0.11°	Aharonian et al. (2008e)
HESS J1718−385	348.83°	−0.49°	Aharonian et al. (2007a)
HESS J1731−347	353.57°	−0.62°	Aharonian et al. (2008a)

Table 2.1: Names and positions of the 66 Galactic VHE γ-ray sources detected by H.E.S.S. to date, sorted by increasing right ascension. 60 of these are located within the region surveyed by H.E.S.S.. The positions were determined by fitting the uncorrelated γ-ray excesses with 2D symmetric Gaussian profiles convolved with the H.E.S.S. PSF; they are given in Galactic coordinates. The references for the most recent H.E.S.S. publication with positional data are given in the last column. New sources detected since Hoppe (2008) are denoted by a superscript dagger. References to H.E.S.S. Source of the Month (SOM) articles can be found at `http://www.mpi-hd.mpg.de/hfm/ HESS/pages/home/som`; respective journal publications are in preparation. References to TEXAS2010 refer to proceedings of the 25th Texas Symposium on Relativistic Astrophysics which are in preparation. Uncertainties in position are as low as $10''$ in the case of the GC (HESS J1745−290) but more typically between $0.01°$ and $0.05°$ (see respective references for details).

Identifier	ℓ	b	Reference
HESS J1741−302[†]	358.28°	0.12°	Tibolla et al. (2009)
HESS J1745−290	359.94°	−0.04°	Acero et al. (2010b)
HESS J1745−303	358.71°	−0.64°	Aharonian et al. (2008b)
HESS J1747−281	0.87°	0.08°	Aharonian et al. (2005b)
HESS J1800−240A	6.14°	−0.63°	Aharonian et al. (2008f)
HESS J1800−240B	5.90°	−0.36°	Aharonian et al. (2008f)
HESS J1800−240C	5.71°	−0.06°	Aharonian et al. (2008f)
HESS J1801−233	6.66°	−0.27°	Aharonian et al. (2008f)
HESS J1804−216	8.40°	−0.03°	Aharonian et al. (2006d)
HESS J1809−193	11.18°	−0.09°	Aharonian et al. (2007a)
HESS J1813−178	12.81°	−0.03°	Aharonian et al. (2006d)
HESS J1825−137	17.71°	−0.70°	Aharonian et al. (2006f)
HESS J1826−148	16.90°	−1.28°	Aharonian et al. (2006g)
HESS J1832−084[†]	23.29°	0.30°	Chapter 5
HESS J1833−105	21.51°	−0.88°	Djannati-Ataï et al. (2008)
HESS J1834−087	23.24°	−0.32°	Aharonian et al. (2006d)
HESS J1837−069	25.18°	−0.11°	Aharonian et al. (2006d)
HESS J1841−055	26.80°	−0.20°	Aharonian et al. (2008a)

Table 2.1: Names and positions of the 66 Galactic VHE γ-ray sources detected by H.E.S.S. to date, sorted by increasing right ascension. 60 of these are located within the region surveyed by H.E.S.S.. The positions were determined by fitting the uncorrelated γ-ray excesses with 2D symmetric Gaussian profiles convolved with the H.E.S.S. PSF; they are given in Galactic coordinates. The references for the most recent H.E.S.S. publication with positional data are given in the last column. New sources detected since Hoppe (2008) are denoted by a superscript dagger. References to H.E.S.S. Source of the Month (SOM) articles can be found at `http://www.mpi-hd.mpg.de/hfm/HESS/pages/home/som`; respective journal publications are in preparation. References to TEXAS2010 refer to proceedings of the 25th Texas Symposium on Relativistic Astrophysics which are in preparation. Uncertainties in position are as low as $10''$ in the case of the GC (HESS J1745−290) but more typically between $0.01°$ and $0.05°$ (see respective references for details).

Identifier	ℓ	b	Reference
HESS J1843−033	29.08°	0.15°	Hoppe (2008)
HESS J1846−029	29.71°	−0.24°	Djannati-Ataĭ et al. (2008)
HESS J1848−018	30.98°	−0.16°	Chapter 6
IGR J18490−0000[†]	32.64°	0.53°	Terrier et al. (2008)
HESS J1852−000[†]	33.0°	−0.2°	Kosack et al. (TEXAS2010)
HESS J1857+026	35.96°	−0.06°	Aharonian et al. (2008a)
HESS J1858+020	35.58°	−0.58°	Aharonian et al. (2008a)
HESS J1908+062	40.39°	−0.79°	Aharonian et al. (2009a)
W49B[†]	42.26°	−0.19°	Brun et al. (TEXAS2010)
HESS J1912+101	44.39°	−0.07°	Aharonian et al. (2008c)
HESS J1923+141[†]	49.10°	−0.39°	Fiasson et al. (2009)
HESS J1943+213[†]	57.76°	−1.29°	SOM 2010-11

Chapter 3

Detection of very-high-energy γ-ray emission from the vicinity of PSR B1706−44 and G 343.1−2.3

This chapter pertains to the discovery of VHE γ-ray emission from the vicinity of the EGRET-detected γ-ray pulsar PSR B1706−44 and the supernova remnant G 343.1−2.3 using H.E.S.S. data. It includes a comprehensive summary of the efforts to observe PSR B1706−44 in the VHE domain, a re-analysis of data previously published by H.E.S.S., and a detailed discussion of both leptonic and hadronic scenarios for the origin of the detected VHE γ-rays. It is based in part upon a preliminary draft and analysis by Hoppe (2008) but has undergone substantial changes since then; in particular, the text has been re-written, the introduction has been significantly extended, the analysis has been revised, the discussion made more thorough, and an appendix has been added. Radio data reduction was performed by G. Dubner and E. Giacani. The paper appears here (with minor typographical changes) as published in:

Abramowski, et al. (**H.E.S.S. Collaboration**)[1]
Astronomy & Astrophyiscs, in press

Abstract

The γ-ray pulsar PSR B1706−44 and the adjacent supernova remnant (SNR) candidate G 343.1−2.3 were observed by H.E.S.S. during a dedicated observation campaign in 2007. As a result of this observation campaign, a new source of very-high-energy (VHE; $E > 100$ GeV) γ-ray emission, HESS J1708−443, was detected with a statistical significance of 7 σ, al-

---

[1]Corresponding authors: R.C.G. Chaves and S. Hoppe; External (non-H.E.S.S.) authors: G. Dubner and E. Giacani

though no significant point-like emission was detected at the position of the energetic pulsar itself. In this chapter, the morphological and spectral analyses of the newly-discovered TeV source are presented. The centroid of HESS J1708−443 is considerably offset from the pulsar and located near the apparent center of the SNR, at $\alpha_{J2000} = 17^h08^m11^s \pm 17^s$ and $\delta_{J2000} = -44°20' \pm 4'$. The source is found to be significantly more extended than the H.E.S.S. point spread function (∼0.1°), with an intrinsic Gaussian width of 0.29° ± 0.04°. Its integral flux between 1 and 10 TeV is ∼ 3.8×10^{-12} ph cm^{-2} s^{-1}, equivalent to 17% of the Crab Nebula flux in the same energy range. The measured energy spectrum is well-fit by a power law with a relatively hard photon index $\Gamma = 2.0 \pm 0.1_{stat} \pm 0.2_{sys}$. Additional multi-wavelength data, including 330 MHz VLA observations, were used to investigate the VHE γ-ray source's possible associations with the pulsar wind nebula of PSR B1706−44 and/or with the complex radio structure of the partial shell-type SNR G 343.1−2.3.

3.1 Introduction

The energetic pulsar PSR B1706−44 (also PSR J1709−4429) is one of the first pulsars from which pulsed emission was detected not only in the radio (Johnston et al. 1992) and in X-rays (Gotthelf et al. 2002), but also in high-energy (HE; E ∼ GeV) γ-rays (Swanenburg et al. 1981). The pulsar was first detected in a high-frequency radio survey by Johnston et al. (1992) and has a spin period $P = 102$ ms, a characteristic age $\tau_c = 17\,500$ yr, and a spin-down luminosity $\dot{E} = 3.4 \times 10^{36}$ erg s^{-1}. It belongs to the class of relatively young and powerful pulsars, of which the Vela Pulsar is the most prominent example in the southern hemisphere. The putative wind nebulae of these pulsars are prime candidates for being sources of very-high-energy (VHE; E > 100 GeV) γ-rays. A bright, HE γ-ray source, 2CG 342−02, was discovered by the *COS-B* satellite (Swanenburg et al. 1981) and later found to be positionally coincident with the radio pulsar. The γ-ray source was firmly associated with PSR B1706−44 after EGRET (the Energetic Gamma Ray Experiment Telescope, onboard the *Compton Gamma-Ray Observatory*) observed pulsations from 3EG J1710−4439 (also EGR J1710−4435) which matched the period seen in the radio waveband (Thompson et al. 1992). More recently, the pulsar has been detected at GeV energies by the latest generation of spaceborne HE γ-ray detectors: by *AGILE* (*Astrorivelatore Gamma ad Immagini LEggero*) as 1AGL J1709−4428 (Pittori et al. 2009) and by the *Fermi*/LAT (Large Area Telescope) as 1FGL J1709.7−4429 (Abdo et al. 2010).

Radio observations of PSR B1706−44 reveal the presence of a synchrotron nebula, with an extension of ∼3′, surrounding the pulsar (Frail et al. 1994; Giacani et al. 2001). The observed polarization and the flat spectrum, with a flux density spectral slope $\alpha = 0.3$ (where the flux density $S \propto \nu^{-\alpha}$), suggest it is a pulsar wind nebula (PWN). However, the implied conversion efficiency from spin-down energy to radio flux of ∼2×10^{-6} would be the lowest of any known radio PWN (Giacani et al. 2001). Observations by the X-ray telescopes

onboard *ROSAT* (*Roentgen Satellite*) and *ASCA* (*Advanced Satellite for Cosmology and Astrophysics*) reveal that the nebula is also visible in X-rays (Finley et al. 1998). The morphology of the PWN was mapped in detail at arcsecond scales utilizing the superior resolution of the *Chandra X-ray Observatory* (Romani et al. 2005). The X-ray analyses suggest the presence of a diffuse X-ray PWN, with a spectral index of 1.77, which surrounds a more complex structure consisting of a torus and inner and outer jets. The diffuse X-ray PWN has a radius of 1.8′ and also exhibits a fainter, longer extension to the West. The presence of non-deformed X-ray jets is consistent with the pulsar's low apparent speed, $v = 89$ km s^{-1}, as deduced from scintillation measurements (Johnston et al. 1998).

The pulsar PSR B1706−44 is also located at the southeast end of an incomplete arc of radio emission (McAdam et al. 1993), which has been suggested to be the partial shell of a faint supernova remnant (SNR G 343.1−2.3). The arc is embedded in weak diffuse radio emission, which is present both inside and outside of the arc (Frail et al. 1994). Polarization measurements suggest that this diffuse emission is associated with synchrotron radiation from the SNR itself (Dodson & Golap 2002). The SNR has not been detected in any other waveband (see e.g. Becker et al. 1995; Aharonian et al. 2005e). There are various estimates of the distance to the pulsar, ranging from 1.8 kpc (Johnston et al. 1992; Taylor & Cordes 1993) to 3.2 kpc (Koribalski et al. 1995). The distance 2.3 ± 0.3 kpc, derived from the dispersion measure and the most recent Galactic free electron distribution model (Cordes & Lazio 2002), is adopted throughout this thesis. This distance is compatible with the less reliable $\Sigma - D$ distance of ~3 kpc for the SNR (McAdam et al. 1993).

Observation dates	Instrument	Test position	Extension	Integral flux (ph cm^{-2} s^{-1})	Reference
1992	CANGAROO-I	PSR B1706−44	n/a	$F(> 1\,\mathrm{TeV}) \sim 1 \times 10^{-11}$	Ogio et al. (1993)
1993	CANGAROO-I	PSR B1706−44	n/a	$F(> 3.2 \pm 1.6\,\mathrm{TeV}) < 8.0 \times 10^{-13}$	Yoshikoshi et al. (2009)
1993–1994	CANGAROO-I	PSR B1706−44	n/a	$F(> 3.2 \pm 1.6\,\mathrm{TeV}) < 6.1 \times 10^{-13}$	Yoshikoshi et al. (2009)
1995	CANGAROO-I	PSR B1706−44	n/a	$F(> 3.2 \pm 1.6\,\mathrm{TeV}) < 8.9 \times 10^{-13}$	Yoshikoshi et al. (2009)
1997	CANGAROO-I	PSR B1706−44	n/a	$F(> 1.8 \pm 0.9\,\mathrm{TeV}) < 4.1 \times 10^{-12}$	Yoshikoshi et al. (2009)
1998	CANGAROO-I	PSR B1706−44	n/a	$F(> 2.7 \pm 1.4\,\mathrm{TeV}) < 1.3 \times 10^{-12}$	Yoshikoshi et al. (2009)
1993–1994	BIGRAT	PSR B1706−44	n/a	$F(> 0.5\,\mathrm{TeV}) < (7.0 \pm 0.7) \times 10^{-11}$	Rowell et al. (1998)
1996	Durham Mark 6	PSR B1706−44	n/a	$F(> 0.3\,\mathrm{TeV}) = (3.9 \pm 0.7) \times 10^{-11}$	Chadwick et al. (1998)
2000–2001	CANGAROO-II	PSR B1706−44	n/a	n/a	Kushida & et al. (2003)
2003	H.E.S.S.	G 343.1−2.3 center	0.6°	$F(> 0.50\,\mathrm{TeV}) < 7.6 \times 10^{-12}$	Sect. 3.5
2003	H.E.S.S.	G 343.1−2.3 center	0.6°	$F(> 0.60\,\mathrm{TeV}) < 6.3 \times 10^{-12}$	Sect. 3.5
2004–2007	CANGAROO-III	PSR B1706−44	0.26°	$F(> 1\,\mathrm{TeV}) = (3.0 \pm 0.6) \times 10^{-12}$	Enomoto et al. (2009)
2004–2007	CANGAROO-III	PSR B1706−44	1.0°	$F(> 1\,\mathrm{TeV}) \approx 2.2 \times 10^{-11}$	Enomoto et al. (2009)
2007	H.E.S.S.	PSR B1706−44	0.1°	$F(> 0.6\,\mathrm{TeV}) < 3.3 \times 10^{-13}$	Sect. 3.3
2007	H.E.S.S.	G 343.1−2.3 center	0.6°	$F(> 0.6\,\mathrm{TeV}) \approx 6.5 \times 10^{-12}$	Sect. 3.3

Table 3.1: Summary of the efforts to observe PSR B1706−44 in the VHE γ-ray domain. The CANGAROO upper limits (ULs) are at a 95% confidence level (CL), the BIGRAT UL is at 3 σ (99.7% CL), and the H.E.S.S. ULs are at a 99% CL. The CANGAROO-I integral flux based on the 1992 dataset (Ogio et al. 1993) likely suffered from systematics similar to those that affected the 1993 data, which has since been re-analysed along with an analysis of the previously unreleased 1994–1998 CANGAROO-I data; the ULs assume a Crab-like spectral index $\Gamma = -2.5$ (Yoshikoshi et al. 2009). Only the latest, revised results are shown in this table; see Sect. 3.1 for further discussion. The BIGRAT UL is subject to an additional ± 50% systematic uncertainty (Rowell et al. 1998). The integral flux from the 2000–2001 CANGAROO-II data analysis was not disclosed but was claimed to confirm previous results (Kushida & et al. 2003). The 2003 H.E.S.S. ULs are based on the re-analysis presented in Sect. 3.5; the first UL (row 10) assumes $\Gamma = -2.5$ for comparison to the CANGAROO ULs, while the second UL (row 11) assumes $\Gamma = -2.0$ for comparison to the 2007 H.E.S.S. detection. The CANGAROO-III fluxes are from the ON-OFF analysis presented in Enomoto et al. (2009). The 2007 H.E.S.S. results are described in Sect. 3.3, where the center of G 343.1−2.3 is also defined; the point-source UL assumes $\Gamma = -2.5$.

The possible physical association between PSR B1706−44 and G 343.1−2.3 has been questioned based on the differing age and distance estimates for the SNR and pulsar (see Sec. 4.2 and 4.3, respectively) and the lack of visible interaction. Furthermore, if the pulsar originated at the apparent center of the SNR, then its inferred velocity ($\sim$700 km s^{-1}) is incompatible with its scintillation velocity (89 km s^{-1}). Bock & Gvaramadze (2002) suggested a scenario where an off-center cavity explosion could relax the restrictions on the inferred velocity and invalidate the age estimate for the SNR of $\sim$5 000 yr (McAdam et al. 1993), which is based on a Sedov-Taylor model. In this scenario, PSR B1706−44 and G 343.1−2.3 are physically associated; however, the radio arc is not identified with the SNR shell, but rather with the former boundary of the wind-blown cavity that was overtaken and compressed by the expanding SNR (Dodson & Golap 2002).

In the VHE domain, both the pulsar and the SNR have been observed using ground-based, imaging atmospheric-Cherenkov telescopes (IACTs). The findings of the various observations are, however, not fully consistent (see Table 3.1). The CANGAROO (Collaboration of Australia and Nippon (Japan) for a Gamma Ray Observatory in the Outback) Collaboration reported the detection of steady emission, coincident with the pulsar, using the 3.8 m CANGAROO-I telescope in 1992–1993 (Kifune et al. 1995). They measured an integral flux $F(\gtrsim 1 \text{ TeV}) \approx 1 \times 10^{-11}$ ph cm^{-2} s^{-1}, equivalent to $\sim$44% of the Crab Nebula flux[2]. However, the CANGAROO Collaboration recently undertook a comprehensive re-analysis of their archival CANGAROO-I data and no longer find a signal; instead, they calculate an upper limit (UL; here, at 95% confidence level and assuming a spectral index of −2.5) to the integral flux of $F(\gtrsim 3.2 \text{ TeV}) < 8.0 \times 10^{-13}$ ph cm^{-2} s^{-1} ($\sim$24% Crab) (Yoshikoshi et al. 2009). The 4-m BIGRAT (BIcentinnial Gamma RAy Telescope) telescope (Rowell et al. 1998) also observed the pulsar in 1993–1994 and reported a compatible UL. Observations in 1996 with the Durham Mark 6 telescope (Chadwick et al. 1998) appeared to confirm the earlier CANGAROO-I detection, with a reported integral flux that was compatible within the large systematic uncertainties (±30% for CANGAROO-I and ±50% for the Mark 6). Further observations with the CANGAROO-II telescopes in 2000–2001 again seemed to validate the detection (Kushida & et al. 2003). However, when the H.E.S.S. (High Energy Stereoscopic System) Collaboration observed the pulsar in 2003 during its commissioning phase, they did not detect any significant VHE γ-ray emission from PSR B1706−44 or its vicinity. The derived UL (99% confidence level) on the integral flux from an extended region encompassing the SNR was found to be $F(> 0.5 \text{ TeV}) < 3.5 \times 10^{-12}$ ph cm^{-2} s^{-1} ($\sim$5% Crab) (Aharonian et al. 2005e), in stark disagreement with all of the previous findings (see also Sec. 3.5). Shortly thereafter, preliminary analysis of stereo observations with the 4 × 10-m CANGAROO-III telescope array also disagreed with the initial CANGAROO-I detection and resulted in an UL at the pulsar position (95% confidence level) of $F(\gtrsim 0.6 \text{ TeV}) \lesssim 5 \times$

---

[2]The Crab Nebula spectrum published in Aharonian et al. (2006a) is adopted as the reference Crab spectrum throughout this thesis.

10^{-12} ph cm^{-2} s^{-1} (~10% Crab) (Tanimori & et al. 2005), which agreed with the H.E.S.S. results at the time.

In 2007, H.E.S.S. followed up on their initial result by carrying out additional dedicated observations of the pulsar, now utilizing the superior sensitivity of the fully-operational H.E.S.S. telescope array. This campaign resulted in the discovery of extended emission from the vicinity of PSR B1706−44 and G 343.1−2.3, with preliminary results published in Hoppe et al. (2009). The latest results from CANGAROO-III also indicate the presence of an extended source of VHE γ-ray emission from the vicinity of the pulsar, although the spectrum and morphology of the emission vary considerably depending on the method used for background subtraction (Enomoto et al. 2009). For example, integrating within $1.0°$ of the pulsar position and using an ON-OFF background method (see Sect. 3.2.2), they find a Crab Nebula-level integral flux. In this chapter, we present new VHE data on PSR B1706−44 and G 343.1−2.3 which was obtained during H.E.S.S.'s 2007 observational campaign.

3.2   H.E.S.S. observations and analysis

The section "The H.E.S.S. telescope array" has been incorporated into Chapter 1.

3.2.1   VHE γ-ray observations

The region of interest, which includes PSR B1706−44 and SNR G 343.1−2.3, was observed with the full four-telescope H.E.S.S. array in 2007. The observations were dedicated to search for VHE γ-ray emission from the pulsar and were therefore taken in *wobble* mode centered on its position in the radio ($\alpha_{2000} = 17^h09^m42.73^s$, $\delta_{2000} = -44°29'08.2''$; Wang et al. (2000)). In this observation mode, the array is pointed toward a position offset from the source of interest to allow simultaneous background estimation. Observations of 28-min duration were taken, alternating between offsets of $±0.7°$ in declination and right ascension. After standard quality selection (Aharonian et al. 2006a) to remove data affected by unstable weather conditions or hardware-related problems, the total live-time of the dataset is ~15 h. The zenith angle of the observations ranges from $20°$ to $30°$, with a mean of $24°$. We only use data from the 2007 observations of PSR B1706−44, because at that time the full four-telescope array was in operation along with the central stereo trigger system, resulting in a higher sensitivity compared to earlier observations in 2003 (Aharonian et al. 2005e) when H.E.S.S. was in its commissioning phase, with only two telescopes and no central trigger (see also Sect. 3.5).

3.2.2   Analysis methods

The dataset was analyzed using the Hillas second moment method (Hillas 1985) and the H.E.S.S. standard analysis described in Aharonian et al. (2006a). For γ-hadron separation, *hard cuts* were used, which require a minimum of 200 photoelectrons (p.e.) to be recorded per EAS image. Compared to *standard cuts* (80 p.e.), this relatively strict requirement results in better background rejection and an improved angular resolution but also in an increased energy threshold (560 GeV for this dataset). The time-dependent optical response of the system was estimated from the Cherenkov light of single muons passing close to the telescopes (Bolz 2004). Three different background estimation procedures (Berge et al. 2007) were used in this analysis.

For 2D image generation, the *ring background method* (Berge et al. 2007) was used with a mean ring radius of 0.85°. Since this method includes an energy-averaged model for the camera acceptance to account for the different offsets of the signal and background regions from the camera center, it was not used for spectral extraction. The *reflected region background method* (Berge et al. 2007) was instead used to measure the flux from the pulsar position.

Since the observations of PSR B1706−44 were performed in *wobble* mode (see Sect. 3.2.2), half are actually pointed inside the extended emission from HESS J1708−443, which was not known to exist at that time. Therefore, for spectral extraction from extended regions which also enclose the pointing positions of the telescopes, the background was estimated using the *ON-OFF background method* (Berge et al. 2007), where off-source (OFF) data taken is taken from extragalactic regions of the sky where no γ-ray sources are known. To match the observing conditions between on-source (ON) and OFF data, the two observations had to be taken within six months of each other and at similar zenith angles. The *ON-OFF background method* was also used for the analysis of Vela Junior (Aharonian et al. 2005h). The normalization between ON and OFF observations (Berge et al. 2007) was calculated from the total event number in the two observations, excluding regions with significant VHE γ-ray signal. The background is thus normalized in an approximately ring-shaped region (depicted in Fig. 3.4) with inner radius 1.0° and outer radius 2.5°, excluding a small region which overlaps the known source HESS J1702−420 (Aharonian et al. 2008a). With this background normalisation, the analysis is obviously only sensitive to a localized excess of γ-rays but not to emission which would be more or less uniform across the entire H.E.S.S. FoV.

3.3   Results

Two different circular regions were defined *a priori* in order to reduce the number of trials during a search for statistically-significant VHE γ-ray emission. Since other IACTs have reported point-like emission from the pulsar position, one of these regions, hereafter Re-

gion A, is centered at this position and has a radius of 0.10°, which is the standard radius used to search for point sources in the H.E.S.S. standard analysis. The second region, hereafter Region B, is identical to the region referred to as the *Radio arc* in Aharonian et al. (2005e); it is centered at the approximate apparent center of the radio arc ($\alpha_{2000} = 17^h08^m$, $\delta_{2000} = -44°16'48''$; as defined in Aharonian et al. (2005e)) and has a radius of 0.60° in order to enclose the entire radio structure.

No statistically-significant emission is observed from the pulsar position (Region A); therefore, an upper limit of 14.8 excess γ-ray events is calculated at a 99% confidence level, following the unified approach of Feldman & Cousins (1998). From Region B, however, a clear signal is detected with 543 excess γ-rays and a significance of 7.0 σ. The measured signal corresponds to a flux ~13% that of the Crab Nebula above 0.6 TeV. Table 3.2 summarizes the event statistics for Regions A and B.

Figure 3.1 presents an image of the VHE γ-ray excess in the 2° × 2° region around the source, smoothed with a Gaussian of width 0.09° to reduce statistical fluctuations. The smoothing radius is chosen to be on the same scale as the H.E.S.S. point-spread function (PSF; 68% containment radius ~ 0.1°), so that resolvable morphological features are largely maintained. The emission clearly extends beyond the PSF, which is depicted in the lower left inlay of Fig. 3.1. Figure 3.2 shows the number of excess events within the emission region along with their statistical errors, in quadratic bins of 0.175° width, without smoothing. This figure demonstrates that the current statistics do not permit a detailed study of the source morphology. However, the lack of a significant VHE γ-ray excess at the position of the pulsar is clear in both figures.

The centroid of the new H.E.S.S. source is determined by fitting the unsmoothed γ-ray excess image with a radially-symmetric Gaussian profile ($\phi = \phi_0\, e^{-r^2/(2\sigma^2)}$) convolved with the H.E.S.S. PSF (0.07° for this analysis). The centroid of the best fit is at $\alpha_{\mathrm{J2000}} = 17^h08^m11^s \pm 17^s$ and $\delta_{\mathrm{J2000}} = -44°20' \pm 4'$ ($\ell \sim 343.06°, b \sim -2.38°$). The pointing precision of the H.E.S.S. telescope array is 20″ (Gillessen et al. 2005), which adds an additional systematic uncertainty. The combined errors are reflected in the size of the cross in Fig. 3.1. Consequently, the new VHE γ-ray source is designated HESS J1708−443. The fit also gives the source's intrinsic Gaussian width $\sigma = 0.29° \pm 0.04°_{\mathrm{stat}}$.

Spectral analyses were performed for two regions, Region A, which was introduced above, and Region C, which is centered on the centroid (i.e. best-fit position) and has a radius of 0.71° (see Table 3.2). The size of Region C represents an ~95% enclosure of the excess, chosen as a compromise between an optimal signal-to-noise ratio and independence of source morphology. Both regions are indicated by dashed circles in Fig. 3.1. From Region A, an integral flux limit of $F(> 0.6\text{ TeV}) < 3.3 \times 10^{-13}$ ph cm^{-2} s^{-1} was derived with a 99% confidence level according to Feldman & Cousins (1998), assuming that the underlying γ-ray spectrum follows a power law with photon index $\Gamma = 2.5$, an index close to that of the Crab Nebula (Aharonian et al. 2006a). This upper limit corresponds to ~1% of the flux of
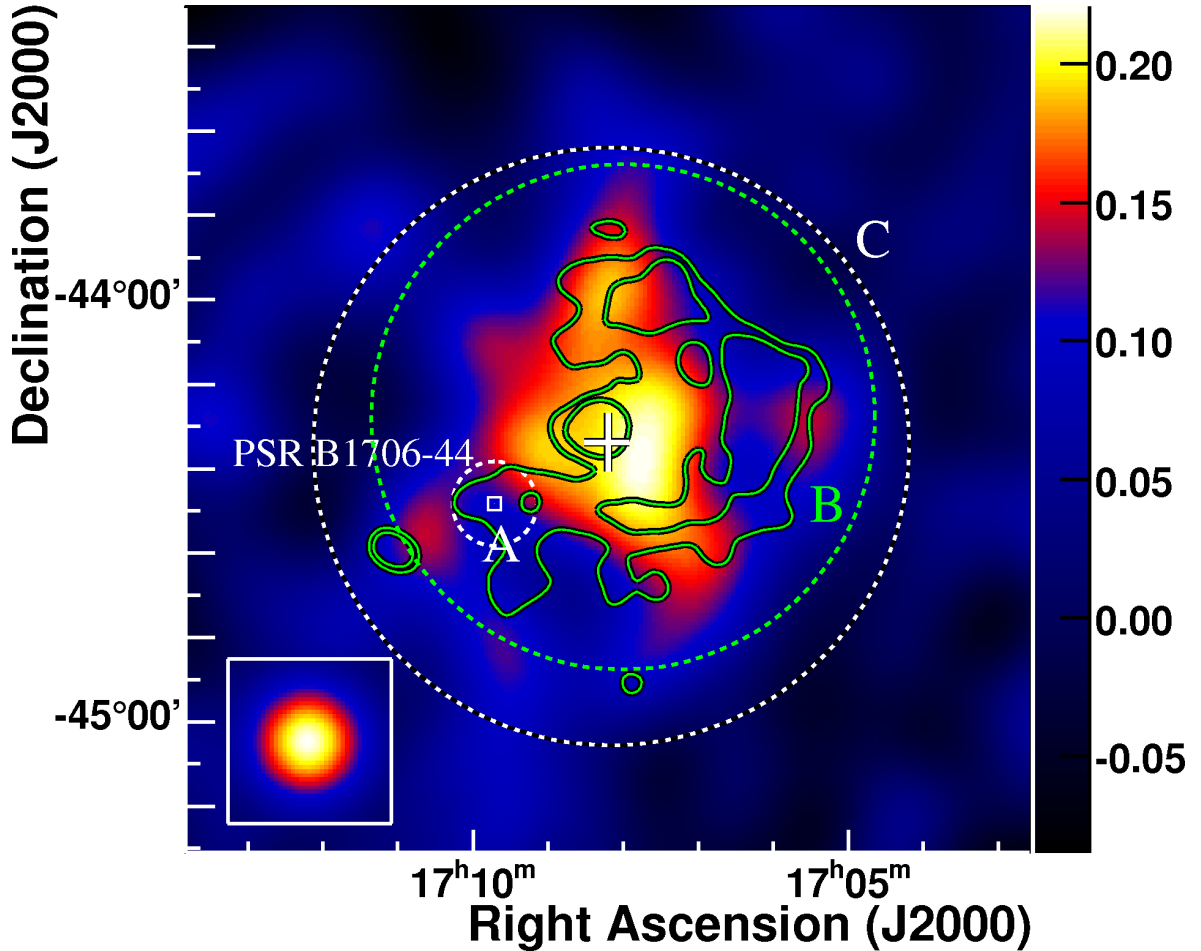
Figure 3.1: Image of the VHE γ-ray excess (in units of γ-rays arcmin^{-2}) from HESS J1708−443, smoothed with a 2D Gaussian with a width $\sigma = 0.10°$. The blue-to-red color transition is chosen to reduce the appearance of features which are not statistically significant. The white cross is located at the best-fit position of the center-of-gravity of the emission and its size represents the statistical error of the fit. The small and large dotted white circles, labeled A and C, respectively, denote the regions used for spectral analysis. The *a priori* defined Region B, from which the detection significance was calculated, is represented by a dotted green circle. The three regions are summarized in Table 3.2. The position of the pulsar PSR B1706−44, at the center of region A, is marked by a square. The inset (bottom-left corner) shows the point-spread function of the H.E.S.S. telescope array for this particular dataset, smoothed in the same manner as the excess image. Radio contours of constant intensity, as seen at 330 MHz with the Very Large Array (VLA), are shown in green. The radio data were smoothed with a Gaussian of width $\sigma = 0.03°$. The local maximum in the radio contours at the center of the image is largely due to PMN J1708−4419, an extragalactic object seen in projection (see Sect. 3.4.3).

Declination (J2000)

Right Ascension (J2000)
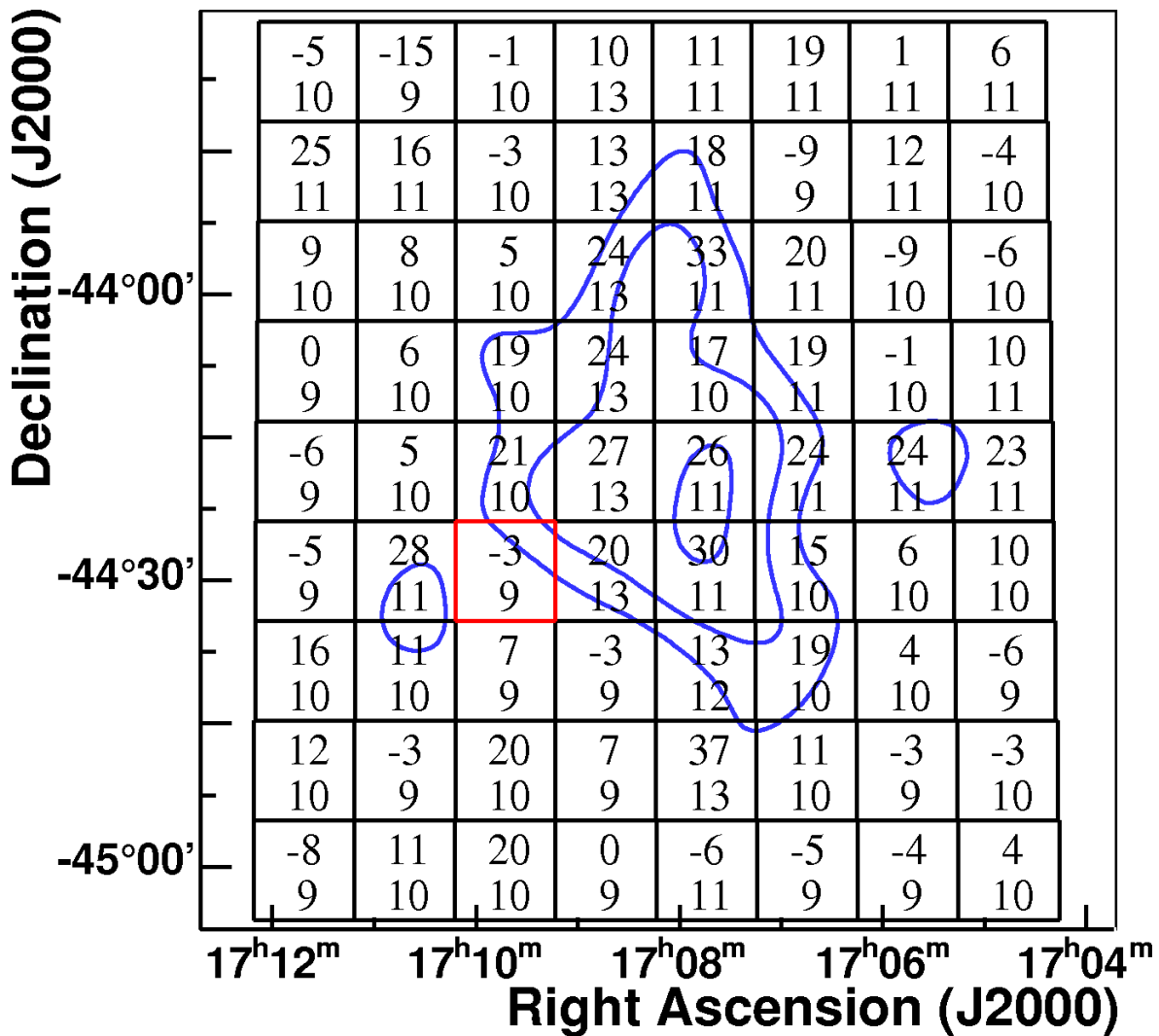
Figure 3.2: Gamma-ray excess in quadratic bins of 0.175° width. The upper number in each bin is the excess summed within this bin, and the lower number is the corresponding statistical error. The blue contours correspond to a smoothed excess of 0.14, 0.17, and 0.21 γ-rays arcmin^{-2}, taken from Fig. 3.1. The red-rimmed bin is centered on the pulsar position. Note the different field-of-view used in the two figures.

the Crab Nebula in the same energy range.

Region	Center		Radius	N_{on}	N_{off}	α	Excess	Significance	Integral flux (> 0.6 TeV)
	α_{2000}	δ_{2000}	[°]					[σ]	[ph cm^{-2} s^{-1}]
A	$17^h09^m42.73^s$	$-44°29'8.2''$	0.10	71	717	0.11	$-9.4^{+9.2}_{-8.7}$	-1.0	$< 3.3 \times 10^{-13}$
B	17^h08^m	$-44°16'48''$	0.60	3180	2488	1.06	543^{+77}_{-77}	7.0	$= 6.5 \times 10^{-12}$
C	$17^h08^m11^s$	$-44°20'$	0.71	4243	3425	1.06	615^{+90}_{-90}	6.8	$= 6.9 \times 10^{-12}$

Table 3.2: Event statistics for Regions A, B, and C. The center and the radius of each circular on-source (ON) region is given in columns 2–4. For Region A, the background was extracted from off-source (OFF) regions in the same field-of-view, while for Regions B and C, it was estimated from observations of separate OFF regions. Due to the smaller extent of Region A, more OFF regions could be used, which resulted in a smaller normalization factor α than for Regions B and C. The number of events in the ON and OFF integration regions, N_{on} and N_{off}, respectively, are given in columns 5 and 6. The significance (column 7) was calculated following the approach of Li & Ma (1983). The integral flux (or UL thereof) for each region is given in column 8. Note that the statistics presented here were obtained from a dataset comprised only of observations in 2007, which does not overlap with the one used in Aharonian et al. (2005e).

The energy spectrum of the entire source is extracted from Region C. Within the large integration circle, 615 excess γ-ray events were found, corresponding to a statistical significance of 6.8 σ (pre-trials). The differential spectrum (Fig. 3.3) is well-described by a power law $\phi = \phi_0 \, (E \, / \, 1 \, \text{TeV})^{-\Gamma}$ with a spectral photon index $\Gamma = 2.0 \pm 0.1_{\text{stat}} \pm 0.2_{\text{sys}}$ and a flux normalization at 1 TeV of $\phi_0 = (4.2 \pm 0.8_{\text{stat}} \pm 1.0_{\text{sys}}) \times 10^{-12} \, \text{cm}^{-2} \, \text{s}^{-1} \, \text{TeV}^{-1}$. The integral flux $F(1{-}10 \, \text{TeV}) = 3.8 \times 10^{-12} \, \text{ph} \, \text{cm}^{-2} \, \text{s}^{-1}$ is ~17% of the Crab Nebula flux in the same energy range. The extracted flux points from the extended emission and the fitted power law are shown in Fig. 3.3. The results presented above have been cross-checked, using an independent calibration of the raw data and an alternative analysis chain. The cross-checks included a spectral analysis using the *reflected region background method* (Berge et al. 2007), which requires observations to be centered outside of the emissive region and thus used only half of the available dataset. All cross-checks confirmed the primary results within the stated statistical uncertainties.

The most recent observations and analysis by CANGAROO-III also give an indication of extended emission in the vicinity of PSR B1706−44 (Enomoto et al. 2009). However, their results differ significantly from those given in this chapter. For example, the morphology of the VHE γ-ray excess reported by Enomoto et al. (2009), using an ON-OFF background technique, is that of a source centered roughly at the pulsar position, as opposed to HESS J1708−443., whose centroid is clearly offset from the pulsar. Furthermore, CANGAROO-III measures a Crab Nebula-level integral flux (above 1 TeV) within 1.0° of the pulsar, which is inconsistent with the ~18% Crab flux measured by H.E.S.S. in the same energy range. The difference is possibly due to the exact methods used for background subtraction; in the H.E.S.S. analysis, the OFF data are normalized to source-free regions of the ON data, because the background can vary significantly depending on the observing conditions.

3.4   Origin of the VHE γ-ray emission

While a superposition of a relic PWN created by PSR B1706−44 and SNR G 343.1−2.3 cannot be excluded, each of these objects individually could account for the observed VHE γ-ray emission. The possible associations with HESS J1708−443. will be discussed in the following sections and both leptonic and hadronic scenarios will be considered.

3.4.1   A relic nebula from PSR B1706−44

The pulsar PSR B1706−44, which has a high spin-down luminosity $\dot{E} = 3.4 \times 10^{36} \, \text{erg} \, \text{s}^{-1}$, is energetic enough to power the observed VHE γ-ray emission, which has a luminosity between 1 and 10 TeV of $L_\gamma \approx 9.9 \times 10^{33} \, (D \, / \, 2.3 \, \text{kpc})^2 \, \text{erg} \, \text{s}^{-1}$. The apparent conversion

HESS J1708-443: Spectrum

$$\phi_0 = (4.2 \pm 0.8_{\text{stat}} \pm 1.0_{\text{sys}}) \times 10^{-12} \text{ ph cm}^{-1} \text{s}^{-1}$$
$$\Gamma = 2.0 \pm 0.1_{\text{stat}} \pm 0.2_{\text{sys}}$$
$$F(1\text{-}10 \text{ TeV}) \approx 17\% \text{ Crab}$$
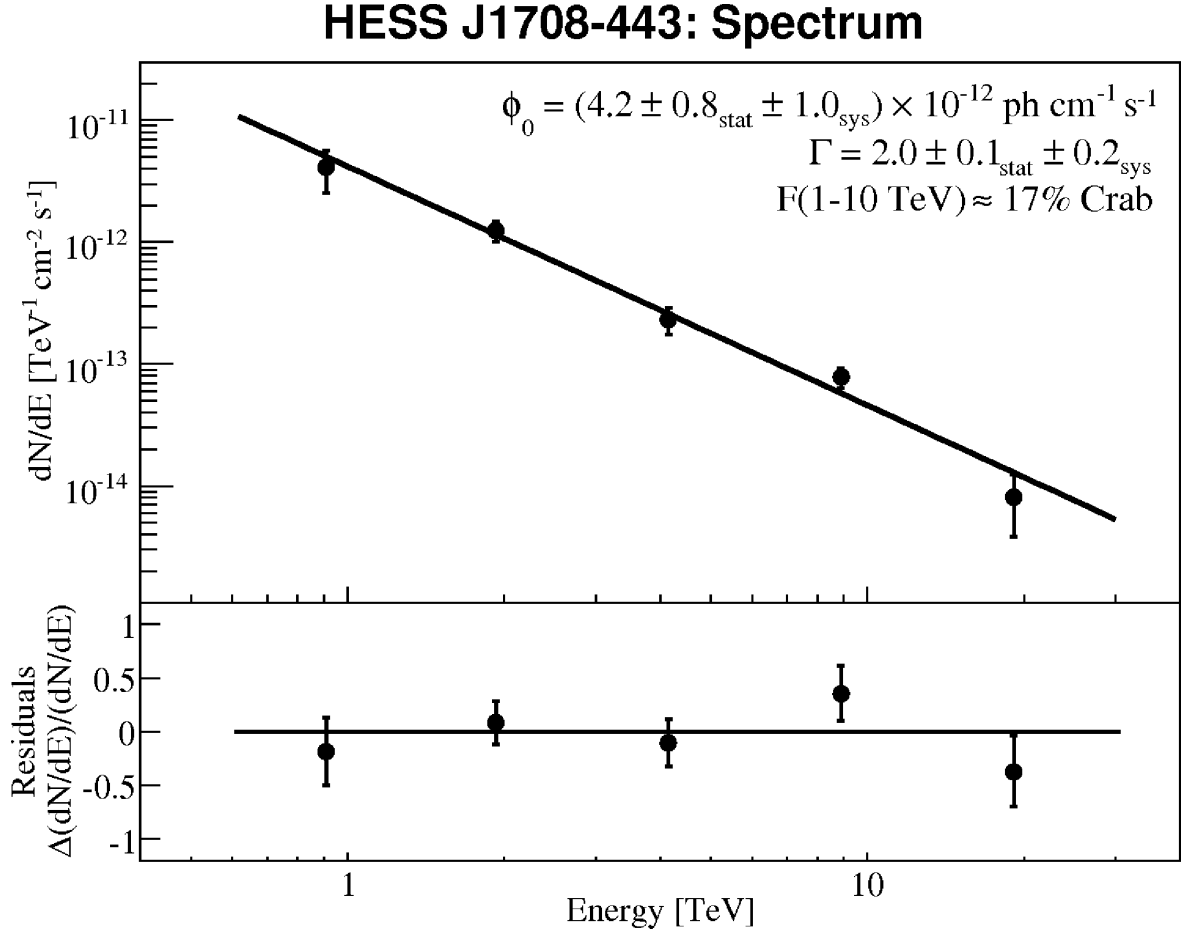
Figure 3.3: Differential energy spectrum of HESS J1708−443, extracted from Region C (see Table 3.2). The solid line shows the result of a power-law fit. The error bars denote 1-σ statistical errors. The bottom panel shows the residuals of the power-law fit. Events with energies between 0.6 and 28 TeV were used in the determination of the spectrum, and the minimum significance per bin is 1 σ.

efficiency from rotational energy to γ-rays in this energy range can be defined as

$$\epsilon_{1-10 \text{ TeV}} \equiv \frac{L_\gamma}{\dot{E}} \tag{3.1}$$

and for this case is ~0.3%, compatible with the efficiencies ($\lesssim 10\%$) of other VHE γ-ray sources which have well-established associations with PWN (Gallant 2007). The projected size of HESS J1708−443 corresponds to a physical size of ~12 (D / 2.3 kpc) pc (68% containment radius). These characteristics suggest a possible association between the VHE γ-ray emission and the PWN of PSR B1706−44, similar to other PWN/VHE associations, e.g. Vela X (Aharonian et al. 2006b) and HESS J1825−137 (Aharonian et al. 2006f).

In a leptonic scenario, the VHE γ-radiation originates from accelerated electrons which up-scatter ambient photons to VHE γ-ray energies via inverse Compton (IC) scattering.

Compared to the size of the PWN in the radio (radius ~1.5′) (Giacani et al. 2001) and the "bubble" nebula seen in X-rays (radius ~1.8′) (Romani et al. 2005), the VHE γ-ray PWN (sometimes referred to as a TeV PWN) would be a factor of ~10 larger. Similar differences in size have been observed in other TeV PWN associations, e.g. HESS J1825−137 (Aharonian et al. 2006f), and can be explained by the different energies, and hence cooling times, of the electrons which emit the X-rays and VHE γ-rays. Assuming the magnetic field is uniform and that the average wind convection speeds in the γ-ray and X-ray emitting zones are both constant and similar, Aharonian et al. (2005i) estimate the ratio of sizes

$$\frac{R_\gamma}{R_X} = 4 \left(\frac{B}{10\,\mu G} \right)^{-\frac{1}{2}} \left(\frac{E_{keV}}{E_{TeV}} \right)^{\frac{1}{2}} , \qquad (3.2)$$

where E_{keV} is the mean energy in X-rays (2 keV) and E_{TeV} is the mean energy in VHE γ-rays (0.9 TeV). However, in contrast to the PWN of PSR J1826−1334, where a magnetic field strength $B = 10\,\mu G$ was inferred from X-ray observations (Gaensler et al. 2003), Romani et al. (2005) estimate a magnetic field B as strong as $140^{+210}_{-60}\,\mu G$ within the 110″ radius X-ray PWN of PSR B1706−44, assuming the spectral break between the extrapolation of radio and X-ray spectra is due to radiative cooling of electrons. In such a high magnetic field, electrons that emit keV X-rays have comparable energies to those that emit TeV γ-rays and therefore have comparable cooling times as well. Thus, the TeV PWN should be approximately the same size as the X-ray PWN, i.e. it should appear point-like considering the ~5′ H.E.S.S. PSF. Furthermore, given that the ratio of X-ray to VHE γ-ray energy flux is determined by the energy density in magnetic fields and IC target photon fields (only the cosmic microwave background (CMB) is considered here),

$$\frac{F_\gamma}{F_X} \approx 0.1(0.1B_{-6})^{-2}, \qquad (3.3)$$

where $B = 10^{-6}B_{-6}$ G (Aharonian et al. 1997), the observed X-ray flux $F_X = 3.3 \times 10^{-13}$ erg cm^{-2} s^{-1} at $E_{keV} = 1.2$ keV (Becker et al. 1995) can be used to predict the γ-ray flux (de Jager & Djannati-Ataï 2008) F_γ at

$$E_{TeV} = 167 E_{keV} B_{-6}^{-1} = 1.4\,TeV \qquad (3.4)$$

assuming the value of B estimated by Romani et al. (2005). This results in a predicted $F_\gamma(1.4\,\text{TeV}) = 1.7 \times 10^{-16}$ erg cm^{-2} s^{-1}, well below the level observable by H.E.S.S. Conversely, the absence of VHE γ-rays from the compact nebula (c.f. H.E.S.S. UL from Region A in Sect. 3.3) can be used together with F_X to calculate a lower limit on the magnetic field using Eq. 2. The resulting limit, $B \gtrsim 2.5\,\mu G$, is consistent with the magnetic field estimated by Romani et al. (2005).

One way to reconcile the difference in emission region size and the high flux of the VHE γ-ray emission is to assume that the size of the X-ray PWN is primarily governed by the extent of the high B-field region and that the magnetic field decreases by a large factor beyond
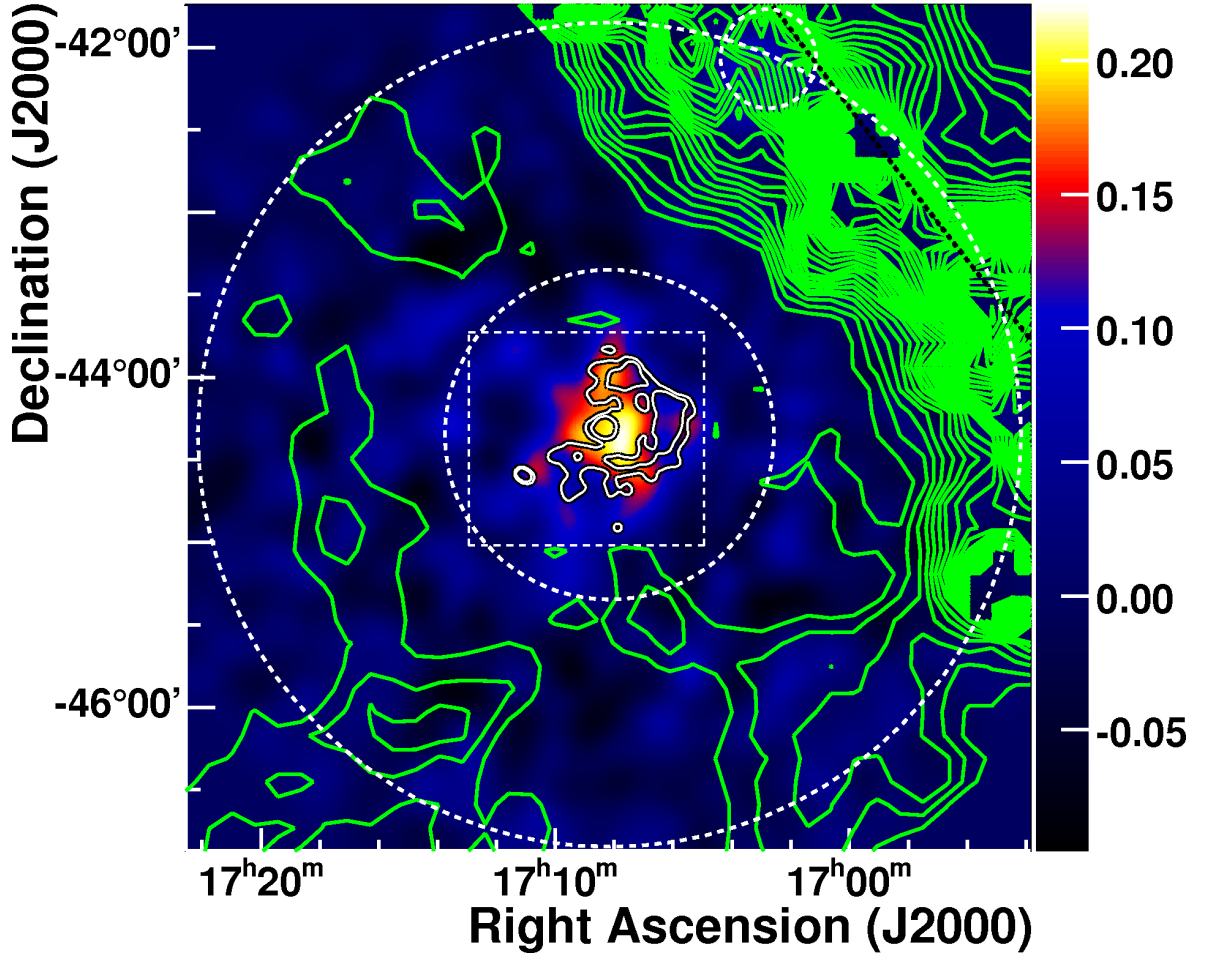
Figure 3.4: Large field-of-view (FoV; $5.1° \times 5.1°$) VHE γ-ray image of the region containing HESS J1708−443. The Gaussian-smoothed ($\sigma = 0.10°$) VHE γ-ray excess from Fig. 3.1 is shown in color. The white contours indicate the intensity of the 330 MHz radio emission detected with Very Large Array (VLA) observations (see also the green contours in Fig. 3.1). The dotted white box represents the FoV covered by the VLA observations. Outside of this region, green contours indicate the lower-resolution 2.4 GHz radio continuum data (Duncan et al. 1995) taken with the Parkes telescope; these observations have a half-power beamwidth of $\sim$10.4′. This image also shows the approximately ring-shaped region used for normalizing the background in the *ON-OFF background method* (see Sect. 3.2.2); this region is delimited by the large dashed white circles, excluding the known TeV source HESS J1702−420 located toward the Northwest. The Galactic plane is also located toward the NW and is indicated by a thick black dotted line.

the X-ray PWN. The electrons can then escape from the high *B*-field region and, by accumulating over a significant fraction of the lifetime of the pulsar, form a larger nebula which is visible only in VHE γ-rays. The synchrotron cooling time of electrons that up-scatter CMB

photons to energies E_γ is given by

$$\tau_{\text{synch}} \approx 40 \left(\frac{B}{140\,\mu\text{G}}\right)^{-2} \left(\frac{E_\gamma}{\text{TeV}}\right)^{-1/2} \text{yr}\,. \tag{3.5}$$

In the $140\,\mu$G field inside the X-ray PWN, the cooling time of up-scattered electrons produc-ing 1 TeV γ-rays is $\sim$40 yr. Assuming a dominantly advective, rather than diffusive, transport process, the average flow speed needed to drive electrons from the pulsar position to the edge of the X-ray PWN ($r \approx 110''$) within 40 yr is $0.1\,(D\,/\,2.3\,\text{kpc})$ c. The implied flow speed is reasonable following the arguments of Kennel & Coroniti (1984), although their model considers the case of the symmetric Crab Nebula, which is admittedly a simplification of the asymmetric PWN considered here. If the magnetic field within the X-ray PWN was much higher than $140\,\mu$G in the past, when most of the electrons were emitted, the restrictions on the flow speed would become more stringent. However, in the low B-field region outside the X-ray PWN, the synchrotron lifetime increases. Even for a magnetic field strength of $10\,\mu G$, a value about three times as large as the interstellar magnetic field, the cooling time of the aforementioned electrons is about 8 000 yr, almost half of the characteristic age of the pulsar (17 500 yr).

This relic TeV PWN scenario does not, however, explain the asymmetric morphology of HESS J1708$-$443, in particular its offset from the pulsar location, nor does it explain the lack of detectable VHE γ-ray radiation from the location of the pulsar itself, assuming that the pulsar and X-ray PWN are embedded in an extended shell of relic electrons. Such asymmetries have been observed previously in other TeV PWNs, e.g. HESS J1718$-$385, HESS J1809$-$193 (Aharonian et al. 2007a) and HESS J1825$-$137 (Aharonian et al. 2005i, 2006f). These asymmetries could be accounted for in two ways: as a direct result of a high proper motion of the pulsar or as a result of a density gradient in the ambient medium. The density gradient could lead to an asymmetry in the reverse shock of the supernova, or it could lead to a different expansion velocity for the TeV γ-ray emitting electrons (Blondin et al. 2001; van der Swaluw et al. 2001). Simulations by van der Swaluw et al. (2001) demonstrate that a displaced PWN can indeed be well-separated from its pulsar. These explanations are in principle applicable to the case of HESS J1708$-$443; however, the pulsar's measured scintillation velocity, less than 100 km s^{-1}, renders the first explanation unlikely. The latter explanation favors a TeV PWN which is offset toward a low density region. The available H I line emission data (see Fig. 3.5 and the subsequent section) suggest that this might be the case, although it is not clear given the complex H I morphology.

In the preceeding discussion, it was assumed that the pulsar dominantly accelerates elec-trons. If a considerable fraction of the accelerated particles are instead hadrons (e.g. Horns et al. (2006); Amato et al. (2003); Bednarek & Bartosik (2003)), the constraints imposed by the large magnetic field within the X-ray PWN are removed. In a hadronic scenario, π^0 mesons are produced by inelastic interactions between accelerated protons and the ambient

gas; they then decay, emitting VHE γ-ray photons. In such a scenario, the VHE γ-ray emission would trace the distribution of the target material. The bright radio arc, interpreted by Bock & Gvaramadze (2002) as the compressed outer boundary of the former wind-blown bubble, could act as such a target due to its enhanced density, thereby also explaining the spatial coincidence with the H.E.S.S. source. Since the proton interaction time is long compared to the age of the pulsar, and assuming that the escape of protons from the region is sufficiently slow, all protons accelerated since the birth of the pulsar can contribute to the γ-ray emission. However, to account for the high luminosity of the VHE γ-ray emission, the pulsar must have a high rotational energy and must efficiently convert rotational energy into proton acceleration. The total energy in accelerated protons W_p in the energy range 10–100 TeV which is necessary to produce the observed γ-ray luminosity L_γ can be estimated from the relation

$$W_p(10--100 \text{ TeV}) \approx \tau_\gamma \times L_\gamma(1--10 \text{ TeV}),\tag{3.6}$$

where

$$\tau_\gamma \approx 5 \times 10^{15}\left(\frac{n}{\text{cm}^{-3}}\right)^{-1}\text{ s}\tag{3.7}$$

is the characteristic cooling time of protons through the π^0 production channel. The total energy within the entire proton population

$$W_P(\text{tot}) \approx 3 \times 10^{49}\left(\frac{n}{\text{cm}^{-3}}\right)^{-1}\left(\frac{D}{2.3\text{ kpc}}\right)^2\text{ erg}\tag{3.8}$$

is then estimated by extrapolating the proton spectrum down to 1 GeV assuming the same spectral shape as the VHE γ-ray spectrum, i.e. a power law with index $\Gamma = 2.0$. Assuming that a fraction η of the pulsar's rotational energy E_{rot} is converted into the energy within the proton population

$$W_P(\text{tot}) = \eta E_{\text{rot}}\tag{3.9}$$

then

$$\left(\frac{n}{\text{cm}^{-3}}\right) \approx 0.2\left(\frac{D}{2.3\text{ kpc}}\right)^2\eta^{-1}\left(\frac{P_0}{10\text{ ms}}\right)^2,\tag{3.10}$$

where

$$E_{\text{rot}} = \frac{(2\pi)^2}{2}\frac{I}{P_0^2}\tag{3.11}$$

and $I \approx 1 \times 10^{45}$ g cm^2 is the moment of inertia of the pulsar. For a distance $D = 2.3$ kpc and an efficiency $\eta = 0.3$, the initial rotation period P_0 has to be as small as 6–12 ms for the ambient medium density to be in the range $n \approx 1$–5 cm^{-3}. Although pulsars are thought to be born with initial periods which are considerably shorter than their present periods, the initial rotation period implied for PSR B1706−44, in the above hadronic TeV PWN scenario, is even smaller than that of the Crab pulsar, the only case for which P_0 is well-determined (19 ms) (Manchester & Taylor 1977).
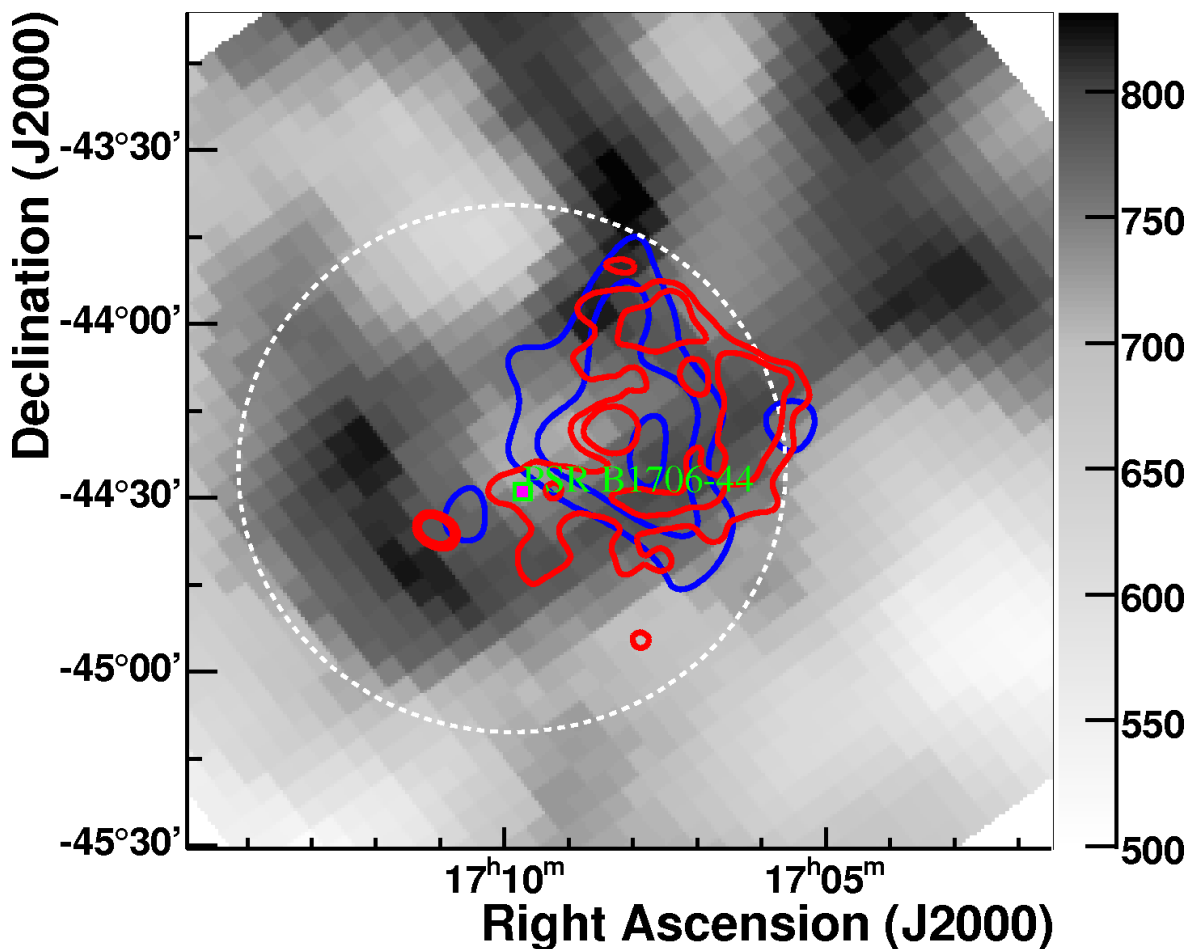
Figure 3.5: The grayscale image shows the intensity of H I line emission in units of K km s^{-1}, measured by the Parkes radio telescope during the Southern Galactic Plane Survey (SGPS) (McClure-Griffiths et al. 2005). The intensities are integrated in the velocity range −13.79 km s^{-1} to −21.21 km s^{-1} (shown as a shaded region in the velocity profile in Fig. 3.6), corresponding to a near/far kinematic distance of 1.6–2.3 kpc / 13.0–13.7 kpc. Contours of the Gaussian-smoothed ($\sigma = 0.10°$) VHE γ-ray excess are shown in blue. The red contours depict the intensity of the radio emission measured by the Very Large Array (VLA) at 330 MHz (see also Fig. 3.1). The radio data have been smoothed with $\sigma = 0.03°$. The white circle illustrates the integration region for the velocity profile shown in Fig. 3.6.

The hadronic PWN scenario is further disfavored by constraints on the proton escape time. Under the common assumption that the proton diffusion coefficient is energy-dependent, i.e.

$$D(E_{\mathrm{p}}) = D_0 \, (E_{\mathrm{p}} \, / \, 10 \, \mathrm{GeV})^{\delta} \, , \qquad (3.12)$$

with a power-law index $\delta \approx 0.5$, where D_0 is the diffusion coefficient at 10 GeV, one can estimate D_0 required to contain protons with energy $E_p = 100$ TeV within a certain distance
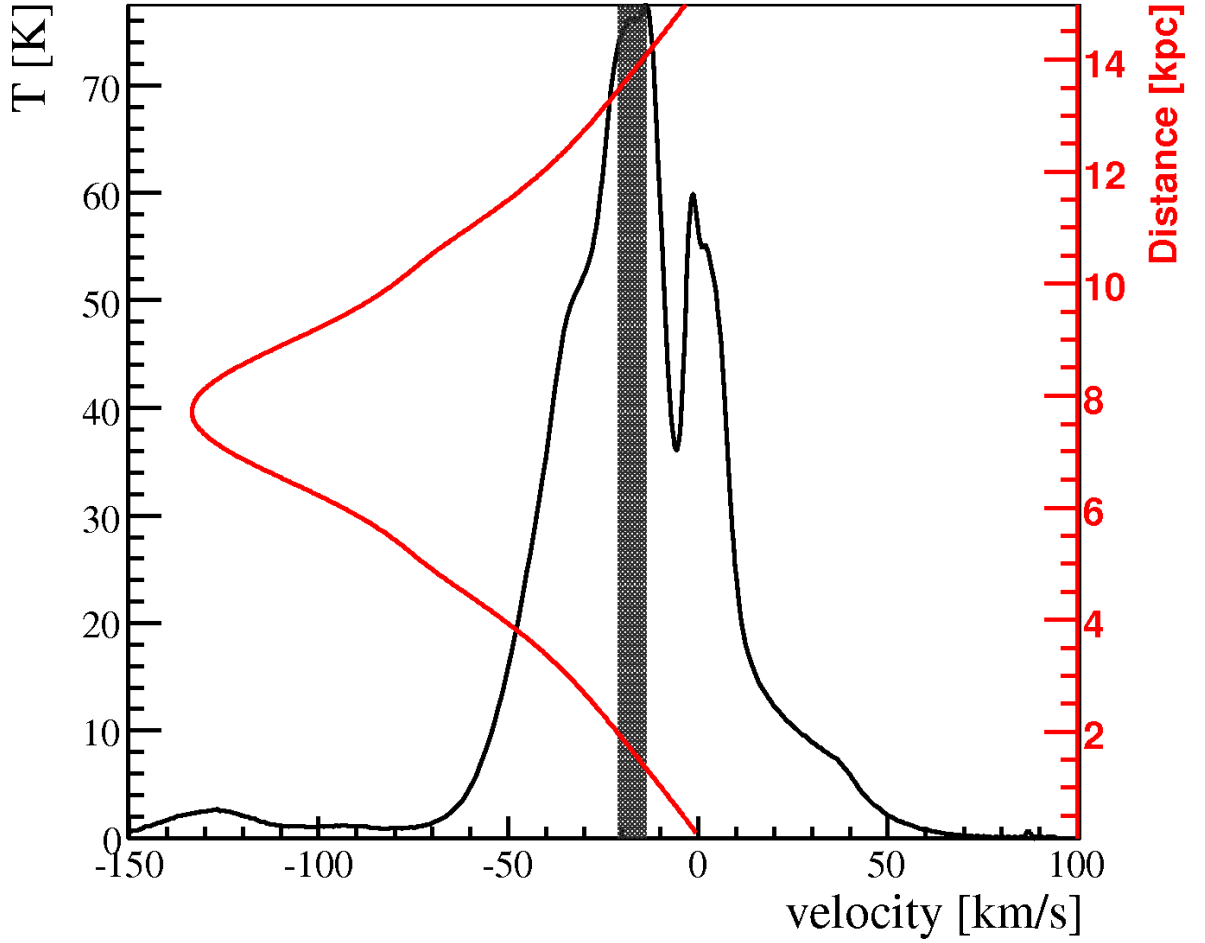
Figure 3.6: Velocity profile of H I line emission intensity, integrated over the region enclosed by the dashed circle in Fig. 3.5. The velocity resolution is 0.08 km s^{-1}. The kinematic distance, shown in red, is derived from the velocity using the Galactic rotation curve of Fich et al. (1989).

of the pulsar after $t = \tau_c$, since the diffusion radius

$$R_{dif} = 2\sqrt{D(E)\,t} \qquad\qquad (3.13)$$

for timescales less than the proton energy loss time, $t \ll \tau_\gamma$. This containment region can be estimated to have an angular size of ~0.7°, which is the approximate distance between the pulsar and the farthest significant VHE γ-ray emission. At the assumed pulsar distance, this region would have a physical size of 28 (D / 2.3 kpc) pc. The required diffusion coefficient $D_0 \approx 3.4 \times 10^{25}$ (D / 2.3 kpc)^2 cm^{2}s^{-1} is found to be prohibitively low by a factor of 10–100 and can only be reconciled by assuming a very weak energy dependence, $\delta \lesssim 0.2$.
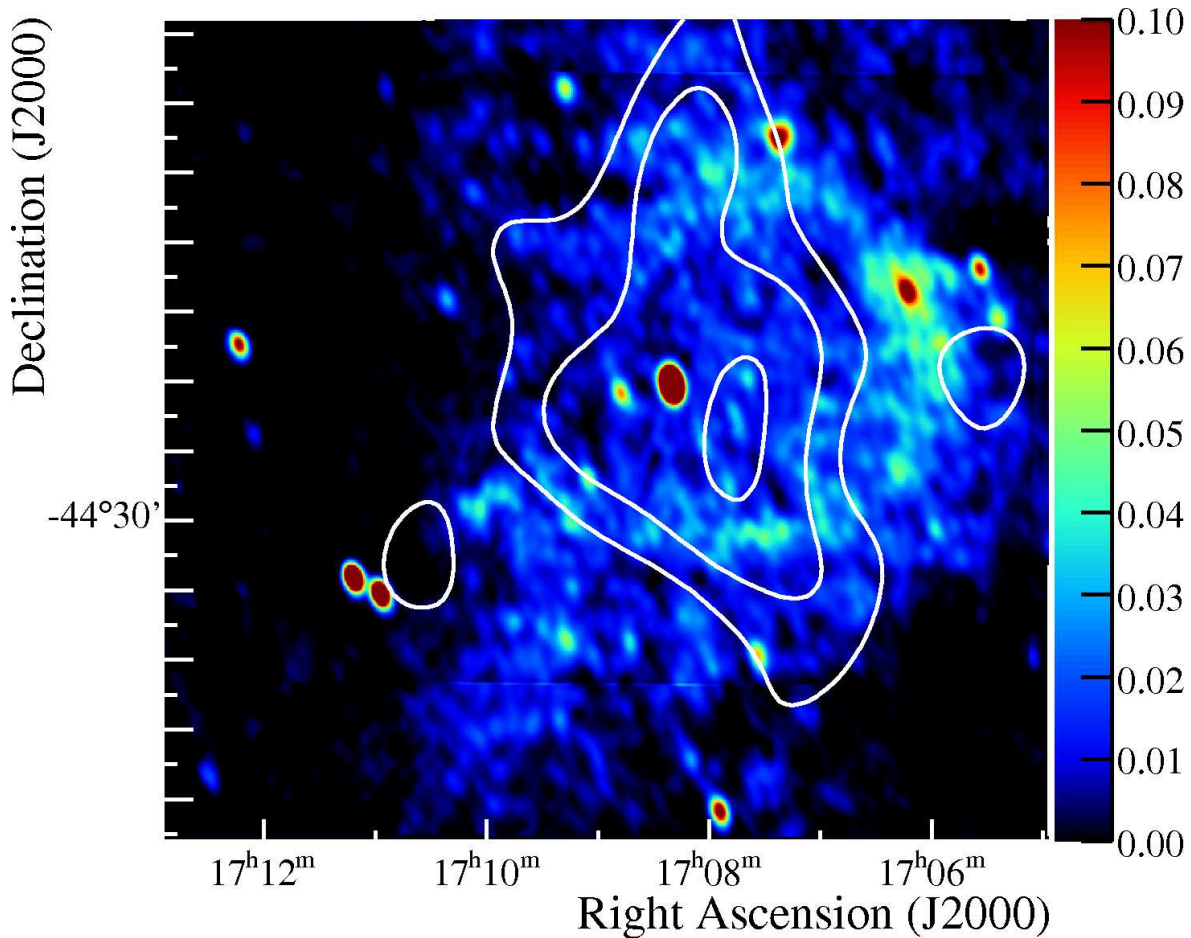
Figure 3.7: Image showing the intensity of the radio emission measured by the Very Large Array (VLA) (Frail et al. 1994) at 330 MHz in the vicinity of PSR B1706−44, smoothed with a Gaussian of width $\sigma = 0.03°$. The observations have a half-power beamwidth of $0.03° \times 0.015°$. The radio arc of the partial shell-type SNR G 343.1−2.3 is clearly visible as well as the diffuse emission both inside and outside the arc. The white contours correspond to a smoothed VHE excess of 0.14, 0.17, and 0.21 γ-rays arcmin^{-2}, taken from the image in Fig. 3.1. The horizontal stripes visible at Dec = −44°40′ and Dec = −43°47.5′ are imperfections which resulted from the joining of data to form the final wide-field image (Frail et al. 1994). The bright point source at the center of the radio image is PMN J1708−4419, likely an extragalactic object seen in projection (see Sect. 3.4.3).

3.4.2 Supernova remnant G 343.1−2.3

The VHE γ-ray source HESS J1708−443 is partially coincident with the bright radio arc and the surrounding diffuse emission of the SNR, visible in the 330 MHz observations taken with the VLA (see contours in Fig. 3.1 and Fig. 3.7). The centroid of the H.E.S.S. source is consistent with the apparent center of the bright radio arc ($\alpha_{2000} = 17^h08^m$, $\delta_{2000} = -44°16'48''$; as defined in Aharonian et al. (2005e). The extension of the VHE γ-ray excess (68% containment radius: $0.29° \pm 0.04°$) is compatible with the the radius of the radio shell ($\sim$0.27°) fit by Frail et al. (1994) using VLA observations at 90 cm. The 95% containment radius (0.71°; used for spectral extraction) of the γ-ray excess completely encloses the radio shell, whose approximate boundary was estimated at a radius of ~0.42° by Romani et al. (2005) using ATCA (Australia Telescope Compact Array) observations at 1384 MHz (Dodson & Golap 2002). Thus, while the majority of the VHE γ-ray emission is located within the radio shell, emission from the shell itself cannot be excluded. Due to low statistics in the current VHE dataset, no further conclusions can be made regarding morphological similarities. No significant VHE emission was detected from the spatially-extended, diffuse emission visible farther to the Southeast of the bright radio arc, seen in the low-resolution 2.4 GHz continuum radio data (Duncan et al. 1995) shown in Fig. 3.4, although the offset-corrected exposure in this region is very low (between ~4 and 10 h) since all the H.E.S.S. observations were centered near the pulsar. This diffuse radio emission was interpreted by Bock & Gvaramadze (2002) as originating from the eastern half of the expanding SNR shell, propagating into a low-density region.

Similar to the potential association with the PWN of PSR B1706−44, both leptonic and hadronic scenarios will be considered for VHE γ-ray production. The leptonic scenario suffers from the non-detection of the SNR at X-ray energies. The VHE γ-ray spectrum is hard and extends up to 20 TeV; assuming IC scattering in the Thomson regime, the electrons which up-scatter CMB photons to 20 TeV have an energy of ~80 TeV. For a reasonable magnetic field strength of 5 μG, these electrons would emit synchrotron photons with an energy of ~1 keV, i.e. photons within the detectable energy range of current X-ray telescopes. Unfortunately, this prediction cannot be tested because the X-ray UL calculated by Becker et al. (1995) using *ROSAT* was derived from a relatively small part of the shell; no stringent UL on the X-ray flux from an extended region within 0.7° of the H.E.S.S. source can be derived (W. Becker, personal communication) due to its large extension and the vicinity of the luminous low-mass X-ray binary (LMXB) 4U 1705−440 (Becker et al. 1995), whose stray light may be obscuring diffuse X-ray emission from the SNR. It is also possible that the X-ray emission is inherently weak and cannot be detected due to the relatively high interstellar absorption (Becker et al. 1995).

In the hadronic scenario, synchrotron radiation is expected only from secondary electrons, and the lack of X-ray detection can easily be accounted for. Assuming a total energy of

10^{51} erg is released in the supernova explosion, an acceleration efficiency of $\epsilon = 0.15$ and a distance $D = 2.3$ kpc, an average proton density of $n \approx 1.5$ cm^{-3} – a value slightly larger than the average Galactic ambient density – is sufficient to explain the previously estimated (Sect. 3.4.1) energy content of $W_{\mathrm{P}}(\mathrm{tot}) \approx 3 \times 10^{49}$ erg within the proton population.

Given the various scenarios that have been proposed to explain the origin of the bright radio arc, there are many different possibilities as to how the SNR could be associated with HESS J1708−443. In one scenario, the SNR G 343.1−2.3 is expanding symmetrically into the interstellar medium (ISM), and the intensity variations which form the radio arc are due to local density differences in the ISM. An association between the SNR and the pulsar PSR B1706−44, a controversial scenario which is still debated in the community (see e.g. Bock & Gvaramadze 2002; Romani et al. 2005), would make the SNR rather old, $O(10\,000$ yr), and place it in the late Sedov-Taylor phase, or, more likely, in the radiative phase. If the SNR is in the radiative phase, the ambient material swept up by the SNR should be visible in CO or H I data. Unfortunately, no high-resolution CO data are publicly available at the moment, but there is evidence for a ring-like structure in the H I line emission survey of the Parkes telescope, as shown in Fig. 3.5. The structure is best visible in the velocity range -13.79 km s^{-1} to -21.21 km s^{-1} corresponding to a near/far kinematic distance of 1.6–2.3 kpc / 13.0–13.7 kpc (Fig. 3.6). The near distance is compatible with the pulsar distance (2.3 kpc). A rough estimate of the mass of the H I structure, extracted from the circular region in Fig. 3.5, is $\sim 6 \times 10^3$ M$_\odot$. Assuming radial symmetry, this corresponds to an original density of the swept-up mass of a few protons cm^{-3}, comparable to the density requirements imposed by the observed γ-ray flux. The bright radio arc and the VHE γ-ray emission spatially coincide with only one half of the H I shell-like structure. This morphology could arise because of the additional dependence of the radio and γ-ray emission on the target density, which is likely larger closer to the parent MC.

The H I shell has a radius of $\sim 0.4°$, which, assuming a distance of $D = 2.3$ kpc, corresponds to a physical radius of ~ 16 pc. Following the approaches of Cioffi et al. (1988) and Truelove & McKee (1999) and further assuming an age of 17 000 yr, a 10 M$_\odot$ progenitor star, and an energy release of 10^{51} erg, the ambient density necessary to explain the size of the H I shell is $n \sim 0.7$ cm^{-3} and the resulting shock velocity is ~ 400 km s^{-1}. Following Ptuskin & Zirakashvili (2005), the maximum proton energy attainable is then $O(10$ TeV), likely too low to explain the observed TeV emission, which extends up to 20 TeV. The spectral energy distribution (SED) of γ-rays produced in the interactions of mono-energetic protons (and subsequent decay of pions) drops sharply beyond roughly 15% of the original proton energy (see e.g., Kelner et al. 2006). Therefore, the parent proton population giving rise to the observed VHE γ-ray emission should extend up to about 100 TeV, a limit which is – as the example calculation above illustrates – increasingly difficult to explain as the age of the system increases. Indeed, the γ-ray emitting SNR shells which have been unambiguously identified so far, such as RX J1713.7−3946 (Aharonian et al. 2007c) and RX J0852.0−4622

(Aharonian et al. 2007d), are much younger (~2 000 yr).

The aforementioned constraints are removed if the SNR expands first into a bubble blown by the progenitor star's wind into the ISM. Due to the low density inside the wind-blown bubble, the velocity of the expanding shock is much higher than anticipated and protons can be accelerated to very high energies. When the shockfront reaches the outer boundary of the wind-blown bubble, the high-energy protons are released to interact with the dense environment outside of the bubble and produce VHE γ-rays in the process. In this scenario, first proposed by Bock & Gvaramadze (2002), the bright radio arc is created by the former boundary of the wind-blown bubble which has been overtaken by the expanding SNR shockfront. The offset of the pulsar position from the center of the radio arc does not hinder the association between the SNR and the pulsar, since the progenitor star, whose wind has produced the bubble, can have traversed the bubble's boundary during its evolution, before it became a supernova. The constraints on the VHE γ-ray production imposed by the large implied age of 17 000 yr do not apply in this case since the protons now interacting within the dense ambient medium to produce γ-rays could have been accelerated in the past, when the SNR shock velocity was still high. However, this would require an extremely low diffusion coefficient ($D_0 \approx 2 \times 10^{25}$ cm^2 s^{-1}), similar to the case of the hadronic PWN scenario (see Sect. 3.4.1).

This discussion of a putative association between HESS J1708$-$443 and the SNR G 343.1$-$2.3 is based on the assumption that the SNR and the pulsar PSR B1706$-$44 were created at the same time. If this assumption proves to be wrong, then very little is known about the SNR. The age estimate using a Sedov-Taylor model is about 5 000 yr (McAdam et al. 1993; Nicastro et al. 1996). The younger age would further ease the proton acceleration to energies beyond 100 TeV.

To summarize, the radio emission from SNR G 343.1$-$2.3, which may originate from the interaction of the SNR with an ambient MC, is partially coincident with HESS J1708$-$443, suggesting a plausible association which could account for at least part of the VHE γ-ray emission observed. However, the putative associations between the SNR and the pulsar or between the SNR and the shell-like structure discovered in H I suggest that the SNR is in a later evolutionary stage than other SNRs previously-detected in the VHE regime.

3.4.3   Other nearby celestial objects

There are other celestial objects nearby, i.e. within the emission region of HESS J1708$-$443, notably the LMXB 4U 1705$-$440 (Forman et al. 1978) and the radio source PMN J1708$-$4419 (Wright et al. 1994). The LMXB is a well-studied type 1 burster (Sztajno et al. 1985) located at $\alpha_{2000} = 17^{\rm h}08^{\rm m}54.46^{\rm s}$ and $\delta_{2000} = -44°6'7.35''$ (Di Salvo et al. 2005), i.e. it is offset from the centroid of the VHE emission by 0.25°. Considering this offset and the extended nature of the VHE γ-ray source, an association is highly unlikely since an X-ray binary would ap-

pear point-like to H.E.S.S. Theoretical predictions for VHE γ-ray emission from LMXBs focus on those with relativistic jets (microquasars); 4U 1705−440 does not exhibit jets. Furthermore, no LMXBs have been detected in the VHE γ-ray regime, despite the extensive coverage of the H.E.S.S. Galactic Plane Survey.

The radio source PMN J1708−4419 is located at $\alpha_{2000} = 17^h08^m30^s$ and $\delta_{2000} = -44°19'07''$ (Wright et al. 1994). The local maximum in the radio contours at the center of Fig. 3.1 is largely due to this very bright point source, clearly visible in the 330 MHz VLA radio image (see Fig. 3.7). Although its position is compatible with the centroid of the H.E.S.S. source, an association between the two is unlikely given the spectrum of the radio source. Using data from the VLA (at 330 MHz and 1.4 GHz), Molonglo Galactic Plane Survey (MGPS; cataloged as J 170828−441823 at 840 MHz, and Parkes-MIT-NRAO (PMN; cataloged as PMN J1708−4419 at 4.8 GHz), we derive a spectral index $\alpha = -0.81 \pm 0.08$ in the radio domain, consistent with the value $\alpha = -0.9$ derived by Frail et al. (1994) over a narrower range in frequency, from 330 to 840 MHz. The steep spectral index suggests that PMN J1708−4419 is extragalactic, since Galactic point-like sources are typically compact H II regions, for which the radio spectral index is positive; therefore, it is unlikely to be associated with the extended emission of HESS J1708−443. Upon a deeper inspection of this source using high-resolution unpublished ATCA radio data (Dodson & Golap, personal communication), this bright source can be further resolved into two sources. However, the spectral indices above were calculated on the basis of observing it as a single unresolved source, because this is the way that the low-resolution radio surveys detected them.

In order to quantify the contribution any putative, unresolved point source could make to the flux observed from HESS J1708−443, one can compare the symmetric 2D Gaussian curve of a point source to that of the extended H.E.S.S. source. This demonstrates that any single unresolved point source could not account for more than ∼6% of the total flux from HESS J1708−443.

3.5   Comparison with H.E.S.S. 2003 dataset

This section appeared as an appendix in the published paper.

3.5.1   Recalculation of upper limits using the 2003 dataset

In its commissioning phase, the H.E.S.S. IACT observed the region around the energetic PSR B1706−44 between April and July 2003 (Aharonian et al. 2005e). No evidence for statistically-significant VHE γ-ray emission was found at the pulsar position nor from a region encompassing the partial shell-type SNR G 343.1−2.3. Upper limits (ULs) to the integral flux were published in (Aharonian et al. 2005e). The integral flux now measured by H.E.S.S. (see Sect. 3.3) is not compatible with those originally-published ULs, a discrepancy

which motivated a re-analysis of the 2003 H.E.S.S. dataset for this region, using the current H.E.S.S. software.

Although H.E.S.S. is currently an array of four IACTs, it was operating as a two-telescope array from February to December 2003. The 2003 observations yielded a dataset with a livetime of 14.3 h, an average zenith angle of ~26°, and an energy threshold, estimated from Monte Carlo simulations, of ~350 GeV. For γ-hadron separation, *standard cuts* were used, which require a minimum of 80 p.e. to be recorded per shower image.

Integral flux ULs were calculated from three *a priori* defined circular regions: a *Standard* point-like ($\theta = 0.14°$) region centered at the position of PSR B1706−44, a *CANGAROO*-like region ($\theta = 0.22°$) also centered at the pulsar position, and a *Radio arc* region centered at the apparent center of the SNR G 343.1−2.3 ($\alpha_{2000} = 17^{\mathrm{h}}08^{\mathrm{m}}$, $\delta_{2000} = -44°16'48''$; as defined in Aharonian et al. (2005e)), with a radius $\theta = 0.60°$ in order to completely enclose the complex radio structure. The *CANGAROO* region is disregarded for the remainder of this re-analysis, because its sole purpose was to compare the H.E.S.S. result with the original CANGAROO-I detection, which has since been rescinded (Yoshikoshi et al. 2009), and focus primarily on the *Radio arc* region (equivalent to Region B; see Sect. 3.3), which is very similar to the region from which extended VHE γ-rays are now detected (Region C; see Sect. 3.3).

Background subtraction was performed using the Ring Background Method (Berge et al. 2007) in both the original and revised analysis. The exact inner and outer ring radii, r_{inner} and r_{outer} respectively, used in the original analysis were not documented; however, the inner ring radius is typically chosen to be slightly larger than the on-source (ON) region (radius $\theta = 0.60°$) and the normalization factor $\alpha = 1/7$ (the ratio of the ON to off-source (OFF) area). Therefore, for the re-analysis, the inner ring radius is chosen to be 0.65°, which, given α, leads to $r_{\mathrm{outer}} = 1.35°$. The number of events in the ON and OFF regions, N_{ON} and N_{OFF}, respectively, is found to match those given in Aharonian et al. (2005e) to within 8% (see Table 3.3), demonstrating that the ring parameters adopted in the re-analysis are approximately equal to those in the original analysis. No exclusion region was placed on the now known-to-exist source, HESS J1708−443, i.e. the source is not excluded from OFF regions. In practice this has a negligible effect, since there is little γ-ray emission from HESS J1708−443 beyond $r_{\mathrm{inner}} = 0.65°$ from its centroid.

The UL (99% confidence level using Feldman & Cousins 1998) on the integral flux from the *Radio arc* region (Region B) was originally found to be $F(> 0.35 \text{ TeV}) < 5.8 \times 10^{-12}$ ph cm^{-2} s^{-1}, equivalent to ~5% Crab, assuming the spectrum is described by a power law with a spectral index $\Gamma = 2.5$ (*Method A* in Aharonian et al. 2005e). An alternative UL, $F(> 0.50 \text{ TeV}) < 3.5 \times 10^{-12}$ ph cm^{-2} s^{-1}, also equivalent to ~5% Crab, was calculated using a method (*Method B*, described in detail in Aharonian et al. 2005e) which made no assumptions concerning the source spectrum. These ULs are shown in Fig. 3.8, where they are compared to the revised calculation (using *Method A*) of the integral flux UL, plotted as a function of threshold energy E. The revised UL is clearly higher (less stringent) than the
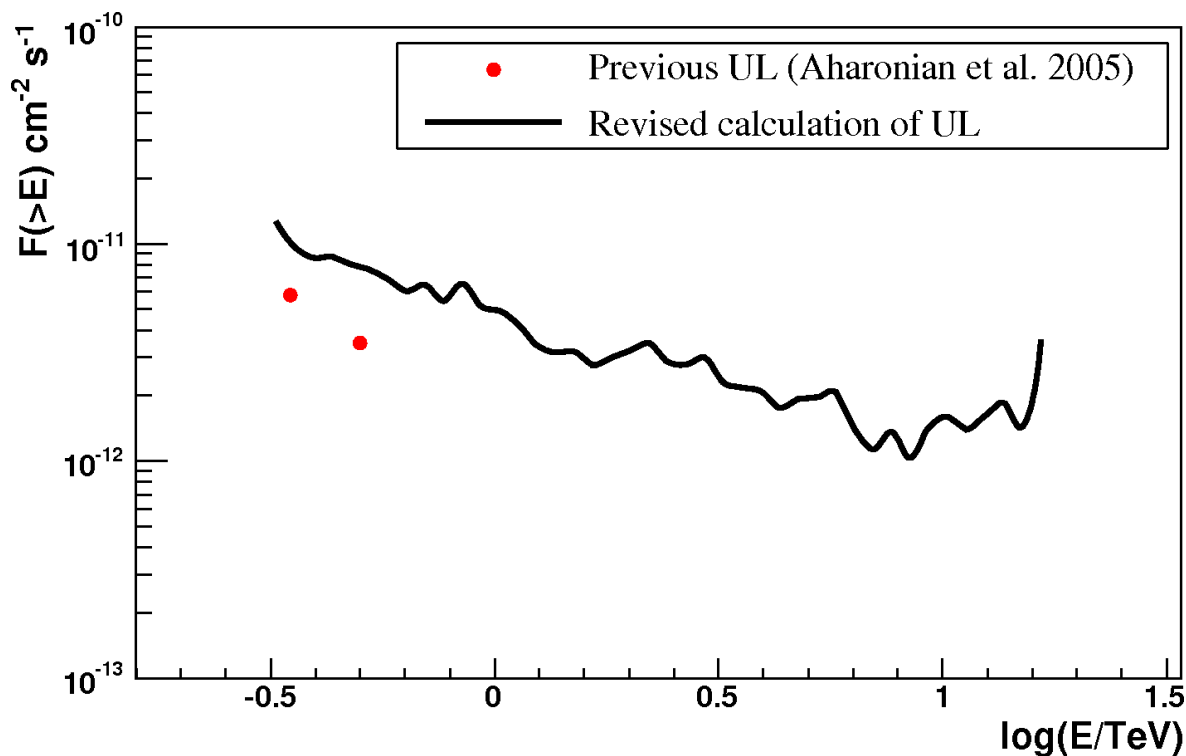
Figure 3.8: Integral flux upper limits (ULs) from the *Radio arc* region encompassing both PSR B1706−44 and SNR G 343.1−2.3. The red points represent the previously-published integral flux ULs from Aharonian et al. (2005e) using the 2003 H.E.S.S. dataset. The black solid line is based on a revised calculation of the UL using the same dataset.

one published in Aharonian et al. (2005e). For example, the integral flux above 0.35 TeV is $F(> 0.35 \text{ TeV}) < 9.7 \times 10^{-12}$ ph cm^{-2} s^{-1}, equivalent to 9% Crab and above 0.50 TeV is $F(> 0.50 \text{ TeV}) < 7.6 \times 10^{-12}$ ph cm^{-2} s^{-1}, equivalent to 12% Crab, again assuming $\Gamma = 2.5$. See Table 3.3 for a summary and comparison of the event statistics and other analysis parameters from both analyses.

The use of two-telescope data resulted in a lower sensitivity at the time but would not have had any negative impact on the original determination of ULs from the vicinity of PSR B1706−44. H.E.S.S. currently uses a stereo trigger implemented at the *hardware* level to select extended air showers (EASs) simultaneously detected by at least two telescopes (Funk et al. 2004). However, from February to July 2003, when the original observations of PSR B1706−44 were carried out, it used an off-line triggering mode, since the central hardware trigger had not yet been installed. In *software* stereo mode, each recorded EAS receives a time stamp via a GPS (Global Positioning System) clock. The time stamps are then used in the offline data analysis to identify EASs which were observed in coincidence by the two telescopes. The use of a software stereo trigger, while not as efficient as the hardware stereo trigger currently in use, is not expected to have contributed significantly to

	Aharonian et al. (2005e)	Re-analysis
$F(> 0.35\,\text{TeV})\,(\text{cm}^{-2}\,\text{s}^{-1})$	$< 5.8 \times 10^{-12}$	$< 9.7 \times 10^{-12}$
N_{ON}	4746	5095
N_{OFF}	13688	14730
α	0.346	0.343
Excess	11	38
Significance	$0.1\,\sigma$	$0.5\,\sigma$
r_{inner}	$> 0.60°$	$0.65°$
r_{outer}	unknown	$1.35°$

Table 3.3: Event statistics and background parameters for the analyses of the *Radio arc* region around PSR B1706−44 and SNR G 343.1−2.3. Row 1 gives the integral flux upper limits (99% confidence level) from both analyses. The number of events N in the circular (radius $\theta = 0.6°$) on-source (ON) and ring-shaped off-source (OFF) regions are given in rows 2 and 3, the normalization factor α (the ratio of ON to OFF area) in row 4, excesses and significances (according to Li & Ma (1983)) in rows 5 and 6, and the ring parameters in rows 7 and 8. The statistics and upper limits presented here were obtained using the 2003 H.E.S.S. dataset only.

the discrepancy between the original ULs and the new results.

After investigating various possible reasons for the discrepancy, it remains unknown why the previously-determined ULs were so low, leaving human error or undocumented changes in the analysis software used at the time as possible explanations. It is important to note that many other published results based on data taken during H.E.S.S.'s commissioning phase have been subsequently confirmed by the full four-telescope array with a hardware trigger, e.g. observations of RX J1713−3946 (Aharonian et al. 2007c) and Sgr A* (Aharonian et al. 2009b).

3.5.2 Compatibility between detected flux and 2003 upper limits

The upper limits calculated in the previous section cannot be directly compared to the new H.E.S.S. results, based on the 2007 dataset (presented in Sect. 3.3), because they assume a spectral index $\Gamma = 2.5$ and a low energy threshold. The new VHE γ-ray source, HESS J1708−443, has a much harder spectral index $\Gamma = 2.0 \pm 0.1_{\text{stat}} \pm 0.2_{\text{sys}}$. Furthermore, the minimum energy threshold of the H.E.S.S. array has increased due to the reflectivity of the IACT mirrors diminishing from 2003 to 2007, which reduces the array's ability to detect faint EASs initiated by lower-energy γ-rays.

A re-analysis of the 2003 dataset, using the current H.E.S.S. software and assuming $\Gamma = 2.0$, yields a flux upper limit (99% confidence level) $F(> 0.6\,\text{TeV}) < 6.3 \times 10^{-12}\,\text{ph cm}^{-2}\,\text{s}^{-1}$,

equivalent to ~13% Crab, for Region B. Analysis of the 2007 dataset shows a statistically-significant signal from Region B, $F(> 0.6\,\mathrm{TeV}) \approx 6.5 \times 10^{-12}\,\mathrm{ph\,cm^{-2}\,s^{-1}}$, equivalent to ~13% Crab. These two flux values are statistically compatible, given the typical uncertainties in the measured flux normalization ($\pm$ ~20%) and spectral index ($\pm$ ~0.2).

Furthermore, the new analysis results for HESS J1708$-$443 (Region C), based on the 2007 dataset, have been confirmed using an independent data calibration and analysis chain, and the cross-check analysis is also compatible with the presented results.

3.6   Summary

H.E.S.S. observations of the γ-ray pulsar PSR B1706$-$44 have led to the detection of an extended ($\sigma = 0.29° \pm 0.04°$) source of VHE γ-ray emission, HESS J1708$-$443, in the Galactic plane. Its energy spectrum is well-described by a power law with a photon index $\Gamma = 2.0 \pm 0.1_{\mathrm{stat}} \pm 0.2_{\mathrm{sys}}$ and a normalization at 1 TeV of $\phi_0 = (4.2 \pm 0.8_{\mathrm{stat}} \pm 1.0_{\mathrm{sys}}) \times 10^{-12}\,\mathrm{cm^{-2}\,s^{-1}\,TeV^{-1}}$. The corresponding integral flux $F(1\text{--}10\,\mathrm{TeV}) = 3.8 \times 10^{-12}\,\mathrm{ph\,cm^{-2}\,s^{-1}}$ is roughly 17% of the Crab Nebula. The possible associations of HESS J1708$-$443 with an offset, relic PWN of PSR B1706$-$44 and with the partial shell-type SNR candidate G 343.1$-$2.3 have been discussed using additional radio and H I line emission data. Given the extended nature of the TeV source and the limited statistics, it is unclear if the emission is associated with the PWN, located at the edge of the H.E.S.S. source, or with the SNR, in which the pulsar is thought to be embedded. Based on energetics and a wealth of information at other wavelengths, neither interpretation can be excluded at this time; furthermore, the possibility remains that both sources contribute to the total observed VHE γ-ray emission. High-spatial-resolution CO mapping of this region would improve our understanding of the molecular environment and might help to identify a preferred MWL counterpart to HESS J1708$-$443. Deeper exposure in the TeV regime would also provide vital statistics and enable more detailed morphological and spectral studies.

Chapter 4

Discovery and multiwavelength study of the unidentified VHE γ-ray source HESS J1503–

This chapter focuses on an enigmatic source of VHE γ-rays, HESS J1503–582, which has been challenging to associate with a counterpart at lower energies, despite a comprehensive search of multi-wavelength archival data and dedicated X-ray observations with two X-ray satellites. The discovery was first published by Renaud, Goret, and Chaves 2008. This chapter is based loosely on those preliminary results but the analysis and interpretation has evolved considerably in the last two years. As a result, I have thoroughly re-written, re-structured, and lengthened the text, and it incorporates a larger and more recent H.E.S.S. dataset. I have performed new morphological and spectral analyses which are shown in the figures and described in the text. These new analyses also reveal a new VHE γ-ray source candidate nearby. Furthermore, the multi-wavelength discussion has also been expanded; for example, it now includes a section on GeV γ-ray counterpart candidates discovered by Fermi/LAT and a comparison with a recent VERITAS non-detection of a forbidden-velocity wing. The ChIcAGO team has provided Chandra data and analysis. This chapter represents a paper draft which will soon undergo internal review in the H.E.S.S. Collaboration prior to being submitted to a journal.

Abramowski, et al. (**H.E.S.S. Collaboration**)[1]

in preparation Renaud, M., Goret, P., & **Chaves, R.C.G.** (H.E.S.S. Collaboration)

AIP Conf. Series (Proc. of the 4th Intl. Mtg. on High Energy Gamma-Ray Astronomy), 2008, 1085, 281

---

[1]Corresponding authors: R.C.G. Chaves and M. Renaud; External (non-H.E.S.S.) authors: ChIcAGO Team and A. Bamba

Abstract

Context: The extended H.E.S.S. survey of the inner Galaxy ($|\ell| \lesssim 60°$, $|b| \lesssim 3°$) in the very-high-energy (VHE; $E > 100\,\text{GeV}$) domain has led to the discovery of numerous γ-ray sources, many of which do not have obvious counterparts at lower energies.

Aims: We aim to reveal the nature of newly-discovered VHE γ-ray sources, and to understand the mechanisms responsible for VHE γ-ray production.

Methods: The latest data from the on-going H.E.S.S. Galactic Plane Survey are used, in addition to data obtained in 2009 during a dedicated observation campaign of the region-of-interest, and the standard H.E.S.S. analyses are performed in order to investigate morphology and spectrum. New *Chandra* observations are analyzed to probe the region-of-interest in a complimentary energy domain and constrain the level of X-ray emission which could be associated with the VHE γ-ray emission. An extensive search of archival multi-wavelength data is also conducted in order to identify potential counterparts at lower energies.

Results: A new source of VHE γ-rays, HESS J1503–582, has been discovered at $\alpha_{\text{J2000}} = 15^{\text{h}}03^{\text{m}}31^{\text{s}} \pm 16^{\text{s}}$, $\delta_{\text{J2000}} = -58°14' \pm 2'$ with a statistical significance of $\sim 7\,\sigma$. It is extended ($0.16° \pm 0.02°_{\text{stat}} \pm 0.03°_{\text{syst}}$) with respect to the H.E.S.S. point spread function ($0.07°$) and its spectrum is well-fit by a power-law $dN/dE \propto E^{-\Gamma}$ in the 0.8–10 TeV energy range, with a photon index $\Gamma = 2.3 \pm 0.2_{\text{stat}} \pm 0.2_{\text{syst}}$ and an integral flux equivalent to $\sim 5\%$ of the Crab Nebula above 1 TeV. The source is found to be partially coincident with a forbidden-velocity wing, FVW 319.8+0.3, revealed in H I 21 cm line radio emission, three faint *Chandra* point sources discovered during recent, follow-up X-ray observations of *ASCA* source AX J150436–5824, and a GeV γ-ray source detected by *Fermi*. Additionally, a nearby VHE γ-ray source candidate has been serendiptiously detected, also coincident with a *Fermi* source.

Conclusions: The potential associations of HESS J1503–582 with the FVW, *Chandra* sources, and/or *Fermi* source are discussed, in light of the new observational evidence in the keV through TeV energy regimes. However, HESS J1503–582 remains unidentified pending more detailed analyses and dedicated *Suzaku* observations recently performed in August 2010.

4.1   Introduction

A significant fraction of the known Galactic VHE γ-ray sources do not appear to be associated with objects that are known to be potential sources of VHE γ-rays, such as supernova remnants (SNRs) and pulsar wind nebulae (PWNe). This is in part due to the difficulty of identifying extended (i.e. on the order of tens of arcmins) sources at lower energies which may be related to the typically large (i.e. $\sim 0.2°$) VHE sources. Furthermore, the archival multiwavelength data available is often incomplete, requiring dedicated observations with

other telescopes. Although current imaging atmospheric Cherenkov telescopes (IACTs) have reached sensitivities and angular resolutions which are unprecedented compared to their predecessors, many faint γ-ray sources are still difficult to physically associate with phenomena at lower energies. Instruments in these other domains (e.g. radio, infrared, X-rays) usually feature angular resolutions at sub-arcminute / arcsecond scales, often coupled with relatively small fields-of-view (FoVs) compared to H.E.S.S. (FoV $\sim$5°), thus hindering them from revealing large-scale structures. To make matters worse, most catalogs of potential VHE sources are known to be biased and incomplete, as exemplified by that of Galactic SNRs (Green 2009). Therefore, some sources may show up in VHE γ-ray images while going unnoticed in other observational windows.

In this chapter, H.E.S.S. observations and data analysis of one of these "dark", or unidentified, sources, HESS J1503–582, are presented. Its properties are given, together with the findings of an extensive search for potential counterparts such as SNRs, energetic pulsars and PWNe, star-forming complexes, H II regions and Wolf-Rayet (WR) stars. Results from new observations with the *Chandra X-ray Observatory* of the nearby *ASCA* source AX J150436–5824 are also shown. Preliminary results were published by Renaud et al. (2008a) based on a much smaller H.E.S.S. dataset ($\sim$50% of the current effective exposure); furthermore, *Chandra* observations were not yet available at that time. Finally, the VHE γ-ray source's possible associations with a forbidden-velocity wing (FVW; a characteristic structure seen in 21 cm H I line emission) or with nearby X-ray sources are investigated.

4.2 Observations and analysis

4.2.1 VHE γ-ray observations

The H.E.S.S. telescope array is described in Chapter 1.

The region-of-interest was first targeted in March 2004 as part of H.E.S.S.'s observational program on TeV PWN candidates, in this case the nearby MSH 15−52 (Aharonian et al. 2005g). The region was observed regularly until March 2010 under the auspices of the extended H.E.S.S. Galactic Plane Survey (Chapter 2). Dedicated *wobble*-mode observations of HESS J1503–582 were also scheduled for $\sim$15 h in June–July 2009 after a *hotspot*, or source candidate, became evident in the survey dataset. In this observation mode, the array is pointed towards a position offset from the source of interest, which allows simultaneous background estimation within the FoV (Berge et al. 2007). Observation *runs* of 28-min duration were taken, alternating between offsets of ±0.7° in declination and right ascension from the preliminary source position.

The final dataset includes all observations performed with three or four telescopes and offset less than 2.0° from the nominal source position, for a total live-time of 55 h. The relatively strict cut on the maximum offset is necessary to minimize the exposure gradient in

the FoV due to observations of the heavily-exposed MSH 15−52. Since the average run offset is $1.2° \pm 0.5°$, the offset-corrected live-time is ~45 h at the position of HESS J1503–582, after correcting for the γ-ray acceptance across the camera FoV. The zenith angles (ZAs) of the observation runs range from $34°$ to $46°$ with a mean of $37° \pm 2°$.

The dataset was selected using standard quality criteria (Aharonian et al. 2006a) to remove data affected by hardware-related problems but with relaxed cuts on weather-related criteria (e.g. the system trigger rate), in order to retain the maximum amount of usable data for source discovery purposes. However, spectral analysis was performed on a limited dataset, obtained using the standard, stricter weather criteria and by selecting only runs where the full four-telescope array was operational, to ensure the highest data quality and reduce systematics. This spectral dataset comprises 49 h live-time of observations and has similar offset and ZA distributions.

4.2.2   VHE γ-ray analysis methods

The dataset was analyzed using the Hillas second moment method (Hillas 1985) and the H.E.S.S. standard analysis described in Aharonian et al. (2006a). For γ-hadron separation, *hard cuts* were used, which require a minimum of 200 photoelectrons (p.e.) to be recorded per EAS image. Compared to *standard cuts* (80 p.e.), this relatively strict requirement results in better background rejection and an improved angular resolution but also in an increased energy threshold (0.8 TeV for this dataset).

Two different background estimation procedures (Berge et al. 2007) were used in this analysis. For determining the source detection significance and for 2D image generation, the *ring background method* was used with an inner ring radius $R_i = 0.70°$ and outer ring radius $R_o = 0.92°$. The area of this ring (the OFF-source region) was chosen such that the ratio of the OFF area to the ON area was ~7. For this analysis, the on-source region (ON) was defined *a priori* as a circle of radius $\theta = \sqrt{0.05}°$, one of the standard source search radii employed in the H.E.S.S. GPS, in order to avoid additional trial factors when determining the statistical significance of the source detection.

Since the above method includes an energy-averaged model for the camera acceptance to account for the different offsets of the signal and background regions from the camera center, it was not used for spectral extraction. The *reflected region background method* was instead used to measure the spectrum. The time-dependent optical response of the system was estimated from the Cherenkov light of single muons passing close to the telescopes (Bolz 2004). In both background methods, known sources and source candidates are excluded from OFF regions.

Two independent data analyses, namely the Hillas (Hofmann et al. 1999) and Model++ (de Naurois & Rolland 2009) methods, were used to generate images and spectra. The analyses not only use different techniques for γ-ray-hadron separation but also use data which

were indepedently calibrated. Both give results which are fully consistent within statistical errors. In this paper, results obtained with the primary Hillas method are preferentially shown.

4.2.3 X-ray observations and analysis methods

4.2.3.1 *ASCA* **and** *Chandra*

The X-ray source AX J150436–5824 was discovered during the *ASCA* Galactic Plane Survey, which studied the inner region of the Galactic plane ($-45° < \ell < 63°$ and $|b| < 0.4°$) in the energy band 0.7–10 keV with a spatial resolution of 3′ (Sugizaki et al. 2001). Due to *ASCA*'s poor spatial resolution, the vast majority of the 163 discovered *ASCA* sources, including AX J150436–5824, are unidentified.

To address this problem, some of the unidentified sources have been re-observed with *Chandra* and *XMM-Newton*, utilizing their sub-arcsecond resolution to reveal the underlying X-ray source(s), often in combination with multi-wavelength observations (Gelfand & Gaensler 2007; Gaensler et al. 2008; Kaplan et al. 2007; Lemiere et al. 2009). Spurred by these efforts, the ChIcAGO (Chasing the Indentification of *ASCA* Galactic Objects) survey was proposed to systematically follow-up unidentified *ASCA* sources with *Chandra* and *XMM-Newton* (Anderson et al. 2006). X-ray observations of the field around AX J150436–5824 were taken with *Chandra* on 6 June 2009 starting at 20:40:09 UTC (Obs ID: 10508). Data were collected with the Advanced CCD Imaging Spectrometer (ACIS) operating in faint mode, for a total exposure $T_{\mathrm{exp}} = 4.36$ ks. A search for point sources was carried out using the CIAO[2] source detection algorithm `wavdetect`.

4.2.3.2 *Suzaku*

Suzaku observations were proposed (PI: A. Bamba; CoIs: R.C.G. Chaves et al.) in response to AO-5 in order to search for an X-ray counterpart of HESS J1503–582 and investigate its possible identification with a FVW. The proposal was accepted for 100 ks of exposure, with 50 ks on HESS J1503–582 and 50 ks in an adjacent field from which to estimate the background.

The *Suzaku* observations in the 0.5–8.0 keV energy range were carried out on 5–6 August 2010, exposures of 51.4 ks centered at (RA,Dec) = (225.9130°, −58.2332°) (approximate center of HESS J1503–582) and 51.6 ks centered at (RA,Dec) = (225.4141°, −58.3766°), an adjacent region used for background estimation. The observations were performed in full-window mode with spaced-row charge exchange, and the standard screening criteria used by the *Suzaku* team was applied. The images were corrected for vignetting and exposure

---

[2]CIAO: *Chandra*'s data analysis system (Fruscione et al. 2006)

variations using `XISSIM` and `XISEXPMAPGEN`. Spectral analyses of detected point-like and extended sources are underway.

4.3   Results

4.3.1   Discovery of HESS J1503–582

A new source of VHE γ-rays, HESS J1503–582, was detected with a (pre-trial) statistical significance of $\sim 7\,\sigma$, confirming the preliminary discovery published by (Renaud et al. 2008a). This corresponds to a significance of $5.0\,\sigma$ after conservatively accounting for all trials involved, including e.g. the size of the survey search grid (Chapter 2). The signal consists of 254 excess γ-rays integrated over a circular ON-source region ($\theta = \sqrt{0.05}\,\mathrm{deg}^2$) centered at the peak significance.

The unsmoothed exposure-corrected excess is well-fit (χ^2 / ndf = 1.15) by a radially-symmetric Gaussian profile ($\phi = \phi_0\,e^{-r^2/(2\sigma^2)}$) convolved with the H.E.S.S. point spread function (PSF; 68% containment radius of 0.07° for this analysis). The new source is found to have an intrinsic size (68% containment radius) $0.16° \pm 0.02°_{\mathrm{stat}} \pm 0.03°_{\mathrm{syst}}$, and its centroid is located at $\alpha_{\mathrm{J2000}} = 15^{\mathrm{h}}03^{\mathrm{m}}31^{\mathrm{s}} \pm 16^{\mathrm{s}}_{\mathrm{stat}}$, $\delta_{\mathrm{J2000}} = -58°14' \pm 2'_{\mathrm{stat}}$. There is an additional systematic error of $20''$ introduced by the uncertainty in the pointing precision (Gillessen et al. 2005). The source is therefore considered extended since its size is greater than the H.E.S.S. PSF. An image of the VHE γ-ray excess in a $2° \times 2°$ region around HESS J1503–582 is shown in Fig. 4.1, smoothed with a Gaussian of width 0.13° to reduce statistical fluctuations. The smoothing radius is chosen to be roughly on the same scale as the H.E.S.S. PSF so that resolvable morphological features are largely maintained.

The spectrum of HESS J1503–582 was extracted from a circular region with a radius $\theta = 0.3°$. The spectral extraction region (depicted in Fig. 4.1) encloses $\sim$90% of the excess γ-rays from HESS J1503–582 and is chosen such that it is essentially indepedent of the source morphology yet retains a high signal-to-noise ratio. Within the integration circle, 230 excess γ-rays were found in the energy range 0.8–10 TeV, corresponding to a statistical significance of $6.9\,\sigma$ (pre-trials). The differential spectrum can be fit (χ^2 / ndf = 0.58) by a power law $\phi = \phi_0\,(E\,/\,1\,\mathrm{TeV})^{-\Gamma}$ with a spectral photon index $\Gamma = 2.2 \pm 0.2_{\mathrm{stat}} \pm 0.2_{\mathrm{syst}}$ and a flux normalization at 1 TeV of $\phi_0 = (1.4 \pm 0.3_{\mathrm{stat}} \pm 0.4_{\mathrm{syst}}) \times 10^{-12}\,\mathrm{cm}^{-2}\,\mathrm{s}^{-1}\,\mathrm{TeV}^{-1}$. The integral flux above 1 TeV is $\sim 1.0 \times 10^{-12}\,\mathrm{ph\,cm}^{-2}\,\mathrm{s}^{-1}$, which corresponds to $\sim$5% of the Crab Nebula flux in the same energy range. The differential flux points from HESS J1503–582 and the fitted power law are shown in Fig. 4.2. The above results are all compatible with the preliminary ones based on a $\sim$50% smaller dataset and published by Renaud et al. (2008a).
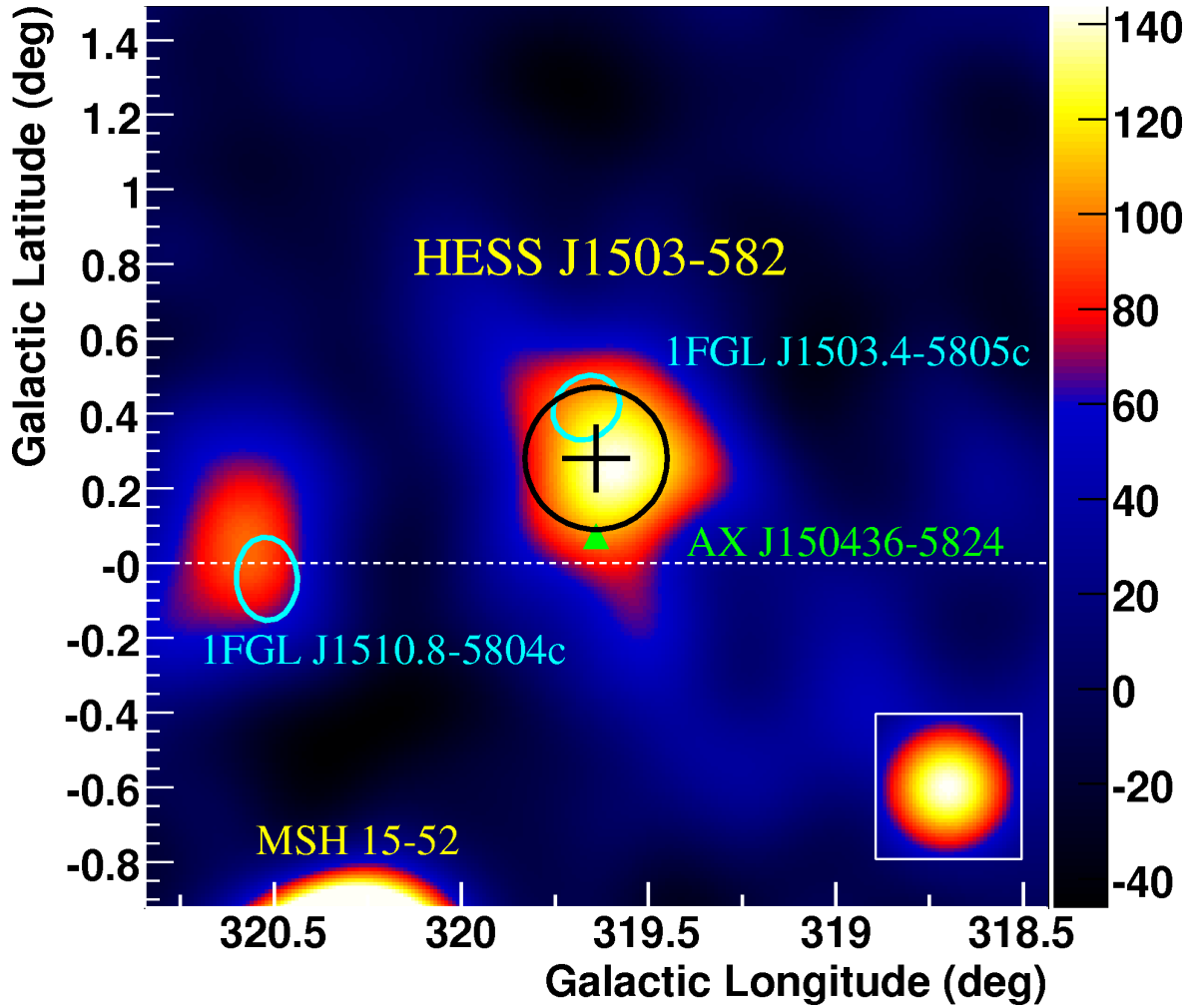
Figure 4.1: H.E.S.S. image of the VHE γ-ray excess, smoothed with a Gaussian profile of width $\theta/\sqrt{3} = 0.13°$, centered on HESS J1503–582. The black cross is placed at the source centroid, and its size reflects the uncertainty in the centroid position. The black circle (radius 0.16°) reflects the source's intrinsic size. The keV–GeV counterpart candidates, including AX J150436–5824 and FVW 319.8+0.3 and the detected *Chandra* X-ray sources, are also shown. Finally, the Galactic plane is depicted as a white dashed line. The bright source in the lower left corner is MSH 15–52.

4.3.2 A new faint TeV source candidate

In the course of observing HESS J1503–582, a faint γ-ray source candidate was serendipitously detected thanks to the increased exposure in the region possible because of H.E.S.S.'s large FoV. The TeV *hotspot*, visible in Fig. 4.1, is located to the East of HESS J1503–582 at roughly $\alpha_{J2000} \approx 15^{\mathrm{h}}10^{\mathrm{m}}35^{\mathrm{s}}$, $\delta_{J2000} \approx -58°49'$. It is very faint and cannot be statistically confirmed, with a significance of only $\sim 5\sigma$ pre-trials. Further morphological and spectral analyses are currently not possible due to the low statistics. There are no energetic pulsars nor SNRs spatially coincident with this hotspot, although its position is compatible
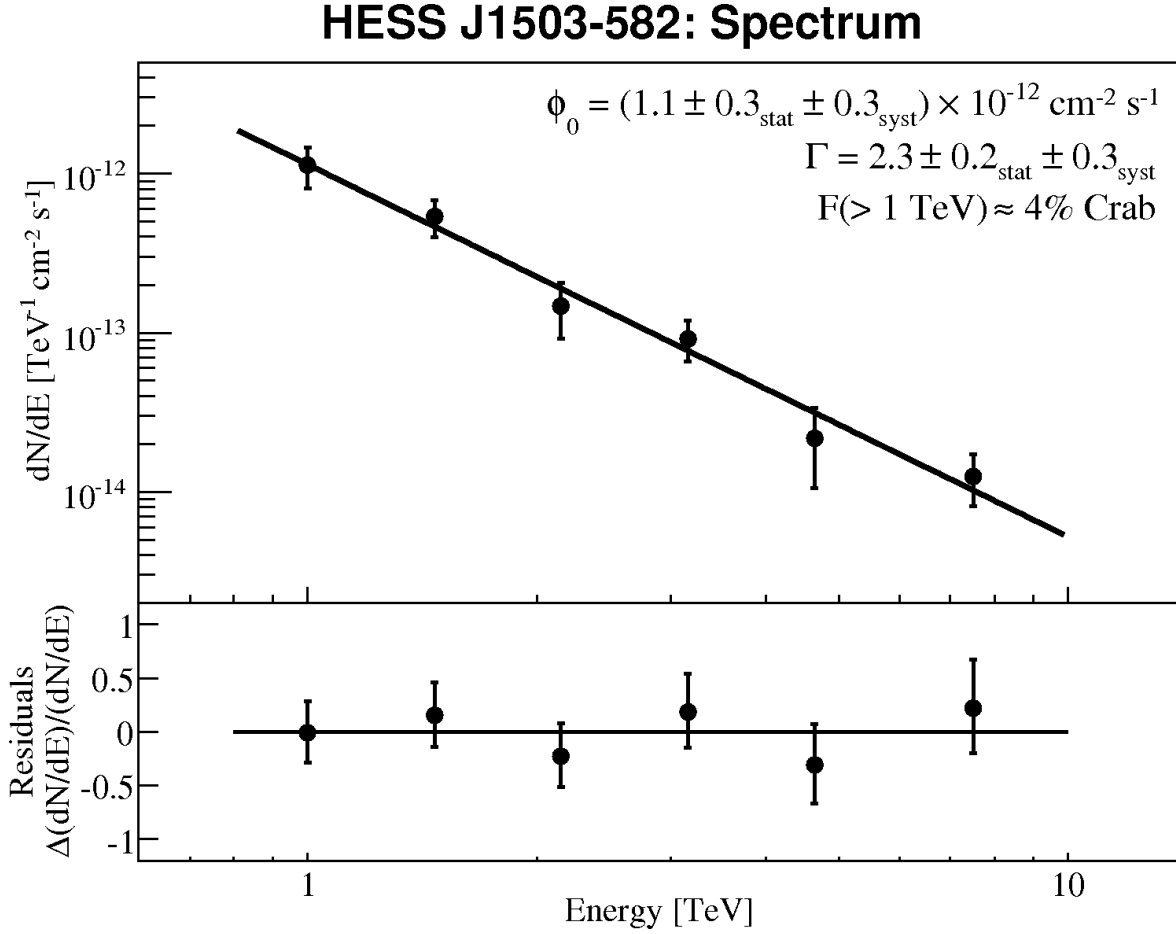
HESS J1503-582: Spectrum

$$\phi_0 = (1.1 \pm 0.3_{stat} \pm 0.3_{syst}) \times 10^{-12} \ cm^{-2} \ s^{-1}$$
$$\Gamma = 2.3 \pm 0.2_{stat} \pm 0.3_{syst}$$
$$F(> 1 \ TeV) \approx 4\% \ Crab$$

Figure 4.2: Differential energy spectrum of HESS J1503–582 from 0.8 to 10 TeV, extracted from a circular region with radius $\theta = 0.3°$. Events with energies between 0.8 and 10 TeV were used in the determination of the spectrum, and there was no cut on the minimum significance per bin. The error bars denote 1-σ statistical errors. The solid line shows the result of a power-law fit to the data points, and the residuals of the fit are shown in the bottom panel.

with an unidentified high-energy (HE; $E > 100$ MeV) γ-ray source discovered by *Fermi*/LAT, 1FGL J1510.8−5804c[3] (Abdo et al. 2010). Given the already-high exposure at this location (~67 h live-time), confirming the detection at a level of 5σ (post-trials) with H.E.S.S. is likely not feasible in the near future.

4.3.3   Discovery of three *Chandra* point sources

An X-ray source was found in the vicinity of HESS J1503–582 using the SIMBAD database, while searching MWL catalogs for potential counterparts. The *ASCA* source AX J150436–5824 (Sugizaki et al. 2001) is offset from the TeV centroid by 0.2°but within the extended

---

[3]The designator "c" indicates that this source is potentially confused with interstellar diffuse GeV emission or is a spurious detection; therefore, its location may not be reliable.

emission, in particular within the 4σ significance contour. Due to its high column density $N_H = 1.29 \times 10^{22}$ cm^{-2} and hard photon index $\Gamma = 1.44$ in the 2–10 keV band, this source was tentatively classified as a cataclysmic variable (CV) (Sugizaki et al. 2001). While cataclysmic variables are prolific emitters of keV X-rays, they are not known nor expected to emit much higher-energy TeV γ-rays. Nonetheless, its tentative classification as a CV merited further investigation with higher-quality X-ray observations.

To that end, *Chandra* observations were performed (Sect. 4.2.3) by the ChIcAGO Team and analyzed in cooperation with the H.E.S.S. Collaboration. Three X-ray point sources were discovered within 4′ of AX J150436–5824, using the `CIAO` source detection algorithm `wavdetect`. Their properties are summarized in Table 4.1. No other significant sources were detected in the *Chandra* FoV (~0.4°), which encompasses the centroid of HESS J1503–582.

The faintest source is comprised of only eight counts, all below 2 keV. It appears to be associated with an ordinary star, 2MASS J15045112−5824582, ruling out an association with the H.E.S.S. source.

Table 4.1: Properties of three *Chandra* X-ray sources detected in the vicinity HESS J1503–582.

Source (CXO J)	R.A. (J2000.0)	Dec (J2000.0)	Counts (0.3–2 keV)	Counts (2–8 keV)	Counts (0.3–8 keV)	Count Rate (0.3–2 keV)	Count Rate (2–8 keV)	Count Rate (0.3–8 keV)
150430.9−582411	15:04:30.990	−58:24:11.38	38	107	145	8.72 cnt s^{-1}	24.54 cnt s^{-1}	33.26 cnt s^{-1}
150413.5−582507	15:04:13.544	−58:25:07.50	17	32	49	3.9 cnt s^{-1}	7.34 cnt s^{-1}	11.24 cnt s^{-1}
150451.1−582458	15:04:51.141	−58:24:58.36	8	0	8	1.8 cnt s^{-1}	0 cnt s^{-1}	1.8 cnt s^{-1}

Neither of the brighter sources appears to have a counterpart in the near-infrared 2MASS (Two Micron All Sky Survey) Point Source Catalog (Skrutskie et al. 2006), in the optical DSS2 (Digitized Sky Survey 2) atlas, or in the infrared *Spitzer*/GLIMPSE survey catalog. The two point sources are clearly unresolved in the *Chandra* data, with no evidence of surrounding extended emission. However, the short exposure (4.36 ks), combined with the high angular resolution, makes it unlikely that any of the diffuse emission seen with *ASCA* would have been detected. Given the low number of counts, it is difficult to fit the spectra of either source with any confidence. Figure 4.3 shows the spectrum of CXO J150430.9−582411, which has the larger number of counts of the two sources, poorly fit ($\chi^2 = 0.7$) with a power-law model. Similarly inconclusive fits result from Raymond-Smith and Mekal models. The lack of statistics (counts) prevents any conclusions to be drawn from the spectra.
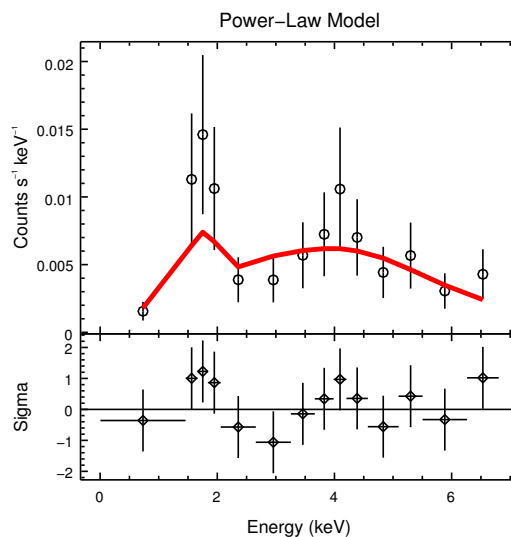
Figure 4.3: *Top*: Spectrum of CXO J150430.9−582411 (black circles) fitted with a power law (red line; $\chi^2 = 0.7$). *Bottom*: Residuals of the power-law fit.

4.4 Discussion

4.4.1 Association with a forbidden-velocity wing

The search for traditional counterparts of Galactic TeV sources, such as SNRs, PWNe, or HMXBs, did not reveal any likely candidates. However, Kang & Koo (2007) recently published a catalog of 87 extended and faint radio structures detected through the 21 cm H I line in the Southern Galactic Plane Survey (SGPS) and Leiden/Dwingeloo Survey (LDS) data. These structures, forbidden-velocity wings (FVWs), appear as winglike features of line emission in (ℓ, v) diagrams, i.e. they are present at velocities forbidden by the canonical Galac-

tic rotation curve in limited spatial regions over velocity extents of more than ∼20 km s^{-1}. Among them, FVW 319.8+0.3 (Fig. 4.4), marked with the highest detection rank by Kang & Koo (2007), is spatially coincident with HESS J1503–582, though with an offset of ∼0.1°, as shown in Fig. 4.5 (left). This FVW appears in the H I line image integrated between −123 and −98 km s^{-1}, two velocities which are not permitted by the canonical Galactic rotation curve (e.g., Fich et al. 1989) along this line-of-sight (Fig. 4.5, right).

This FVW does not coincide with any known objects that could be responsible for its large velocity, e.g. SNRs, nearby galaxies, or high-velocity clouds. Most of the detected FVWs are located off the Galactic plane, and their atypical latitude distribution lead Kang & Koo (2007) to discuss possible origins. For instance, previously unknown ("missing"), old SNRs in the radiative phase could be the most likely candidates, as in the case of the discovery of the SNR associated with FVW 190.2+1.1 (Koo et al. 2006). To investgiate this, the SGPS/ATCA H I data (McClure-Griffiths et al. 2005) have been inspected to search for any shell-type diffuse emission in the velocity range of FVW 319.8+0.3, since ATCA features a better angular resolution (∼ 2′) than Parkes (∼ 15′). No shell-type structure was found (Fig. 4.5), but the low ATCA sensitivity of ∼ 1.6 K renders the identification of faint and extended emission difficult.

It has been proposed that VHE γ-rays may be emitted from OB associations following hadronic interactions of cosmic rays in the collective stellar winds of massive O and B stars (Torres et al. 2004; Domingo-Santamaría & Torres 2006) In fact, six VHE γ-ray sources, TeV J2032+4131 (Cygnus OB2), HESS J1648−458 (Westerlund 1), HESS J1023−575 (Westerlund 2), HESS J1303−631 (Cen OB6), HESS J1614−518 (Pismis 22), and HESS J1848−048 (W 43), have so far been investigated in the context of similar scenarios (Aharonian et al. 2005a; Ohm et al. 2010; Aharonian et al. 2007b, 2005d, 2006d; Chaves et al. 2008b, respectively). Some of the proposed models (Torres et al. 2004, e.g.) also predict that the TeV γ-ray source would be weak or undetectable at lower γ-ray energies (MeV–GeV), leading to an intriguing possibility for associations between stellar clusters (or stellar associations) and dark sources such as HESS J1503–582. Furthermore, in all of the models considered by Torres et al. (2004), no coincident EGRET source is expected, which is consistant with the case of HESS J1503–582.

The strong stellar winds from early-type OB stars or WR stars may also be linked to FVWs due to their ability to sweep up the ambient medium into observable shells which may not follow the bulk Galactic rotation (Kang & Koo 2007). Indeed, Kang & Koo (2007) find that the joint activity of stellar winds and SN explosions from massive stars in nearby (≲ 4 kpc) and powerful ($L_{\mathrm{wind}} ≳ 10^{37}$ erg s^{-1}) OB associations could produce fast-moving neutral hydrogen gas detectable at the sensitivity level of the current H I surveys and be responsible for as many of ∼15% of the unidentified FVWs. However, after consulting the Galactic O-star catalog of Garmany et al. (1982) and the 7$^{\mathrm{th}}$ Galactic WR catalog of van der Hucht (2001), no O-type stars or WR stars were found within 1° of FVW 319.8+0.3 which match
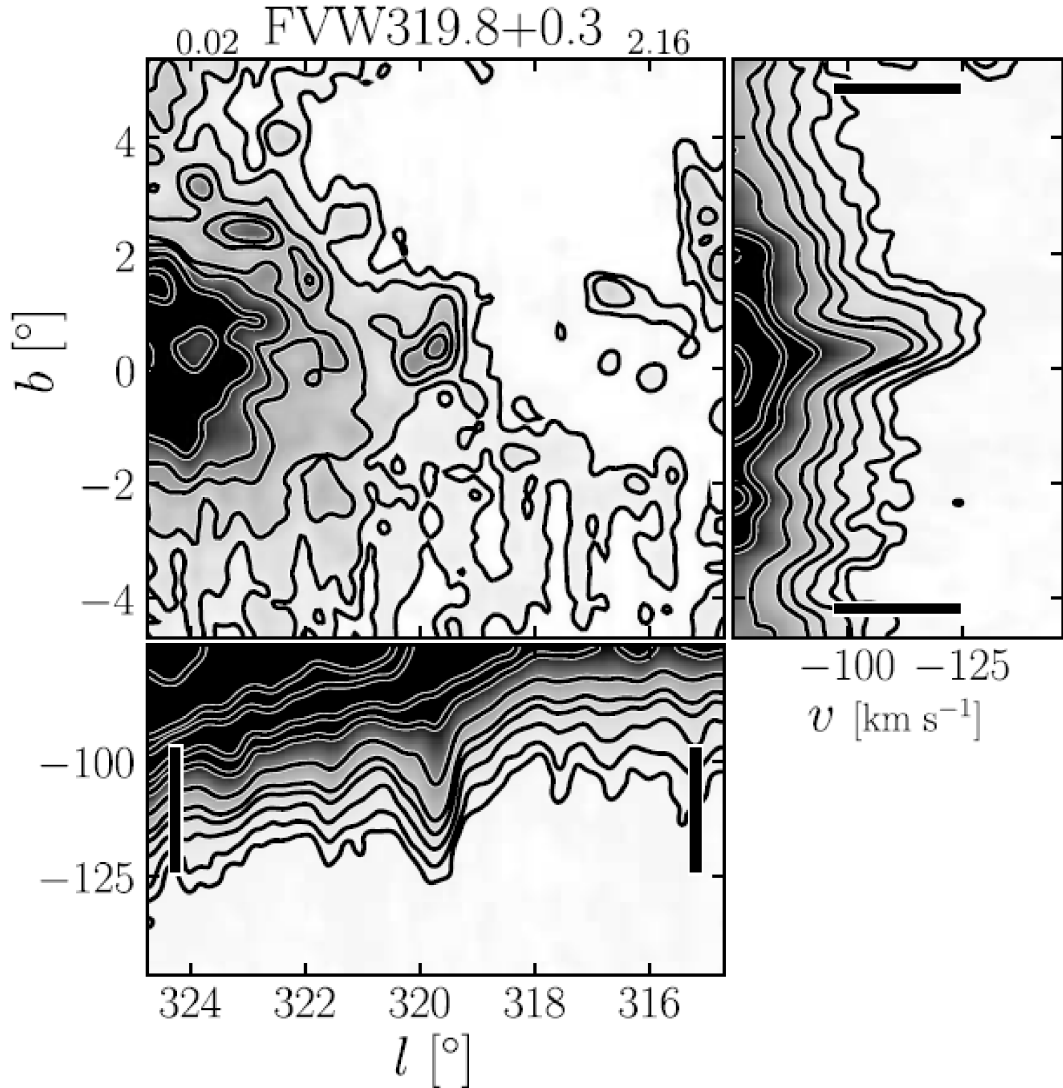
Figure 4.4: The forbidden-velocity wing FVW 319.8+0.3 as seen at radio wavelengths. Its (ℓ-v) and (b-v) profiles are presented at the bottom and to the right, respectively. The central image is integrated over the kinematic velocity range indicated by thick black lines in the position-velocity profiles. The minimum and maximum values of the contours in the integrated map are in units of $K\,km\,s^{-1}$ and noted on the left and right side of the FVW name at the top, respectively. The profiles are cut at the longitude or the latitude of the FVW. The contour levels in the profiles are at brightness temperatures of 0.1, 0.2, 0.4, 0.7, 1, 2, 5, 10, 30, 50, and 100 K. From Kang & Koo (2007).

these criteria (Kang & Koo 2007). A recently updated catalog of Galactic OB associations by Mel'Nik & Dambis (2009) was also checked, but no known OB associations were found within 1° of FVW 319.8+0.3. Such a large search radius precludes the existence of the above
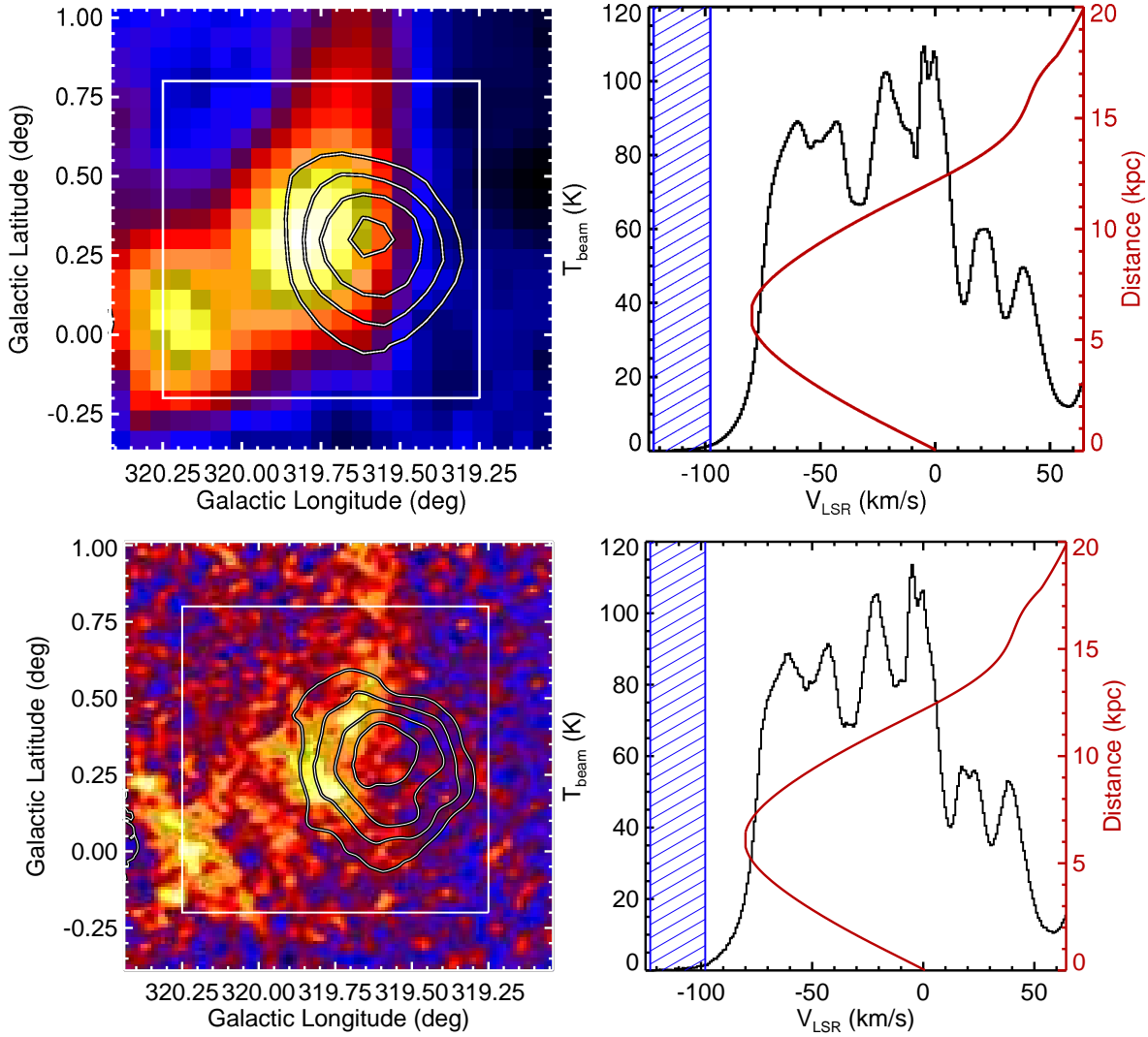
Figure 4.5: *Left panels*: SGPS-Parkes (top) and SGPS/ATCA (bottom) velocity-integrated (between −123 and −98 kms⁻¹) images of the H I line emission centered on FVW 319.8+0.3. H.E.S.S. significance contours are shown in black from 3 to 7σ with steps of 1σ. *Right panels*: Velocity profiles of H I intensity integrated over the white square region shown in the left images. The red curve represents the canonical Galactic rotation curve according to Fich et al. (1989) at the position of FVW 319.8+0.3. The velocity range of the images on the left are marked by blue dashed regions.

counterpart candidates from the vicinity of HESS J1503−582 as well, to the extent to which the catalogs are considered complete.

Old and isolated SNRs, with an age greater than the onset of the radiative phase ∼ 4×10⁴ y (Cioffi et al. 1988), are not expected to accelerate multi-TeV particles any longer, mainly because of the very low shock speed (Ptuskin & Zirakashvili 2005). However, Yamazaki et al. (2006) suggest that the TeV to X-ray flux ratio might significantly increase as an SNR ages, which could account for the large number of unidentified VHE γ-ray sources which

are dark at lower energies, including in X-rays.

Old SNRs have, in fact, already been detected in the VHE domain, e.g. W 28 (HESS J1801−233) (Aharonian et al. 2008f), with an estimated age in the range 0.4–1.5×10^5 y. However, in this case, the emission is likely associated with the interaction of W 28 with nearby molecular clouds, which are not present near HESS J1503–582. Another case, the originally unidenti-fied H.E.S.S. source, HESS J1731−347 (Aharonian et al. 2008a) is now thought to be asso-ciated with a recently-identified shell-type SNR, G 353.6−0.7, that is $\sim 3 \times 10^4$ y old.

The VERITAS Collaboration recently reported the non-detection of VHE γ-rays from an-other FVW, located in the northern sky, after 18 h of good-quality observations (Holder & for the VERITAS Collaboration 2009). The observation campaign was motivated by the ini-tial report of discovery of HESS J1503–582 emission from the direction of FVW 319.8+0.3 (Renaud et al. 2008a), which suggested that some FVWs might represent old, undiscovered SNRs, still capable of emitting γ-rays in the VHE domain. The target, FVW 190.2+1.1, has a clear shell-like morphology (Koo et al. 2006) in the radio which appears to support this hy-pothesis and make it an ideal candidate for follow-up observations with an IACT. However, VERITAS found no evidence for VHE γ-ray emission and set fairly stringent flux ULs at the level of <1% Crab. Nevertheless, FVWs are not currently well-studied individually nor well-understood as a class. There is a great diversity in their possible progenitors, so it is not possible to draw any conclusive parallels between FVW 190.2+1.1 and FVW 319.8+0.3 and HESS J1503–582.

4.4.2   Association with X-ray counterparts

There is no clear evidence for diffuse X-ray emission in the region, which might have pro-vided evidence for an undiscovered PWN in the vicinity of HESS J1503–582. Unfortunately, the search was hindered by the low statistics in the *Chandra* dataset. As a result, the nature of the two brighter X-ray sources discovered remains unknown.

Deeper observations of AX J150436–5824 with *Chandra*, *XMM-Newton*, or *Suzaku* are needed to determine whether the *ASCA* source in the vicinity of HESS J1503–582 is indeed a CV, as originally classified by (Sugizaki et al. 2001), or to see if there is any indication of extended X-ray emission, unresolved by *ASCA* and the recent *Chandra* observation. The latter could provide evidence for the existance of a hitherto undetected PSR/PWN system; the TeV emission discovered by H.E.S.S. might then be interpreted as a relic nebula from the past evolution of the putative PSR (de Jager & Djannati-Ataï 2008).

Analysis of a recent and relatively deep exposure of this region using *Suzaku* has just begun and will hopefully reveal the keV-energy environment at and around the position of HESS J1503–582.

4.4.3   Association with a GeV γ-ray source

The centroid of HESS J1503–582 is notably compatible with an unidentified high-energy (HE; $E > 0.1$ GeV) γ-ray source discovered by *Fermi*, 1FGL J1503.4−5805c[4] (Abdo et al. 2010), as can be seen in Fig. 4.1. The GeV source is detected with a significance (here, *TS* value, as defined in Abdo et al. 2010) level of 7.3. Interestingly, the case for association with HESS J1503–582 goes beyond a position coincidence. The spectrum of 1FGL J1503.4−5805c in the *Fermi* energy range follows a power law with a spectral index of 2.25±0.11. By extrapolating the MeV–GeV spectrum to the TeV regime, it is found that the broadband emission can be described by a single power-law component extending over five decades in energy, providing spectral evidence that HESS J1503–582 and 1FGL J1503.4−5805c could be physically associated. However, since the original analysis of the *Fermi* source may be affected by uncertainties in the diffuse background model (see footnote), a dedicated and careful analysis of 1FGL J1503.4−5805c must be performed. Such an analysis may also benefit from the increased *Fermi* exposure since the 1FGL catalog was originally published.

4.4.4   Association with PSR J1502–5828

The pulsar PSR J1502–5828[5] (Manchester et al. 2005) lies offset from the centroid of HESS J1503–582 by ∼0.2°. The pulsar has a characteristic age $\tau_c = 288$ kyr, a distance estimated to be $D = 8.2$ kpc (Cordes & Lazio 2002), a spin period $P = 668$ ms, and a spin-down flux $\dot{E}/D^2 = 7.1 \times 10^{31}$ (D/8.2 kpc)$^{-2}$ ergs^{-1}kpc^{-2}. No PWN has been observed in radio / H_α or in the GeV domain Kargaltsev & Pavlov (2010). These properties make PSR J1502–5828 a very poor candidate for harboring a TeV PWN, although it has recently been considered as such by Kargaltsev & Pavlov (2010). In particular, it would require a conversion efficiency from rotational pulsar energy to γ-rays on the order of 1000%, i.e. the γ-ray luminosity is a factor of ∼10 larger that the spin-down luminosity. On this alone, PSR J1502–5828 and any hypothetical relic PWN it might harbor can be ruled out as a counterpart to HESS J1503–582.

4.4.5   Other counterparts

No additional counterpart candidates were found in other catalogs of potential VHE γ-ray emitters, such as Galactic SNRs (Green 2009), H II regions (Paladini et al. 2003), star-forming complexes (Russeil 2003) and WR stars (van der Hucht 2001). Archival radio images from Molonglo at 843 MHz, ATCA at 1.4 GHz, Parkes at 2.4 GHz, and Parkes-MIT-NRAO (PMN) at 4.85 GHz, as well as the infrared images from *MSX* (at 8.28, 12.13

---

[4]The designator "c" indicates that this source is potentially confused with interstellar diffuse GeV emission or is a spurious detection; therefore, its location may not be reliable.

[5]ATNF Pulsar Catalogue version 1.40, `http://www.atnf.csiro.au/research/pulsar/psrcat`

and $14.65\,\mu\text{m}$ [6]) and *Spitzer*/GLIMPSE[7] (at $8\,\mu\text{m}$ [8]) were also inspected to search for hints of diffuse emission coincident with FVW 319.8+0.3, but no such emission was found. Finally, the clear extended nature of the H.E.S.S. source ($0.16°$) strongly disfavors an extragalactic (e.g. an active galactic nucleus) origin of the VHE γ-ray emission.

4.5 Conclusion

Despite extensive multi-wavelength analyses, including new *Chandra* observations, the recently-discovered HESS J1503–582 remains unidentified; it does not appear to emit significant radiation at lower energies and is therefore one of the most enigmatic, "dark" sources yet observed by H.E.S.S.. The most plausible counterparts relate to the FVW 319.8+0.3 seen in radio or a faint putative X-ray source (e.g. a PSR/PWN system) which lies below the sensitivity limit of current X-ray observations.

The fact that FVWs have excessive emission at high velocities that are forbidden by Galactic rotation models indicates that there should be some associated dynamical phenomena (Kang & Koo 2007), e.g. the expanding shell of a missing SNR or the combined stellar winds of an OB association. However, no supporting evidence for these scenarios, besides the positional coincidence of FVW 319.8+0.3 and HESS J1503–582, could be found in archival data. If FVW 319.8+0.3 is in fact an old, missing SNR, then the detection of VHE γ-rays from it would imply that SNRs remain efficient particle accelerators for much longer than commonly believed.

The GeV γ-ray source 1FGL J1503.4−5805c discovered by *Fermi* is not only positionally coincident with HESS J1503–582, but also spectrally compatible, suggesting that a single power law can describe the broadband MeV–TeV emission. The actual existence of the GeV source must be confirmed with more data and an dedicated analysis, since it may be in fact be an artifact resulting from uncertainties in the background model employed by *Fermi*. Alternatively, HESS J1503–582 may turn out to belong to the largest class of VHE γ-rayemitters, that associated with PWNe; deep X-ray observations have been recently carried out with *Suzaku* to explore this possibility in the hopes of identifying HESS J1503–582.

---

[6]see `http://irsa.ipac.caltech.edu/data/MSX`
[7]Galactic Legacy Infrared Midplane Survey Extraordinaire
[8]see `http://irsa.ipac.caltech.edu/data/SPITZER/GLIMPSE`

Chapter 5

Discovery of HESS J1832−084, a TeV PWN candidate

This chapter presents the discovery of VHE γ-ray emission from the vicinity of pulsar PSR J1832−0827 using H.E.S.S. observations. The combination of a small-sized TeV emission region, relatively old age of the pulsar, and moderate spin-down luminosity challenge the conventional TeV PWNe scenario. A paper based on this chapter is currently in preparation within the H.E.S.S. Collaboration, and preliminary results are presented here.

Abramowski, et al. (**H.E.S.S. Collaboration**)

in preparation

Abstract

Aims: The goal of this chapter is to present the discovery of a source of VHE γ-rays recently detected by H.E.S.S. and to investigate its nature through observations at lower energies. In particular, its potential association with the positionally-coincident pulsar PSR J1832−0827 is addressed.

Methods: The H.E.S.S. IACT array observed PSR J1832−0827 and its vicinity for an effective exposure of ~25 h from May 2004 to August 2010. The dataset comprises observations from the on-going Galactic Plane Survey, observations of nearby W 41 (HESS J1834−087), and, more recently, dedicated observations to confirm the source detection and increase the level of statistics available for analysis. Standard VHE γ-ray analysis methods are performed in order to determine the statistical significance, morphology, and spectrum of the source. Archival radio, infrared, and X-ray data are used to search for potential counterparts. The TeV source characteristics are compared to the pulsar properties and evaluated in the context of a putative TeV PWN scenario. The probability that the positional coincidence between the pulsar and the VHE γ-ray source is due to chance is estimated.

Results: The VHE γ-ray source HESS J1832−084 is detected with a post-trials statistical

significance of $\sim 5\,\sigma$. The emission is marginally extended with respect to the H.E.S.S. PSF ($\sim 5'$), in contrast to the vast majority of Galactic TeV sources which are typically an order of magnitude larger. Its spectrum in the VHE domain is well fit by a power law with a relatively steep photon index $\Gamma = 2.8 \pm 0.3_{\mathrm{stat}} \pm 0.2_{\mathrm{syst}}$. The integral flux from the source is $\sim 6.7 \times 10^{-13}\,\mathrm{cm}^{-2}\,\mathrm{s}^{-1}$ above 0.38 TeV, equivalent to $\sim 0.7\%$ of the Crab Nebula flux. There are no SNRs nor high-mass X-ray binaries (HMXBs) in the vicinity, but the centroid of the TeV emission is compatible with the location of the pulsar PSR J1832−0827. However, the conversion efficiency required for the moderately energetic PSR J1832−0827 to power the γ-ray luminosity is $\sim 56\%$, large compared to other known TeV PWNe. The combination of a relatively old age of the PSR J1832−0827 ($\sim 10^5$ yr) and small size when viewed at TeV energies (less than or similar to the H.E.S.S. PSF, or $\sim 6\,\mathrm{pc}$ at the distance of the pulsar) challenge the conventional PWN scenario, as does the lack of an established PWN at lower energies; however, an analysis of archival radio and infrared data reveals the presence of diffuse structures which are under investigation. Although HESS J1832−084 remains formally unidentified, the chance positional coincidence between PSR J1832−0827 and HESS J1832−084 is ruled out at the $\sim 2.4\,\sigma$ level.

5.1 Introduction

The on-going survey of the Galactic plane in the VHE domain by the H.E.S.S. IACT (Chapter 2) has revealed a large population of ~ 20–30 VHE γ-ray-emitting PWNe (Gallant 2007; Gallant et al. 2008; Mattana et al. 2009a; Kargaltsev & Pavlov 2010), which may account for more than a third of all known Galactic TeV sources. These so-called TeV PWNe represent the largest Galactic VHE source class and share similar key properties. In particular, virtually all of them are extended in the TeV domain with respect to the H.E.S.S. PSF ($\sim 5'$) and are associated with highly energetic and very young pulsars, i.e. pulsars with spin-down luminosities $\dot{E} \gtrsim 10^{35}\,\mathrm{erg}\,\mathrm{cm}^{-2}\,\mathrm{s}^{-1}$ and characteristic ages $\tau_{\mathrm{c}} \lesssim 50\,000$ yr. Many of them are also significantly offset from the pulsar with which they are presumed to be associated; this offset is usually interpreted to be a result of inhomogeneities in the nearby intestellar medium (ISM), the pulsar kick velocity, and/or the long cooling time of the electrons responsible for the VHE γ-ray emission.

Galactic VHE γ-ray sources are as a whole significantly extended, with only a handful of notable exceptions, most of those belonging to the γ-ray binary source class. In this chapter, we report the recent discovery of a unique Galactic VHE γ-ray source that is both relatively small in size and appears to be associated with an atypical pulsar counterpart, PSR J1832−0827. When viewed in the context of the currently-known population of energetic pulsars with TeV PWNe, this discovery challenges our current understanding of TeV PWNe (e.g. Gaensler & Slane 2006; de Jager & Djannati-Ataï 2008).

The energetic pulsar PSR J1832−0827 (also PSR B1829−08) was discovered by Clifton

& Lyne (1986), with a period $P = 647$ ms, during a high-frequency (1.4 GHz) radio survey for young pulsars at the Jodrell Bank Observatory. After measuring its spin-down period $\dot{P}$, the characteristic age

$$\tau_c = P/(n-1)\dot{P} \tag{5.1}$$

for the pulsar was found to be 160 000 yr (Clifton et al. 1992), where the braking index n is assumed to be the canonical value of three. The braking index has only been measured for a handful of pulsars (for a review, see Johnston & Galloway 1999), due to the difficulties of measuring $\ddot{\nu}$ (the second derivative of the rotation frequency). However, Johnston & Galloway (1999) have developed an alternative method for estimating n of moderate-aged pulsars which circumvents the need for long, phase-connected timing solutions and find $n = 2.5 \pm 0.9$ in the case of PSR J1832−0827; therefore, $\tau_c \approx 210\,000$ yr.

The pulsar PSR J1832−0827 is moderately energetic, with a spin-down luminosity of $\dot{E} = 9.3 \times 10^{33}$ erg s^{-1} (Taylor & Cordes 1993). The pulsar's distance D was constrained to the relatively narrow range 4.4–6.1 kpc using Very Large Array (VLA) radio observations of absorption and emission features in the neutral hydrogen (H I 21 cm line) spectra (Frail & Weisberg 1990; Frail et al. 1991) along with the Galactic rotation curve of Fich et al. (1989). The distances estimated from the pulsar's observed dispersion measure $DM = 301$ cm^{-3} pc (e.g. Frail et al. 1991) is 4.75 kpc (Taylor & Cordes 1993) and 4.85 kpc (Cordes & Lazio 2002), depending on the model used for the Galactic distribution of free electrons, and is in good agreement with those found using the kinematic method. For the analyses in this paper, we adopt the latter distance, where the H.E.S.S. PSF (68% containment radius) of $0.07°$ (∼$5'$) corresponds to a physical size of 6 pc and the pulsar's spin-down flux $\dot{E}/D^2 = 4 \times 10^{32}$ erg s^{-1} kpc^{-2}.

Zou et al. (2005) calculated an upper limit to the transverse velocity of PSR J1832−0827, $V_t < 410$ km s^{-1}, which only poorly constrains the distance over which the pulsar could have traversed from its current position during its lifetime to within $0.78°$ (a physical distance of 67 pc at the distance of the pulsar).

Minter (2008) searched for hydroxyl (OH) absorption in the direction of PSR J1832−0827 with the Green Bank Telescope and found none after 10 h of integration time. In other sources, OH absorption has been observed to arise in the interaction between a molecular cloud and SNR or H II region, so it has the potential to serve as a marker for the presence of hadronic interaction; however, its non-detection for this and ∼94% of the pulsars surveyed suggests that OH absorption toward pulsars is rare or below the detection threshold of surveys with current radio telescopes (Minter 2008).

This γ-ray pulsar candidate was not detected by EGRET (Energetic Gamma Ray Experiment; $E > 100$ MeV) nor OSSE (Oriented Scintillation Spectrometer Experiment; $20 < E < 500$ keV), onboard the *Compton Gamma Ray Observatory* (*CGRO*). McLaughlin & Cordes (2000) reported an upper limit of $F < 1.9 \times 10^{32}$ erg s^{-1} kpc^{-1} in the OSSE energy range versus a predicted flux $F_{\text{predicted}} = 9.1^{+23.2}_{-9.0} \times 10^{24}$ erg s^{-1} kpc^{-1} (assuming $D = 4.75$ kpc, Taylor

& Cordes 1993). It also does not belong the growing class of GeV γ-ray-emitting pulsars detected by *Fermi* (Abdo & for the Fermi LAT collaboration 2009).

It is not the first time that PSR J1832−0827 has been considered as a candidate for TeV γ-ray emission. The HEGRA (High Energy Gamma Ray Astronomy) IACT array, the predecessor of H.E.S.S., selected the pulsar as a target in its early survey of the Galactic plane since it fulfilled the criteria $D < 10\,\text{kpc}$, $P < 1\,\text{s}$, and $\tau_c < 10^6\,\text{yr}$ (Aharonian et al. 2002). After 2.3 h of observations in 1997–1998 with a 4-telescope array, they published an upper limit $F^{99\%}(E > 1.4\,\text{TeV}) < 1.0 \times 10^{-11}\,\text{cm}^{-2}\,\text{s}^{-1}$, equivalent to $\lesssim 75\%$ of the Crab Nebula flux (Aharonian et al. 2002). Deeper observations of this target were not possible due to HEGRA's location in the northern hemisphere (Canary Islands), which severely limits the visibility of the inner Galaxy. Even when visible, the unavoidable large zenith angle results in a correspondingly high energy threshold. The MAGIC (Major Atmospheric Gamma Imaging Cherenkov) IACT also observed the region around PSR J1832−0827 during 20 h of observations of the nearby SNR W 41 (G 23.3−0.3) in 2005 (Albert et al. 2006). Evidence for a γ-ray excess at the location of the pulsar can be seen in their Fig. 3, which shows VHE γ-ray images for three different energy thresholds ($E > 250$, 360, and 590 GeV). There is a suggestive excess at the pulsar location, in particular for $E > 360\,\text{GeV}$, where the statistical significance approaches $\sim 3\,\sigma$; there is no mention of this *hotspot* in their publication, presumably because it is below their detection threshold (Albert et al. 2006).

5.2   VHE γ-ray observations and analysis

5.2.1   H.E.S.S. observations

H.E.S.S. (Chapter 1) observed PSR J1832−0827 and its vicinity over a six-year period from May 2004 to August 2010. The dataset comprises observations from the on-going Galactic Plane Survey (Chapter 2), observations of nearby W 41 (HESS J1834−087), and, more recently, dedicated *wobble*-mode observations to confirm the source detection and increase the level of statistics available for analysis. The latter observations were offset 0.7° from the position of PSR J1832−0827 ($\alpha_{2000} = 18^\text{h}32^\text{m}37.02^\text{s}$, $\delta_{2000} = -08°27'3.64''$). The maximum offset for both observations and individual events to be included in the analysis is set to 3.0°. After selecting only observations where the full four-telescope array was in operation and after applying standard quality selection (Aharonian et al. 2006a) to remove data affected by unstable weather conditions or hardware-related problems, the total live-time of the dataset is ~ 59 h. Many of these observations are significantly offset from PSR J1832−0827, resulting in a mean offset of $1.8 \pm 0.6°$. Since the acceptance to γ-rays diminishes as a function of distance from the camera center, the total live-time reduces to an offset-corrected effective exposure of ~ 25 h. The zenith angle (ZA) also varies from observation to observation and has a mean of $27° \pm 11°$. The ZA strongly influences the minimum energy threshold, which

is a relatively low 0.38 TeV for this analysis.

5.2.2   Analysis methods

The dataset was analyzed using the Hillas second moment method (Hillas 1985) and the
H.E.S.S. standard analysis described in Aharonian et al. (2006a). For γ-hadron separation,
hard cuts were used, which require a minimum of 200 photoelectrons (p.e.) to be recorded
per EAS image. Compared to *standard cuts* (80 p.e.), this relatively strict requirement results
in better background rejection and an improved angular resolution but also in an increased
energy threshold (0.38 TeV for this dataset). The time-dependent optical response of the sys-
tem was estimated from the Cherenkov light of single muons passing close to the telescopes
(Bolz 2004). Two different background estimation procedures (Berge et al. 2007) were used
in this analysis to determine suitable OFF regions.

For 2D image generation and morphological studies, the *ring background method* (Berge
et al. 2007) was used with an inner ring radius of 0.4° and $\alpha = 0.04$. Since this method
includes an energy-averaged model for the camera acceptance to account for the different
offsets of the signal and background regions from the camera center, it was not used for
spectral extraction. The *reflected region background method* (Berge et al. 2007) was instead
used to measure the flux from the putative source.

A circular ON region was used to search for statistically-significant VHE γ-ray emission,
centered *a priori* at the position of PSR J1832−0827 and with a radius of 0.10°, which is the
standard radius used to search for point-like sources in the H.E.S.S. standard analysis. The
same region was used for spectral extraction.

The morphology was investigated by fitting the unsmoothed γ-ray excess image with
a radially-symmetric Gaussian profile ($\phi = \phi_0 e^{-r^2/(2\sigma^2)}$) convolved with the H.E.S.S. PSF
(0.07° for this analysis), within 0.3° of the pulsar position (to avoid the emission from nearby
W 41). The centroid and size (σ, the width of the Gaussian) of the source are then determined
from the best fit.

5.3   Radio observations and analysis

Due to the positional coincidence between HESS J1832−084 and PSR J1832−0827 and the
fact that a large fraction of VHE γ-ray sources are identified as PWN, archival radio data
were obtained from online repositories in order to search for a previously-undetected radio
PWN around PSR J1832−0827.

5.3.1   330 MHz

MAGPIS (The Multi-Array Galactic Plane Imaging Survey) is a meta-survey which comprises observations at multiple frequencies and from multiple telescopes; the bulk of the data are radio observations with the NRAO (National Radio Astronomy Radio Observatory) VLA. Data at 328 MHz was acquired in FITS (Flexible Image Transport System) format from the MAGPIS website[1]. The data is from a ~26-min observation performed on 2 September 2001 with the VLA in the C configuration as part of the Galactic Plane Survey at 90 cm (Helfand et al. 2006). The data were reduced using a 15″ pixel size and have a relatively poor resolution of ~ 70″. More precisely, the HPBW (half-power beamwidth) is defined by a beam major axis $BMAJ = 66''$, minor axis $BMIN = 45''$, and position angle $BPA = 0.00°$. This archival data has been previously CLEANed using the standard software package for radio data calibration and analysis, AIPS (Astronomical Image Processing System). AIPS is further used to determine the integral flux density at this frequency with the tasks FITLD, JMFIT, and TVSTAT. Since the noise (rms) in the image is not constant across the FoV, the noise (i.e. flux density error) is measured only in the vicinity of the PSR J1832−0827 were there are no other visible sources.

5.3.2   1.4 GHz

Four archival datasets are available at 1.4 GHz, from MAGPIS, NVSS (NRAO VLA Sky Survey), and the Effelsberg telescope.

The first MAGPIS dataset comprises a short, ~90-s snapshot observation taken on 23 December 1983 by Dickey et al. (unpublished) with the VLA in the B configuration. This so-called *old GPS 20 cm* data has been re-processed and re-published several times since, most recently by White et al. (2005), who also use an automated source detection algorithm to search the newly reduced images for compact radio sources with flux densities having significances greater than or equal to $5.5\,\sigma$. The catalog does not contain any such sources within 0.1° of PSR J1832−0827. The radio maps are sensitivity-limited to a threshold of ~14 mJ and suffer from highly variable levels of noise along the plane. Extended sources are known to be severely undersampled by high-resolution snapshot observations (White et al. 2005) such as these, which makes them unsuitable for searching for an extended radio nebula in the vicinity of PSR J1832−0827.

The second MAGPIS dataset comprises more recent and higher-quality observations at 1.4 GHz (Helfand et al. 2006). taken with the VLA in multiple configurations in 2000–2001 for a total duration of ~30 min. The archival data have been reduced using a 2″ pixel size, have a relatively good resolution of ~6″, and have been pre-CLEANed. The resulting HPBW is defined by $BMAJ = 6''$, $BMIN = 5''$, and $BPA = 0.00°$. The "human eye-brain detec-

---

[1] http://third.ucllnl.org/gps

tion system" was used in conjunction with the aforementioned automated source detection algorithm to search for discrete point sources and diffuse extended sources (Helfand et al. 2006).

Reduction and analysis of the NVSS and Effelsberg datasets at 1.4 GHz is ongoing and will serve both to cross-check the MAGPIS-derived results and to provide a complementary view oweing to differences in resolution and sensitivity between telescope arrays and observations.

5.3.3 2.7 GHz

Archival observations from the Effelsberg telescope in 2000 have been retrieved but not yet `CLEAN`ed. Efforts are underway to reduce and analyze this dataset.

5.3.4 5 GHz

Two archival datasets are available at 5 GHz, both from MAGPIS.

The first MAGPIS dataset is from the so-called *GPS 6 cm Epoch 1* observations on 23 June 1989 at 4.86 GHz with the VLA in the C configuration. These data have been reprocessed by White et al. (2005), similar to what was done for the older 90 cm observations. Likewise, these data consist of high-resolution but short-duration snapshot observations, which renders the data problematic for all but the most compact radio sources (Helfand et al. 2006). The resulting catalog of high-probability sources does not reveal any discrete sources within $0.1°$ of PSR J1832−0827 (White et al. 2005). The radio maps are sensitivity-limited to a threshold of ∼3 mJ.

The second MAGPIS dataset is from the so-called *GPS 6 cm Epoch 3* observations on 15 March 2005 at 4.86 GHz with the VLA in the B configuration. The data have a $0.6''$ pixel size and a very high resolution of ∼$2''$. More precisely, the HPBW is defined by $BMAJ = 2''$, $BMIN \sim 2''$ and $BPA = 0.00°$. This data also suffers from its short duration and high-resolution, rendering it unsuitable for the analysis of diffuse emission. No bright point sources are visible within the vicinity of PSR J1832−0827.

5.4 Infrared observations

Analysis of the region around PSR J1832−0827 using archival infrared data has also recently begun. In general, infrared observations, used in combination with radio observations, can provide vital information on the nature of HESS J1832−084, since they can be used to differential thermal from non-thermal emission for potential counterparts. As a first step, $24\,\mu m$ MIPSGAL data has been retrieved from MAGPIS in FITS format and visually inspected for evidence of any extended structures which could be associated with PSR J1832−0827

and/or HESS J1832−084. MIPSGAL is an infrared survey of the Galactic plane using the Multiband Infrared Photometer instrument onboard the *Spitzer Space Telescope*.

5.5   X-ray observations

No sensitive X-ray observations in the vicinity of PSR J1832−0827 exist. *ROSAT* observations cover this region but unfortunately do not reveal a nearby source. This is perhaps not surprising since there is significant intestellar absorption in this direction of the sky (Ebisawa et al. 2005), which, combined with the presence of VHE γ-ray emission, would suggest a relatively hard spectrum for any putative source in the X-ray domain. Such a hard source would be difficult for *ROSAT* to detect in its narrow 0.1–2.5 keV energy range. Therefore, X-ray observations which utilize the improved sensitivity and broader energy ranges of the current generation of X-ray telescopes are needed to properly investigate the presence of an X-ray counterpart to HESS J1832−084 and PSR J1832−0827. To that end, observations with *Suzaku* were proposed in response to AO-5 (PI: G. Pühlhofer, 2009), motivated by the marginally point-like nature of the VHE γ-ray emission and its positional coincidence with an atypical pulsar counterpart. The observations were accepted for 20 ks of Priority C observations, which have a ∼50% chance of occuring before March 2011.

5.6   Results

5.6.1   VHE γ-rays

A signal is detected with 75 excess γ-rays in the point-like ON region, corresponding to a a pre-trial statistical significance of ∼7 σ. After conservatively accounting for the trials involved in the search for new sources using the H.E.S.S. GPS (**?**), the post-trial significance is found to be ∼5 σ, confirming the excess as a new source of VHE γ-rays. Figure 5.1 presents an image of the VHE γ-ray excess in the 1° × 1° region around the source, smoothed with a Gaussian of width 0.06° to reduce the appearance of statistical fluctuations. The smoothing radius is chosen to be approximately equal to the H.E.S.S. PSF (0.07°; 68% containment radius) so that resolvable morphological features are visible. The emission appears to be only marginally extended when compared to the PSF, which is depicted in the lower right corner of Fig. 5.1.

The best-fit centroid is located at $\alpha_{J2000} = 18^{\rm h}32^{\rm m}38^{\rm s} \pm 5^{\rm s}_{\rm stat} \pm 5^{\rm s}_{\rm syst}$ and $\delta_{J2000} = -8°25'48'' \pm 72''_{\rm stat} \pm 72''_{\rm syst}$ ($\ell \sim 23.29°, b \sim 0.30°$) and, consequently, the new VHE γ-ray source is designated HESS J1832−084. The pointing precision of the H.E.S.S. telescope array is 20″ (Gillessen et al. 2005), which adds an additional systematic uncertainty. The combined errors are reflected in the size of the cross in Fig. 5.1. The relatively poor quality of the fit ($\chi^2/\rm ndf = 1.4$) is likely due to contamination of the signal from nearby W 41 and/or nearby
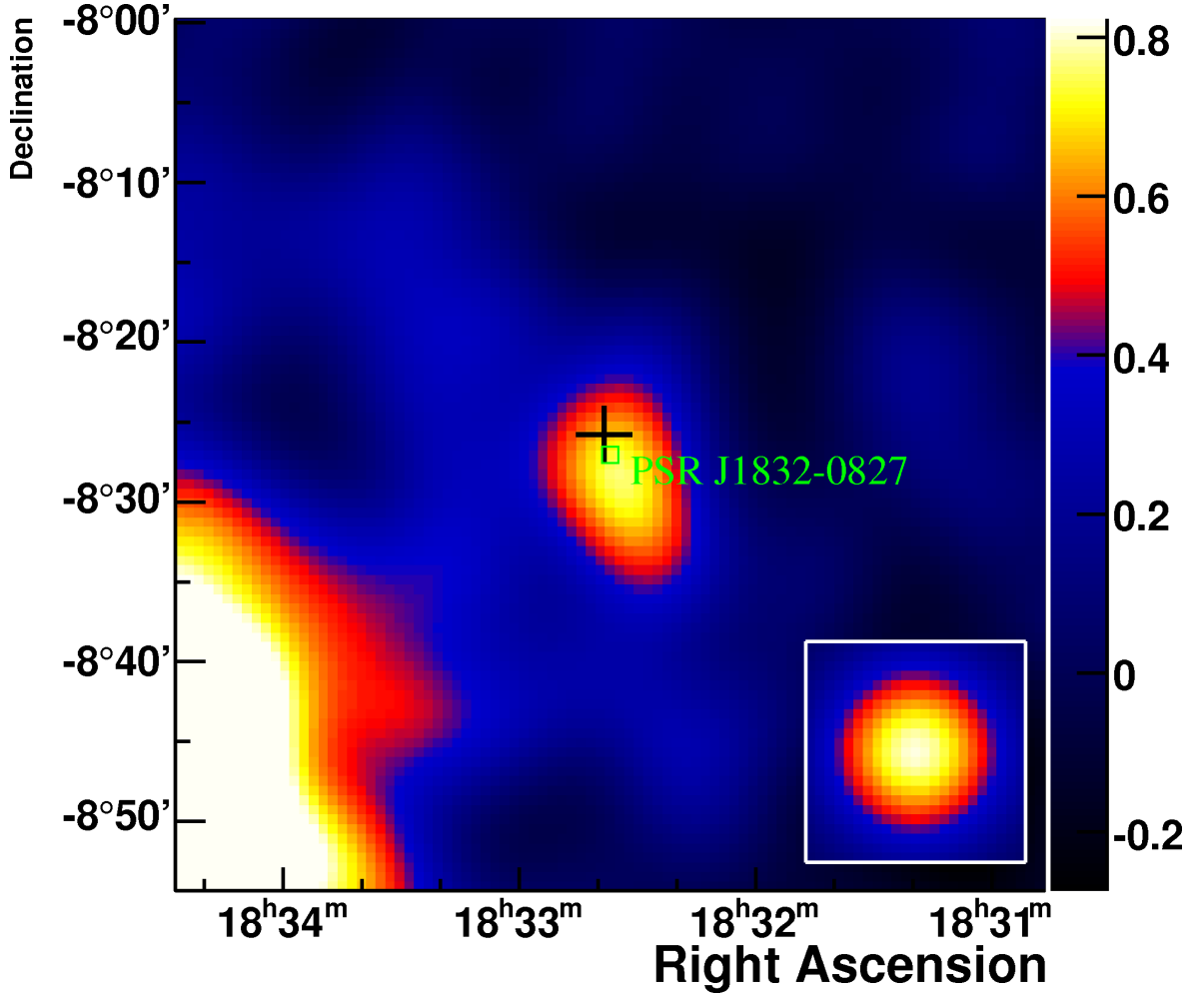
Figure 5.1: Image of the VHE γ-ray excess (in units of γ-rays arcmin^{-2}) from HESS J1832$-$084, smoothed with a 2D Gaussian with a width $\sigma = \text{PSF}/\sqrt{3} = 0.06°$. The blue-to-red color transition is chosen to reduce the appearance of features which are not statistically significant. The black cross is located at the best-fit position of the center-of-gravity of the emission and its size represents the combined statistical and systematic errors of the fit. The position of the pulsar PSR J1832$-$0827 is marked by a green square. The inset in the bottom-right corner shows the H.E.S.S. PSF for this particular dataset. The bright source to the southeast is W 41.

diffuse/unresolved emission and is under investigation. The best fit also returns the source's intrinsic Gaussian width $\sigma = 0.04° \pm 0.01°_{\text{stat}} \pm 0.02°_{\text{syst}}$, only marginally extended beyond the H.E.S.S. PSF ($\sigma = 0.07°$).

The differential energy spectrum is well fit ($\chi^2/\text{ndf} = 1.0$) by a power law $\phi = \phi_0(E/1\,\text{TeV})^{-\Gamma}$ with a relatively steep spectral photon index $\Gamma = 2.8 \pm 0.3_{\text{stat}} \pm 0.2_{\text{syst}}$ and a flux normalization at 1 TeV of $\phi_0 = (3.5 \pm 0.7_{\text{stat}} \pm 0.7_{\text{syst}}) \times 10^{-13}\,\text{cm}^{-2}\,\text{s}^{-1}\,\text{TeV}^{-1}$. The integral flux $F(> 0.38\,\text{TeV}) \approx 6.7 \times 10^{-13}\,\text{cm}^{-2}\,\text{s}^{-1}$, equivalent to ~0.7% of the Crab Nebula flux in the
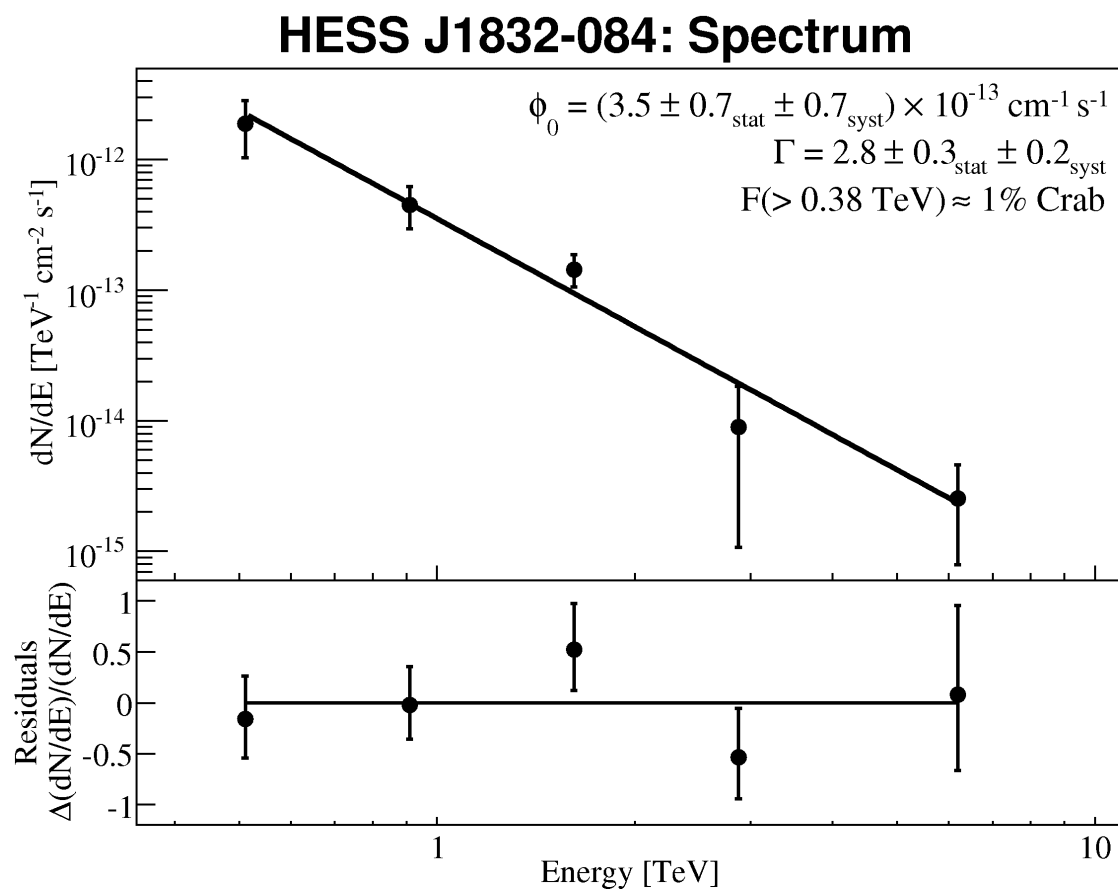
Figure 5.2: Differential energy spectrum of HESS J1832−084, extracted from a point-like region centered on PSR J1832−0827. The solid line shows the result of a power-law fit, and the bottom panel shows the respective residuals. The error bars denote $1\,\sigma$ statistical errors. Events with energies between 0.38 and 10 TeV were used in the determination of the spectrum, with no constraint on the minimum significance per bin.

same energy range. The extracted flux data points from the soft, marginally point-like emission and the fitted power law are shown in Fig. 5.2.

The spectral analysis presented above has been cross-checked, using an independent calibration of the raw data and an alternative analysis chain which uses the powerful `Model++` method for γ-hadron separation (de Naurois & Rolland 2009). The cross-checks confirm the primary results within the stated statistical uncertainties. The discovery-level significance is also verified by the cross-check, although a cross-check of the morphological analysis is pending.

5.6.2 Multi-wavelength

In the field around PSR J1832−0827, there appears to be weak, point-like, radio emission at 328 MHz centered at the pulsar position (Fig. 5.3 *Left*). Fitting the radio continuum emission with a Gaussian confirms its point-like nature with respect to the HPBW (~0.019°) and yields a best-fit position of $\alpha_{\text{J2000}} = 18^h32^m36.8^s \pm 2.2^s_{\text{stat}}$ and $\delta_{\text{J2000}} = -8°27'16'' \pm 34''_{\text{stat}}$, with a position angle of $138° \pm 90°$ with respect to the Galactic plane. This position is compatible with the location of PSR J1832−0827. The best-fit ellipse is shown in Fig. 5.3 *Left*, superimposed on an image of the radio continuum emission. The flux density (integral intensity) S is measured to be 10.4 ± 7.8 mJ at 328 MHz, and the result has been confirmed by an independent analysis. The source appears to be rather weak in this short-duruation observation and is, as a result, difficult to resolve from the background, which is additionally non-uniform across the FoV of the observation. The stated error is therefore conservatively large.

The pulsar PSR J1832−0827 is itself detected at 1.4 GHz (Fig. 5.3 *Middle*) and listed in the MAGPIS Galactic Discrete 20 cm Source Catalog (Helfand et al. 2006) as G 23.27199+0.29805, with an integral flux density of 4.38 mJ. Diffuse emission is also seen in the vicinity of the pulsar and is detected in the MAGPIS Galactic Diffuse 20 cm Source Atlas (Helfand et al. 2006) as G 23.2556+0.2917, with an integral flux density of 334 mJ over a square region $1.7' \times 1.7'$ which encloses the majority of the diffuse source but not the discrete emission from the pulsar itself, which is ~1′ offset from the center of the diffuse region.
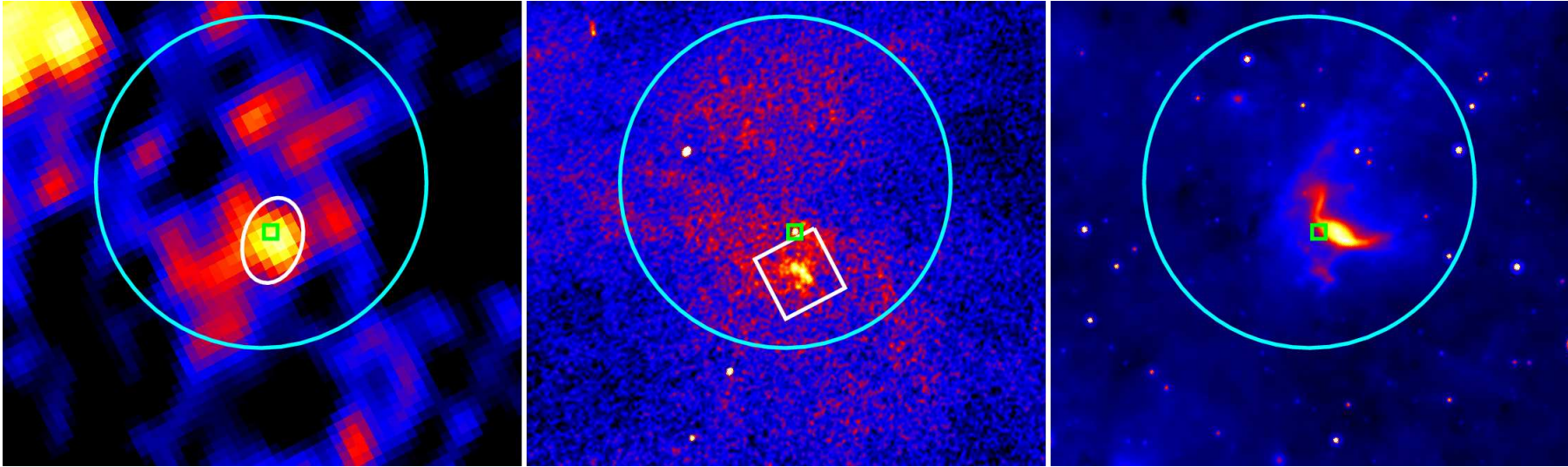
Figure 5.3: Multi-wavelength radio and infrared view in the vicinity of HESS J1832−084 and PSR J1832−0827. The FoV of each panel is approximately $0.22° \times 0.22°$. In all panels, the green square indicates the location of PSR J1832−0827. The cyan circles are centered at the best-fit centroid of HESS J1832−084 and are equal in size to the H.E.S.S. PSF (68% containment radius). *Left*: VLA radio continuum observations at 328 MHz. The white ellipse is centered at the position of the detected point-like radio source and is equal in size to the HPBW of the observations. *Middle*: VLA radio continuum obserations at 1.4 GHz. The white rectangle shows the region from which a diffuse radio source was detected. *Right*: *Spitzer* infrared observations at 24 μm showing an extended infrared structure.

A first glance at the infrared data from *Spitzer* at $24\,\mu$m reveals the presence of a bright, arc-like, extended region of infrared emission (Fig. 5.3 *Right*), coincident with the diffuse radio emission at 1.4 GHz, the pulsar, and the H.E.S.S. source centroid.

5.7 Discussion: H.E.S.S. as a TeV PWN

We investigate here whether the VHE γ-ray emission observed by H.E.S.S. could be explained by a leptonic scenario where the observed γ-rays originate from accelerated electrons which up-scatter ambient photons to VHE γ-ray energies via IC scattering (see e.g. de Jager & Djannati-Ataï 2008). In this scenario, the VHE γ-rays of HESS J1832−084 would originate in a PWN associated with PSR J1832−0827.

5.7.1 Energetics

An important criterion when considering the association of a VHE γ-ray source with the putative PWN of a pulsar is the apparent efficiency ϵ for converting that pulsar's rotational energy into VHE γ-rays, defined as

$$\epsilon \equiv 4\pi D^2 F_{0.3-30\,\text{TeV}}/\dot{E}. \tag{5.2}$$

Based on the spectral analysis presented in the previous section, the extrapolated integral energy flux $F_{0.3-30\,\text{TeV}} \approx 1.1 \times 10^{-12}\,\text{TeV cm}^{-2}\,\text{s}^{-1}$. Thus, for the putative association between PSR J1832−0827 and HESS J1832−084 the required efficiency is $\epsilon \approx 55\%$, which is considerably larger than the efficiencies found for most confirmed or candidate TeV PWNe (Gallant 2007; Gallant et al. 2008, e.g.), for which $\epsilon \lesssim 10\%$. The largest known efficiencies (Gallant et al. 2008) are 7% for the established PWN HESS J1825−137 of PSR B1823−13 and 11% for the PWN candidate HESS J1702−420 of PSR J1702−4128. However, the apparent efficiency only reflects the true efficiency if it is assumed that the emitting particle lifetimes are short compared to the evolutionary timescale of the PWN (Gallant 2007). The electrons responsible for the VHE γ-ray emission may have been injected during earlier phases of the PWN evolution, when the pulsar's $\dot{E}$ was larger; therefore, the apparent efficiency may overestimate the true efficiency.

5.7.2 Age

While relatively young compared to the population of pulsars as a whole (median age $\sim 10^6$ yr), PSR J1832−0827 is older, by a factor of ~ 3 or more (see e.g. Kargaltsev & Pavlov 2010), than most of those pulsars known or suspected to be associated with VHE γ-ray sources via their PWNe. The oldest pulsar which is thought to be associated with a PWN candidate is PSR J1913+1011 (and the TeV emission presumably HESS J1912+101), for which

$\tau_c(n = 3) = 170\,000$ yr, and a few other cases exist with $\tau_c(n = 3) \gtrsim 50\,000$ yr. Interestingly, PSR J1832−0827 is one of only a handful of pulsars for which the braking index n has been (indirectly) measured ($n = 2.5 \pm 0.9$; Johnston & Galloway 1999); nonetheless, the uncertainty in this parameter remains large and a braking index as large as 3.4 can be accomodated, which would imply a corresponding characteristic age as young as $\sim 130\,000$ yr. It is also possible that the characteristic age τ_c itself substantially overestimates the true age of the pulsar, e.g. if the pulsar's initial spin period was only slightly less than its current value or if the n was larger in the past (Manchester & Taylor 1977).

5.7.3   Particle lifetimes

As a PWN evolves and expands over time, its magnetic field strength is expected to decrease as a result of the expansion. The lifetime of the TeV γ-ray-emitting electrons with energy E_{TeV} is dependent on this decreasing magnetic field $B_{\mu G}$ (de Jager & Djannati-Ataï 2008) as

$$\tau(E) \sim 100\,\text{kyr} \frac{1}{1 + \frac{0.144}{B_{\mu G}^2}} \frac{1}{\sqrt{E_{\text{TeV}}}} \tag{5.3}$$

This suggests that for very weak magnetic fields, the lifetime of these 1 TeV γ-ray-emitting electrons could approach $\sim 100\,000$ yr. The steep spectrum of HESS J1832−084 also fits this scenario, where higher-energy electrons would have already cooled, but lower-energy electrons persist. For example, 0.38 TeV γ-ray-emitting electrons could radiate for as long as $\sim 160\,000$ yr. Although the magnetic field strength in this case is unfortunately unknown, these particle lifetimes are marginally compatible with the age of PSR J1832−0827.

5.7.4   Size

Since the VHE γ-ray source coincident with PSR J1832−0827 is observed to be marginally point-like with H.E.S.S., this sets an upper limit to the size of the presumed TeV PWN at ~ 6 pc. The size is compatible with that of other TeV PWNe, which is distributed over a rather wide range of values, from a few parsces to as large as ~ 60 pc (e.g. Kargaltsev & Pavlov 2010). However, based on the presumably long particle lifetimes ($\sim 10^5$ yr), a larger extended TeV PWNe would naively be expected, unless the advection/diffusion speed of the electrons is restricted to $v \lesssim 60\,\text{km s}^{-1}$ on average, e.g. by a dense ambient medium.

5.7.5   MWL evidence

The firm identification of HESS J1832−084 as a TeV PWN depends on the detection of a PWN at lower energies, e.g. in radio, infrared, or X-rays.

The identification of an extended radio source (e.g. Fig. 5.3 *Middle*) as a radio PWN hinges significantly on its having a flat radio spectral index ($\alpha \sim 0$ to -0.3) (Gaensler &

Slane 2006). While diffuse radio continuum emission in the vicinity of PSR J1832−0827 and within HESS J1832−084 has been detected at 1.4 GHz in archival observations, a determination of the spectral index necessarily requires that the flux density be calculated at several frequencies. Unfortunately, the bulk of the archival radio data are high-resolution snapshot observations from Galactic surveys and are unfortunately not suitable for the detection of diffuse emission, although efforts continue to extract as much information as possible from the available data. Although the radio source seen at 328 MHz radio observation (Fig. 5.3 *Left*) partially coincides with the diffuse source seen at 1.4 GHz, the poor resolution of the observation is not sufficient to resolve the discrete emission from the pulsar from any putative extended emission; furthermore, a comparison of the measured flux density $S(\nu = 328\,\mathrm{MHz}) = 10.4 \pm 7.8\,\mathrm{mJ}$ with the ATNF-cataloged flux density (9.4 mJ) at a similar frequency (400 MHz) suggests that this emission is mostly or completely from the pulsar itself. Since analyses are still ongoing at 2.7 GHz and 5 GHz, the only evidence at present for a radio PWN is from the 1.4 GHz observations, and this diffuse radio source cannot be differentiated from an H II region until, e.g. the spectral index is determined.

A quick look at the archival 24 μm infrared data from *Spitzer* has revealed the presence of a bright, extended, arc-like structure which is positionally compatible with the H.E.S.S. centroid, pulsar location, and the diffuse radio source. Infrared emission at 24 μm is typically due to stocastically-heated, very-small dust grains (VSGs). Point-like objects at this wavelength are typically very old, cool stars which are surrounded by a shell composed of VSGs, while extended emission is often associated with stars in the process of forming, i.e. very-young proto-stellar objects which are still gravitationally contracting. However, infrared PWNe may also emit at this wavelength, as in the case of G 54.10.3 (Temim et al. 2010), where 24 μm emission is visible as a diffuse shell just outside of the radio and X-ray PWNe. A comparison with infrared emission at other wavelengths detected with *Spitzer* is underway to follow up this interesting discovery and its implications for the identification of HESS J1832−084 as a PWN.

5.7.6 Chance coincidence

Given the unlikely characteristics (namely $\dot{E}$, $\dot{E}/D^2$, and τ_c) of PSR J1832−0827 in light of the current population of known TeV PWNe, we evaluate the probability that the spatial coincidence between PSR J1832−0827 and HESS J1832−084 is due to a chance alignment. There are 179 pulsars in the ATNF Pulsar Catalog[2] (Manchester et al. 2005) for which $\dot{E} \geq 9.3 \times 10^{33}\,\mathrm{erg\,cm^{-2}\,s^{-1}}$, the spin-down luminosity of PSR J1832−0827, and which are located within the region surveyed by the extended H.E.S.S. Galactic Plane Survey (Chaves & for the H.E.S.S. Collaboration 2009), i.e. a Galactic longitude ℓ between $-85°$ and $60°$ and latitude $|b| \geq 3°$. Using a binned likelihood analysis, the latitudinal distribution of these pulsars

---

[2]v1.40, http://www.atnf.csiro.au/research/pulsar/psrcat

can be fit (equivalent $\chi^2/\text{ndf} = 37.9/24 \approx 1.6$) by a Gaussian with a mean at $b = -0.16°$ and width $0.77°$. The pulsars are then randomly redistributed in ℓ and according to the Gaussian in b, and it is determined whether or not a pulsar is at a distance $d \leq 0.13°$ (the H.E.S.S. PSF plus the statistical uncertainty in the centroid) from PSR J1832−0827; this is repeated 100 000 times. It is thus estimated that the chance probability P that a pulsar within the H.E.S.S. GPS as energetic as PSR J1832−0827 is by chance spatially coincident with HESS J1832−084 is $P = 0.014$ or 1.4%. This is considered highly unlikely at the $\sim$2.4-σ level and, therefore, it is argued that PSR J1832−0827 is likely to be physically associated with HESS J1832−084.

5.8   Conclusions

The VHE γ-ray source HESS J1832−084 is detected with a significance of $\sim$5 σ and the emission is found to be marginally point-like with respect to the H.E.S.S. PSF ($\sim$5′), in contrast to the vast majority of Galactic TeV sources. Its spectrum in the VHE domain is well fit by a power law with a relatively steep photon index $\Gamma = 2.8 \pm 0.3_{\text{stat}} \pm 0.2_{\text{syst}}$. The integral flux from the source is $\sim 1.1 \times 10^{-12}\,\text{cm}^{-2}\,\text{s}^{-1}$ above 0.38 TeV, equivalent to $\sim$1% of the Crab Nebula flux and compatible with an earlier upper limit measured by the HEGRA IACT array.

The centroid of the discovered TeV emission is compatible with the location of the pulsar PSR J1832−0827. However, the apparent conversion efficiency required for the moderately energetic PSR J1832−0827 to power the γ-ray luminosity is $\sim$56%, quite large compared to other known TeV PWNe. The relatively old age of the pulsar ($\sim 10^5$ yr) and its small size when viewed at TeV energies (similar to the H.E.S.S. PSF) also challenge the conventional PWN scenario, as does the lack of a known PWN at lower energies; however, a comprehensive analysis of archival radio and infrared data reveals the presence of positionally-coincident diffuse structures which are under investigation. In order to further study this unique source and search for a PWN associated with PSR J1832−0827, X-ray observations with *Suzaku* are pending and dedicated radio observations will be proposed. Although HESS J1832−084 remains formally unidentified, a chance positional coincidence between PSR J1832−0827 and HESS J1832−084 can be ruled out at the $\sim$2.4 σ level.

Chapter 6

Discovery of VHE γ-ray emission from the direction of W 43

This short chapter presents the H.E.S.S. discovery of very extended VHE γ-ray emission from the direction of the radio complex W 43, which is also a "mini starburst" star-forming region. Recently, a Fermi Bright Source was also discovered in the vicinity. Preliminary results appears here, with minor changes and updates, as previously published (reference below). The introduction and description of the H.E.S.S. telescopes is omitted since it has already been presented in Chapters and 1, respectively.

Chaves, R.C.G., Renaud, M., Lemoine-Goumard, M. & Goret, P. (H.E.S.S. Collaboration)
AIP Conf. Series (Proc. of the 4th Intl. Mtg. on High Energy Gamma-ray Astronomy),
2008, 1085, 372

Abstract

The extended H.E.S.S. Galactic Plane Survey has resulted in the discovery of numerous VHE γ-ray emitting sources. One of the most recent discoveries is HESS J1848−018, which is detected with a post-trial significance of over $5\,\sigma$. HESS J1848−018 is found to be significantly extended with respect to the H.E.S.S. point spread function ($\sim 0.1°$) and has a complex morphology. An extensive search for multi-wavelength counterparts (from radio to X-ray) has found it to be in the direction of, but slightly offset from, the star-forming region W 43, which hosts a giant H II region (G 30.8−0.2), a giant molecular cloud, and the Wolf-Rayet star WR 121a in the main stellar cluster. If HESS J1848−018 is indeed associated with W 43, it would be only the second known case, after Westerlund 2[1], of VHE γ-ray emission asso-

---

[1]Recently, *Fermi* detected a GeV pulsar coincident with the TeV emission observed by H.E.S.S. in the direction of Wd 2, which calls into question its previous identification as a star-forming region and suggests a more standard interpretation as a PWN.

ciated with a star-forming region. We report on the details of this new detection, including a comprehensive analysis of the multi-wavelength data currently available.

We first present the preliminary results of the observations which resulted in the detection of HESS J1848−018 with H.E.S.S.. We then give an overview of the multi-wavelength data, which suggest an association between HESS J1848−018 and the star-forming region W 43. Finally, we briefly consider a possible hadronic origin for the VHE γ-rays due to cosmic ray interaction with a giant molecular cloud (GMC) found in the Boston University-Five College Radio Astronomy Observatory (BU-FCRAO) Galactic Ring Survey (GRS) of ^{13}CO by Jackson et al. (2006). This relatively high-resolution survey overlaps a large portion of the H.E.S.S. GPS region above $l > 18°$ and has revealed a plethora of molecular clouds distributed along the plane of the Galaxy. These molecular clouds are potential counterparts to VHE γ-ray emitters, since they could serve as target material for cosmic rays, thereby producing the VHE photons that are detected from sources like HESS J1848−018.

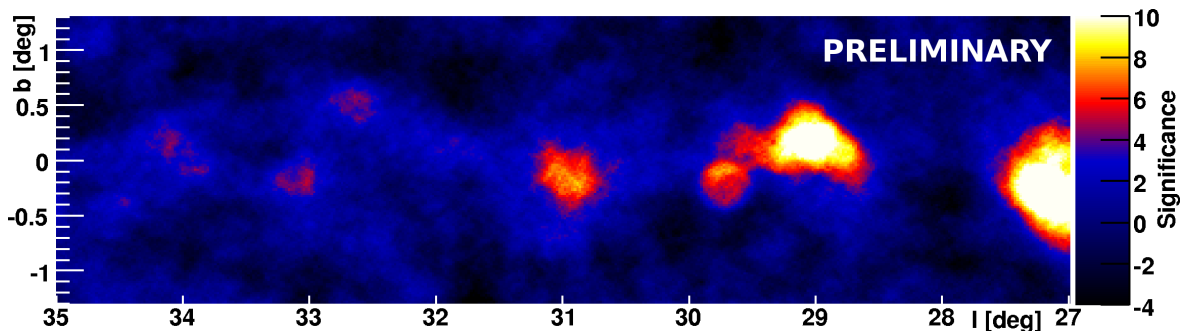## 6.1   H.E.S.S. Observations & Analysis

Figure 6.1: H.E.S.S. image, from the extended H.E.S.S. Galactic Plane Survey (as of Spring 2008; for more recent images, see Chapter 2), of the correlated significance ($\theta = 0.22°$) in the region of the Scutum-Crux spiral arm tangent ($l = 33° \pm 3°$ (Vallée 2008)). HESS J1848−018 is in the center of the image.

The region of interest (see Fig. 6.1) was first targeted during the original H.E.S.S. GPS (Aharonian et al. 2006d). A hotspot of excess VHE γ-rays was detected, and the region was then scheduled for additional targeted observations in August 2007. The combined data set was processed using the standard Survey analysis (a ring background region with a radius of 0.8° and hard cuts, which require a minimum of 200 photo-electrons per shower image for γ-ray selection), as described by Aharonian et al. (2006d), except with a larger on-source region of radius $\theta_{cut} = 0.3°$, which is better suited to this very extended source. An excess with a pre-trial significance of over 9 σ was discovered at $(l, b) \sim (31.0°, -0.16°)$, namely HESS J1848−018.
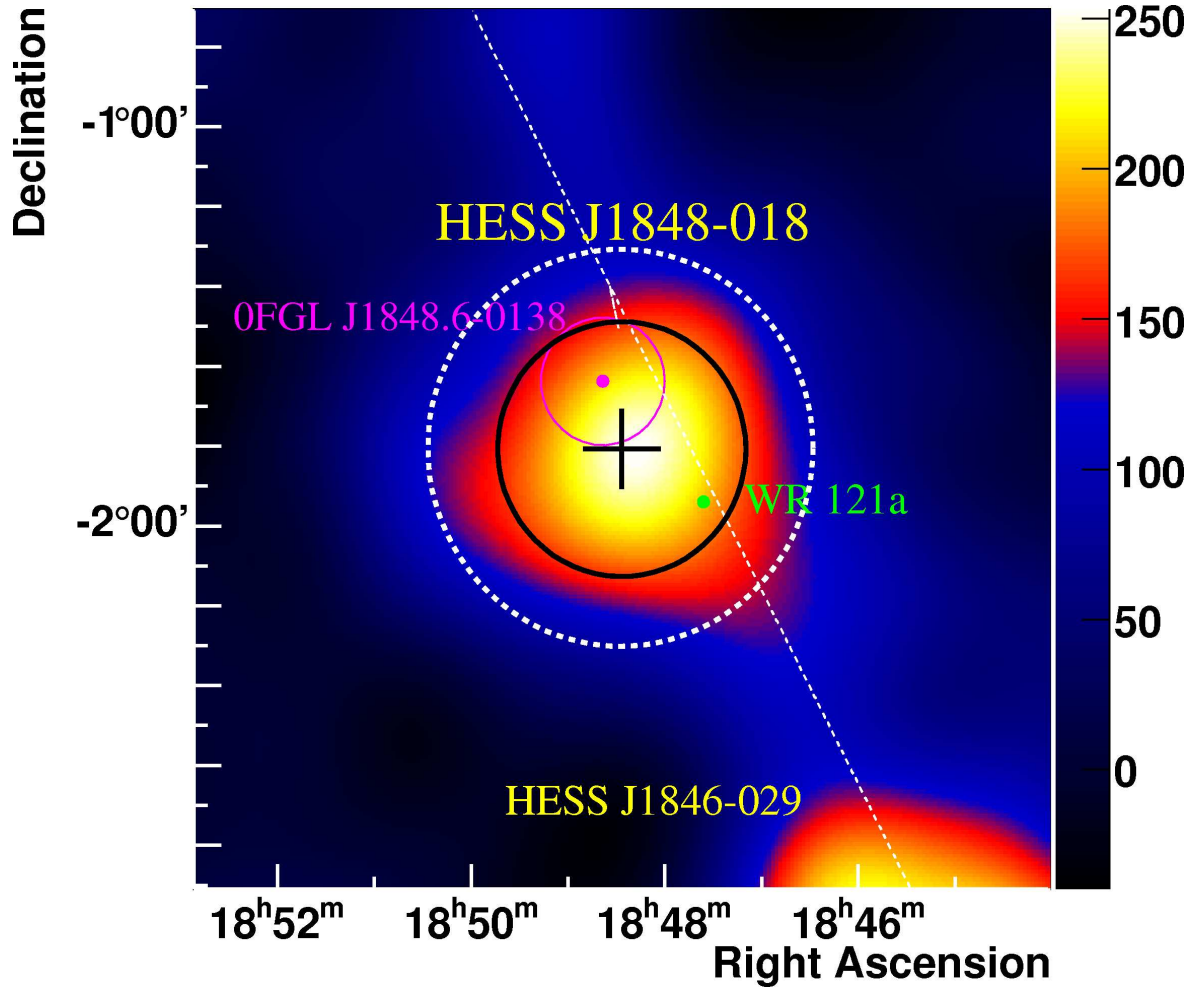
Figure 6.2: H.E.S.S. image of the Gaussian-smoothed ($\theta = 0.30/\sqrt{3} = 0.17°$) γ-ray excess (in units of γ-ray arcmin^{-}2) centered on HESS J1848−018, whose peak significance reaches over 9 σ (pre-trials). The black circle denotes the source's intrinsic rms size of $0.32°\pm 0.02°$, the white dashed circle denotes the $0.5°$ radius region used for spectral analysis, and the white dashed line indicates the location of the Glactic plane. The black cross represents the approximate uncertainty in the source centroid. The location of WR 121a is marked in green while the recently discovered *Fermi* Bright Source 0FGL J1848.6−0138 (Abdo et al. 2009b) is marked in magenta, with the size of the circle representing the uncertainty in the source position (95% confidence level). The bright VHE γ-ray source, HESS J1846−029, in the bottom-right is the supernova remnant Kes 75 (H. E. S. S. Collaboration: A. Djannati-Atai et al. 2007).

After selecting only runs with 4 telescopes which also pass the standard quality criteria (in order to remove data affected by variable weather conditions or hardware issues), the data set has a live-time of ∼50 h at the position of HESS J1848−018. Two independent data analyses, namely the Hillas (Hillas 1985) and Model Combined (**?**) methods, were used to generate sky maps and spectra. Both analyses give consistent results. In the following, only
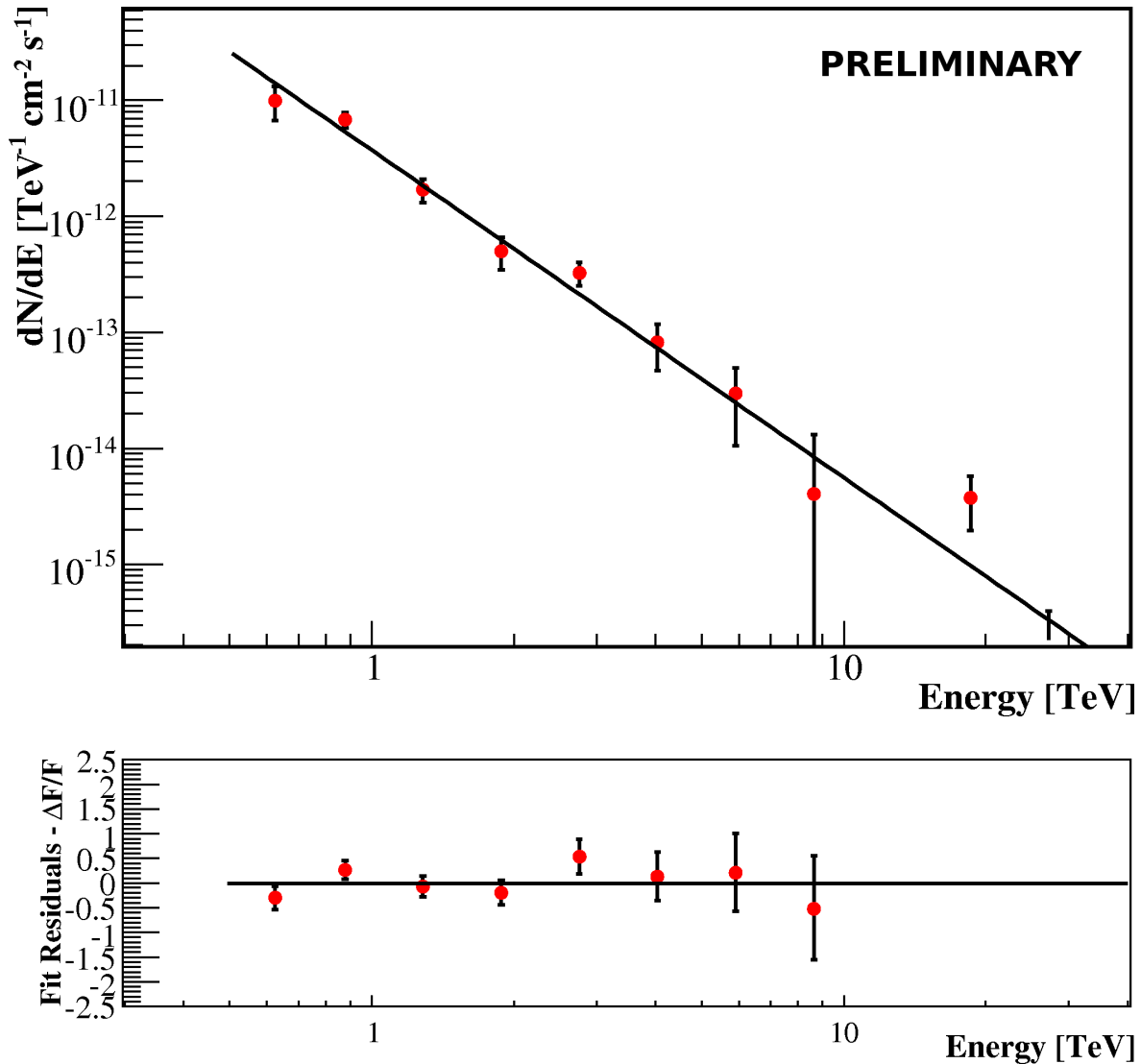
Figure 6.3: Differential energy spectrum of HESS J1848−018 between 0.9 and 12 TeV. The coordinates (J2000) of the spectral extraction region are centered on the fit position, $(l, b) \sim (31.0°, -0.16°)$, and the extraction region has a radius of 0.5°. The data points are fit with a power law with photon index $\Gamma = 2.8 \pm 0.2$ and a normalization at 1 TeV of $(3.7 \pm 0.4_{stat}) \times 10^{-12}\,\text{cm}^{-2}\,\text{s}^{-1}\,\text{TeV}^{-1}$. Its integrated flux above 1 TeV, $\sim 2 \times 10^{-12}\,\text{cm}^{-2}\,\text{s}^{-1}$, corresponds to roughly 8% of the flux from the Crab nebula. The residuals are also shown in the bottom panel. *Erratum*: The originally published integrated flux value was incorrect.

those obtained with the Hillas method are shown. Sky maps (Figs. 6.1, 6.2) were produced with the Ring Background method for background subtraction, while the spectrum (Fig. 6.3) was generated using the Reflected Region Background method (Berge et al. 2007). The discovered excess was found to be significantly extended with respect to the H.E.S.S. point spread function (∼0.1°), with an intrinsic rms size of 0.32° ± 0.02°, after fitting the excess with a 2-dimensional Gaussian.

Figure 6.4: *Left*: BU-FCRAO GRS velocity-integrated (85 to 95 km s^{-1}) image of ^{13}CO emission centered on HESS J1848−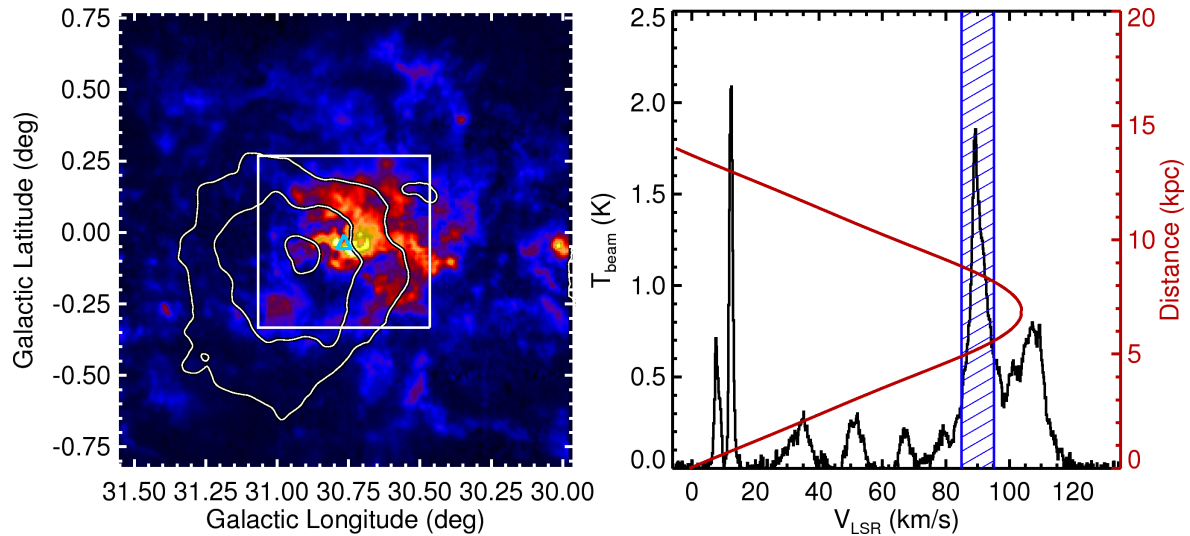018. H.E.S.S. significance contours are overlaid in white at 5, 7, and 9 σ (pre-trials). The position of WR 121a is marked by a cyan triangle. *Right*: Velocity profile of ^{13}CO intensity, integrated over the region delineated by the white square in the left panel. The red curve represents the canonical Galactic rotation curve according to Fich et al. (1989) at the position of HESS J1848−018. The velocity range used to produce the image on the left corresponds to the blue, dashed region.

6.2 Search for Multi-wavelength Counterparts

6.2.1 WR 121a

While searching multi-wavelength catalogs, from radio to X-ray, in the vicinity of HESS J1848−018, no obvious counterparts were initially found. For example, there are no energetic pulsars[2] (Manchester et al. 2005) nor supernova remnants[3] (SNR) (Green 2006) within 0.5°. However, upon inspection of the *VIIth Catalogue of Galactic Wolf-Rayet Stars* (van der Hucht 2001), WR 121a (also W 43 #1) was found at $(l, b) = (30.77°, −0.03°)$, offset from the centroid of HESS J1848−018 by ~0.2° but well within its region of extended emission. WR 121a is located at a distance of ~5.3 kpc (van der Hucht 2001) and is spectrally classified in the WN7 subtype, characterized by extreme mass loss rates (Blum et al. 1999). Its spectrum also hints at the existence of a possible binary companion, but further observations are needed to confirm this.

---

[2]see the *ATNF Pulsar Catalogue* version 1.33, available at `http://www.atnf.csiro.au/research/pulsar/psrcat`

[3]see Green's *Catalogue of Galactic SNRs*, available at `http://www.mrao.cam.ac.uk/surveys/snrs`

6.2.2   W 43

A more detailed search at the position of WR 121a reveals it to be associated with the prominent star-forming region W 43 (Russeil 2003), which is optically obscured but visible in the radio as the Giant H II region G 30.8−0.2 (see e.g. Liszt et al. 1993) as well as in the infrared, e.g. with *Midcourse Space Experiment*[4] (MSX) observations and in the *Spitzer Space Telescope*'s Galactic Legacy Infrared Mid-Plane Survey Extraordinaire[5] (GLIMPSE). The near-infrared observations reveal three separate dust emission sources in the dense, young, stellar cluster at the center of W 43 (Blum et al. 1999). Two of these sources have been identified as O-type supergiants, while the third has been identified as the aforementioned WR 121a. The W 43 star-forming complex is located along the Scutum-Crux spiral arm tangent at a distance of 6.2 ± 0.6 kpc (Russeil 2003).

6.2.3   Molecular Clouds

In addition to hosting WR 121a and the Giant H II region G 30.8−0.2, W 43 also contains $\sim 10^6$ $M_\odot$ of molecular gas (Liszt 1995) which can be seen in BU-FCRAO GRS observations of the ^{13}CO line. This GMC is evident on a velocity-integrated (85 to 95 km s^{-1}) image of ^{13}CO emission centered on HESS J1848−018 (Fig. 6.4). The average kinematic velocity corresponds to a distance of ~ 5 kpc, when adopting a standard Galactic rotation curve (e.g. Fich et al. 1989). The GMC is quite extended, with an apparent size of $\sim 0.5°$, and its centroid is spatially coincident with, but offset ($\sim 0.3°$) from, the centroid of the extended VHE γ-ray emission from HESS J1848−018.

Dense GMCs can provide an effective target for cosmic rays, which can produce VHE γ-rays from π^0-meson decays following pp collisions in the ambient gas of the cloud (Aharonian 1991). The spatial coincidence between HESS J1848−018 and the entire W 43 star-forming region, including the GMC, has prompted an on-going and in-depth look into a variety of potential models which might account for the observed VHE γ-ray emission, as well as the offset between W 43 / WR 121a and the centroid of HESS J1848−018. A similar offset is also observed between the position of the massive Wolf-Rayet binary WR 20a in Wd 2 (Aharonian et al. 2007b) and the VHE γ-ray emission believed to be associated with this young stellar cluster.

6.3   Conclusions

The H.E.S.S. IACT array is very efficient at revealing new, faint, and extended sources of VHE γ-ray emission. Among them, HESS J1848−018 is noteworthy in that it is quite ex-

---

[4]available at `http://irsa.ipac.caltech.edu/data/MSX`
[5]available at `http://irsa.ipac.caltech.edu/data/SPITZER/GLIMPSE`

tended (with an rms size > 0.3°), it is located in the direction of the Scutum-Crux spiral arm tangent, and it appears to be associated with the star-forming region W 43, which encompasses the Giant H II region G 30.8−0.2, the Wolf-Rayet star WR 121a, and a GMC. The association with W 43, if confirmed, would make HESS J1848−018 only the second known VHE γ-ray source to be associated with a star-forming region, after Wd 2 (Aharonian et al. 2007b). Additional observations in the region around HESS J1848−018 are underway in 2008, which could help better resolve the true morphology of the source. While the observed source extension argues against a single-star origin of the observed VHE γ-ray emission, the emission scenarios which may account for this VHE γ-ray emission are still under investigation.

Chapter 7

Deep TeV γ-ray observations of the youngest Galactic SNR G 1.9+0.3 with H.E.S.S.

This focus of this chapter is on potential VHE γ-ray emission from the unique supernova remnant G 1.9+0.3, recently identified as the youngest in the Galaxy, and on which H.E.S.S. has significant exposure due to the Galactic Plane Survey and observations of the nearby Galactic Center. A paper based on this chapter is currently in preparation:

Abramowski, et al. (**H.E.S.S. Collaboration**)

in preparation

Abstract

Context: The age of the shell-type supernova remnant (SNR) G 1.9+0.3 was recently determined to be only ~150 yr, establishing it as the youngest SNR discovered in the Galaxy. SNRs represent one of the most prominent classes of very-high-energy (VHE; $E \gtrsim 0.1$ TeV) γ-ray sources, but little is known about the potential VHE γ-ray emission from SNRs in such an early stage of evolution.
Aims: The goal of this chapter is to investigate whether or not SNR G 1.9+0.3 emits VHE γ-rays at a level detectable by the current generation of imaging atmospheric Cherenkov telescopes (IACTs) and to combine multi-wavelength observations with observations in the VHE domain to constrain the physical properties of G 1.9+0.3.
Methods: The H.E.S.S. IACT array has deeply observed the region of the sky around G 1.9+0.3 over a more than six-year period spanning 2004–2010, largely due to the H.E.S.S. Galactic Plane Survey's extensive and continuing coverage of the nearby Galactic Center, itself well-studied in the VHE domain. Standard VHE γ-ray analysis methods are performed in order to determine the level of VHE γ-ray flux detected from G 1.9+0.3. The flux (or upper limit thereof) can then be compared to other MWL observations of the SNR and to theoretical

expectations.

Results: Unprecedently deep observations of SNR G 1.9+0.3 with the H.E.S.S. array have resulted in a conservative measurement of the upper limit (UL; 99% confidence level) to the integral VHE γ-ray flux above 0.26 TeV of 2.5×10^{-13} cm^{-2} s^{-1}, equivalent to ~0.15% of the Crab Nebula flux (or ~1.5 mCrab) in the same energy range and assuming a spectral index $\Gamma = 2.5$.

Conclusions: Despite H.E.S.S.'s exceptionally long exposure of G 1.9+0.3, the young SNR is not found to be emitting an appreciable amount of VHE γ-rays in its current phase of evolution, in agreement with both hadronic and leptonic models for particle acceleration in SNRs. The resulting UL allows certain SNR properties to be constrained, in particular its distance, which is found to be larger than ~5.7 kpc if one assumes a hadronic scenario for particle acceleration. Predictions for the expected γ-ray flux suggest that a detection of SNR G 1.9+0.3 in the VHE domain will also require deep observations with the future, next-generation CTA Observatory.

7.1   Introduction

Supernova remnants (SNRs) represent the aftermath of the violent and final stages of stellar evolution, where fast-moving ejecta propagate outward from the center of the supernova explosion, in the process sweeping up and shocking the ambient matter. Observations of SNRs in the very-high-energy (VHE; $E \gtrsim 0.1$ TeV) γ-ray domain are especially important because these shock waves are thought to be sites of cosmic ray (CR) acceleration (see e.g. Drury et al. 1994).

Current catalogs of SNRs (Green 2009) are unfortunately incomplete; they suffer from observational selection effects which have made it difficult to detect faint SNRs close to the Galactic Center (GC) as well as young but distant SNRs (see e.g. Green 1991). In 1984, a radio survey using the Very Large Array (VLA) at 4.9 GHz searched for some of these missing SNRs and discovered G 1.9+0.3 (also G 1.87+0.33), identified as an SNR based on its shell-like morphology and non-thermal radio emission. G 1.9+0.3 was found to have a surface brightness $\Sigma \sim 7 \times 10^{-20}$ W m^{-2} Hz^{-1} sr^{-1} (at the reference frequency of 1 GHz) (Green & Gull 1984), less than those of Tycho and Kepler's SNRs, but significantly larger, by a factor of ~20, than that of SN 1006. Its steep radio spectral index was found to be comparable with that of other known shell-type and historical SNRs. The variations in the intensity of the radio emission around the nearly-circular, ~1′-diameter shell was reminiscent of Kepler's SNR (Green & Gull 1984). G 1.9+0.3 had the smallest angular size ever measured for a SNR, already suggesting a young age $\lesssim 10^3$ yr and/or a far distance. It was first included in Green's Catalogue of Galactic Supernova Remnants in 1998.

Recent studies have identified G 1.9+0.3 as the youngest supernova remnant in the Galaxy, using observations at both X-ray (Reynolds et al. 2008) and radio (Green et al. 2008) wave-

Figure 7.1: A composite image of X-ray (orange) and radio (blue) data from NASA's *Chandra X-ray Observatory* and the NRAO Very Large Array, respectively, showing SNR G 1.9+0.3. These images are overlaid on a 2MASS infrared image, which shows stars in the vicinity (yellow and white). *Credit*: X-ray (NASA/CXC/NCSU/S. Reynolds et al.); Radio (NSF/NRAO/VLA/Cambridge/D. Green et al.)

lengths (Fig. 7.1). The *Chandra* X-ray observations permit a measurement of the column density N_H, which suggests G 1.9+0.3 lies close to the GC at a distance of ~8.5 kpc (Reynolds et al. 2008). Although there is still uncertainty in this distance estimate, it is a significant improvement over the estimate of ~ 32.8 ± 13.1 kpc obtained using the $\Sigma - D$ relation (Case & Bhattacharya 1998). This distance estimate would suggest that the SNR actually lies outside of the Galaxy, demonstrating that the $\Sigma - D$ is unreliable for the case of SNR G 1.9+0.3. The new distance estimate, combined with the increase in angular size observed from 1985 to 2007–2008, implies a mean physical radius of ~2 pc and a mean expansion velocity of ~12 000 km s^{-1}. It also allows an age of ~150 yr to be determined, although the true age may be lower if the SNR shock wave wave has undergone deceleration.

With a putative age of ~150 yr, this young, shell-type SNR can serve as a unique astrophysical laboratory for investigating the multi-wavelength (MWL) properties of young SNRs. Observations in different energy regimes can provide valuable information on different aspects of the structure and evolution of SNRs. Numerous shell-type SNRs have been

observed to emit VHE γ-rays, including RX J1713.7−3946 (Aharonian et al. 2007c), Vela Junior (Aharonian et al. 2007d), RCW 86 (Aharonian et al. 2009c), and the two historical SNRs Cas A (~300 yr old Aharonian et al. 2001) and SN 1006 (1006 yr old Acero et al. 2010a). A preliminary detection of a third historical remnant, Tycho's SNR (440 yr old), has also been recently announced (VERITAS). However, it is not yet known whether an SNR as young as G 1.9+0.3 would emit VHE γ-rays already at such an early stage of its evolution.

This chapter presents a thorough overview of the MWL observations of G 1.9+0.3, including an analysis of deep observations performed by H.E.S.S. and a comparison with both previous upper limits (ULs) in the VHE γ-ray domain and with theoretical predictions.

7.2 Multi-wavelength observations

7.2.1 Radio observations

SNR G 1.9+0.3 has been observed in the radio domain numerous times with different instruments and at multiple frequencies (e.g. Green & Gull 1984; Zoonematkermani et al. 1990; Becker et al. 1990; Gray 1994b; Kovalenko et al. 1994; Douglas et al. 1996; Condon et al. 1998; LaRosa et al. 2000; Yusef-Zadeh et al. 2004; Nord et al. 2004; Green et al. 2008; Reynolds et al. 2008; De Horta et al. 2008; Gómez & Rodríguez 2009), even before its identification as an SNR (Clark & Crawford 1974; Caswell et al. 1975; Altenhoff et al. 1979; Douglas et al. 1980; Reich et al. 1984). These multi-frequency radio continuum observations can be used to constrain the SNR's radio spectral index, although care must be taken to use observations which are approximately contemporaneous since many of the flux density measurements are not consistent. The latest determination of the spectral index is $\alpha_s = 0.62 \pm 0.06$ (Green et al. 2008). Furthermore, a comparison of single-frequency observations from different epochs has demonstrated that G 1.9+0.3's brightness is increasing as it ages (Green et al. 2008). A study using observations from 25 epochs from 1988 to 2007 at the same frequency (843 MHz) and using the same telescope (Molonglo Observatory Synthesis Telescope; MOST) has shown the flux density to be increasing at a rate of $1.22^{+0.24}_{-0.16}\%$ yr^{-1}, suggesting that the SNR has been undergoing magnetic field amplification during this period (Murphy et al. 2008).

One of SNR G 1.9+0.3's rare properties is that the brightness of the radio emission from its shell is bipolar in nature, a property which only a handful of SNRs share, including SN 1006 (Fulbright & Reynolds 1990). This bipolar symmetry is particularly strong in G 1.9+0.3 (Fig. 7.1), suggesting that the processes which produce relativistic particles in the SNR are themselves asymmetric (Fulbright & Reynolds 1990). This would have obvious implications for the distribution of any related VHE γ-ray emission from the SNR shell, but unfortunately the current size of the SNR (~1.2′) and the angular resolution of current-generation IACTs like H.E.S.S. (~5′) precludes any morphological studies.

In addition to the radio continuum observations, observations of specific radio emission lines have also been performed. Observations of the H I 21 cm emission line toward SNR G 1.9+0.3 did not reveal the presence of a high-velocity H I shell (Koo & Heiles 1991). Such shells are expected only for older SNRs, e.g. those in the pressure-driven snowplow phase, and its non-detection in the case of G 1.9+0.3 is consistent with early estimates of the SNR's age (400–1000 yr Green & Gull 1984) as well as recent estimates (~150 yr, e.g. Green et al. 2008). Additionally, a signal from the 1720 MHz emission line typically attributed to a hydroxyl OH(1720 MHz) maser was observed; however, the presence of a maser was not confirmed by follow-up interferometric observations, suggesting that the emission is thermal in nature and comes from extended, heated gas with a temperature $15 < T < 40$ K (Green et al. 1997).

7.2.2 Infrared observations

Since the interstellar medium (ISM) is optically thin in the infrared (IR), observations in this energy regime are able to detect thermal emission from SNRs even at large distances and in areas of the Galactic Plane which are otherwise obscured, e.g. near the Galactic Center. The IR emission (radiation losses) from dust grains which are swept-up by an expanding SNR, or which condense out of SNR ejecta, may be large enough to affect the rate at which a SNR evolves (Dwek 1981; Graham et al. 1987). However, radiation losses in the IR appear to be negligible in the case of G 1.9+0.3, which was not detected in the IR during two surveys of Galactic SNRs by the *Infrared Astronomical Satellite* (IRAS) (Arendt 1989; Saken et al. 1992). Upper limits to the IR flux density were set at 2.0 Jy (12 μm), 1.8 Jy (25 μm), 45.0 Jy (60 μm), and 270.0 Jy (100 μm) (Arendt 1989). The total IR flux was found to be less than 7.7×10^{-9} erg s^{-1} cm^{-2} (Arendt 1989).

7.2.3 X-ray observations

SNR G 1.9+0.3 was first detected in the X-ray domain by the *ASCA Observatory* during a survey of the GC region and cataloged as AX J1748.7−2709 (Sakano et al. 2002). It was observed several times from 1995 to 1999 in the 0.7–10 keV band; its flux F_X was found to be 30×10^{-13} erg cm^{-2} s^{-1} and, although not resolved due to *ASCA*'s limited angular resolution, its apparent size in X-rays was constrained to $< 1.5'$, in agreement with its size in the radio (Sakano et al. 2002). The hydrogen column density N_H was estimated to be very high, $\sim 10 \times 10^{22}$ cm^{-2}, ruling out a close distance.

More recent X-ray observations with the *Chandra Observatory* have resolved the shell-like structure of G 1.9+0.3 (Fig. 7.1) and provided the first evidence for the SNR's expansion after X-ray images were compared to radio images taken 13 yr earlier (Reynolds et al. 2008). The observations have also allowed a more accurate measurement of the column density, 5.5×10^{22} cm^{-2}. The X-ray spectrum is featureless and well-described by a synchrotron

model with an exponential cut-off (Reynolds et al. 2008). With a purely synchrotron spectrum in the X-ray domain, G 1.9+0.3 belongs to the small ($n = 5$) class of X-ray-synchrotron-dominated SNRs.

7.2.4 VHE γ-ray observations

The HEGRA system of stereoscopic IACTs was the first to observe SNR G 1.9+0.3 in the VHE γ-ray domain during its survey of the Galactic plane (Aharonian et al. 2002). The SNR is not visibile at favorable zenith angles (θ_{ZA}) from HEGRA's location in the northern hemisphere (Canary Islands, Spain); however, they did observe it for a very short duration of 1.0 h with a minimum energy threshold of 4 TeV. The γ-ray signal had a statistical significance of $-0.2\,\sigma$, and an upper limit (UL; 99% confidence level) was reported, $F(> 4\,\text{TeV}) = 1.90 \times 10^{-11}\,\text{cm}^{-2}\,\text{s}^{-1}$, equivalent to ~8.7 Crab[1].

Further observations with the current-generation IACT H.E.S.S. have also been performed and are presented in the next section.

7.3 H.E.S.S. observations and analysis methods

For more information on the H.E.S.S. telescope array, please see Chapter 1.

Due to deep exposure of the nearby Galactic center (GC) region ~2° away (Aharonian et al. 2004), an unprecedented 219 h of H.E.S.S. observations (live-time) are now available within 3.0° of SNR G 1.9+0.3 in the H.E.S.S. Galactic Plane Survey dataset (Chapter 2). The observation dates span a six-year period from March 2004 to June 2010 and use the standard quality selection (Aharonian et al. 2006a) to exclude observations performed during poor or variable weather conditions. This dataset is one of the largest ever used to search for a VHE γ-ray signal from a source candidate.

The extensive dataset permits very strict data quality selection; for example, since many of the observations are centered near the GC itself and significantly offset from G 1.9+0.3, only those centered within 1.5° of G 1.9+0.3 are retained, in order to reduce the mean angular offset and avoid any potential systematic effects due to G 1.9+0.3 being in outer regions of an overlapping H.E.S.S. FoV. The dataset is further restricted to observations which use the full 4-telescope H.E.S.S. array, such that the final live-time of the dataset amounts to 68 h and has a mean offset ~1.2°. The relatively small mean $\theta_{ZA} = 20°$ also results in a correspondingly low minimum energy threshold of 0.20 TeV for individual γ-rays and a threshold of 0.26 TeV for the cumulative analysis.

---

[1]The flux UL reported by Aharonian et al. (2002) was normalized to the Crab Nebula flux measured by HEGRA. It has been rescaled to the Crab Nebula flux currently measured by H.E.S.S. (Aharonian et al. 2006a), in order to facilitate direct comparisons.

Gamma-hadron separation (Chapter 1) is performed with the Hillas method (Hillas 1985) and *std cuts*, which require each extensive area shower (EAS) image to have an integrated intensity of at least 80 photoelectrons (p.e.) in order for it to be be included in the dataset. Compared to *hard cuts* (200 p.e.), this relatively loose requirement allows the inclusion of fainter EASs, in order to probe the lower-energy part of the VHE γ-ray spectrum. The time-dependant optical response of the IACT system was estimated from the Cherenkov light created by single muons passing close to the telescopes (Bolz 2004).

The *reflected background method* (Berge et al. 2007) was used to measure the flux from an *a priori* determined test region (ON region) which was positioned at the apparent SNR center as observed in radio: $\alpha_{2000} = 17^{\text{h}}48^{\text{m}}45^{\text{s}}$, $\delta_{2000} = -27°10'$ (Green & Gull 1984). Since SNR G 1.9+0.3 has a diameter of ~1′ when observed at both radio and X-ray wavelengths, and since the H.E.S.S. PSF (68% containment) is much larger (~10′ diameter), the test region from which the signal was measured (ON region) was defined as a circle with radius 0.1°, the standard size used to search for point-like sources with H.E.S.S.. Both ON and background (OFF) regions are identical in size and have identical offsets from the camera center, such that they are affected by the radially-varying γ-ray acceptance in the same manner and are therefore appropriate for spectral analysis. Nearby regions with known VHE γ-ray emission, including the diffuse emission near the GC, were excluded from OFF regions in order to avoid contaminating the background estimation.

7.4 H.E.S.S. results

7.4.1 Upper limit

Despite a deep exposure, no statistically-significant VHE γ-ray emission is detected from a point-like region coincident with SNR G 1.9+0.3. The analysis uses events ranging in energy from 0.20 TeV to 51 TeV. The number of ON events $n_{\text{ON}} = 1240$, the number of OFF events $n_{\text{OFF}} = 35015$, and the ratio of the OFF to ON region areas is ~27 ($\alpha = 0.036$). There is thus a negative excess of -33.5 γ-ray events, resulting in a statistical significance of $-0.9\,\sigma$ (Li & Ma 1983).

The results can be used to derive an upper limit (UL) to the integral VHE γ-ray flux F above a given energy threshold E_{th} with a 99% confidence level (CL; Feldman & Cousins 1998). This derivation requires an assumption on the source's spectral slope (photon index; Γ). Figure 7.2 shows the dependency of $F(> E_{\text{th}})$ on E_{th}, beginning with the minimum energy threshold of 0.26 TeV and assuming a Crab Nebula-like spectral index $\Gamma = 2.5$. In this case, the upper limit is found to be $F(E > 0.26\,\text{TeV}) < 2.5 \times 10^{-13}\,\text{cm}^{-2}\,\text{s}^{-1}$, equivalent to 0.15% Crab or 1.5 mCrab in the same energy range. In practice, there is only a weak dependence on the assumed spectral index; for example, assuming $\Gamma = 2.0$ lowers $F(> E_{\text{th}})$ by ~19% while assuming $\Gamma = 3.0$ increases $F(> E_{\text{th}})$ by ~16% (with respect to assuming
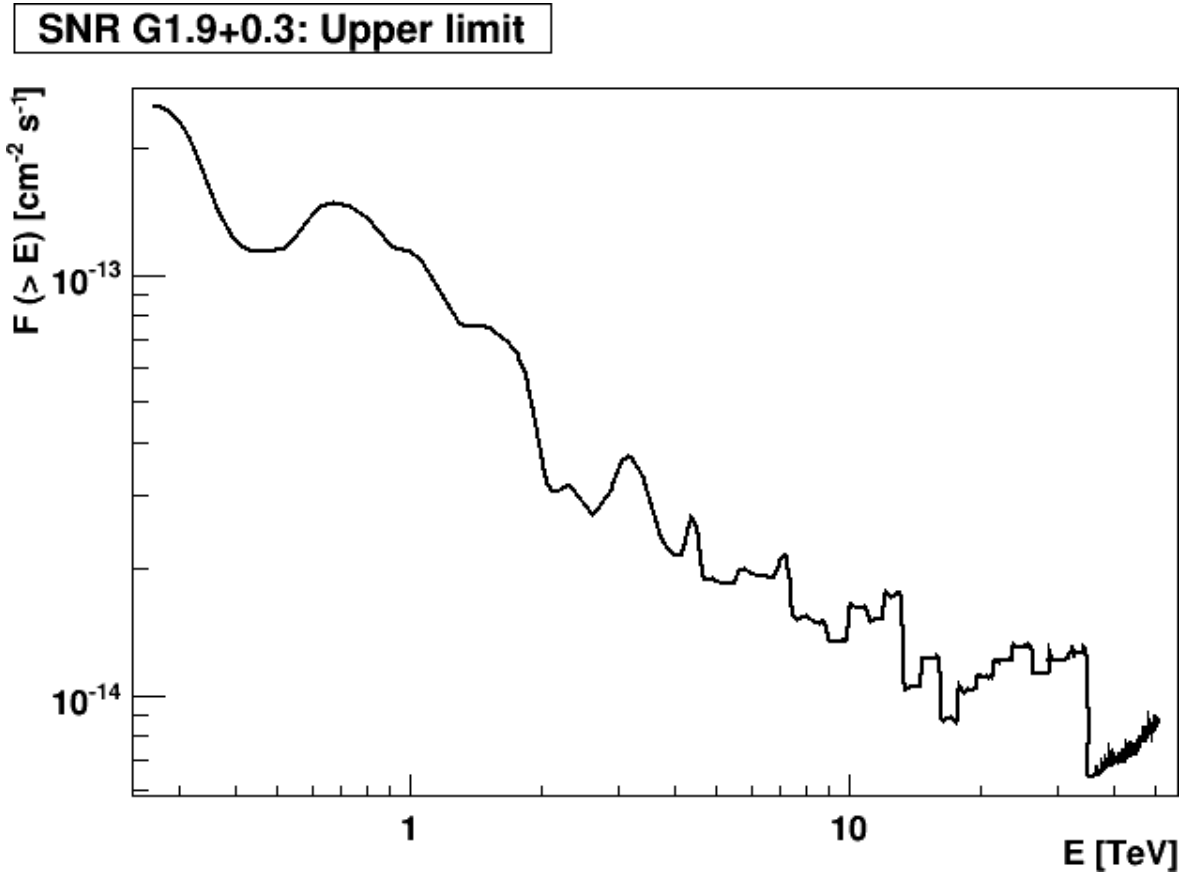
Figure 7.2: Integral flux upper limits (ULs) from a point-like region centered on SNR G 1.9+0.3, as a function of energy threshold E in the VHE γ-ray domain.

$\Gamma = 2.5$).

The spectral analysis has been cross-checked using the alternative `Model++` method for γ-hadron separation (de Naurois & Rolland 2009) as well as an independent calibration of the raw data and quality selection criteria. The resulting upper limit is a less stringent $F(E_{th} > 0.26\,\text{TeV}) < 7 \times 10^{-13}\,\text{cm}^{-2}\,\text{s}^{-1}$. This difference is being investigated and may be related to the negative significance of the signal measured. If it cannot be resolved, the more conservative value will be officially adopted by H.E.S.S.. In the meantime, the preliminary value found with the primary analysis is used throughout this chapter.

7.4.2   Comparison with previous upper limits

In order to compare the newly-derived VHE γ-ray flux UL to that first reported by HEGRA, the H.E.S.S. UL is derived above the same energy threshold as HEGRA and assuming an index $\Gamma = 2.5$. The H.E.S.S. UL is thus $F(E_{th} > 4\,\text{TeV}) = 2.2 \times 10^{-14}\,\text{cm}^{-2}\,\text{s}^{-1}$, equivalent to 1% Crab. Compared to the early HEGRA UL of 8.7 Crab (spectral index assumed unknown), the new H.E.S.S. UL is nearly four orders of magnitude lower (more stringent). This signifi-

cant improvement in sensitivity is not surprising since H.E.S.S. has a superior sensitivity and since the live-time has also increased by a factor of ~70.

The first H.E.S.S. survey of the inner Galaxy ($\ell \pm 30°$; Aharonian et al. 2006d) also provided an rough estimate[2] of the UL to the integral flux above 0.20 TeV in the latitudinal range $|b| < 1.5°$ and averaging over all longitudes surveyed.

The earlier 2004 dataset has a live-time of only 25 h at the position of SNR G 1.9+0.3, using the same quality selection described in the previous section. A re-analysis of this limited dataset, again using the same procedure described in the previous section, results in an upper limit (99% CL) $F(E_{th} > 0.26\,\mathrm{TeV}) < 4.8 \times 10^{-13}\,\mathrm{cm}^{-2}\,\mathrm{s}^{-1}$, equivalent to 0.3% Crab (3 mCrab) in the same energy range. Therefore, a ~2.7-fold increase in live-time has resulted in a flux UL which is approximately two times lower (more stringent).

7.5 G 1.9+0.3 in the context of VHE γ-ray emission scenarios

7.5.1 Hadronic scenario

The H.E.S.S. UL on the γ-ray ($E > 0.26$ TeV) flux from G 1.9+0.3 can now be compared to predictions of the γ-ray flux. In any putative hadronic interactions, π^0 mesons would be created when cosmic-ray (CR) ions accelerated in the SNR collide with the ambient thermal gas, producing γ-ray photons during the resulting π^0 decay. Drury et al. (1994) (hereafter, DAV94) predict the expected γ-ray luminosity above 100 MeV from such a hadronic interaction, which can then be scaled as follows to the H.E.S.S. energy range after taking into account the observed parameters of G 1.9+0.3.

Standard first-order Fermi shock acceleration in the test particle limit predicts a synchrotron photon index $\alpha_s = 0.5$ for strong shocks, although steeper indices are typically observed in young (historical) SNRs. In the case of G 1.9+0.3, Green et al. (2008) measure $\alpha_s = 0.62 \pm 0.06$ using contemporaneous radio observations at 1.45 and 4.86 GHz and assuming the flux density S scales with the frequency ν as

$$S \propto \nu^{-\alpha_s}. \tag{7.1}$$

This value agrees well with $\alpha_S = 0.65 \pm 0.02$ inferred by Reynolds et al. (2008) based on a model fit of X-ray observations with *Chandra* and under the assumption that the radio flux originates from the same population of electrons that produces the X-rays flux, i.e. α_s is the radio-to-X-ray photon index (before steepening). (However, some archival radio

---

[2] *N.B.* The point-source sensitivity in Aharonian et al. (2006d) was reported for a $6.3\,\sigma$ detection, compared to the 99% confidence levels ($2.5\,\sigma$) used in this paper.

observations exhibit steeper indices, see e.g. LaRosa et al. (2000), which are difficult to reconcile.)

The synchrotron index is an important observable parameter since it is related to the γ-ray production rate via the parent CR momentum distribution in SNRs, which is assumed to follow

$$f(p) \propto p^{-\alpha_p}. \tag{7.2}$$

For extreme relativistic energies, the CR particle momentum index

$$\alpha_p = 2\alpha_s + 3. \tag{7.3}$$

Scaling appropriately Eqns. 6–9 of DAV94, the expected γ-ray flux is then:

$$F(> E) \approx 4.4 \times 10^{-7} \left(\frac{q_\gamma(> 1\,\text{TeV})}{q_\gamma(> 100\,\text{MeV})} \right) \left(\frac{E}{\text{TeV}} \right)^{3-\alpha_p} \theta \left(\frac{E_{\text{SN}}}{10^{51}\,\text{erg}} \right) \left(\frac{d}{\text{kpc}} \right)^{-2} \left(\frac{n}{\text{cm}^{-3}} \right) \text{cm}^{-2}\text{s}^{-1} \tag{7.4}$$

where q_γ is the γ-ray emmisivity normalized to the CR energy density, θ is the fraction of total supernova (SN) explosion energy E_{SN} which is converted to CR energy, d is the distance to G 1.9+0.3, and n is the hydrogen atom density of the interstellar medium (ISM). Adopting $\alpha_p = 4.2$ gives $q_\gamma(> 1\,\text{TeV}) = 4.9 \times 10^{-18}$ and $q_\gamma(> 100\,\text{MeV}) = 0.58 \times 10^{-13}$ (from values tabulated in DAV94) and implies that the differential energy spectrum inside the SNR scales roughly as $E^{-2.2}$.

Direct measurements of the ambient gas density around G 1.9+0.3 are unfortunately complicated due to its proximity to the GC, where measurements of the H I 21-cm line become saturated due to the strong radio continuum emission from the GC region. Meas" of molecular matter in ^{12}CO are also hindered by the prohibitively large kinematic distance ambiguity close to the GC. However, the ambient gas density n can be estimated by assuming that the SN that produced G 1.9+0.3 was of Type Ia, which, although not certain, is supported by the high inferred shock velocity $v = 12\,000\,\text{km s}^{-1}$ (Green et al. 2008), the absence of a visible pulsar wind nebula (PWN) at the center of the SNR, and the bilateral symmetry of the X-ray synchrotron emission and spectrum (Reynolds et al. 2008). If the temporal evolution of the forward shock velocity follows a Type Ia model exponential profile (Dwarkadas & Chevalier 1998), then an ambient density $n \approx 3.6 \times 10^{-2}\,\text{cm}^{-3}$ matches the SNR's inferred v and age $t = 150\,\text{yr}$ (Green et al. 2008), for a distance $d = 8.5\,\text{kpc}$, $E_{\text{SN}} = 10^{51}\,\text{erg}$, and ejecta mass $M_{\text{ej}} = M_{\text{Ch}}$. This density is roughly consistant with the hot phase of the ISM and similar to values found for other SNRs (McKee & Ostriker 1977).

The expected γ-ray flux above the same energy threshold ($E > 0.26\,\text{TeV}$) as the H.E.S.S. observations, is then

$$F(E > 0.26\,\text{TeV}) \approx 0.5 \times 10^{-14} \left(\frac{\theta}{0.05} \right) \left(\frac{d}{8.5\,\text{kpc}} \right)^{-2} \left(\frac{3.6 \times 10^{-2}}{\text{cm}^{-3}} \right) \text{cm}^{-2}\text{s}^{-1}, \tag{7.5}$$

equivalent to 0.03 mCrab, adopting a rough estimate for the particle efficiency, $\theta = 0.05$. This is significantly lower than even the new, stringent, H.E.S.S. UL of 1.4 mCrab, here calculated assuming a photon index $\Gamma = 2.2$ for direct comparison. However, it must be noted that there are non-negligible uncertainties in many of the parameters which lead to this prediction, not the least of which is the unknown efficiency θ and the large dependency on the distance d (itself assumed for many of the other parameters such as v and t). Still, it is clear that unless the SNR is significantly closer than the GC (an unlikely possibility due to the large column density N_H observed in X-rays; Reynolds et al. (2008)), the expected γ-ray flux lies well-below the sensitivity of current-generation IACTs and thus remains a challenge for the future CTA (Cherenkov Telescope Array) Observatory (CTA Consortium 2010).

The H.E.S.S. UL can be used to calculate an upper limit to the ambient gas density around G 1.9+0.3 based on the above flux prediction, such that $n\theta < 8.5 \times 10^{-2}\,\mathrm{cm}^{-3}$. Due to the SNR's age and shock velocity, it is safe to assume that it is still in the free expansion phase of SNR evolution and has not yet reached the Sedov-Taylor phase, the onset of which would be nominally associated with an efficiency $\theta \sim 0.1$. This leads to a loose UL on the ambient density $n < 8.5 \times 10^{-1}\,\mathrm{cm}^{-3}$ which is in agreement with the density derived above using the exponential ejecta profile of Dwarkadas & Chevalier (1998). This in turn can be used to estimate an UL on the mass M_{sw} swept-up by the SNR. Since the shock velocity is very high and the SNR is very young, M_{sw} must be much less than the SN ejecta mass M_{ej}, where $M_{ej} \approx 1.44\,M_\odot$ for a Type Ia SN. If the SNR is spherically symmetric, $M_{sw} < (4/3)\pi r^3 n m_H$, where $r = 1.9\,\mathrm{pc}$ is the current radius of the SNR and m_H is the mass of a Hydrogen atom (proton). This suggests that $M_{sw} < 0.6\,M_\odot$, compatible with a Type Ia scenario.

Recently, hadronic predictions for γ-ray emission from G 1.9+0.3 have been revisited by Ksenofontov et al. (2010) in the framework of the non-linear kinetic theory of cosmic ray acceleration in SNRs, under the assumption that G 1.9+0.3 is the result of a Type Ia SN near the GC. This framework also incorporates the gas dynamics of thermal plasma, and assumes that the plasma physics responsible for the temporal dependence on the magnetic field amplification can be extrapolates to such an early evolutionary phase (Ksenofontov et al. 2010).

Ksenofontov et al. (2010) find that the best model-fit suggests the SN is current 80 yr old, compatible with the 150 yr upper limit determined assuming no deceleration has occurred. This recent model predicts a VHE γ-ray flux $F(E = 0.26\,\mathrm{TeV}) = 9 \times 10^{-16}\,\mathrm{TeV}^{-1}\,\mathrm{cm}^{-2}\,\mathrm{s}^{-1}$, approximately three orders of magnitude lower than the H.E.S.S. UL $F(E = 0.26\,\mathrm{TeV}) < 1.2 \times 10^{-12}\,\mathrm{TeV}^{-1}\,\mathrm{cm}^{-2}\,\mathrm{s}^{-1}$ (99% CL; assuming $\Gamma = 2.2$). Furthermore, Ksenofontov et al. (2010) note the strong dependence of this prediction on the distance

$$F \propto d^{-11} \tag{7.6}$$

which arises since the flux is not only proportional to the distance, but also to the column density, shell radius, and velocity, which are themselves also dependent on the distance. This

allows the H.E.S.S. UL to be used to constrain the distance to SNR G 1.9+0.3 to $d > 5.7\,\mathrm{kpc}$ at a 99% confidence level, ruling out nearby distances.

7.5.2 Leptonic scenario

The VHE γ-ray UL can also be compared to predictions from a purely leptonic particle acceleration models as well. For this comparison, a simplified one-zone synchrotron self-Compton (SSC) model (e.g. Aharonian et al. 1997) is adopted, where electrons are accelerated after inverse-Compton (IC) scattering on the cosmic microwave background radiation (CMBR) and nearby radiation fields. The interstellar optical and infrared radiation fields (ISRFs) in the vicinity of the GC are considerably stronger than those in the solar neighborhood and are adopted from recent estimates by Porter et al. (2006). In particle the energy density of infrared radiation ($\lambda = 248\,\mu\mathrm{m}$; $E = kT = 0.005\,\mathrm{eV}$) from dust scattering is $\sim 1.3 \times 10^5\,\mathrm{eV\,m^{-3}}$ while the energy density of optical radiation ($\lambda = 620\,\mathrm{nm}$; $E = kT = 2.0\,\mathrm{eV}$) from ambient starlight is $\sim 8 \times 10^6\,\mathrm{eV\,m^{-3}}$ (Porter et al. 2006).

The electron spectrum is assumed to follow a power law with an exponential cut-off

$$Q_e(E) = Q_0 E^{-\delta} e^{-E/E_{\max}} \tag{7.7}$$

where the electron luminosity Q_0, the electron spectral index δ, and the electron exponential cut-off energy E_{cutoff} are adjustable parameters in the model. However, the *Chandra* X-ray observations of G 1.9+0.3 can be used to determine the electron cut-off energy (Reynolds & Keohane 1999) since

$$E_{\mathrm{cutoff}} = 39 E_{\mathrm{rolloff}}^{1/2} B_{10}^{-1/2}\,\mathrm{TeV} \tag{7.8}$$

where E_{rolloff} is the roll-off energy of the fitted synchrotron X-ray photon spectrum and B_{10} is in units of $10\,\mu\mathrm{G}$. Thus an energy $E_{\mathrm{cutoff}} = 94\,\mathrm{TeV}$ is adopted as in Reynolds et al. (2008). The synchrotron emission is then calculated based on the assumed magnetic field B.

The SSC model is fit to the broad-band spectral energy distribution (SED; Fig. 7.3) of SNR G 1.9+0.3 assuming $d = 8.5\,\mathrm{kpc}$. The parameters are adjusted in order to fit the radio and X-ray measurements of SNR G 1.9+0.3 as well as UL constraints in the infrared and VHE γ-ray domains. The best fit is obtained for the following parameters: $Q_0 = 4 \times 10^{32}\,\mathrm{erg\,s^{-1}}$, $\delta = 2.3$, $E_{\mathrm{cutoff}} = 94\,\mathrm{TeV}$, and $B = 10\,\mu\mathrm{G}$; however, these values do not represent a unique solution and other combinations are possible. Furthermore, the H.E.S.S. UL appears to contradict the prediction for IC emission in the γ-ray regime. A stronger assumed B-field would supress the IC peak but results in a synchrotron peak which is not consistant with the observed radio and X-ray fluxes. The incompatibility of this model with the H.E.S.S. UL is likely due to the oversimplification of the SSC model employed, e.g. the electron spectrum may be better represented by a broken power law as is the case for some SNRs. Further investigation into a leptonic model which fits all observational data is underway.
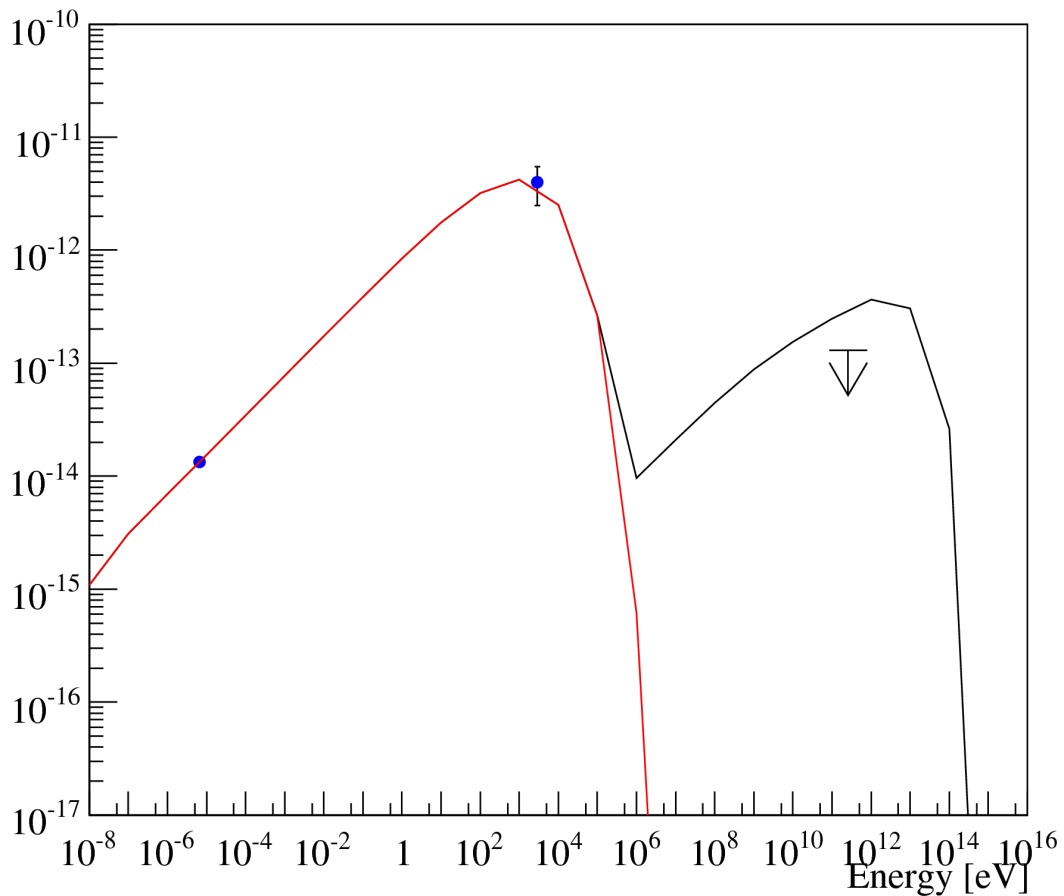
Figure 7.3: Spectral energy distribution of SNR G 1.9+0.3 with a recent VLA radio (Green et al. 2008) measurement, (approximate) *Chandra* X-ray (Reynolds et al. 2008) measurement, and the H.E.S.S. upper limit. A simple synchrotron self-Compton model was fit to the data, where inverse Compton scattering is considered on a target field composed of the cosimc microwave background radiation, starlight, and radiation from dust. The upper limit in the IR domain (Arendt 1989) is out of the range of plotted energy fluxes and is not constraining.

7.6 Conclusions

Until recently, Cas A was the youngest known SNR in the Galaxy, with an age of ~340 yr and a positive detection in the VHE γ-ray domain (Albert et al. 2007a). Recent observations of G 1.9+0.3 have shown it to be significantly younger (~150 yr), begging the question of whether this small, young, shell-type SNR is also a TeV γ-ray emitter. Deep H.E.S.S. observations of the nearby Galactic Center and from the H.E.S.S. Galactic Plane Survey have provided an unprecendented dataset with which to investigate the VHE γ-ray emission from

an SNR at the very early stages of its evolution. Preliminary analysis has yielded an UL (99% confidence level) to the VHE γ-ray flux (above 0.26 TeV) at ~1.5 mCrab.

This stringent UL is approximately four orders of magnitude lower than that previously reported by HEGRA. The dynamic range of almost four orders of magnitude between this new UL and the strongest VHE γ-ray sources observed so far (e.g. AGN outbursts exceeding 10 Crab) highlights both the instrumental capabilities of H.E.S.S. as well as the scientific potential of the large datasets which have resulted from seven years of regularly observing the Galaxy.

The H.E.S.S. UL can be used to set constraints on the ambient density around SNR, its efficiency in converting SN energy to cosmic-ray energy, its magnetic field, and, importantly, its distance, which, assuming a hadronic origin of the γ-rays, must be greater than or similar to 5.7 kpc. Predictions based on hadronic models are still two orders of magnitude lower than the H.E.S.S. UL, suggesting that a detection of SNR G 1.9+0.3 in the VHE regime is out of the reach of the current-generation of IACTs and remains a challenge for the next-generation Cherenkov Telescope Array (CTA).

Chapter 8

A search for VHE counterparts of Galactic *Fermi* bright sources and MeV to TeV spectral characterization

This chapter presents the first study performed to identify plausible VHE γ-ray counterparts of Fermi/*LAT-detected Galactic Bright Sources, based on spatial and spectral data publicly available at the time. It appears here, with minor typographical changes, as published (reference below). The bulk of the paper was written by P.H.T. Tam. I have contributed in particular to the VHE γ-ray side of the analysis and to a substantial revision of the manuscript, relating to both interpretation and language.*

P.H.T. Tam, S. Wagner, O. Tibolla, & **R.C.G. Chaves**
Astronomy & Astrophyiscs, 2010, 518, A8

Abstract

Very-high-energy (VHE; $E > 100\,\mathrm{GeV}$) γ-rays have been detected in a wide range of astronomical objects, such as pulsar wind nebulae (PWNe), supernova remnants (SNRs), giant molecular clouds, γ-ray binaries, the Galactic center, active galactic nuclei (AGN), radio galaxies, starburst galaxies, and possibly star-forming regions. At lower energies, observations using the Large Area Telescope (LAT) onboard *Fermi* provide a rich set of data that can be used to study the behavior of cosmic accelerators in the MeV to TeV energy bands. In particular, the improved angular resolution of current telescopes in both bands compared to previous instruments significantly reduces source confusion and facilitates identification of associated counterparts at lower energies. In this paper, a comprehensive search for VHE γ-ray sources that are spatially coincident with Galactic *Fermi*/LAT bright sources is performed, and the available MeV to TeV spectra of coincident sources compared. It is found that bright LAT GeV sources are correlated with TeV sources, in contrast to previous studies

using EGRET data. Moreover, a single spectral component seems unable to describe the MeV to TeV spectra of many coincident GeV/TeV sources. It has been suggested that γ-ray pulsars may be accompanied by VHE γ-ray emitting nebulae, a hypothesis that can be tested with VHE observations of these pulsars.

8.1 Introduction

Our understanding of the very high-energy (VHE; E >100 GeV) sky has greatly improved during the last few years, thanks to the high sensitivity of current imaging atmospheric Cherenkov telescopes (IACTs), e.g., H.E.S.S., MAGIC, and VERITAS. They typically cover the energy range of ~100 GeV up to several tens of TeV, and provide an angular resolution of ~ 6′. This allows spectral and morphological studies of the various types of VHE sources: pulsar wind nebulae (PWNe), supernova remnants (SNRs), giant molecular clouds, γ-ray binaries, the Galactic center, active galactic nuclei (AGN), radio galaxies, starburst galaxies, and possibly star-forming regions. See Aharonian et al. (2008g) for a review of the field in 2008, with more recent updates given by the H.E.S.S. (Chaves & for the H.E.S.S. Collaboration 2009), MAGIC (Zanin & for the MAGIC collaboration 2009), and VERITAS collaborations (Ong et al. 2009; Weinstein & for the VERITAS Collaboration 2009). However, many of the sources have not yet been identified at other wavelengths; e.g., nearly a third of the Galactic H.E.S.S. sources have no firm identification, and in many cases, there are multiple plausible counterparts while in others, no viable counterparts have been identified.

Gamma-ray observations of Galactic sources can help us solve a number of important astrophysical questions, including (1) the physics of pulsars, PWN, and SNR; and (2) the origin of cosmic rays. Our Galaxy contains several cosmic accelerators, where particles are accelerated to highly-relativistic energies (up to at least 10^{14} eV). The origin of cosmic rays is still not well known, largely because of the lack of directional information of these particles. These very energetic particles can be traced within our Galaxy by a combination of nonthermal X-ray emission and γ-ray emission via leptonic (such as inverse Compton scattering of electrons, Bremsstrahlung and synchrotron radiation) or hadronic (via the decay of charged and neutral pions, due to interactions of energetic hadrons) processes. Therefore, observations of γ-rays at energies $\gtrsim$100 MeV can probe the sources of particle acceleration.

The Large Area Telescope (LAT), onboard the *Fermi Gamma-ray Space Telescope*, provides the best information of the nonthermal sky in the energy range from 20 MeV to 300 GeV. The point-source sensitivity of LAT is ~10^{-8} ph cm^{-2} s^{-1} above 100 MeV in one year of survey-mode observations (Atwood et al. 2009), which is an order of magnitude better than that of its predecessor, the Energetic Gamma Ray Experiment Telescope (EGRET). Its angular resolution is $\lesssim$ 0.6 above 1 GeV, which is particularly important for identifying γ-ray sources with multi-wavelength counterparts and revealing their nature (Atwood et al. 2009). As an important step towards the first source catalog, the LAT collaboration has published

a bright source list (BSL) that includes 205 sources, designated with the prefix 0FGL, using data taken during the first three months of observations (Abdo et al. 2009b). Among them, 121 sources are identified with AGN and one with the Large Magellanic Cloud. Most of the remaining 83 sources are believed to have originated in our own Galaxy. It is natural to investigate which of them also have been detected at energies $\gtrsim$100 GeV.

The search for VHE counterparts of LAT sources is important for the following reasons:

1. it aids the identification of the true nature of the LAT sources through their VHE counterparts;

2. for pulsars, it helps us to identify their VHE-emitting nebulae;

3. it may provide us with broad-band γ-ray spectra, thereby better constraining the emission mechanisms (e.g. distinguish between hadronic and leptonic scenarios).

Funk et al. (2008) compare γ-ray sources in the third EGRET (3EG) catalog (Hartman et al. 1999) and the 22 H.E.S.S. sources known at the time within the region of $l = -30°$ to $30°$, $b = -3°$ to $3°$ (Aharonian et al. 2006d). They do not find any spatial correlation between the two populations. Though some coincidence cases are found, the authors conclude that these few cases can be explained by coincidence. However, thanks to the capabilities of EGRET, this study suffers from the following limitations. (1) The sensitivity of EGRET is lower than that of LAT. The lack of photon statistics leads to poorly constrained spectral indices and the spectra terminate $\lesssim$10 GeV at the upper end for a typical source. (2) EGRET sources are only localized at degree scales, which is much greater than the angular resolution of IACTs. The second point is the instrumental reason, which explains the weak correlation of EGRET and H.E.S.S. sources (Funk et al. 2008). These shortcomings are now largely overcome by the enhanced performance of LAT over EGRET. In addition to the above caveats, they do not consider the extension of the VHE γ-ray sources in their analysis. As such, the full potential of this search has not been realized for very extended sources like the SNR RX J1713.7−3946, as pointed out by Tibolla (2009). After the launch of LAT, one largely benefits from the increased LAT angular resolution over previous studies. As noted in Atwood et al. (2009), EGRET could not distinguish the GeV emission of RX J1713.7−3946 from 3EG J1714−3857, while the capabilities of LAT allow study of individual sources in this region, which contains three VHE γ-ray sources (See Fig. 1 in Aharonian et al. 2008e).

The water Cherenkov detector MILAGRO covers the energies above ~1 TeV, and its angular resolution can reach $< 1°$. Using MILAGRO, a search for γ-rays from the Galactic LAT BSL was performed by Abdo et al. (2009g). They find that 14 sources (of the selected 34) show evidence of multi-TeV γ-ray emission at a significance of $\geq 3\sigma$, although most of the source candidates cannot be established as firm detection on an individual basis (Abdo et al. 2009g).

In this paper, a search for VHE counterparts of all the presumed Galactic sources in Abdo et al. (2009b) and Abdo & for the Fermi LAT collaboration (2009) is performed, with spatial coincidence as the primary criterium for association. The extensions of the VHE γ-ray sources are taken into account, and the search is not limited to the H.E.S.S. Galactic plane survey region. The broad-band MeV to TeV spectra of coincident sources are then presented.

8.2   Search for spatial coincidence

8.2.1   The *Fermi* and VHE catalogs

Abdo et al. (2009b) present 205 point-like sources that were detected at or above the 10-σ level in the 0.2–100 GeV band, based on three months of observations (August 4, 2008 – October 30, 2008). The list is not flux-limited, and so is not uniform. The following information is given for each source: its position, positional uncertainty (95% confidence level, C.L.), significance, flux in two energy bands (100 MeV–1 GeV and 1–100 GeV), and any evidence of variability over the above-mentioned period. In addition, Abdo et al. (2009b) assign the source class for each source, as well as γ-ray and lower energy association (if any). Those sources that are classified as extragalactic (all AGN and the Large Magellanic Cloud) are not considered in this work.

The remaining source list contains 83 sources, comprising 15 radio/X-ray pulsars, 15 pulsars newly discovered by the LAT, two high-mass X-ray binaries (HMXBs), one globular cluster (47 Tucanae), 13 SNR/PWN candidates[1], and 37 sources without obvious counterparts at lower energies (among them the Galactic center; Abdo et al. 2009b). Abdo & for the Fermi LAT collaboration (2009) presents the first LAT pulsar catalog. Those 16 pulsars that are not present in the above BSL are also included in this study. Therefore, most of the LAT bright sources considered in this work should be Galactic in origin.

There are more than 50 VHE γ-ray sources as of Fall 2009 (Aharonian et al. 2008g; Chaves & for the H.E.S.S. Collaboration 2009; Zanin & for the MAGIC collaboration 2009; Ong et al. 2009; Weinstein & for the VERITAS Collaboration 2009). Galactic sources summarized in the above publications are used in the search for coincidence in this work. Therefore, our comparison is only based on published sources. The VHE γ-ray source positions and source extensions in this work have been taken from the corresponding publications shown in Tables 8.2.1, 8.2, and 8.3. At higher energies, the MILAGRO collaboration reported evidence of multi-TeV γ-ray emission from several LAT source positions (Abdo et al. 2009g). Only those source candidates with a significance greater than 5σ are regarded as TeV sources here and are included in this study[2]. With several tens of known sources in both

---

[1]possibly associated with SNR or PWN, but the emission may come from unknown pulsars

[2]For example, HESS J1833−105 (Djannati-Ataĭ et al. 2008) with only a significance of 4.0σ but included in Abdo & for the Fermi LAT collaboration (2009) as a counterpart of LAT pulsar PSR J1833−1034, is not

the GeV and TeV bands, a systematic cross-correlation study can be conducted.

---

considered here.

Table 8.1: 0FGL sources and LAT pulsars with spatially coincident VHE counterpart

LAT source	Association[a]	Class[b]	l (°)	b (°)	Error[c] (°)	VHE γ-ray source	Association[d]	l (°)	b (°)	Extension[e] (°)	References
0FGL J0534.6+2201	Crab	PSR	184.56	−5.76	0.05	HESS J0534+220	Crab nebula	184.56	−5.78	PS	1
0FGL J0835.4−4510	Vela	PSR	263.56	−2.77	0.04	HESS J0835−455	Vela X	263.86	−3.09	0.43	2
0FGL J1418.8−6058		PSR	313.34	0.11	0.07	HESS J1418−609	G313.3+0.1 (Rabbit)	313.25	0.15	0.06	3
PSR J1420−6048		PSR	313.5	0.2	PS	HESS J1420−607	PSR J1420−6048	313.56	0.27	0.07	3
0FGL J1709.7−4428	PSR B1706−44	PSR	343.11	−2.68	0.05	HESS J1708−443[f]	PSR B1706−44?	343.04	−2.38	0.29	4
PSR J1718−3825		PSR	349.0	−0.4	PS	HESS J1718−385		348.83	−0.49	0.015	5
0FGL J1907.5+0602		PSR	40.14	−0.82	0.08	HESS J1908+063		40.39	−0.79	0.34	6
0FGL J2032.2+4122		PSR	80.16	0.98	0.09	TeV J2032+4130		80.23	1.10	0.10	7
0FGL J0617.4+2234		SNR/PWN	189.08	3.07	0.06	VER J0616.9+2230	IC 443	189.08	2.92	0.16	8
0FGL J1615.6−5049		SNR/PWN	332.35	−0.01	0.23	HESS J1616−508	PSR J1617−5055?	332.39	−0.14	0.14	9
0FGL J1648.1−4606		SNR/PWN	339.47	−0.71	0.18	Westerlund 1 region[f,g]		339.55	−0.40	~0.9[h]	10
0FGL J1714.7−3827		SNR/PWN	348.53	0.1	0.13	HESS J1714−385	CTB 37A	348.39	0.11	0.07	11
0FGL J1801.6−2327		SNR/PWN	6.54	−0.31	0.11	HESS J1801−233	W 28	6.66	−0.27	0.17	12
0FGL J1834.4−0841		SNR/PWN	23.27	−0.22	0.1	HESS J1834−087	W 41	23.24	−0.32	0.09	9
0FGL J1923.0+1411	W 51C[i]	SNR	49.13	−0.4	0.08	HESS J1923+141[f]	W 51	49.14	−0.6	~0.15[j]	13
0FGL J1024.0−5754		Unid	284.35	−0.45	0.11	HESS J1023−575	Westerlund 2?	284.19	−0.39	0.18	14
0FGL J1805.3−2138		Unid	8.54	−0.17	0.19	HESS J1804−216	W 30/PSR J1803−2137?	8.40	−0.03	0.20	9
0FGL J1839.0−0549		Unid	26.34	0.08	0.12	HESS J1841−055		26.8	−0.2	0.42	15
0FGL J1844.1−0335		Unid	28.91	−0.02	0.15	HESS J1843−033[f]		~29.08	~0.16	~0.2[j]	16
0FGL J1848.6−0138		Unid	31.15	−0.12	0.16	HESS J1848−018[f]		30.98	−0.16	0.32	17
0FGL J0240.3+6113	LS I +61 303	HMXB	135.66	1.08	0.07	VER J0240+612	LS I +61 303	135.70	1.08	PS	18
0FGL J1826.3−1451	LS 5039	HMXB	16.89	−1.32	0.11	HESS J1826−148	LS 5039	16.90	−1.28	PS	19

Notes. [a] Based on timing information. [b] Source class according to Abdo et al. (2009a). PSR: pulsar; SNR/PWN: supernova remnant/PWN; HMXB: high-mass X-ray binary; Unid: unidentified sources. The classification of those sources as SNR/PWN is based on spatial coincidence only. [c] 95% positional error. [d] Based on spatial coincidence only. [e] An entry of "PS" indicates that the source is point-like with respect to the point spread function of the respective instrument. [f] These recent source discoveries are preliminary and they have been published in the referenced conference proceedings only. [g] The VHE emission has been detected by HESS towards the direction of the massive stellar cluster. The coordinates refer to the nominal position of Westerlund 1. [h] The extent of the source is not clear. The given value is estimated from the radial profile shown in Fig. 4 of the corresponding reference. [i] The association is based on a morphological study (Abdo et al. 2009e). [j] The extent of the source is not clear. The given value is estimated from the sky excess map in the corresponding reference.

References. (1) Aharonian et al. (2006d); (2) Aharonian et al. (2006b); (3) Aharonian et al. (2006g); (4) Hoppe et al. (2009); (5) Aharonian et al. (2007b); (6) Aharonian et al. (2009); (7) Aharonian et al. (2005b); (8) Acciari et al. (2009b); (9) Aharonian et al. (2006f); (10) Ohm et al. (2009); (11) Aharonian et al. (2008b); (12) Aharonian et al. (2008c); (13) Fiasson et al. (2009); (14) Aharonian et al. (2007a); (15) Aharonian et al. (2008d); (16) Hoppe et al. (2008); (17) Chaves et al. (2009b); (18) Acciari et al. (2009a); (19) Aharonian et al. (2006e).

Table 8.2: 0FGL sources with coincident MILAGRO source, but without plausible coincident reported VHE γ-ray sources. See Table 8.2.1 for the nomenclature.

LAT source	Class	l	b	error	MILAGRO source	l	b	extension	references
		(°)	(°)	(°)		(°)	(°)		
0FGL J0634.0+1745	PSR	195.16	4.29	0.04	MGRO C3	195.3	3.8	1.3	Abdo et al. (2009g)
0FGL J2020.8+3649	PSR	75.182	0.131	0.060	MGRO J2019+37	74.8	0.4	~0.1	Abdo et al. (2009g)

Table 8.3: 0FGL sources with a possibly coincident VHE γ-ray source. See Table 8.2.1 for the nomenclature.

LAT source	class	l (°)	b (°)	error (°)	VHE γ-ray source	association	l (°)	b (°)	extension (°)	references
0FGL J1814.3−1739	SNR/PWN	13.05	−0.09	0.19	HESS J1813−178	G12.8−0.2/AX J1813−178	12.81	-0.03	0.04	1
0FGL J1634.9−4737	Unid	336.84	−0.03	0.08	HESS J1634−472		337.11	0.22	0.11	1
0FGL J1741.4−3046	Unid	357.96	−0.19	0.2	HESS J1741−302[a]		358.4	0.01	?	2
0FGL J1746.0−2900	Unid	359.99	−0.11	0.07	HESS J1745−290	Sgr A*/G359.95−0.04	359.94	−0.04	PS	3
0FGL J1836.1−0727	Unid	24.56	−0.03	0.22	HESS J1837−069		25.18	−0.12	7$.\!'$2×3′	1
0FGL J2021.5+4026	PSR	78.23	2.07	0.05	VER J2019+407[a]	γ Cygni SNR?	78.33	2.54	0.16×0.11	4
0FGL J2229.0+6114	PSR	106.64	2.96	0.08	VER J2227+608		106.35	2.71	0.27×0.18	5

Notes. [a] These recent source discoveries are preliminary and they have been published in the referenced conference proceedings only.

References. (1) Aharonian et al. (2006d); (2) Tibolla et al. (2009); (3) Acero et al. (2010b); (4) Weinstein & for the VERITAS Collaboration (2009); (5) Acciari et al. (2009a).

8.2.2 Level of spatial coincidence

To quantify the level of spatial coincidence, the following scheme is employed. Let d be the distance between a centroid position best fit by LAT and the best-fit centroid of a nearby VHE γ-ray source. The radius of the 95% confidence region for the LAT source is the uncertainty on the centroid position of the given LAT source, which is typically $\sim 0°.1$. Most VHE γ-ray sources are extended, with a typical size of $0°.1 - 0°.5$. Let e be the sum of the radius of the 95% confidence region and the size of the VHE γ-ray source.

For each LAT source, if a VHE γ-ray source was found where $d - e < 0$, the source pair is classified as a spatially coincident case (i.e. category Y – yes). Given the possible extended nature of many LAT bright sources, a category P (for possible) is defined for pairs where $0 < d - e < 0.3°$, so that the sources seen by LAT and the VHE instruments may actually overlap, and are possibly coincident cases. If no reported VHE γ-ray source was found with $d - e < 0.3°$, the LAT source falls into the coincidence level N (for no), i.e., no coincidence with any VHE γ-ray source. If there are several nearby VHE γ-ray sources, only the closest VHE γ-ray source would be considered.

8.2.3 Spatial coincidence of GeV/TeV pairs

In the search, 24 coincident cases (Y, among them two are coincident with MILAGRO source only) and 7 possibly-coincident cases (P) are found. The results are presented in Tables 8.2.1, 8.2, and 8.3. No reported VHE γ-ray sources are found in the remaining 68 sources.

According to the nature of the LAT sources, the results are summarized as follows:

1. Eight LAT pulsars are spatially coincident with a source detected using IACTs, which may be the VHE-emitting PWN. There are two additional pulsars that are possibly coincident with an IACT source. Two others have a MILAGRO counterpart, but have not yet been detected by IACTs.

2. Among the 13 SNR/PWN candidates in the *Fermi* BSL, more than half (7) are spatially coincident with a VHE γ-ray source, and another one is a possibly coincident case. The seemingly high fraction of coincidence is partly due to better coverage of the inner Galaxy region, where most SNR/PWN candidates are located. This results in a generally better sensitivity for this class of sources than for other classes.

3. The two HMXBs listed in the BSL (0FGL J0240.3+6113 / LS I +61 303 and 0FGL J1826.3−1451 / LS 5039) are both found to be spatially coincident with a VHE γ-ray source, identified with the same corresponding binary.

4. Five of the 37 unidentified 0FGL sources are spatially coincident with a VHE γ-ray source. The number increases to nine if possibly coincident cases are included.

In addition, we are aware that a new VHE source near PSR J1119−6127 was announced in an oral presentation[3], but it has not been published with any written reference to our knowledge. Given that the best-fit centroid and extension were not given, we do not treat it as an entry in our sample[4].

With such a large number of coincident cases, the relationship between the GeV and TeV sources is explored. In the next section, the γ-ray spectral energy distributions (SEDs) are constructed for those coincident and possibly coincident GeV/TeV source pairs with published VHE spectrum.

8.3 The γ-ray spectral energy distributions

8.3.1 Construction of power-law spectra in the LAT energy range

Abdo et al. (2009b) provide photon fluxes and respective errors in two energy bands: low energy (100 MeV–1 GeV) and high energy ($1 - 100$ GeV). Since photon spectra are not given in the BSL, we attempt to estimate the spectra of individual sources.

Assuming that a single pure power law represents the spectrum in the LAT energy range, the photon flux in the low (10^2–10^3 MeV) and high energy (10^3–10^5 MeV) bands, respectively, are given by

$$F_{23} = k \int_{0.1}^{1} E^{-\Gamma} dE \tag{8.1}$$

and

$$F_{35} = k \int_{1}^{100} E^{-\Gamma} dE, \tag{8.2}$$

where E is measured in GeV, Γ is the photon index, and k the normalization at 1 GeV. Both k and Γ can be calculated from these two expressions. Using the available flux errors (ΔF_{23} and ΔF_{35}), uncertainties in k and Γ (Δk and $\Delta\Gamma$) are obtained by error propagation. The spectra are then constructed in the form of "bowties". For those where F_{23} is given as a 2-σ upper limit, the calculated Γ can be treated as an upper limit, and the reconstructed spectra can be seen as the "softest possible" power-law spectra. The power-law spectra are plotted from 100 MeV up to a certain maximum energy, $E_{\max}$ ($\leq$ 100 GeV), which is defined by requiring that the photon spectrum above $E_{\max}$ contains 10 photons over the three months of

---

[3]See http://cxc.harvard.edu/cdo/snr09/pres/DjannatiAtai_Arache_v2.pdf
[4]In the first LAT catalog, that can be found at http://fermi.gsfc.nasa.gov/ssc/data/access/lat/1yr_catalog/, the authors claim that there is an association of the LAT source 1FGL J1119.4−06127 with a VHE source, designated HESS J1119−614, which may be the same VHE source.

observations[5]. This results in a range of values for E_{max} from ~3 GeV to 100 GeV. The single power-law assumption does not hold in general. Given the limited information available in the BSL, such an assumption should be seen as a very rough estimation of the source spectra and it is used in this work for a visual GeV/TeV spectral comparison. A cut-off between the GeV and TeV bands has been measured for several sources including pulsars. Therefore, we also plot the best-fit spectra when a detailed LAT spectrum is available in the literature (Vela, Crab, Geminga, PSR J1706−44, and LS I +61 303). For the cases of 0FGL J0617.4+2234 and 0FGL J1746.0−2900, the double power-law spectra derived for 3EG J0617+2238 and 3EG J1746−2851, respectively, by Bertsch et al. (2000) are also shown for comparison.

8.3.2   The MeV–TeV SEDs

The sources considered here are those 0FGL/VHE pairs with spatial coincidence levels Y and P and with VHE spectral information available in the literature. For HESS J1923+141 where only a VHE flux is given, a typical spectral index is assumed. In addition, there are two pulsars for which a MILAGRO candidate counterpart is reported but there is no VHE γ-ray detection using IACTs (see Table 8.2).

The SEDs of the 28 cases in the energy range from 100 MeV to >1 TeV are depicted in Figs. 8.1 to 8.9. Systematic errors in spectral indices and normalization are not shown, which for TeV spectra are ~20% for most sources and for GeV spectra are ~20–30% (the latter inferred from flux estimation systematics in Abdo et al. 2009b). An overall inspection of the SEDs immediately shows that single power laws from 200 MeV to ~10 TeV cannot describe most GeV–TeV γ-ray spectra. This is not surprising given the large range in photon energy (i.e. five orders of magnitude), as no photon spectrum from any emission mechanism is expected to be unbroken for such a broad energy span. The only example for which a pure power law may still work is 0FGL J1836.1−0727 / HESS J1837−069, which is a possibly coincident pair (P). The most common board-band behaviors are a cut-off at energies below ~100 GeV (dominating in the pulsar class) and a spectral break between the LAT and the VHE bands (dominating in the unidentified LAT sources).

The SEDs of the LAT source classes including pulsars, SNR/PWN candidates, and unidentified γ-ray sources are presented in this section. LS I +61 303 and the Galactic center region are discussed in Sects. 8.4.5 and 8.4.6, respectively.

8.3.2.1   Pulsars

Figure 8.1 shows the four γ-ray pulsars known in the EGRET era, Fig. 8.2 shows the four radio pulsars first detected in γ-rays by LAT, and Fig. 8.3 shows the three new pulsars after

---

[5]using the LAT on-axis effective area above 1 GeV of ~8000 cm^2 and a mean on-axis exposure of ~1 Ms (Abdo et al. 2009b)
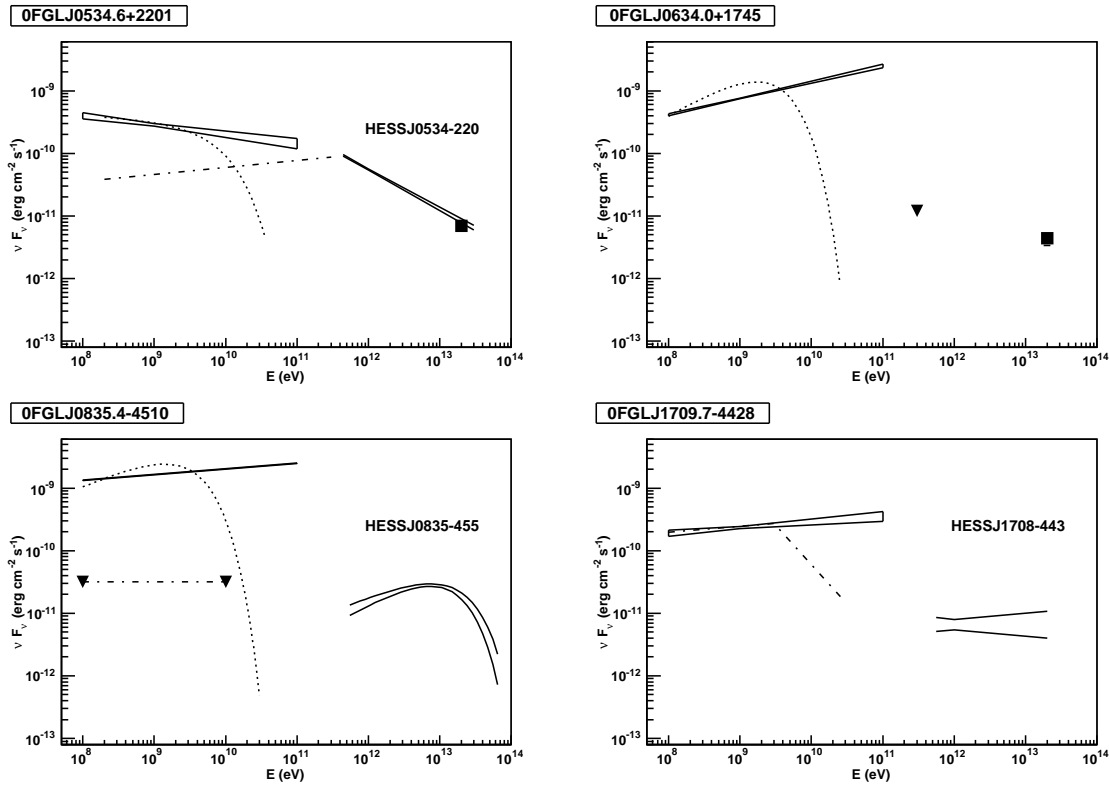
Figure 8.1: MeV to TeV spectra of four EGRET pulsars and their proposed nebulae. *Upper left*: Crab (0FGL J0534.6+2201). The pulsar (dotted line) and nebula (dashed-dotted line) spectral components are those reported in Grondin & on behalf of the *Fermi*-LAT Collaboration (2009). The VHE spectra are taken from Aharonian et al. (2006a), and the MILAGRO measurement at 20 TeV is shown (Abdo et al. 2007). *Upper right*: Geminga (0FGL J0634.0+1745). The pulsar spectrum (dotted line) is the one reported in Celik & on behalf of the *Fermi*-LAT Collaboration (2009). The triangle denotes the upper limit reported in Finnegan & for the VERITAS Collaboration (2009), and the MILAGRO measurement at 20 TeV is also indicated (Abdo et al. 2007). *Lower left*: Vela (0FGL J0835.4−4510). The dotted line represents the Vela spectrum as shown in Abdo et al. (2009f), while the nebula component is constrained by the two triangles joined by the dashed-dotted line. The curved VHE spectrum is taken from Aharonian et al. (2006b). *Lower right*: PSR B1706−44 (0FGL J1709.7−4428). The dashed-dotted line denotes the two power-law model spectra derived in Gargano & on behalf of the *Fermi*-LAT Collaboration (2009). Both LAT energy spectra (though different above 3 GeV) are consistent with the photon flux in the 1–100 GeV band of this source (Abdo et al. 2009b). The VHE spectrum is taken from Hoppe et al. (2009).
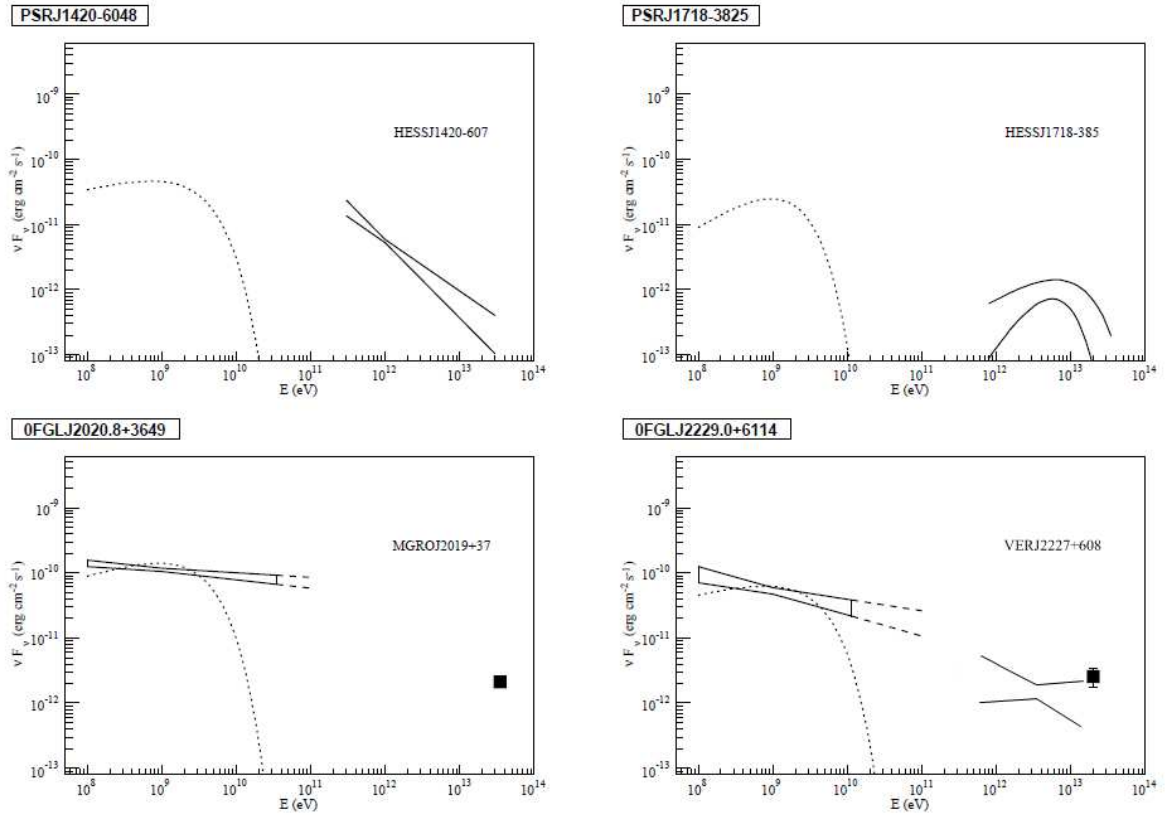
Figure 8.2: MeV to TeV spectra of the four radio pulsars first detected in γ-rays by LAT. The spectra below 300 GeV are taken from Abdo & for the Fermi LAT collaboration (2009). *Upper left*: The VHE spectrum is taken from Aharonian et al. (2006e). *Upper right*: The VHE spectrum presented in Aharonian et al. (2007a) is shown. The two curves represent the upper and lower limits of the spectrum, taking measurement errors into account. *Lower left*: The flux at 35 TeV is taken from Abdo et al. (2009g). *Lower right*: The flux at 20 TeV is taken from Abdo et al. (2007) and the VHE spectrum is taken from Acciari et al. (2009a).

a blind search for pulsations in the LAT data (Abdo et al. 2009a). Besides the Crab, no off-pulse emission is found in the LAT data of the other 10 pulsars, suggesting that most of the emission from pulsars seen with LAT is pulsed and comes from the pulsars themselves. On the other hand, extended regions are seen at energies above 100 GeV in these 10 cases (except for the Crab, which appears point-like to all IACTs). Their VHE emission (>100 GeV) is unpulsed, and for many of them (e.g. Vela X) this emission have been attributed to PWNe, although in some cases other possibilities exist to explain the VHE γ-ray source (e.g. a spatially coincident SNR).

   The SEDs of the pulsars mainly depict the pulsed component in the LAT energy band and the unpulsed component in the VHE band. Previous observations suggest that the emission below and above ~100 GeV mainly comes from two different emission regions, e.g. pulsed emission from the pulsar magnetosphere and unpulsed emission from the PWN. It
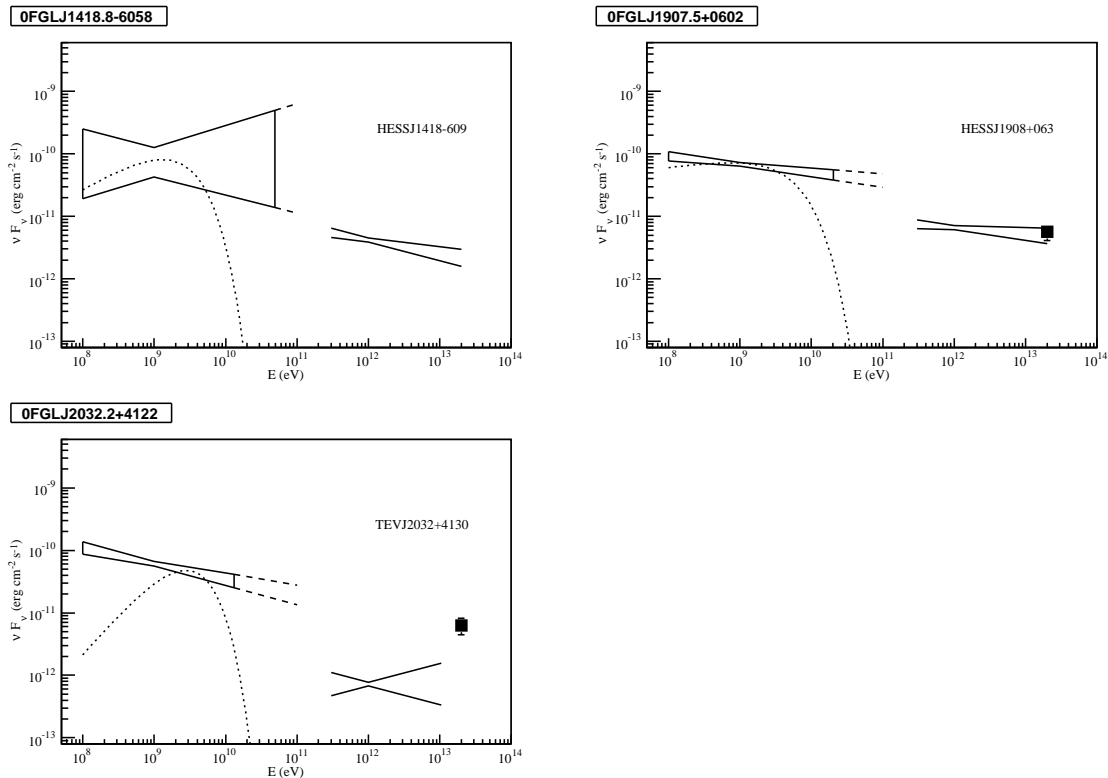
Figure 8.3: MeV to TeV spectra of the three new pulsars discovered in a blind search for pulsation in the LAT data. The spectra below 300 GeV are taken from Abdo & for the Fermi LAT collaboration (2009). *Upper left*: The VHE spectrum is taken from Aharonian et al. (2006e). *Upper right*: The VHE spectrum presented in Djannati-Atai et al. (2008) is shown, together with the coincident MILAGRO source flux at 20 TeV (Abdo et al. 2007). *Lower left*: The VHE spectrum is the one presented in Aharonian et al. (2005a), while the MILAGRO flux at 20 TeV is also shown (Abdo et al. 2007).

can be seen that (1) a cut-off must exist between the LAT "bowties" and the corresponding VHE spectra (with the notable exception of the Crab), which is demonstrated with a detailed spectral study of pulsars (e.g., Abdo & for the Fermi LAT collaboration 2009); (2) the energy output at GeV energies is at least an order of magnitude higher than in the VHE band. This indicates that, for the pulsar population presented in this section, the PWNe radiate less energy than the γ-ray pulse emitting regions.

However, the power-law derived LAT spectra are not always good representations of the reported spectra for individual sources. This is demonstrated in Fig. 8.1 where both the "bowtie" spectra and the derived spectra in Abdo & for the Fermi LAT collaboration (2009) are shown. In all the other cases, only the spectra as presented in Abdo & for the Fermi LAT collaboration (2009) are depicted.

8.3.2.2 SNR/PWN candidates

The SEDs of those 0FGL sources classified as SNR/PWN candidates are shown in Figs. 8.4 and 8.5. The GeV–TeV spectral connection varies among the sources in this class. The TeV spectra are not simply the power-law tails of the GeV spectra. There are cases where the extrapolation of the LAT "bowtie" to TeV energies is at least an order of magnitude higher than the measured VHE flux level (e.g. the spatially coincident case 0FGL J1801.6−2327 / HESS J1801−233, a cut-off occurs between the two energy bands), while for another coincident case (0FGL J1834.4−0841 / HESS J1834−087), the power-law extrapolation to the VHE band is below the measured VHE level and a second spectral component above ~200 GeV is needed to explain the TeV excess.

There is only one case (0FGL J0617.4+2234) where a broken power law describes the LAT spectrum better than a single power law. The "bowties", which are derived *a priori* from power laws, may be closer to the real spectra compared to the case of pulsars. If that is the case for 0FGL J1801.6−2327 / HESS J1801−233 and 0FGL J1923.0+1411 / HESS J1923+141, a spectral break may occur at energies in the largely unexplored energy range of 10–100 GeV for these two sources[6].

8.3.2.3 Unidentified LAT sources

The SEDs of those 0FGL sources without obvious counterparts are shown in Figs. 8.6 and 8.7. There is so far no published spectra of this LAT source class. For the case of 0FGL J1839.0−0549 / HESS J1841−055, the spectrum may span from ~100 MeV to ~80 TeV, with a possible break within or close to the "energy gap" at ~60–500 GeV. If the GeV and TeV sources are indeed associated, they might represent a group of "dark

---

[6]The LAT spectrum for 0FGL J1801.6−2327 is the softest possible power law, while the HESS J1923+141 spectrum is derived assuming a power-law index $\Gamma = 2.8$.

accelerators" which have a broad γ-ray spectrum. All SEDs are consistent with the assumption that a spectral break exists between the two energy bands, except for the case of 0FGL J1805.3−2138 / HESS J1804−216, a spatially coincident case (Y).

8.3.3 Comparison of the flux and photon indices in the GeV and TeV energy bands

A comparison of the flux levels in the GeV and TeV energy bands for coincident GeV/TeV sources (category Y) is depicted. Figure 8.10 shows the photon flux in the 100 MeV – 1 GeV band plotted against the one in the 1–10 TeV band (derived according to Sect. 8.3.1). For most sources, the photon flux in the 1–10 TeV band, $F_{1-10\,\mathrm{TeV}}$, is about 10^{-5} to 10^{-6} the flux in the 0.1–1 GeV band. Figure 8.11 shows the photon flux in the 1–100 GeV band plotted against that in the 1–10 TeV band. For most sources, photon flux in the 1–10 TeV band, $F_{1-10\,\mathrm{TeV}}$, is about 10^{-4} to 10^{-5} of that in the 1–100 GeV band.

Figure 8.12 depicts the photon indices in the 0.1–100 GeV band derived according to Sect. 8.3.1 against the photon index in the 1–10 TeV band. It can be seen that the TeV spectra are similar to or harder than the GeV spectra for most sources, i.e. $0 \lesssim (\Gamma_{1-10\,\mathrm{TeV}} - \Gamma_{0.1-100\,\mathrm{GeV}}) \lesssim 1$.

8.4 Notes on selected sources

Although detailed analysis of the LAT data for each individual source is beyond the scope of this paper, some comments on the following sources are given.

8.4.1 Crab pulsar and nebula

The Crab pulsar and nebula are among the best-studied nonthermal objects in the sky. The pulsed emission above 100 MeV and up to ~10 GeV is clearly detected with LAT. Two strong peaks are seen in the phase histogram. A spectral fit of the pulsed emission using a power law with an exponential cut-off gives a cut-off energy of ~8.8 GeV (Grondin & on behalf of the *Fermi*-LAT Collaboration 2009). There is evidence of pulsed emission up to ~25 GeV, as measured using the MAGIC telescope (see Fig. 8.1, Aliu et al. 2008). The flux reported by MAGIC is consistent with the exponential cut-off in the spectrum measured by LAT.

Evidence of unpulsed emission was already present in the EGRET data (de Jager et al. 1996). The LAT measurement of this component can be well fit by a single power law with $\Gamma \sim 1.9$ up to ~300 GeV. This unpulsed spectrum agrees well with the VHE spectra measured by the IACTs MAGIC, H.E.S.S., and VERITAS (Grondin & on behalf of the *Fermi*-LAT Collaboration 2009). In particular, there appears to be a deviation from a pure power law in the MAGIC spectrum below ~100 GeV (Albert et al. 2008).

8.4.2 Vela pulsar and Vela X

The Vela pulsar is the strongest persistent GeV source and was the first target of LAT observations. The complex pulse profile is dominated by two peaks with a pronounced "bridge" between them. The phase-averaged spectrum, which is essentially the pulsed emission, can be described well by a power law with an exponential cut-off at ~2.9 GeV. The off-pulse emission is much weaker, and a 95% C.L. upper limit of the photon flux of $1.8 \times 10^{-7} \text{cm}^{-2} \text{ s}^{-1}$ is derived at the pulsar position in the 0.1–10 GeV band (shown in Fig. 8.1, Abdo et al. 2009f).

To the south of the pulsar, an extended VHE γ-ray source spatially coincident with the Vela X region, HESS J0835−455, has been detected. The observations represent the first measurement of an SED peak in a VHE γ-ray source (Aharonian et al. 2006b). The power law with exponential cut-off fit of this PWN is reproduced in Fig. 8.1. An analysis of the Vela X region does not establish a nebula component based on the first three months of LAT observations (Lemoine-Goumard et al. 2009).

8.4.3 Geminga

The Geminga pulsar is the first known radio-quiet γ-ray pulsar in the sky (Bertsch et al. 1992). See Fig. 8.1 for its SED. While EGRET data are well fit by a single power law up to 2 GeV (but shows evidence of a cut-off above 2 GeV; Mayer-Hasselwander et al. 1994), the cut-off energy is determined to be ~2.6 GeV using the first seven months of LAT data (Celik & on behalf of the *Fermi*-LAT Collaboration 2009). There appears to be an excess at ~20 GeV when compared to the fit with a power law with exponential cut-off. The reason may be the low statistics or effects of the fitting method, but it might also indicate a separate and harder spectral component (Celik & on behalf of the *Fermi*-LAT Collaboration 2009). There is as yet no evidence of unpulsed emission.

Evidence of multi-TeV emission around the pulsar was reported in the MILAGRO survey of the Galactic plane (Abdo et al. 2007) and in the search for MILAGRO counterparts of *Fermi* sources (Abdo et al. 2009g), using a point source analysis at ~3σ (post-trial) significance levels. Assuming that the emission is extended, the significance increases to 6.3σ at the position of the pulsar. If the detection is real, the size of the MILAGRO emission is ~$2°.6$. At a distance of only ~250 pc, this extent is similar to more distant PWN (Abdo et al. 2009g). On the other hand, VERITAS observations resulted in no detection but rather a 99% C.L. flux upper limit (above 300 GeV) of $2 \times 10^{-12} \text{ cm}^{-2} \text{ s}^{-1}$, assuming point source emission from the pulsar (Finnegan & for the VERITAS Collaboration 2009). Although IACTs suffer from reduced sensitivity when observing very extended source (which scales as θ^{-1} with θ being the extension), observations of Geminga with IACTs are crucial for verifying the MILAGRO claim and helping us to understand the γ-ray emission from Geminga.

8.4.4   PSR B1706−44

Gamma-ray pulsations from PSR B1706−44 were discovered by EGRET; the observations revealed a triple-peaked pulse profile but no evidence of unpulsed emission (Thompson et al. 1996). More recently, the pulsar was also detected by *Fermi*/LAT as the bright source 0FGL J1709.7−4428. The phase-averaged spectra measured by EGRET and LAT are both described well by a broken power law (up to 30 GeV, in the case of the LAT spectrum). The break energy measured by LAT is 3 GeV, while in deriving the EGRET spectrum, it is fixed at 1 GeV (Thompson et al. 1996; Bertsch et al. 2000). The LAT power-law index steepens from a value of ∼1.9 (below 3 GeV) to ∼3.3 (above 3 GeV), as shown in Fig. 8.1. This spectrum and the power-law spectrum derived using the method described in Sect. 8.3.1 are both consistent with the photon flux in the 1–100 GeV band reported in Abdo et al. (2009b).

The discovery of an extended source of VHE emission in the vicinity of PSR B1706−44 was recently reported by H.E.S.S. (Hoppe et al. 2009). The TeV source is quite hard ($\Gamma \sim$ 2.0), more so than the high-energy part of the pulsar spectrum. The VHE γ-ray emission might be related to a relic PWN of PSR B1706−44 and/or to the SNR G343.1−2.3 (Hoppe et al. 2009).

See also Chapter 3.

8.4.5   LS I +61 303

LS I +61 303 is the first X-ray binary where periodic γ-ray emission has been detected at both GeV (Abdo et al. 2009c) and TeV energies (Acciari et al. 2009b; Albert et al. 2009). Its SED is shown in Fig. 8.8. The "bowtie" looks nicely connected to the measured VHE spectrum, but a cut-off energy at ∼6 GeV is reported (Abdo et al. 2009c). Furthermore, the timing measurements in both the GeV and TeV bands show that the maximum emission occurs at different orbital phases, namely, close to periastron for <100 GeV emission and close to apastron for VHE emission. This suggests different emission mechanisms in the two bands, as noted in Abdo et al. (2009c).

8.4.6   Galactic center Region

The Galactic center is among the richest and most complex regions in the Galaxy, owing to the large number of possible sources and the difficulty of correctly modeling the diffuse emission due to cosmic-ray interaction with the local molecular clouds. This problem is extremely relevant at GeV energies, as demonstrated by EGRET measurements. The discovery of new VHE γ-ray sources close to the Galactic center is important for studying the role of diffuse Galactic emission versus the emission from resolved sources in this region (Tibolla 2009).

One GeV source, 0FGL J1746.0−2900, is detected with a significance of 36σ in the neighborhood of the Galactic center. The best-fit position for 0FGL J1746.0−2900 is R.A.= $17^h46^m1\rlap{.}''4$, Decl.= −29°0′18″ (J2000) with a 95% C.L. error radius of 4′ (Abdo et al. 2009b). The H.E.S.S. Collaboration also reports a detection of a source towards the Galactic center, localized at R.A.= $17^h45^m39\rlap{.}''6\pm0\rlap{.}''4$ (stat) $\pm0\rlap{.}''4$ (sys), Decl.= −29°0′22″ ±6″ (stat) ± 6″ (sys) (J2000; Acero et al. 2010b). Based on the procedure described in Sect. 8.2.2, the 0FGL J1746.0−2900 / HESS J1745−290 pair falls into the category of possibly coincident cases. With better photon statistics, one of the fundamental questions that the LAT can hopefully address is whether the GeV and TeV sources are indeed spatially coincident.

The spectra of 0FGL J1746.0−2900 and HESS J1745−290 are shown in Fig. 8.9. The spectra in the two bands do not appear to be described by a single power law, and there seems to be an order-of-magnitude drop-off in the energy range ∼10–100GeV. Although detailed analysis of the LAT data is beyond the scope of this paper, this simple inspection does not indicate that they are from the same emission component (although large uncertainties due to systematics in this region do not permit stronger conclusions at this time). For reference, the broken power-law fit of 3EG J1746−2851 (Bertsch et al. 2000) is also shown in Fig. 8.9.

8.5 Discussion

In this work, the first comparison of the GeV and VHE γ-ray sources after the launch of LAT is presented, which takes the advantage of the significantly improved LAT angular resolution and sensitivity compared to EGRET. Below are a list of preliminary results drawn from this work:

1. With the better localization and morphological information of VHE γ-ray sources compared with 0FGL sources, the nature of the LAT sources may be better revealed through their VHE counterparts. Table 8.2.1 lists the potential counterparts of some VHE γ-ray sources that are coincident with 0FGL sources. For example, HESS J1804−216 may be related to W 30, which may help in understanding the nature of the unidentified source 0FGL J1805.3−2138.

2. Results of several LAT-detected pulsars show cut-offs at energies ∼1–10 GeV, similar to the assessment of Funk et al. (2008) for EGRET-detected pulsar systems. Therefore, a VHE counterpart (∼0.1–10 TeV) of a LAT pulsar most likely represents the associated PWN, with a shell-type supernova as a viable alternative. This is particularly important for those new pulsars discovered by LAT. The VHE counterparts coincident with the six LAT pulsars may be the associated PWN, although other explanations (e.g. shell-type SNR) are also possible. The question of whether typical γ-ray pulsars are accompanied by VHE-emitting nebulae can be tested by observing them in the VHE domain.

3. Through broad-band γ-ray spectra of SNRs, one may in principle distinguish between hadronic and leptonic scenarios. A study of RX J1713.7−3946 using five years of simulated LAT observations (Atwood et al. 2009) shows that the energy flux level for the hadronic scenario differs by around a factor of two from that for the leptonic scenario and that a spectral break may be more prominent for the latter. The SNR sample shown in Figs. 8.4 and 8.5 do not seem to support either scenario, although it is too early to draw any conclusion based on the three-month 0FGL dataset. If a hadronic scenario is found to be more viable, this would support the current hypothesis that shell-type SNRs are cosmic-ray sources.

4. Previous studies did not reveal a strong correlation between the GeV/TeV populations. Reimer et al. (2008) list 16 H.E.S.S. sources without counterparts from the 3EG catalog. Among them, new associations are found in the present study and are presented in Table 8.4, thanks mostly to the discovery of new GeV sources with LAT. Reimer et al. (2008) also present 11 sources in the 3EG catalog without H.E.S.S. counterpart. Among them, 0FGL J1709.7−4428 (the 0FGL counterpart of 3EG J1710−4439; Abdo et al. 2009b) is now found to be associated with HESS J1708−443, a source discovery reported in Hoppe et al. (2009).

5. All spatially coincident GeV and TeV pairs during the EGRET era are essentially consistent with one single spectral component (see Figs. 4–6 in Funk et al. 2008). With the significantly enhanced sensitivity of LAT, new relations between the GeV and TeV spectra are apparent in the SEDs. The SNR candidate 0FGL J1834.4−0841 and the unidentified 0FGL J1805.3−2138 (and their likely VHE counterparts) represent the first examples for which the GeV/TeV spectrum cannot be treated as a single emission component. A similar conclusion is reached by Abdo et al. (2009c) for an HMXB (LS I +61 303), based on the light curves and spectral incompatibility of this source in the two bands.

6. Abdo et al. (2009g) consider a probability that many unidentified LAT sources are extragalactic, so as to explain the low rate of finding coincident MILAGRO emission among the unidentified LAT sources. This idea might also explain the nondetection of VHE counterparts of a majority of the unidentified LAT sources. On the other hand, the extended nature of all the five spatially coincident cases (HESS J1023−575, HESS J1804−216, HESS J1841−055, HESS J1843−033, HESS J1848−018; if proved to be real association) would exclude an extragalactic origin of the corresponding LAT sources.

7. Although VHE observations only cover a small part of the whole sky, they do cover the majority of the inner Galaxy, e.g., the H.E.S.S. telescopes have surveyed the region of $l = -85°$ to $60°$, $b = -3°$ to $3°$ (Chaves & for the H.E.S.S. Collaboration 2009). In this

Table 8.4: H.E.S.S. sources which have a coincident 0FGL source but do not have a 3EG counterpart as in Reimer et al. (2008)

H.E.S.S. sources	0FGL sources	coincidence level
HESS J1616−508	0FGL J1615.6−5049	*Y*
HESS J1634−472	0FGL J1634.9−4737	*P*
HESS J1745−290	0FGL J1746.0−2900	*P*
HESS J1804−216	0FGL J1805.3−2138	*Y*
HESS J1834−087	0FGL J1834.4−0841	*Y*
HESS J1837−069	0FGL J1836.1−0727	*P*

region, there are 41 *Fermi* bright sources. Among them, 16 are found to be coincident with a VHE counterpart. This fraction (∼2/5) is higher than for EGRET where about 1/4 of the EGRET sources (in a smaller region) are found to have a coincident VHE counterpart (Funk et al. 2008). Moreover, the number rises to 21 (out of 41) if possibly coincident cases are included and the fraction becomes 50%. The LAT radii of the 95% confidence region are in general much smaller than the EGRET error boxes, which further strengthens the case of a higher fraction for LAT. Even though the VHE extension is taken into account in this study (but not in Funk et al. 2008), the typical extension is of the same order as the LAT positional uncertainties. A breakdown of the number of coincidence cases for each source population in the above-defined region of the H.E.S.S. Galactic Plane Survey is shown in Table 8.5.

8.6   Conclusion

In this work, we searched for VHE counterparts of each Galactic GeV source in the 0FGL catalog (Abdo et al. 2009b), based on spatial coincidence. This study benefits significantly from the increased LAT angular resolution and its better sensitivity over previous instruments.

Compared to the EGRET era, not only are there more coincident sources (improvement in quantity), but improvements in quality also start to emerge. With the much better sensitivity of LAT, weaker sources are detected that were unknown in the EGRET era. New relations between the GeV and TeV spectra are revealed. A single spectral component is unable to describe some sources detected at both GeV and TeV energies. Two spectral components may be needed in these cases to accommodate the SEDs, where the VHE flux is higher than a power-law extrapolation from GeV energies.

A high fraction of *Fermi* bright sources are found to be spatially coincident with a VHE γ-ray source. This shows that a common GeV/TeV source population exists, a conclusion that is in stark disagreement with Funk et al. (2008) in which EGRET data are used.
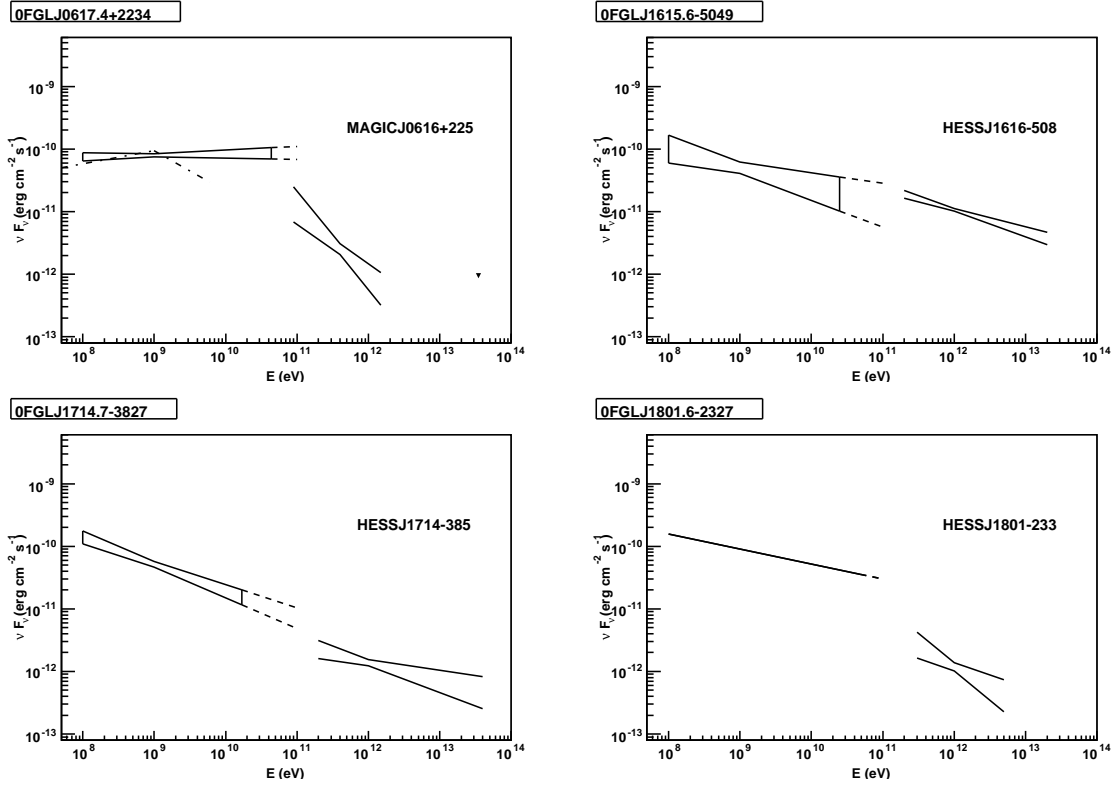
Figure 8.4: MeV to TeV spectra of four SNR/PWN candidate 0FGL sources. Spectra at >100 GeV energies are taken from Albert et al. (2007b) (MAGIC J0616+225), Aharonian et al. (2006d) (HESS J1616−508), Aharonian et al. (2008e) (HESS J1714−385), and Aharonian et al. (2008f) (HESS J1801−233). The broken power-law spectrum (dashed-dotted line) derived for 3EG J0617+2238 is taken from Bertsch et al. (2000). The flux at 35 TeV at the position of 0FGL J0617.4+2234 is that given in Abdo et al. (2009g).

Table 8.5: Number of coincidence cases for each source population (excluding extragalactic sources) in the region $l = -85°$ to $60°$, $b = -3°$ to $3°$.

LAT Source class	0FGL sources	spatially coincident cases[a]
pulsars	10	4
SNR/PWN candidates	11	6 (7)
Unidentified sources	19	5 (9)
Total[b]	41	16 (21)

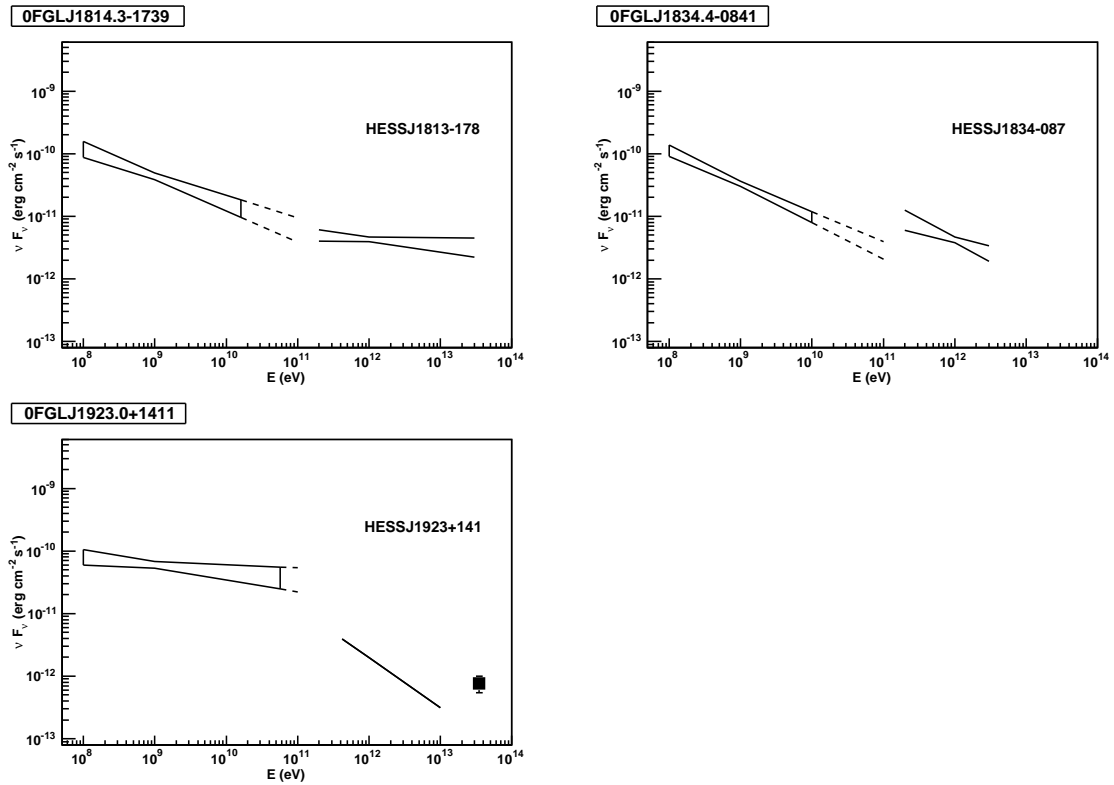**Notes.** [a] The numbers in brackets include possibly coincident cases (*P*). [b] including LS 5039

Figure 8.5: MeV to TeV spectra of three SNR/PWN candidate 0FGL sources. Spectra at >100 GeV energies are taken from Aharonian et al. (2006d) (HESS J1813−178 and HESS J1834−087). For HESS J1923+141, an assumed photon index of 2.8 is used in deriving the spectrum using the flux given in Fiasson et al. (2009), and the flux at 35 TeV is that given in Abdo et al. (2009g). There is evidence of a steepening above several GeV (Abdo et al. 2009e).
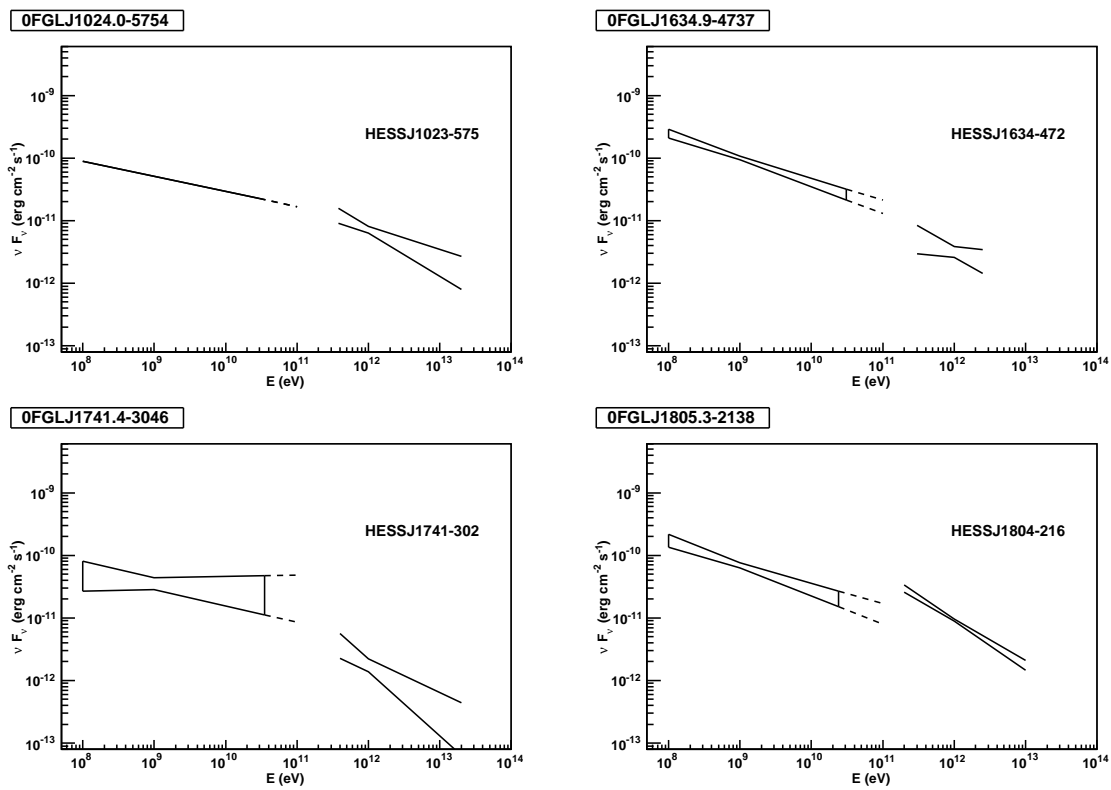
Figure 8.6: MeV to TeV spectra of four unidentified 0FGL sources. Spectra at >100 GeV energies are taken from Aharonian et al. (2007b) (HESS J1023−575), Aharonian et al. (2006d) (HESS J1634−472 and HESS J1804−216), and Tibolla et al. (2009) (HESS J1741−302).
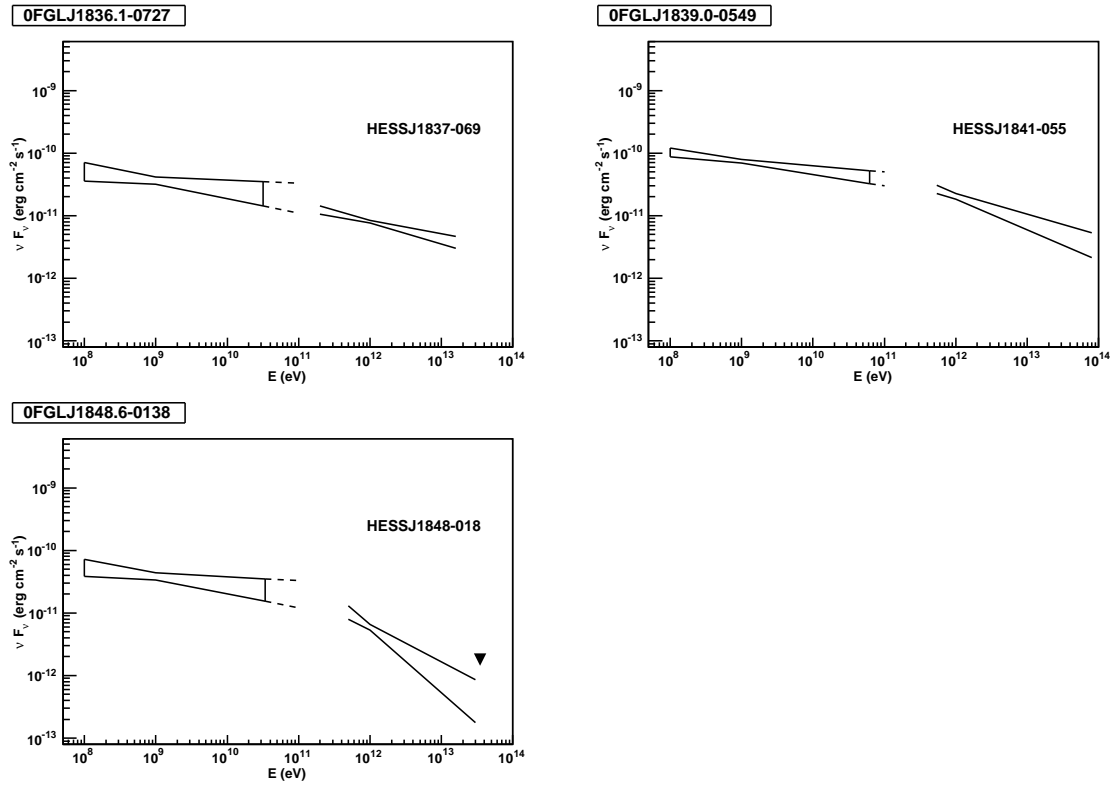
Figure 8.7: MeV to TeV spectra of three unidentified 0FGL sources. Spectra at >100 GeV energies are taken from Aharonian et al. (2006d) (HESS J1837−069), Aharonian et al. (2008a) (HESS J1841−055), and Chaves et al. (2008b) (HESS J1848−018). The flux at 35 TeV at the position of 0FGL J1848.6−0138 is the one given in Abdo et al. (2009g).
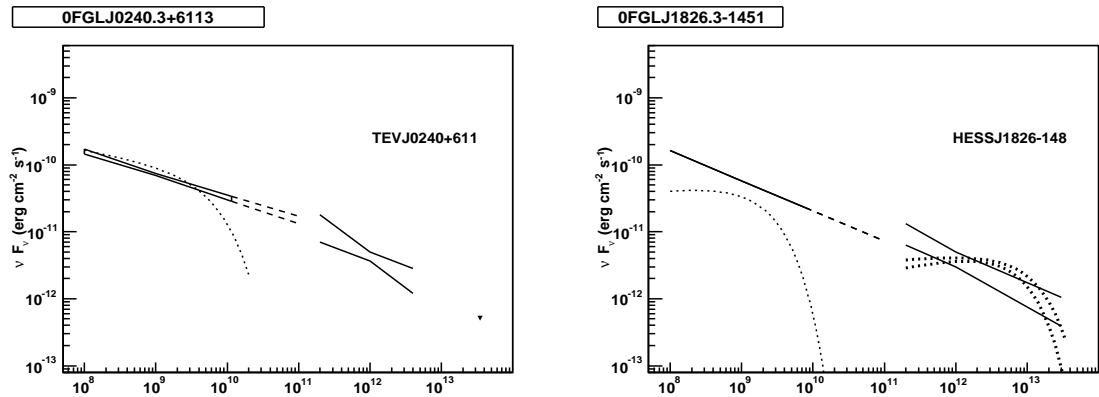

Figure 8.8: MeV to TeV spectra of the two X-ray binaries in the 0FGL catalog. The phase-averaged exponential cut-off spectrum in the GeV range of LS I +61 303 (*left*) is taken from Abdo et al. (2009c). That of LS 5039 is taken from Abdo et al. (2009d). Spectra at >100 GeV energies are taken from Albert et al. (2009) (for a partial phase of LS I +61 303 during which VHE emission is detected) and Aharonian et al. (2006g) (for two phases of LS 5039). The flux at 35 TeV for LS I +61 303 is that given in Abdo et al. (2009g).
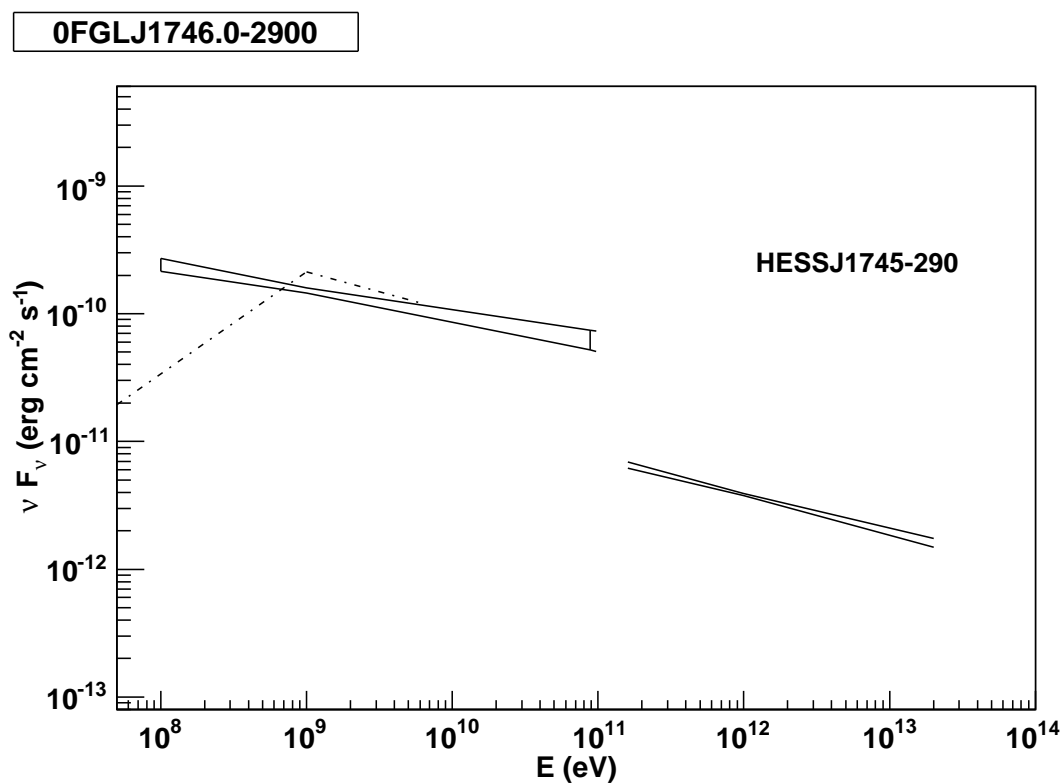
Figure 8.9: MeV to TeV spectrum of the Galactic center. The VHE spectrum is taken from Aharonian et al. (2006c) while the broken power-law spectrum (dashed-dotted line) derived for 3EG J1746−2851 is taken from Bertsch et al. (2000).

Figure 8.10: Photon flux in the 100 MeV – 1 GeV band versus flux in the 1–10 TeV band for coincident GeV/TeV sources.
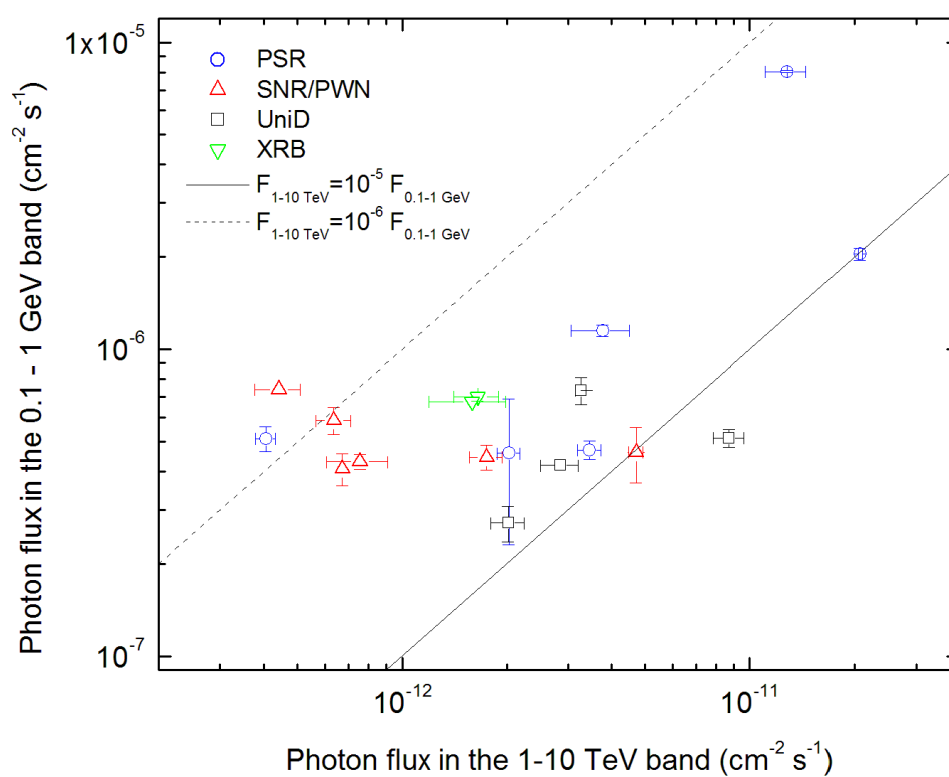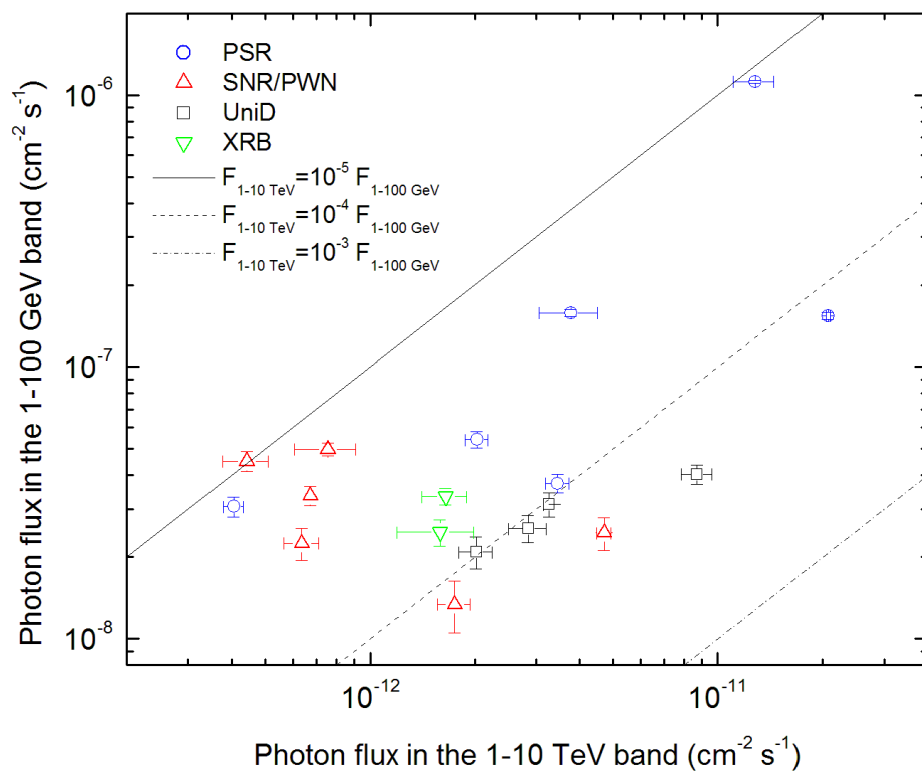
Figure 8.11: Photon flux in the 1–100 GeV band versus flux in the 1–10 TeV band for coincident GeV/TeV sources.
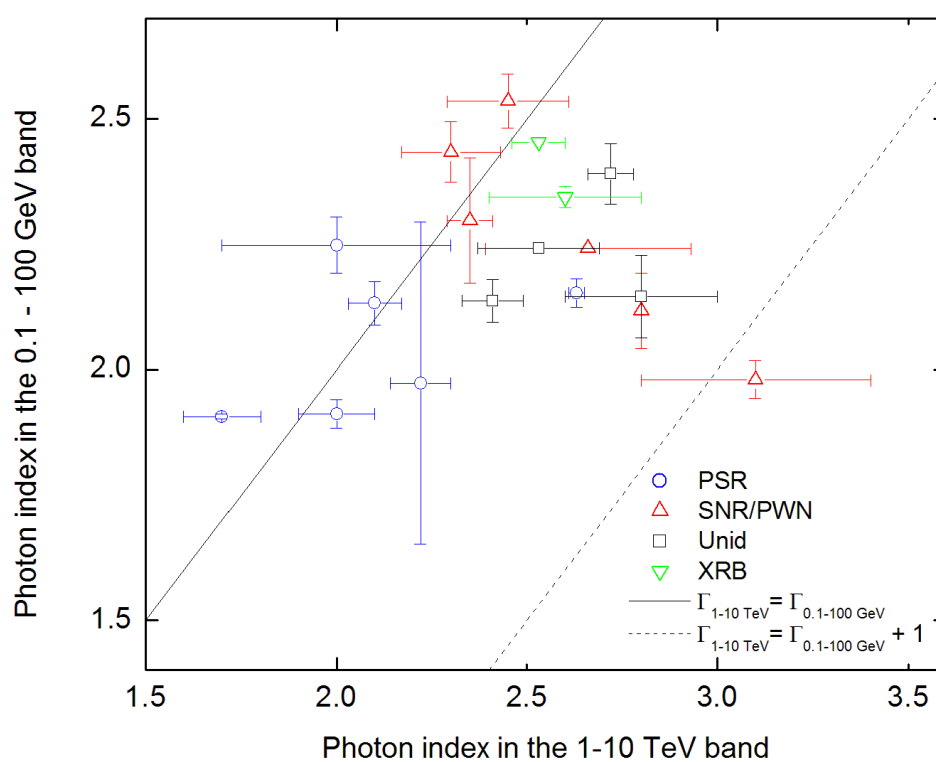
Figure 8.12: Photon index in the 0.1–100 GeV band (derived according to Sect. 8.3.1) versus photon index in the 1–10 TeV band, for coincident GeV/TeV sources. 0FGL J1923.0+1411 / HESS J1923+141 is not included since its VHE photon index is not known.

Chapter 9

Conclusions and outlook

The H.E.S.S. Galactic Plane Survey continues to observe the Galaxy since its inception in 2004. The massive 2300 hr dataset now represents a ten-fold increase in exposure compared to the first published results. The exposure is in general much deeper, with some regions reaching a point-source sensitivity on the order of 0.1% of the Crab Nebula flux. These deep observations permit the detection of faint sources, the detailed study of bright sources, and the derivation of stringent upper limits (ULs) from source candidates. The youngest Galactic supernova remnant (SNR), G 1.9+0.3, is an example of the latter, where an UL of ~0.1% Crab can now be set in the VHE γ-ray domain on this unique shell-type SNR.

Not only has the depth of the H.E.S.S. GPS been increased, but its spatial coverage has also been improved. In many regions, the survey now spans twice the latitudinal range previously covered, out to Galactic latitudes of approximately $b \pm 4°$. The survey strategy has not remained static; in fact, it has evolved considerably over the last six years and currently focuses on achieving a more uniform sensitivity across the H.E.S.S. GPS. This strategy aims to facilitate upcoming source population studies and also to probe the few remaining regions of the plane which are visible to H.E.S.S. but still largely unexplored. A point-source sensitivity of ~2% of the Crab Nebula flux has already been achieved along most of the plane, and efforts will continue in 2011.

The H.E.S.S. GPS continues to reveal new sources of VHE γ-rays in the Galaxy by identifying source candidates which are then typically scheduled for targeted observations. The sources discovered recently are generally faint, preventing advanced VHE γ-ray analyses such as investigations of energy-dependent morphology or shell-like morphology. They also tend to be challenging to firmly identify with phenomena at lower energies. Archival multi-wavelength data — from radio to infrared, X-rays, and GeV γ-rays — are thoroughly exploited. Additionally, dedicated observation time is often sought on complementary telescopes to complete the MWL picture available for the region-of-interest, in hopes of providing additional information for understanding the physical nature of the VHE γ-ray source. Discoveries such as HESS J1503−582, HESS J1832−084, and HESS J1848−018 fall into

this category of newly-revealed sources which elude firm identification. Nonetheless, these new sources are remarkable in the sense that they have provided evidence for intriguing counterpart scenarios.

In the case of HESS J1503−582, a spatial coincidence was initially found with a peculiar forbidden-velocity wing H I structure. However, new data from *Fermi*/LAT reveals another possible counterpart at GeV energies which is spectrally compatible with the H.E.S.S. source. Still more recently, the first deep X-ray observations of this region was performed with *Suzaku*, promising to reveal the X-ray environment around the H.E.S.S. source. HESS J1832−084 is another interesting source which suffers from a scarcity of counterpart possibilities — with the exception of an energetic pulsar coinciding with the centroid of the small VHE γ-ray emission region. Strangely, this pulsar is not particularly energetic and is also fairly old compared to other pulsars typically associated with VHE γ-ray sources via their pulsar wind nebulae (PWNe). If the positional coincidence is not due to a chance alignment, then this discovery would put considerable constraints on TeV PWNe models. Recently, radio and infrared analyses have revealed unknown structures coincident with the H.E.S.S. sources; these will be further investigated with both radio and X-ray observations in the context of a putative PWN scenario. HESS J1848−018, in contrast, is a very large extended source of VHE γ-rays with no clear substructure in a highly complex region located along one of the Galaxy's spiral arm tangents. The W 43 "mini-starburst" region, which harbors an extreme Wolf-Rayet star and other O/B stars, is nearby and is coincident with a giant molecular cloud (GMC). Although the GMC could in principle provide a target for cosmic rays and be connected to the observed VHE γ-rays, there is a morphological mismatch between the GMC and the H.E.S.S. source which is difficult to account for. In contast, the identification of some sources suffers from source confusion. For example, HESS J1708−443 is in the vicinity of both a very energetic pulsar (with known radio and X-ray PWNe) and a shell-type supernova remnant, two well-established VHE γ-ray source classes, yet it remains unidentified even in with the availability of high-quality MWL observations. Such a source may benefit from deeper VHE γ-ray observations, which would enable more advanced analyses.

Galactic observations with H.E.S.S. continue to reveal new and interesting γ-ray sources and advance the quickly maturing field of VHE γ-ray astronomy. The H.E.S.S. GPS provides the foundation for this astronomy with a dataset of unprecendented size and quality. Observations with other telescopes at lower energies supply the missing clues vital to the efforts to identify the nature of these new discoveries. In early to mid-2012, H.E.S.S.-II will become operational, with the addition of a fifth and very-large Cherenkov telescope to the existing array, permitting more sensitive studies of Galactic sources, particularly at lower energies around ∼50 GeV. And, in the near future, the next-generation Cherenkov Telescope Array (CTA) promises to open up the VHE γ-ray window on the Galaxy like never before, with major improvements to all telescope properties, including substantial improvements in sensitivity and angular resolution. Galactic VHE γ-ray astronomy is well-poised for contin-

uing the established trend of rapid discoveries and for improving our understanding of the Galaxy at the highest energies.

Appendix A

H.E.S.S. Galactic Plane Survey: Supplementary material

Supplementary figures and tables related to the H.E.S.S. GPS are presented in this appendix.

Figure A.1: Image showing the pre-trials statistical significance in the H.E.S.S. GPS region, divided into four panels. The significance is correlated over a circular region of radius $\theta = 0.22°$, the standard size used to search for extended VHE γ-ray sources. The significance is truncated in the image above $15\,\sigma$ to increase visibility, and the color transition (from blue to red) is set at $7.4\,\sigma$ pre-trials significance, which (conservatively) corresponds to $\sim 5\,\sigma$ post-trials significance. Maps such as this are used to search for evidence of new VHE γ-ray sources. For version of this plot with labels identifying H.E.S.S. sources, see Fig.2.5.
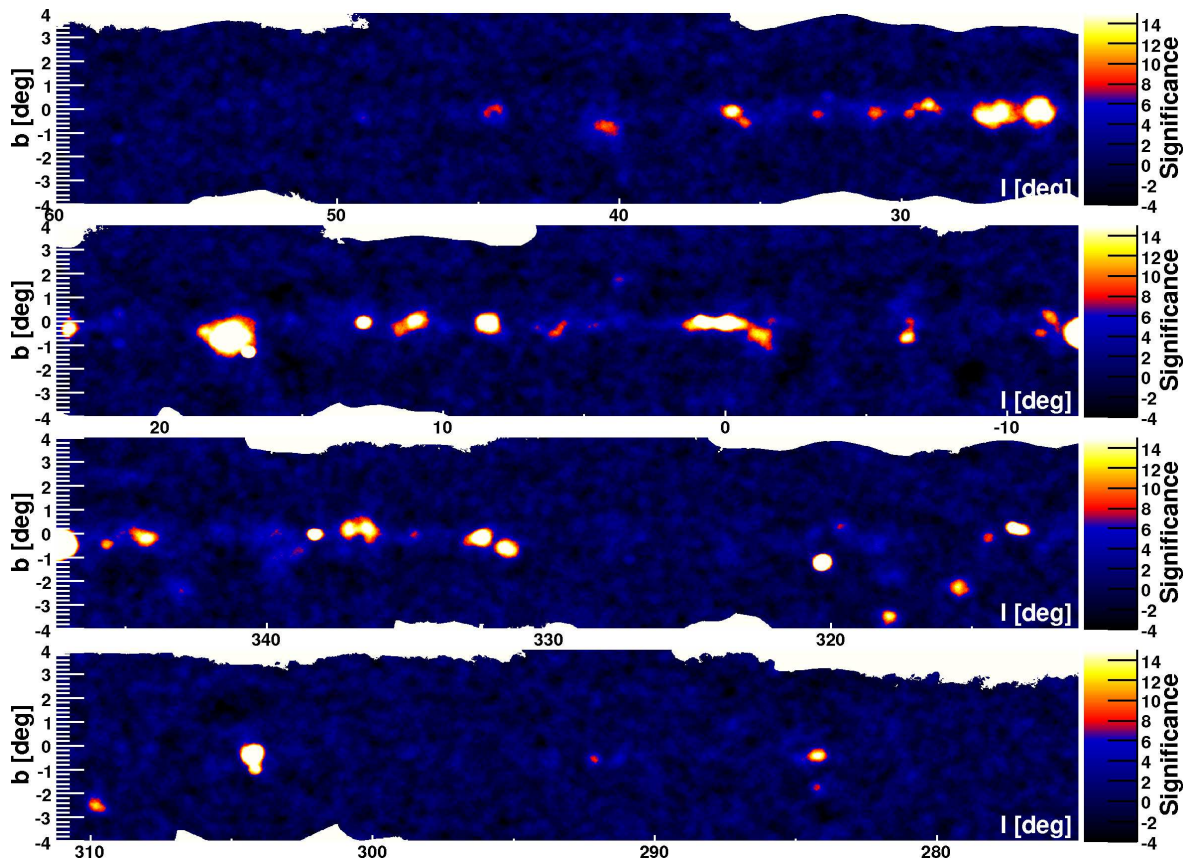
Figure A.2: Image showing the pre-trials statistical significance in the H.E.S.S. GPS region, divided into four panels. The significance is correlated over a point-like circular region of radius $\theta = 0.10°$, and is truncated in the image above $15\,\sigma$ to increase visibility. The color transition (from blue to red) is set at $7.4\,\sigma$ pre-trials significance, which (conservatively) corresponds to $\sim 5\,\sigma$ post-trials significance. Maps such as this are used to search for evidence of new VHE γ-ray sources. For version of this plot with labels identifying H.E.S.S. sources, see Fig.2.6.
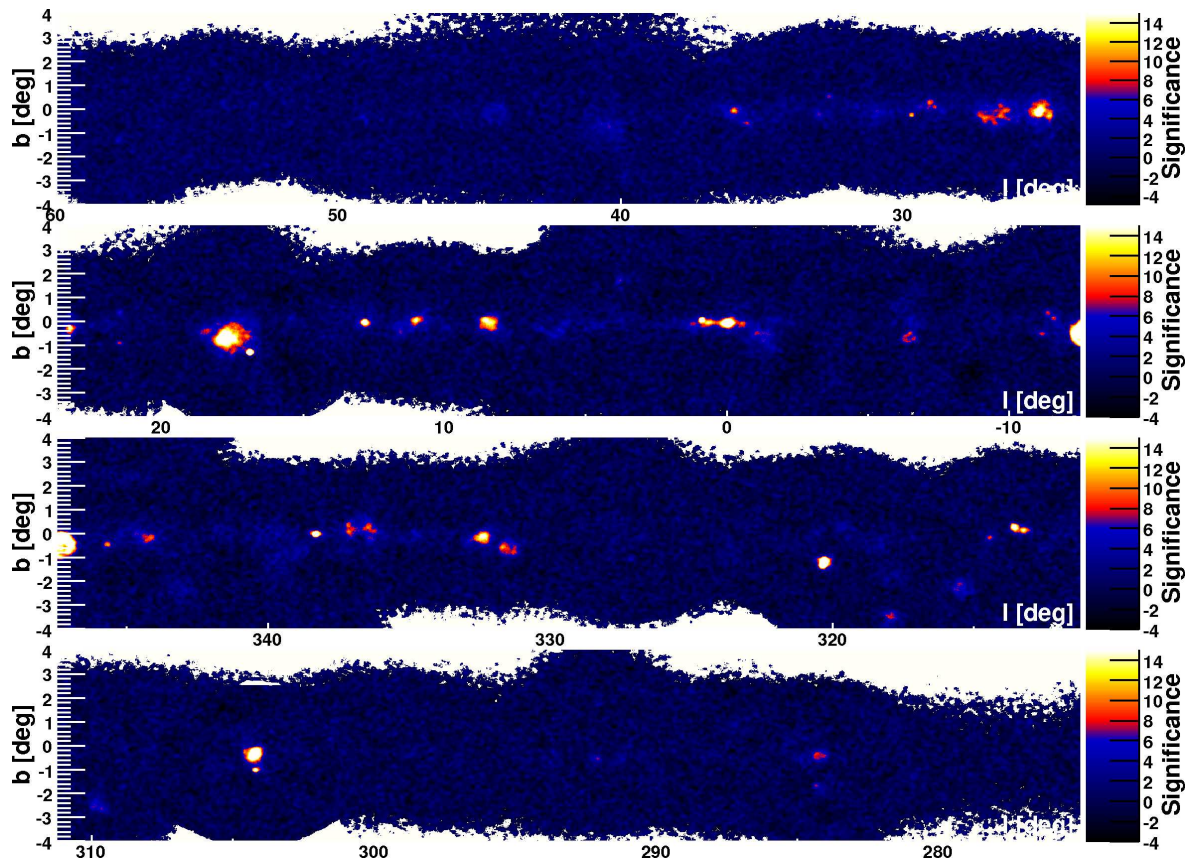
Appendix B

Is the patch size distribution of vegetation a suitable indicator of desertification processes? Comment

Aside from my primary research in astrophysics, I have developed a side interest in the seemingly unrelated field of ecology over the past five years, especially related to the topic of spatial patterns in vegetation, which appear to follow power laws in some circumstances. Ecologists also deal with problems similar to those faced by physicists, e.g. how to properly fit power-law distributions in an unbiased manner. This Appendix presents a recent paper on this subject as published in:

S. Kéfi, C.L. Alados, **R.C.G. Chaves**, Y. Pueyo, & M. Rietkerk

Ecology, in press

With ongoing climate change, the search for indicators of imminent ecosystem shifts is attracting increasing attention (e.g. Scheffer et al. 2009). Recently, the spatial organization of ecosystems has been suggested as a good candidate for such an indicator in spatially structured ecosystems (Rietkerk et al. 2004; Kéfi et al. 2007a; Guttal & Jayaprakash 2009). Arid ecosystems are well known for the spatial organization of their vegetation cover, which is often characterized by clumps of vegetation in an otherwise bare soil matrix. Two recent studies revealed that the distribution of the vegetation patch size can be described by a power law over a wide range of environmental conditions in arid ecosystems (Kéfi et al. 2007a; Scanlon et al. 2007). Furthermore, deviations from power laws to truncated power laws (TPLs) were observed under high grazing pressures, leading to the hypothesis that such deviations could be used as indicators of approaching desertification in Mediterranean arid ecosystems (Kéfi et al. 2007a). We use here the same terminology as in Kéfi et al. (2007a) and Maestre & Escudero (2009), where a TPL refers to a power law with exponential cutoff, i.e., such that

$$N(S) = CS^{-\gamma} \exp(S/S_c), \tag{B.1}$$

with N the number of patches of size S, C a constant, γ the scaling exponent (positive), and S_c the patch size above which N decreases faster than in a power law. This hypothesis now needs to be tested with additional field data, before it can be confidently used as a tool to monitor degradation in Mediterranean arid ecosystems.

In a recent study, Maestre & Escudero (2009) (hereafter referred to as ME09) aimed to test this hypothesis with data from 29 steppes located on a rainfall gradient in southeast Spain. In all of their sites, the patch size distribution was found to be better described by a TPL than by a power law. Relating the scaling exponents of these TPLs to soil variables, the authors concluded that (1) the patch size distribution was not directly related to desertification but rather that (2) vegetation cover should be used to monitor desertification. We argue in this comment that the analyses of ME09 do not allow them to draw such firm conclusions, for the following two reasons. First, because all of their sites were characterized by TPLs, the authors looked only at the scaling exponents γ of the TPLs to compare the degradation level of the sites. However, the exponent γ of the TPLs was not proven to vary with degradation in a consistent manner, and therefore the analyses of ME09 do not allow them to conclude that vegetation cover is better related to degradation than patch size distribution. Second, although the vegetation cover is often a simple, easy-to-use indicator of degradation, the authors do not take into account the increasing amount of theoretical literature that suggests vegetation cover in arid ecosystems is likely to respond in a discontinuous way to gradual, external changes (Rietkerk et al. 1996; Lejeune et al. 1999; Scheffer et al. 2001; Von Hardenberg et al. 2001; Kéfi et al. 2007b). Even though strict proofs of discontinuous transitions are difficult to obtain in the field (see e.g. Scheffer et al. 2001; Schröder et al. 2005) (deMenocal et al. 2000; Foley et al. 2003, but see also e.g.[), the high rate of irreversible degradation and the low restoration success of many dry degraded areas (e.g. Suding et al. 2004; Pueyo & Alados 2007; Sluiter & de Jong 2007; Pueyo et al. 2009) suggest that hysteresis commonly occurs in these ecosystems, which is one of the main components of discontinuous transitions (Beisner et al. 2008). When a discontinuous transition is about to occur, modeling studies have shown that the vegetation cover alone simply does not provide information on the proximity to desertification.

The categorization proposed by (Kéfi et al. 2007a) is a qualitative one in that it does not provide a quantifiable distance to extinction: a shift (in time) from a pure power law to a TPL suggests that an ecosystem is degrading and approaching the desertification threshold. The sites studied by ME09 are all described by TPLs. Among sites characterized by similar patch size distributions, Kéfi et al. (2007a) do not propose any criteria to distinguish among sites of varying degradation; currently, such criteria are sorely lacking. In an attempt to compare the degradation levels of their 29 sites, ME09 investigated changes in the scaling exponent γ of the TPLs among the different sites. This was not part of the hypothesis formulated by Kéfi

et al. (2007a). It is an interesting approach, but it implicitly assumes that γ varies consistently with the level of stress, which has not been proven to be the case. In fact, in the data analyzed by Kéfi et al. (2007a), there does not appear to be any consistent variation of γ among sites characterized by different stress levels (i.e., grazing pressures). For example, with increasing grazing pressure (from medium to high) the absolute value γ of the TPL decreases in the data from Spain but increases in the data from Morocco and Greece (see Fig. 1 in Kéfi et al. 2007a). The lack of a clear relationship between γ and the stress level could very well explain why ME09 find that γ is not related to the perennial cover. It is noteworthy that this result is in agreement with previous studies on steppes dominated by *Stipa tenacissima* in the arid Mediterranean region. For example, it has been shown that the spatial distribution of *S. tenacissima* is not clearly related with its abundance (see Table 1 in Alados et al. 2006). Furthermore, the exponent γ alone does not provide a complete description of the shape of the TPL; the location of the cutoff, S_c, cannot be ignored. Indeed, the latter describes where the deviation from power law behavior begins, and it is this deviation which was proposed to be linked to the level of degradation in Kéfi et al. (2007a). Thus, we doubt whether γ is the correct parameter to investigate. Further theoretical and empirical work is needed in order to identify the parameters which are best correlated to the stress level and which therefore should be monitored.

Another concern regarding the analysis of ME09 is that, when fitting TPLs to their data, they find a negative γ (i.e., a positive slope of the TPL) in the vast majority of their sites (22 of 29 sites listed in ME09: Table 1 and 7 of 8 sites illustrated in ME09: Fig. D1), in stark contrast to the positive γ (i.e., a negative slope of the TPL) observed by Kéfi et al. (2007a). A TPL with a negative γ can be understood as follows: the number of patches $N(S)$ actually increases with size S until some intermediate path size is reached, at which point $N(S)$ begins to decrease. Thus, in ME09s distributions, it is common for smaller patches to be less abundant than patches of intermediate size. For this reason, a TPL does not appear to be the most appropriate model to use to fit the data. The distributions found by ME09 actually suggest the presence of a dominant spatial scale, contrary to the scale invariance observed by Kéfi et al. (2007a). Indeed, some arid areas are characterized by regular vegetation patterns (Rietkerk & van de Koppel 2008), where patch size distributions do not follow power laws but instead reflect a characteristic patch size (or a range of patch sizes). Manor & Shnerb (2008) developed a promising model which can reproduce both the irregular patterns described by power law distributions and the regular patterns characterized by a dominant spatial scale. They showed how the relative strength of competition and facilitation can drive the type of pattern that emerges; strong facilitation favors irregular pattern formation while strong competition favors regular patterns. In systems characterized by regular patterns, it has been suggested that the shape of the patterns can be used to gauge the level of degradation, with spot patterns being the last to occur before desertification (Rietkerk et al. 2004). Further research is needed to determine if these findings can indeed

be applied to the sites studies by ME09. More generally, what is currently lacking is a robust way of characterizing the spatial organization of ecosystems, since, depending on the type of patterns (which emerge from different underlying ecological mechanisms), the indicators that need to be monitored may vary.

Before patch size distributions can be used as a monitoring tool in systems characterized by irregular patterns (e.g., using aerial pictures or satellite images), many technical issues need to be addressed and further tests need to be conducted in the field. From a practical point of view, the patch size distribution is indeed a more complicated tool than the vegetation cover. Among others, there are issues with the binning of the data and the fitting of the mathematical functions.

Traditionally, data is binned when visualizing frequency distributions (Newman 2005; Bauke 2007; White et al. 2008; Clauset et al. 2009). When the data are binned into bins of equal sizes (so-called linear binning), the right-hand side of the distribution is often noisy: the largest elements are rare, and, therefore, each bin contains only a few elements which creates large variations in bin counts among bins (Newman 2005; Bauke 2007). This is a concern when dealing with patch size distributions, since we are especially interested in the behavior of the putative power law in the area around the largest, i.e., the rarest, patches. To decrease the noise in the right-hand tail of the distribution, logarithmic binning is typically employed, where the bins in the tail of distribution receive more elements than with linear binning. Various techniques have been proposed to estimate the optimum bin size (e.g., Sturges rule, Scotts rule, and the Freedman-Diaconis rule); all strive to achieve a reasonable balance between the number of bins and the number of elements in each bin. However, these techniques do not always yield consistent results, which makes the choice of binning fairly arbitrary. A better way of plotting the data is to use the cumulative distribution function, which does not involve the binning of the data (Newman 2005; Bauke 2007; White et al. 2008).

After binning the data, a linear fitting of the log-log transformed data is typically performed using least squares regression (Newman 2005; Bauke 2007; White et al. 2008; Clauset et al. 2009). Fitting methods based on binning and least squares regression are widely used in ecology and in other fields to fit models to data and to estimate the scaling exponents of frequency distribu- tions. White et al. (2008) recently demonstrated that such methods give biased results and therefore cannot be relied upon. While these biases are dangerous with regards to estimating the scaling exponent of a distribution, binned-based methods can also lead to differences in the determination of which distribution best fits the data. For example, a data set that is best described by a power law using a given bin size could be best described by a TPL when using a different bin size.

Independently of the way the data are plotted, a reliable alternative to least square linear regression is to use fitting methods based on maximum likelihood estimation (MLE) to extract the scaling exponent of the frequency distribution (Goldstein et al. 2004, e.g.,). White

et al. (2008) showed that MLE is the single most accurate method for estimating the scaling exponents of frequency distributions. Currently, MLE is available for the pure power law distribution (Goldstein et al. 2004; Newman 2005; Bauke 2007) but not for the TPL distribution as defined here, which limits the application of MLE to this particular case for now, but is a promising line of future research.

In conclusion, although looking at the vegetation cover is still the most straightforward and practical way of assessing the "health of an arid ecosystem, there are cases where the cover may fail to predict desertification. Theoretical studies increasingly suggest that ecosystems which include facilitation may respond to gradual external changes in an abrupt, rather than gradual manner (e.g., Lejeune et al. 1999; Scheffer et al. 2001; Von Hardenberg et al. 2001; Rietkerk et al. 2004; Kéfi et al. 2007b). Desertification then occurs in sudden shifts, where ecosystems switch from an unknown vegetation cover to desert (e.g., deMenocal et al. 2000; Foley et al. 2003). In these cases, the vegetation cover would not be a suitable indicator of proximity to shifts and, therefore, other indicators need to be further developed so that they can be used in addition to the cover. The patch size distribution may, upon validation, be such a complementary indicator since it is hypothesized to work along both continuous and discontinuous transitions to desertification (Kéfi et al. 2007a). We would like to stress that we do not contend that the patch size distribution is a better indicator than the vegetation cover, and we do in fact support the continued use of the cover as a means of gauging an arid ecosystems health. However, since the cover may not work in all cases (e.g., if the system is likely to undergo a discontinuous transition), we reiterate the need to explore additional (either alternative or complementary) indicators of degradation so that more robust and reliable early-warning systems can be implemented.

References

Abdo, A. A., Ackermann, M., Ajello, M., et al. 2010, ApJS, 188, 405

Abdo, A. A., Ackermann, M., Ajello, M., et al. 2009a, Science, 325, 840

Abdo, A. A., Ackermann, M., Ajello, M., et al. 2009b, ApJS, 183, 46

Abdo, A. A., Ackermann, M., Ajello, M., et al. 2009c, ApJ, 701, L123

Abdo, A. A., Ackermann, M., Ajello, M., et al. 2009d, ApJ, 706, L56

Abdo, A. A., Ackermann, M., Ajello, M., et al. 2009e, ApJ, 706, L1

Abdo, A. A., Ackermann, M., Atwood, W. B., et al. 2009f, ApJ, 696, 1084

Abdo, A. A., Allen, B., Berley, D., et al. 2007, ApJ, 664, L91

Abdo, A. A., Allen, B. T., Aune, T., et al. 2009g, ApJ, 700, L127

Abdo, A. A. & for the Fermi LAT collaboration. 2009, ArXiv e-prints

Abramowski, A., Acero, F., Aharonian, F., et al. 2011, A&A, 525, A46+

Acciari, V. A., Aliu, E., Arlen, T., et al. 2009a, ApJ, 703, L6

Acciari, V. A., Aliu, E., Arlen, T., et al. 2009b, ApJ, 700, 1034

Acero, F., Aharonian, F., Akhperjanian, A. G., et al. 2010a, A&A, 516, A62+

Acero, F., Aharonian, F., Akhperjanian, A. G., et al. 2010b, MNRAS, 402, 1877

Acero, F., Aharonian, F., Akhperjanian, A. G., et al. 2011, A&A, 525, A45+

Acero, F., Aharonian, F., Akhperjanian, A. G., et al. 2009, Science, 326, 1080

Aharonian, F., Akhperjanian, A., Barrio, J., et al. 2001, A&A, 370, 112

Aharonian, F., Akhperjanian, A., Beilicke, M., et al. 2005a, A&A, 431, 197

Aharonian, F., Akhperjanian, A. G., Anton, G., et al. 2009a, A&A, 499, 723

Aharonian, F., Akhperjanian, A. G., Anton, G., et al. 2009b, A&A, 503, 817

Aharonian, F., Akhperjanian, A. G., Aye, K., et al. 2005b, A&A, 432, L25

Aharonian, F., Akhperjanian, A. G., Aye, K., et al. 2005c, A&A, 442, 1

Aharonian, F., Akhperjanian, A. G., Aye, K., et al. 2005d, A&A, 439, 1013

Aharonian, F., Akhperjanian, A. G., Aye, K., et al. 2004, A&A, 425, L13

Aharonian, F., Akhperjanian, A. G., Aye, K.-M., et al. 2005e, A&A, 432, L9

Aharonian, F., Akhperjanian, A. G., Aye, K.-M., et al. 2005f, Science, 307, 1938

Aharonian, F., Akhperjanian, A. G., Aye, K.-M., et al. 2005g, A&A, 435, L17

Aharonian, F., Akhperjanian, A. G., Barres de Almeida, U., et al. 2008a, A&A, 477, 353

Aharonian, F., Akhperjanian, A. G., Barres de Almeida, U., et al. 2008b, A&A, 483, 509

Aharonian, F., Akhperjanian, A. G., Barres de Almeida, U., et al. 2008c, A&A, 484, 435

Aharonian, F., Akhperjanian, A. G., Barres de Almeida, U., et al. 2008d, A&A, 486, 829

Aharonian, F., Akhperjanian, A. G., Barres de Almeida, U., et al. 2008e, A&A, 490, 685

Aharonian, F., Akhperjanian, A. G., Bazer-Bachi, A. R., et al. 2008f, A&A, 481, 401

Aharonian, F., Akhperjanian, A. G., Bazer-Bachi, A. R., et al. 2007a, A&A, 472, 489

Aharonian, F., Akhperjanian, A. G., Bazer-Bachi, A. R., et al. 2006a, A&A, 457, 899

Aharonian, F., Akhperjanian, A. G., Bazer-Bachi, A. R., et al. 2006b, A&A, 448, L43

Aharonian, F., Akhperjanian, A. G., Bazer-Bachi, A. R., et al. 2006c, Physical Review Letters, 97, 249901

Aharonian, F., Akhperjanian, A. G., Bazer-Bachi, A. R., et al. 2006d, ApJ, 636, 777

Aharonian, F., Akhperjanian, A. G., Bazer-Bachi, A. R., et al. 2005h, A&A, 437, L7

Aharonian, F., Akhperjanian, A. G., Bazer-Bachi, A. R., et al. 2007b, A&A, 467, 1075

Aharonian, F., Akhperjanian, A. G., Bazer-Bachi, A. R., et al. 2007c, A&A, 464, 235

Aharonian, F., Akhperjanian, A. G., Bazer-Bachi, A. R., et al. 2006g, A&A, 460, 743

Aharonian, F., Akhperjanian, A. G., Bazer-Bachi, A. R., et al. 2007d, ApJ, 661, 236

Aharonian, F., Akhperjanian, A. G., Bazer-Bachi, A. R., et al. 2006e, A&A, 456, 245

Aharonian, F., Akhperjanian, A. G., Bazer-Bachi, A. R., et al. 2006f, A&A, 460, 365

Aharonian, F., Akhperjanian, A. G., de Almeida, U. B., et al. 2009c, ApJ, 692, 1500

Aharonian, F., Buckley, J., Kifune, T., & Sinnis, G. 2008g, Reports on Progress in Physics, 71, 096901

Aharonian, F. A. 1991, Ap&SS, 180, 305

Aharonian, F. A. 2004, Very high energy cosmic gamma radiation : a crucial window on the extreme Universe (River Edge, NJ: World Scientific Publishing)

Aharonian, F. A., Akhperjanian, A. G., Bazer-Bachi, A. R., et al. 2007e, A&A, 469, L1

Aharonian, F. A., Akhperjanian, A. G., Bazer-Bachi, A. R., et al. 2005i, A&A, 442, L25

Aharonian, F. A., Akhperjanian, A. G., Beilicke, M., et al. 2002, A&A, 395, 803

Aharonian, F. A., Atoyan, A. M., & Kifune, T. 1997, MNRAS, 291, 162

Alados, C., Gotor, P., Ballester, P., et al. 2006, Biological Journal of the Linnean Society, 87, 103

Albert, J., Aliu, E., Anderhub, H., et al. 2009, ApJ, 693, 303

Albert, J., Aliu, E., Anderhub, H., et al. 2006, ApJ, 643, L53

Albert, J., Aliu, E., Anderhub, H., et al. 2007a, A&A, 474, 937

Albert, J., Aliu, E., Anderhub, H., et al. 2008, ApJ, 674, 1037

Albert, J., Aliu, E., Anderhub, H., et al. 2007b, ApJ, 664, L87

Aliu, E., Anderhub, H., Antonelli, L. A., et al. 2008, Science, 322, 1221

Altenhoff, W. J., Downes, D., Pauls, T., & Schraml, J. 1979, A&AS, 35, 23

Amato, E., Guetta, D., & Blasi, P. 2003, A&A, 402, 827

Amenomori, M., Ayabe, S., Cui, S. H., et al. 2002, ApJ, 580, 887

Anderson, G. E., Gaensler, B. M., & The ChICAGO Team. 2006, in Bulletin of the American Astronomical Society, Vol. 38, Bulletin of the American Astronomical Society, 374–+

Arendt, R. G. 1989, ApJS, 70, 181

Atkins, R., Benbow, W., Berley, D., et al. 2004, ApJ, 608, 680

Atwood, W. B., Abdo, A. A., Ackermann, M., et al. 2009, ApJ, 697, 1071

Bauke, H. 2007, The European Physical Journal B-Condensed Matter and Complex Systems, 58, 167

Becker, R. H., White, R. L., McLean, B. J., Helfand, D. J., & Zoonematkermani, S. 1990, ApJ, 358, 485

Becker, W., Brazier, K. T. S., & Truemper, J. 1995, A&A, 298, 528

Bednarek, W. & Bartosik, M. 2003, A&A, 405, 689

Beisner, B., Haydon, D., & Cuddington, K. 2008

Berezhko, E. G. & Ksenofontov, L. T. 2006, ApJ, 650, L59

Berge, D., Funk, S., & Hinton, J. 2007, A&A, 466, 1219

Bernlöhr, K., Carrol, O., Cornils, R., et al. 2003, Astroparticle Physics, 20, 111

Bertsch, D. L., Brazier, K. T. S., Fichtel, C. E., et al. 1992, Nature, 357, 306

Bertsch, D. L., Hartman, R. C., Hunter, S. D., et al. 2000, in American Institute of
    Physics Conference Series, Vol. 510, American Institute of Physics Conference Series,
    ed. M. L. McConnell & J. M. Ryan, 504–508

Blackett, P. M. S. 1948, in The Emission Spectra of the Night Sky and Aurorae, 34–+

Blondin, J. M., Chevalier, R. A., & Frierson, D. M. 2001, ApJ, 563, 806

Blum, R. D., Damineli, A., & Conti, P. S. 1999, AJ, 117, 1392

Bock, D. C.-J. & Gvaramadze, V. V. 2002, A&A, 394, 533

Bolz, O. 2004, PhD in Physics, Ruprecht-Karls-Universität Heidelberg

Case, G. L. & Bhattacharya, D. 1998, ApJ, 504, 761

Caswell, J. L., Haynes, R. F., & Clark, D. H. 1975, Australian Journal of Physics, 28, 633

Caswell, J. L. & Stewart, R. T. 1991, Proceedings of the Astronomical Society of Australia,
    9, 103

Celik, O. & on behalf of the *Fermi*-LAT Collaboration. 2009

Chadwick, P. M., Dickinson, M. R., Dipper, N. A., et al. 1998, Astroparticle Physics, 9, 131

Chaves, R. C. G., de Oña Wilhemi, E., & Hoppe, S. H. 2008a, in American Institute of
    Physics Conference Series, Vol. 1085, American Institute of Physics Conference Series,
    ed. F. A. Aharonian, W. Hofmann, & F. Rieger, 219–222

Chaves, R. C. G. & for the H.E.S.S. Collaboration. 2009, ArXiv e-prints

Chaves, R. C. G., Renaud, M., Lemoine-Goumard, M., & Goret, P. 2008b, in American In-
    stitute of Physics Conference Series, Vol. 1085, American Institute of Physics Conference
    Series, ed. F. A. Aharonian, W. Hofmann, & F. Rieger, 372–375

Chevalier, R. A. 1982, ApJ, 258, 790

Cioffi, D. F., McKee, C. F., & Bertschinger, E. 1988, ApJ, 334, 252

Clark, D. H. & Crawford, D. F. 1974, Australian Journal of Physics, 27, 713

Clauset, A., Shalizi, C., & Newman, M. 2009, SIAM review, 51, 661

Clifton, T. R. & Lyne, A. G. 1986, Nature, 320, 43

Clifton, T. R., Lyne, A. G., Jones, A. W., McKenna, J., & Ashworth, M. 1992, MNRAS, 254, 177

Condon, J. J., Cotton, W. D., Greisen, E. W., et al. 1998, AJ, 115, 1693

Cordes, J. M. & Lazio, T. J. W. 2002, ArXiv e-prints, astro-ph/0207156

Cowan, J. J., Ekers, R. D., Goss, W. M., et al. 1989, MNRAS, 241, 613

CTA Consortium, T. 2010, ArXiv e-prints

Dame, T. M., Hartmann, D., & Thaddeus, P. 2001, ApJ, 547, 792

De Horta, A. Y., Filipović, M. D., Crawford, E. J., Stootman, F. H., & Pannuti, T. G. 2008, ArXiv e-prints

de Jager, O. C. & Djannati-Ataï, A. 2008, ArXiv e-prints

de Jager, O. C., Harding, A. K., Michelson, P. F., et al. 1996, ApJ, 457, 253

de Naurois, M. & H. E. S. S. Collaboration. 2003, in International Cosmic Ray Conference, Vol. 5, International Cosmic Ray Conference, 2907–+

de Naurois, M. & Rolland, L. 2009, Astroparticle Physics, 32, 231

deMenocal, P., Ortiz, J., Guilderson, T., et al. 2000, Quaternary Science Reviews, 19, 347

Di Salvo, T., Iaria, R., Méndez, M., et al. 2005, ApJ, 623, L121

Djannati-Atai, A., Oña-Wilhelmi, E., Renaud, M., & et al. 2008, in International Cosmic Ray Conference, Vol. 2, International Cosmic Ray Conference, 863–866

Djannati-Ataǐ, A., de Jager, O. C., Terrier, R., & et al. 2008, in International Cosmic Ray Conference, Vol. 2, International Cosmic Ray Conference, 823–826

Dodson, R. & Golap, K. 2002, MNRAS, 334, L1

Domingo-Santamaría, E. & Torres, D. F. 2006, A&A, 448, 613

Douglas, J. N., Bash, F. N., Bozyan, F. A., Torrence, G. W., & Wolfe, C. 1996, AJ, 111, 1945

Douglas, J. N., Bash, F. N., Torrence, G. W., & Wolfe, C. 1980, University of Texas Publications in Astronomy, 17, 1

Downes, D., Maxwell, A., & Rinehart, R. 1970, ApJ, 161, L123+

Drury, L. O., Aharonian, F. A., & Voelk, H. J. 1994, A&A, 287, 959

Duncan, A. R., Stewart, R. T., Haynes, R. F., & Jones, K. L. 1995, MNRAS, 277, 36

Dwarkadas, V. V. & Chevalier, R. A. 1998, ApJ, 497, 807

Dwek, E. 1981, ApJ, 247, 614

Ebisawa, K., Tsujimoto, M., Paizis, A., et al. 2005, ApJ, 635, 214

Enomoto, R., Kushida, J., Nakamori, T., et al. 2009, ApJ, 703, 1725

Feldman, G. J. & Cousins, R. D. 1998, Phys. Rev. D, 57, 3873

Fiasson, A., Dubois, F., Lamanna, G., Masbou, J., & Rosier-Lees, S. 2010, Astroparticle Physics, 34, 25

Fiasson, A., Marandon, V., Chaves, R. C. G., Tibolla, O., & for the H. E. S. S. Collaboration. 2009

Fich, M., Blitz, L., & Stark, A. A. 1989, ApJ, 342, 272

Finley, J. P., Srinivasan, R., Saito, Y., et al. 1998, ApJ, 493, 884

Finnegan, G. & for the VERITAS Collaboration. 2009, ArXiv e-prints

Foley, J., Coe, M., Scheffer, M., & Wang, G. 2003, Ecosystems, 6, 524

Forman, W., Jones, C., Cominsky, L., et al. 1978, ApJS, 38, 357

Frail, D. A., Cordes, J. M., Hankins, T. H., & Weisberg, J. M. 1991, ApJ, 382, 168

Frail, D. A., Goss, W. M., & Whiteoak, J. B. Z. 1994, ApJ, 437, 781

Frail, D. A. & Weisberg, J. M. 1990, AJ, 100, 743

Fruscione, A., McDowell, J. C., Allen, G. E., et al. 2006, in Society of Photo-Optical Instrumentation Engineers (SPIE) Conference Series, Vol. 6270, Society of Photo-Optical Instrumentation Engineers (SPIE) Conference Series

Fulbright, M. S. & Reynolds, S. P. 1990, ApJ, 357, 591

Funk, S., Hermann, G., Hinton, J., et al. 2004, Astroparticle Physics, 22, 285

Funk, S., Reimer, O., Torres, D. F., & Hinton, J. A. 2008, ApJ, 679, 1299

Gaensler, B. M., Schulz, N. S., Kaspi, V. M., Pivovaroff, M. J., & Becker, W. E. 2003, ApJ, 588, 441

Gaensler, B. M. & Slane, P. O. 2006, ARA&A, 44, 17

Gaensler, B. M., Tanna, A., Slane, P. O., et al. 2008, ApJ, 680, L37

Gallant, Y. A. 2007, Ap&SS, 309, 197

Gallant, Y. A., Carrigan, S., Djannati-Ataï, A., et al. 2008, in American Institute of Physics Conference Series, Vol. 983, 40 Years of Pulsars: Millisecond Pulsars, Magnetars and More, ed. C. Bassa, Z. Wang, A. Cumming, & V. M. Kaspi, 195–199

Gargano, F. & on behalf of the *Fermi*-LAT Collaboration. 2009

Garmany, C. D., Conti, P. S., & Chiosi, C. 1982, ApJ, 263, 777

Gelfand, J. D. & Gaensler, B. M. 2007, ApJ, 667, 1111

Giacani, E. B., Frail, D. A., Goss, W. M., & Vieytes, M. 2001, AJ, 121, 3133

Gillessen, S., Hinton, J., & H. E. S. S. Collaboration. 2005, in American Institute of Physics Conference Series, Vol. 745, High Energy Gamma-Ray Astronomy, ed. F. A. Aharonian, H. J. Völk, & D. Horns, 758–763

Goldstein, M., Morris, S., & Yen, G. 2004, The European Physical Journal B, 41, 255

Gómez, Y. & Rodríguez, L. F. 2009, Rev. Mexicana Astron. Astrofis., 45, 91

Gotthelf, E. V., Halpern, J. P., & Dodson, R. 2002, ApJ, 567, L125

Graham, J. R., Evans, A., Albinson, J. S., Bode, M. F., & Meikle, W. P. S. 1987, ApJ, 319, 126

Gray, A. D. 1994a, MNRAS, 270, 861

Gray, A. D. 1994b, MNRAS, 270, 835

Green, A. J., Frail, D. A., Goss, W. M., & Otrupcek, R. 1997, AJ, 114, 2058

Green, D. A. 1988, Ap&SS, 148, 3

Green, D. A. 1991, PASP, 103, 209

Green, D. A. 2004, Bulletin of the Astronomical Society of India, 32, 335

Green, D. A. 2005, Memorie della Societa Astronomica Italiana, 76, 534

Green, D. A. 2006, A Catalogue of Galactic Supernova Remnants (2006 April version) (Cambridge, United Kingdom: Astrophysics Group, Cavendish Laboratory)

Green, D. A. 2009, Bulletin of the Astronomical Society of India, 37, 45

Green, D. A. & Gull, S. F. 1984, Nature, 312, 527

Green, D. A., Reynolds, S. P., Borkowski, K. J., et al. 2008, MNRAS, 387, L54

Grondin, M.-H. & on behalf of the *Fermi*-LAT Collaboration. 2009

Guseinov, O. H., Ankay, A., & Tagieva, S. O. 2003, Serbian Astronomical Journal, 167, 93

Guttal, V. & Jayaprakash, C. 2009, Theoretical Ecology, 2, 3

H. E. S. S. Collaboration: A. Djannati-Atai, De Jager, O. C., Terrier, R., Gallant, Y. A., & Hoppe, S. 2007, ArXiv e-prints

Hartman, R. C., Bertsch, D. L., Bloom, S. D., et al. 1999, ApJS, 123, 79

HEGRA Collaboration, Konopelko, A., Hemberger, M., et al. 1999, Astroparticle Physics, 10, 275

Helfand, D. J., Becker, R. H., White, R. L., Fallon, A., & Tuttle, S. 2006, AJ, 131, 2525

Hillas, A. M. 1985, in International Cosmic Ray Conference, Vol. 3, International Cosmic Ray Conference, ed. F. C. Jones, 445–448

Hinton, J. 2009, New Journal of Physics, 11, 055005

Hinton, J. A. 2004, New A Rev., 48, 331

Hobbs, G., Lyne, A. G., Kramer, M., Martin, C. E., & Jordan, C. 2004, MNRAS, 353, 1311

Hofmann, W., Jung, I., Konopelko, A., et al. 1999, Astroparticle Physics, 12, 135

Holder, J. & for the VERITAS Collaboration. 2009, ArXiv e-prints

Hoppe, S. 2008, PhD in Physics, Ruprecht-Karls-Universität Heidelberg

Hoppe, S. 2008, in International Cosmic Ray Conference, Vol. 2, International Cosmic Ray Conference, 579–582

Hoppe, S., de Oña-Wilhemi, E., Khélifi, B., et al. 2009, ArXiv e-prints, astro-ph/0906.5574

Horns, D., Aharonian, F., Hoffmann, A. I. D., & Santangelo, A. 2007, Ap&SS, 309, 189

Horns, D., Aharonian, F., Santangelo, A., Hoffmann, A. I. D., & Masterson, C. 2006, A&A, 451, L51

Jackson, J. M., Rathborne, J. M., Shah, R. Y., et al. 2006, ApJS, 163, 145

Johnston, S. & Galloway, D. 1999, MNRAS, 306, L50

Johnston, S., Lyne, A. G., Manchester, R. N., et al. 1992, MNRAS, 255, 401

Johnston, S., Nicastro, L., & Koribalski, B. 1998, MNRAS, 297, 108

Kang, J. & Koo, B. 2007, ApJS, 173, 85

Kaplan, D. L., Levine, A. M., Chakrabarty, D., et al. 2007, ApJ, 661, 437

Kargaltsev, O. & Pavlov, G. G. 2010, in American Institute of Physics Conference Series, Vol. 1248, American Institute of Physics Conference Series, ed. A. Comastri, L. Angelini, & M. Cappi, 25–28

Kéfi, S., Rietkerk, M., Alados, C., et al. 2007a, Nature, 449, 213

Kéfi, S., Rietkerk, M., van Baalen, M., & Loreau, M. 2007b, Theoretical population biology, 71, 367

Kelner, S. R., Aharonian, F. A., & Bugayov, V. V. 2006, Phys. Rev. D, 74, 034018

Kennel, C. F. & Coroniti, F. V. 1984, ApJ, 283, 694

Kerschhaggl, M. & de Naurois, M. 2008, in American Institute of Physics Conference Series, Vol. 1085, American Institute of Physics Conference Series, ed. F. A. Aharonian, W. Hofmann, & F. Rieger, 203–206

Kifune, T., Tanimori, T., Ogio, S., et al. 1995, ApJ, 438, L91

Koo, B., Kang, J., & Salter, C. J. 2006, ApJ, 643, L49

Koo, B.-C. & Heiles, C. 1991, ApJ, 382, 204

Koribalski, B., Johnston, S., Weisberg, J. M., & Wilson, W. 1995, ApJ, 441, 756

Kovalenko, A. V., Pynzar', A. V., & Udal'Tsov, V. A. 1994, AZh, 71, 110

Ksenofontov, L. T., Völk, H. J., & Berezhko, E. G. 2010, ApJ, 714, 1187

Kushida, J. & et al. 2003, in International Cosmic Ray Conference, Vol. 4, International Cosmic Ray Conference, 2493–2496

Large, M. I., Mathewson, D. S., & Haslam, C. G. T. 1961, MNRAS, 123, 113

LaRosa, T. N., Kassim, N. E., Lazio, T. J. W., & Hyman, S. D. 2000, AJ, 119, 207

Lejeune, O., Couteron, P., & Lefever, R. 1999, Acta Oecologica, 20, 171

Lemiere, A., Slane, P., Gaensler, B. M., & Murray, S. 2009, ApJ, 706, 1269

Lemoine-Goumard, M., Grondin, M.-H., & on behalf of the *Fermi*-LAT Collaboration and the Pulsar Timing Consortium. 2009

Li, T.-P. & Ma, Y.-Q. 1983, ApJ, 272, 317

Liszt, H. S. 1995, AJ, 109, 1204

Liszt, H. S., Braun, R., & Greisen, E. W. 1993, AJ, 106, 2349

Lorimer, D. R., Yates, J. A., Lyne, A. G., & Gould, D. M. 1995, MNRAS, 273, 411

MacLeod, J. M. & Doherty, L. H. 1968, ApJ, 154, 833

Maestre, F. & Escudero, A. 2009, Ecology, 90, 1729

Manchester, R. N., Hobbs, G. B., Teoh, A., & Hobbs, M. 2005, AJ, 129, 1993

Manchester, R. N. & Taylor, J. H. 1977, Pulsars. (San Francisco: W. H. Freeman)

Manor, A. & Shnerb, N. 2008, Journal of theoretical biology, 253, 838

Mattana, F., Falanga, M., Götz, D., et al. 2009a, ApJ, 694, 12

Mattana, F., Götz, D., Terrier, R., Renaud, M., & Falanga, M. 2009b, in American Institute of Physics Conference Series, Vol. 1126, American Institute of Physics Conference Series, ed. J. Rodriguez & P. Ferrando, 259–262

Mayer-Hasselwander, H. A., Bertsch, D. L., Brazier, K. T. S., et al. 1994, ApJ, 421, 276

McAdam, W. B., Osborne, J. L., & Parkinson, M. L. 1993, Nature, 361, 516

McClure-Griffiths, N. M., Dickey, J. M., Gaensler, B. M., et al. 2005, ApJS, 158, 178

McKee, C. F. & Ostriker, J. P. 1977, ApJ, 218, 148

McLaughlin, M. A. & Cordes, J. M. 2000, ApJ, 538, 818

Mel'Nik, A. M. & Dambis, A. K. 2009, MNRAS, 400, 518

Mezger, P. G. & Höglund, B. 1967, ApJ, 147, 490

Minter, A. H. 2008, ApJ, 677, 373

Muraishi, H., Tanimori, T., Yanagita, S., et al. 2000, A&A, 354, L57

Murphy, T., Gaensler, B. M., & Chatterjee, S. 2008, MNRAS, 389, L23

Naumann-Godó, M., Lemoine-Goumard, M., & Degrange, B. 2009, Astroparticle Physics, 31, 421

Nel, H. I., de Jager, O. C., Raubenheimer, B. C., et al. 1993, ApJ, 418, 836

Newman, M. 2005, Contemporary physics, 46, 323

Nicastro, L., Johnston, S., & Koribalski, B. 1996, A&A, 306, L49

Nord, M. E., Lazio, T. J. W., Kassim, N. E., et al. 2004, AJ, 128, 1646

Ogio, S., Kifune, T., & et al. 1993, in International Cosmic Ray Conference, Vol. 1, International Cosmic Ray Conference, 392–+

Ohm, S., Horns, D., Reimer, O., et al. 2010, in Astronomical Society of the Pacific Conference Series, Vol. 422, Astronomical Society of the Pacific Conference Series, ed. J. Martí, P. L. Luque-Escamilla, & J. A. Combi, 265–+

Ohm, S., van Eldik, C., & Egberts, K. 2009, Astroparticle Physics, 31, 383

Ong, R. A., Acciari, V. A., Arlen, T., et al. 2009, ArXiv e-prints

Paladini, R., Burigana, C., Davies, R. D., et al. 2003, A&A, 397, 213

Pittori, C., Verrecchia, F., Chen, A. W., et al. 2009, A&A, 506, 1563

Porter, T. A., Moskalenko, I. V., & Strong, A. W. 2006, ApJ, 648, L29

Ptuskin, V. S. & Zirakashvili, V. N. 2005, A&A, 429, 755

Pueyo, Y. & Alados, C. 2007, Basic and Applied Ecology, 8, 158

Pueyo, Y., Alados, C., García-Ávila, B., et al. 2009, Restoration Ecology, 17, 908

Reich, W., Fuerst, E., Haslam, C. G. T., Steffen, P., & Reif, K. 1984, A&AS, 58, 197

Reimer, O., Funk, S., Torres, D. F., & et al. 2008, in International Cosmic Ray Conference, Vol. 2, International Cosmic Ray Conference, 613–616

Renaud, M., Goret, P., & Chaves, R. C. G. 2008a, in American Institute of Physics Conference Series, Vol. 1085, American Institute of Physics Conference Series, ed. F. A. Aharonian, W. Hofmann, & F. Rieger, 281–284

Renaud, M., Hoppe, S., Komin, N., et al. 2008b, in American Institute of Physics Conference Series, Vol. 1085, American Institute of Physics Conference Series, ed. F. A. Aharonian, W. Hofmann, & F. Rieger, 285–288

Reynolds, S. P., Borkowski, K. J., Green, D. A., et al. 2008, ApJ, 680, L41

Reynolds, S. P. & Keohane, J. W. 1999, ApJ, 525, 368

Rietkerk, M., Dekker, S., de Ruiter, P., & van de Koppel, J. 2004, Science, 305, 1926

Rietkerk, M., Ketner, P., Stroosnijder, L., & Prins, H. 1996, Journal of Range Management, 49, 512

Rietkerk, M. & van de Koppel, J. 2008, Trends in Ecology & Evolution, 23, 169

Roberts, M. & et al. 1997, in International Cosmic Ray Conference, Vol. 3, International Cosmic Ray Conference, 281–+

Roger, R. S., Milne, D. K., Kesteven, M. J., Wellington, K. J., & Haynes, R. F. 1988, ApJ, 332, 940

Romani, R. W., Ng, C.-Y., Dodson, R., & Brisken, W. 2005, ApJ, 631, 480

Rowell, G. P., Dazeley, S. A., Edwards, P. G., Patterson, J. R., & Thornton, G. J. 1998, A&A, 332, 194

Russeil, D. 2003, A&A, 397, 133

Sakano, M., Koyama, K., Murakami, H., Maeda, Y., & Yamauchi, S. 2002, ApJS, 138, 19

Saken, J. M., Fesen, R. A., & Shull, J. M. 1992, ApJS, 81, 715

Scanlon, T., Caylor, K., Levin, S., & Rodriguez-Iturbe, I. 2007, Nature, 449, 209

Scheffer, M., Bascompte, J., Brock, W., et al. 2009, Nature, 461, 53

Scheffer, M., Carpenter, S., Foley, J., Folke, C., & Walker, B. 2001, Nature, 413, 591

Schröder, A., Persson, L., & De Roos, A. 2005, Oikos, 110, 3

Skrutskie, M. F., Cutri, R. M., Stiening, R., et al. 2006, AJ, 131, 1163

Sluiter, R. & de Jong, S. 2007, Landscape Ecology, 22, 559

Suding, K., Gross, K., & Houseman, G. 2004, Trends in Ecology & Evolution, 19, 46

Sugizaki, M., Mitsuda, K., Kaneda, H., et al. 2001, ApJS, 134, 77

Swanenburg, B. N., Bennett, K., Bignami, G. F., et al. 1981, ApJ, 243, L69

Sztajno, M., van Paradijs, J., Lewin, W. H. G., et al. 1985, ApJ, 299, 487

Tanimori, T. & et al. 2005, in International Cosmic Ray Conference, Vol. 4, International Cosmic Ray Conference, 215–218

Taylor, J. H. & Cordes, J. M. 1993, ApJ, 411, 674

Taylor, J. H., Manchester, R. N., & Lyne, A. G. 1993, ApJS, 88, 529

Temim, T., Slane, P., Reynolds, S. P., Raymond, J. C., & Borkowski, K. J. 2010, ApJ, 710, 309

Terrier, R., Mattana, F., Djannati-Atai, A., et al. 2008, in American Institute of Physics Conference Series, Vol. 1085, American Institute of Physics Conference Series, ed. F. A. Aharonian, W. Hofmann, & F. Rieger, 312–315

Thompson, D. J., Arzoumanian, Z., Bertsch, D. L., et al. 1992, Nature, 359, 615

Thompson, D. J., Bailes, M., Bertsch, D. L., et al. 1996, ApJ, 465, 385

Tibolla, O. 2009, in American Institute of Physics Conference Series, Vol. 1112, American Institute of Physics Conference Series, ed. D. Bastieri & R. Rando, 211–222

Tibolla, O., Komin, N., Kosack, K., & Naumann-Godo, M. 2009, in American Institute of Physics Conference Series, Vol. 1112, American Institute of Physics Conference Series, ed. D. Bastieri & R. Rando, 233–237

Torres, D. F., Domingo-Santamaría, E., & Romero, G. E. 2004, ApJ, 601, L75

Truelove, J. K. & McKee, C. F. 1999, ApJS, 120, 299

Vallée, J. P. 2008, AJ, 135, 1301

van der Hucht, K. A. 2001, New A Rev., 45, 135

van der Swaluw, E., Achterberg, A., Gallant, Y. A., & Tóth, G. 2001, A&A, 380, 309

Von Hardenberg, J., Meron, E., Shachak, M., & Zarmi, Y. 2001, Physical Review Letters, 87, 198101

Wang, C. 2008, ApJ, 686, 337

Wang, N., Manchester, R. N., Pace, R. T., et al. 2000, MNRAS, 317, 843

Weekes, T. C., Cawley, M. F., Fegan, D. J., et al. 1989, ApJ, 342, 379

Weinstein, A. & for the VERITAS Collaboration. 2009, ArXiv e-prints

Westerhout, G. 1958, Bull. Astron. Inst. Netherlands, 14, 215

White, E., Enquist, B., & Green, J. 2008, Ecology, 89, 905

White, R. L., Becker, R. H., & Helfand, D. J. 2005, AJ, 130, 586

Wilson, R. W. & Bolton, J. G. 1960, PASP, 72, 331

Wright, A. E., Griffith, M. R., Burke, B. F., & Ekers, R. D. 1994, ApJS, 91, 111

Yamazaki, R., Kohri, K., Bamba, A., et al. 2006, MNRAS, 371, 1975

Yoshikoshi, T., Mori, M., Edwards, P. G., et al. 2009, ApJ, 702, 631

Yusef-Zadeh, F., Hewitt, J. W., & Cotton, W. 2004, ApJS, 155, 421

Zanin, R. & for the MAGIC collaboration. 2009, ArXiv e-prints

Zoonematkermani, S., Helfand, D. J., Becker, R. H., White, R. L., & Perley, R. A. 1990,
    ApJS, 74, 181

Zou, W. Z., Hobbs, G., Wang, N., et al. 2005, MNRAS, 362, 1189

Acknowledgements

Curriculum Vitae

I was born near Springfield, Massachusetts (USA), in Ludlow, on June 10, 1980. I graduated from Ludlow Senior High School with high honors in 1998. I then began my undergraduate studies in astronomy and physics at Boston University, having received a University Scholarship. My first research experiences came early at the BU Center for Space Physics, studying the structure and dynamics of the Jovian magnetosphere under the supervision of Prof. Theodore Fritz and supported in part by a research award from the BU Undergraduate Research Opportunities Program. Later, I studied the connection between the solar wind and Earth's magnetosphere under the supervision of Prof. Harlan Spence. In my last year of studies, I also interned part-time at nearby Physical Sciences, Inc., learning about applied space physics, and was the Vice President of the BU Astronomical Society. Graduating *cum laude* in 2002, I then took a full-time position as a Scientist at PSI, where I worked on the research and development of space-based energetic particle detectors and ground-based geophysical infrasound sensors.

I moved to The Netherlands in 2005 to pursue a Masters degree in astrophysics at Utrecht University. My thesis was in astroparticle physics, where, as a member of the IceCube Collaboration, I studied the correlated keV to TeV variability of blazars and the implications for neutrino detection, under the supervision of Prof. Dr. John Heise and Prof. Dr. Nick van Eijndhoven.

In 2007, I moved to Germany to begin my Ph.D. studies in very-high-energy gamma-ray astronomy under the supervision of Prof. Dr. Werner Hofmann at the Max Planck Institute for Nuclear Physics and University of Heidelberg. My duties involved assisting the teaching of practical laboratory courses for physics undergraduates. Now as a member of the H.E.S.S. Collaboration, I focused on the continuation and extension of the H.E.S.S. Galactic Plane Survey and discovery of new astrophysical sources of VHE gamma rays. I attended numerous conferences, giving talks at the Heidelberg International Symposium on High-energy Gamma-ray Astronomy, annual German Physical Society (DPG) Meetings, International Cosmic Ray Conference, Ringberg Workshop on the GeV to TeV Connection, bi-annual H.E.S.S. Collaboration Meetings, and also organized a meeting of the H.E.S.S.

Survey Working Group in Heidelberg. In April 2010, I was named Co-convener of the H.E.S.S. Physics Working Group on Surveys, Galactic Center, Galactic Disc, and Giant Molecular Clouds and thereby also a member of the H.E.S.S. Observation Committee. In my free time, I have developed a professional interest in ecology, in particular the occurance of power-law behavior in arid ecosystems.

Publications

Publications

2010

39. Kéfi, S., Alados, C.L., **Chaves, R.C.G.**, et al., *Is the patch size distribution of vegetation a suitable indicator of desertification processes?: Comment*, 2010, Ecology, in press

38. Acero, F. et al. (**H.E.S.S. Collaboration**), *Discovery and follow-up studies of the extended, off-plane, VHE gamma-ray source HESS J1507-622*, 2010, A&A, in press, arXiv:1010.4907

37. Abramowski, A., et al. (**H.E.S.S. Collaboration**), *Revisiting the Westerlund 2 Field with the H.E.S.S. Telescope Array*, 2010, A&A, in press, arXiv:1009.3012

36. Tam, P.H.T., Wagner, S., Tibolla, O., & **Chaves, R.C.G.**, *A search for VHE counterparts of Galactic Fermi bright sources and GeV to TeV spectral characterization*, 2010, A&A, 518, A8

35. Aharonian, F., et al. (**H.E.S.S. Collaboration**), *Discovery of VHE -rays from the BL Lacertae object PKS 0548-322*, 2010, A&A, 521, A69

34. Abramowski, A., et al. (**H.E.S.S. Collaboration**), *VHE gamma-ray emission of PKS 2155-304: spectral and temporal variability*, 2010, A&A, 510, A83

33. Acero, F. et al. (**H.E.S.S. Collaboration**), *First detection of VHE gamma-rays from SN 1006 by H.E.S.S.*, 2010, A&A, 516, A62

32. Abramowski, A. et al. (**H.E.S.S. Collaboration**), *Multi-wavelength Observations of H 2356-309*, 2010, A&A, 516, A56

31. Acero, F., et al. (**H.E.S.S. Collaboration**), *Localizing the VHE γ-ray source at the Galactic Centre*, 2010, MNRAS, 402, 1877

30. Acero, F., et al. (**H.E.S.S. Collaboration**), *PKS 2005-489 at VHE: four years of monitoring with HESS and simultaneous multi-wavelength observations*, 2010, A&A, 511, A52

2009

29. Acero, F., et al. (**H.E.S.S. Collaboration**), *HESS upper limits on very high energy gamma-ray emission from the microquasar GRS 1915+105*, 2009, A&A, 508, 1135

28. Aharonian, F., et al. (**H.E.S.S. Collaboration**), *Probing the ATIC peak in the cosmic-ray electron spectrum with H.E.S.S.*, 2009, A&A, 508, 561

27. Acero, F., et al. (**H.E.S.S. Collaboration**), *Detection of Gamma Rays from a Starburst Galaxy*, 2009, Science, 326, 1080

26. Aharonian, F., et al. (**H.E.S.S. Collaboration**), *Very high energy gamma-ray observations of the binary PSR B1259-63/SS2883 around the 2007 Periastron*, 2009, A&A, 507, 389

25. Aharonian, F., et al. (**H.E.S.S. Collaboration**), *Spectrum and variability of the Galactic center VHE gamma-ray source HESS J1745-290*, 2009, A&A, 503, 817

24. Aharonian, F., et al. (**H.E.S.S. Collaboration**), *Simultaneous multiwavelength observations of the second exceptional γ-ray flare of PKS 2155-304 in July 2006*, 2009, A&A, 502, 749

23. Aharonian, F., et al. (**H.E.S.S. Collaboration**), *Constraints on the multi-TeV particle population in the Coma galaxy cluster with HESS observations*, 2009, A&A, 502, 473

22. Acciari, V.A., et al. (VERITAS Collaboration, VLBA 43 GHz M87 Monitoring Team, **H.E.S.S. Collaboration**, MAGIC Collaboration), *Radio Imaging of the Very-High-Energy gamma-Ray Emission Region in the Central Engine of a Radio Galaxy*, 2009, Science, 325, 444

21. Aharonian, F., et al. (**H.E.S.S. Collaboration**), *Detection of very high energy radiation from HESS J1908+063 confirms the Milagro unidentified source MGRO J1908+06*, 2009, A&A, 499, 723

20. Aharonian, F., et al. (**H.E.S.S. Collaboration**), *Simultaneous Observations of PKS 2155-304 with HESS, Fermi, RXTE, and Atom: Spectral Energy Distributions and Variability in a Low State*, 2009, ApJ Letters, 696, L150

19. Aharonian, F., et al. (**H.E.S.S. Collaboration**), *HESS upper limit on the very high energy gamma-ray emission from the globular cluster 47 Tucanae*, 2009, A&A, 499, 273

18. Aharonian, F., et al. (**H.E.S.S. Collaboration**), *Discovery of Very High Energy gamma-Ray Emission from Centaurus a with H.E.S.S.*, 2009, ApJ Letters, 695, L40

17. Aharonian, F., et al. (**H.E.S.S. Collaboration**), *Discovery of Gamma-Ray Emission From the Shell-Type Supernova Remnant RCW 86 With HESS*, 2009, ApJ, 692, 1500

16. Aharonian, F., et al. (**H.E.S.S. Collaboration**), *HESS observations of gamma-ray bursts in 2003-2007*, 2009, A&A, 495, 505

15. Aharonian, F., et al. (**H.E.S.S. Collaboration**), *Very high energy gamma-ray observations of the galaxy clusters Abell 496 and Abell 85 with HESS*, 2009, A&A, 495, 27

14. Aharonian, F., et al. (**H.E.S.S. Collaboration**), *A Search for a Dark Matter Annihilation Signal Toward the Canis Major Overdensity with H.E.S.S.*, 2009, ApJ, 691, 175

13. Aharonian, F., et al. (**H.E.S.S. Collaboration**), *HESS Observations of the Prompt and Afterglow Phases of GRB 060602B*, 2009, ApJ, 690, 1068

2008

12. Aharonian, F., et al. (**H.E.S.S. Collaboration**), *Energy Spectrum of Cosmic-Ray Electrons at TeV Energies*, 2008, Phys. Rev. Letters, 101, 261104

11. Aharonian, F., et al. (**H.E.S.S. Collaboration**), *Simultaneous HESS and Chandra observations of Sagitarius Astar during an X-ray flare*, 2008, A&A, 492, L25

10. Aharonian, F., et al. (**H.E.S.S. Collaboration**), *Discovery of a VHE gamma-ray source coincident with the supernova remnant CTB 37A*, 2008, A&A, 490, 685

9. Aharonian, F., et al. (**H.E.S.S. Collaboration**), *Limits on an Energy Dependence of the Speed of Light from a Flare of the Active Galaxy PKS 2155-304*, 2008, Phys. Rev. Letters, 101, 170402

8. Aharonian, F., et al. (**H.E.S.S. Collaboration**), *Search for gamma rays from dark matter annihilations around intermediate mass black holes with the HESS experiment*, 2008, Phys. Rev. D, 78, 072008

7. Aharonian, F., et al. (**H.E.S.S. Collaboration**), *Chandra and HESS observations of the supernova remnant CTB 37B*, 2008, A&A, 486, 829

6. Aharonian, F., et al. (**H.E.S.S. Collaboration**), *Discovery of VHE gamma-rays from the high-frequency-peaked BL Lacertae object RGB J0152+017*, 2008, A&A, 481, L103

2007

5. **Chaves, R.C.G.** (Advisors: N. van Eijndhoven, J. Heise & A. Achterberg), *A Multi-wavelength Approach to Point Source Studies of Blazars with the IceCube Neutrino Telescope*, 2007, Universiteit Utrecht, M.Sc. Thesis

2006

4. Galica, G.E., Coxe, R.L., **Chaves, R.C.G.**, et al. (Physical Sciences, Inc.), *Scintillator-based Low-energy Imaging Particle Spectrometer*, 2006, NASA Scientific and Technical Aerospace Rpts., Volume 44, Issue 13, Page 542, PSI Scientific Report PSI-SR-1223 for U.S. Air Force Research Lab.

3. Kern, F.R., Africk, S.A., Cataldi, P., & **Chaves, R.C.G.** (Physical Sciences, Inc.), *Low Noise Infrasonic Sensor System with High Reduction of Natural Background Noise*, 2006, PSI Technical Report PSI-1370-TR-1896 for U.S. Defense Threat Reduction Agency (DTRA-TR-04-4)

2004

2. Gittins, C. & **Chaves, R.C.G.** (Physical Sciences, Inc.), *Independent Components Analysis for AIRIS [Adaptive InfraRed Imaging Spectroradiometer] Signal Processing*, 2004, PSI Technical Report PSI-9035-TR-2033

2003

1. Sciré-Scapuzzo, F. & **Chaves, R.C.G.** (Physical Sciences, Inc.), *Design and Analysis of High Accuracy Positioning [GPS] Experiment Validation System*, PSI Technical Report PSI-2756-TR-1824 for Mitsubishi Electric Co. Space System Dept.

Conference proceedings

2010

12. Tam, P.H.T., Wagner, S., Tibolla, O., & **Chaves, R.C.G.**, *A search for VHE counterparts of galactic Fermi sources*, 2010, Proc. of the 7th AGILE Workshop: The Bright γ-ray Sky (Frascati, Italy), arXiv:1001.2950

2009

11. Tibolla, O., **Chaves, R.C.G.**, Domainko, W., de Jager, O., Kaufmann, S., Wagner, S., Komin, N., Kosack, K., Fiasson, A., & Renaud, M. (H.E.S.S. Collaboration), *New unidentified H.E.S.S. Galactic sources*, 2009, eProc. of the Fermi Symposium (Washington, D.C.), arXiv:0912.3811

10. **Chaves, R.C.G.**, et al. (H.E.S.S. Collaboration), *Extending the H.E.S.S. Galactic Plane Survey*, 2009, Proc. of the 31st ICRC (Lodz, Poland), arXiv:0907.0768

9. F asson, A., Marandon, V., **Chaves, R.C.G.**, et al. (H.E.S.S. Collaboration), *Discovery of a VHE gamma-ray source in the W51 region*, 2009, Proc. of the 31st ICRC (Lodz, Poland)

8. Tibolla, O., **Chaves, R.C.G.**, et al. (H.E.S.S. Collaboration), *New unidentified H.E.S.S. Galactic sources*, 2009, Proc. of the 31st ICRC (Lodz, Poland), arXiv:0907.0574

7. Hoppe, S., de Oa Wilhemi, E., Khlifi, B., **Chaves, R.C.G.**, et al. (H.E.S.S. Collaboration), *Detection of very-high-energy gamma-ray emission from the vicinity of PSR B1706-44 with H.E.S.S.*, 2009, Proc. of the 31st ICRC (Lodz, Poland), arXiv:0906.5574

6. Feinstein, F., Fiasson, A., Gallant, Y., **Chaves, R.C.G.**, et al. (H.E.S.S. Collaboration), *What do supernova remnants interacting with molecular clouds reveal?*, 2009, AIP Conf. Series (Science with the new generation of high energy gamma-ray experiments: Proc. of the 6th Ed.: Bridging the Gap Between GeV and TeV), 1112, 54

5. Fiasson, A., **Chaves, R.C.G.**, et al. (H.E.S.S. Collaboration), *Probing cosmic ray acceleration through molecular clouds in the vicinity of supernova remnants*, 2009, Proc. of the 44th Rencontres de Moriond - Very High Energy Phenomena in the Universe (La Thuile, Italy)

2008

4. **Chaves, R.C.G.**, et al. (HE.S.S. Collaboration), *The H.E.S.S. Galactic Plane Survey*, 2008, AIP Conf. Series (Proc. of the 4th Intl. Mtg. on High Energy Gamma-Ray Astronomy), 1085, 219

3. **Chaves, R.C.G.**, Renaud, M., et al. (H.E.S.S. Collaboration), *HESS J1848-018: Discovery Of VHE gamma-ray Emission From The Direction Of W 43*, 2008, AIP Conf. Series (Proc. of the 4th Intl. Mtg. on High Energy Gamma-Ray Astronomy), 1085, 372

2. Renaud, M., Goret, P., & **Chaves, R.C.G.** (HE.S.S. Collaboration), *On the nature of HESS J1503-582 revealed by the H.E.S.S. experiment: Coincidence with a FVW?*, 2008, AIP Conf. Series (Proc. of the 4th Intl. Mtg. on High Energy Gamma-Ray Astronomy), 1085, 281

2005

1. G.E. Galica, Coxe, R.L., **Chaves, R.C.G.**, et al. (Physical Sciences, Inc.), *Scintillator-based Low-Energy Imaging Particle Spectrometer*, 2005, JAXA 9th Spacecraft Charging Tech. Conf. (Tsukuba, Japan), PSI Scientific Report PSI-SR-1223 for U.S. Air Force Research Lab.